



ÉCOLE
CENTRALE LYON

N° d'ordre NNT: 2025ECDL0016

THÈSE DE DOCTORAT DE L'UNIVERSITÉ DE LYON
opérée au sein de l'École Centrale de Lyon

École Doctorale N° 162
Mécanique Énergétique Génie Civil Acoustique

Spécialité de doctorat : Acoustique

Soutenue publiquement le 06/06/2025, par

Amal Roy Murali

**Dynamics, Mechanisms, and Surrogate Modelling,
of
Noise from a Leading Edge Slat**

Devant le jury composé de:

Benjamin Cotté	Maître de Conférences HDR	École Nationale Supérieure de Techniques Avancées	Rapporteur
Florent Margnat	Maître de Conférences HDR	Université de Poitiers	Rapporteur
Anita Schulz	Professeure	Hochschule für Technik und Wirtschaft Berlin	Examinaterice
Emmanuel Lévêque	Directeur de recherche CNRS	École Centrale de Lyon	Examinateur
Marc C. Jacob	Professeur des universités	École Centrale de Lyon	Directeur de Thèse
Vincent Clair	Maître de Conférences	École Centrale de Lyon	Co-encadrant
Michel Roger	Professeur de Universités	École Centrale de Lyon	Invité
Florian Guiho	Docteur Ingénieur	Airbus SAS	Invité

“There are many paths to enlightenment. Be sure to take one with a heart.”

~ Lao Tzeu

Acknowledgements

First and foremost, I would like to express my deepest gratitude to my thesis advisors, Prof. Marc C Jacob, Dr. Vincent Clair, and Prof. Michel Roger, for their support, guidance, and feedback throughout this research journey. Their expertise, patience, and encouragement were instrumental in shaping this work and helping me navigate its challenges. Prof. Marc's supervision is the major pillar of this work. Dr. Vincent Clair's well reasoned suggestions regarding the research has enabled a comfortable progress from early on. Special thanks to Prof. Michel Roger for many of his ideas and suggestions. Apart from formal supervision, my heartfelt gratitude to Dr. Jerome Boudet whose sharing of knowledge and time to assist me in the process of this thesis was instrumental to its completion.

My thanks go to my colleagues and peers at École Centrale de Lyon for their camaraderie and technical assistance. The collaborative environment fostered by this group made the research process both productive and enjoyable. I wish to mention the members of my Thesis Monitoring Committee, Dr. Thomas Castelain and Dr. Sébastien Besset, who were instrumental in guiding me through the difficult terrain of completion of PhD. I acknowledge the financial and institutional support provided by Airbus, and the early support from its engineers, namely, Dr. Florian Guiho, Dr. Maxime Itasse, and Dr. Nicolas Molin, which made this research possible.

Special thanks to Prof. Sergey Karabasov and Prof. Rob Krams of Queen Mary University of London, and his research team for their unwavering support both personally and professionally during this academic journey. From managing life as an international research student to invigorating the collaborative research spirit, their timely contributions were inevitable to complete this journey.

I am eternally grateful to my family — my parents, and my brother — for their unconditional love, endless encouragement, and sacrifices that enabled me to pursue my academic goals. My mother's belief in me has been a constant source of motivation and continues to fuel my quest for higher successes. My heartfelt gratitude extends to my dearest family friend Dr. Koshy Idicula and his family, for being my strength and a guardian to my family in my absence at home.

To my girlfriend Anagha, and my friends especially Ananthu, Anjali, Augustin, Isa, Livia, Marie, Nathan, and Stephano, thank you for your moral supports, laughter, games, night outs, homely dinners, and also mindful understanding during difficult times, both personally and communally. You reminded me to stay grounded and persevere even when the path seemed daunting. Even to those who chose not to be friends in this brief journey of life, thank you for motivating me to be careful with my unconditional camaraderie.

While this thesis represents my individual effort, it stands on the collective contributions of everyone mentioned above. Any errors or shortcomings remain my own.

Contents

1	Introduction to Slat Noise	14
2	Literature	20
2.1	TE Noise	20
2.2	Airfoil Self-Noise	21
2.3	Cavity Noise	22
2.4	Slat Cove Dynamics and Noise	24
2.4.1	Slat Noise Mechanisms	24
2.4.2	State of the Art	26
2.5	Conclusion	27
3	LBM for Aeroacoustics	28
3.1	Introduction	28
3.2	Overview	29
3.3	Aeroacoustics	33
3.4	Acoustic Test Case	34
3.4.1	Dissipation and Dispersion	34
3.4.2	Simulation Details	35
3.4.3	Simulation Results	36
3.5	FWH Analogy	38
3.5.1	TurbAcAn (FWH)	42
3.5.1.1	Analytical solution	43
3.5.1.2	Choice of time stepping and cell size	45
3.5.1.3	Results	45
3.6	Validation Case	46
3.6.1	Base template	46
3.6.2	Spanwise Periodic conditions	46
3.6.3	Coordinate System	49
3.6.4	Meshing	49
3.6.5	Temporal scales	51
3.7	Wind Tunnel	52
3.8	Conclusion	53
4	Detailed Study of Nominal Slat Configuration	54
4.1	Introduction	54
4.2	Validation	54
4.2.1	Convergence	55

4.2.2	Mean wall pressure distributions	55
4.2.3	Unsteady Wall pressure data	56
4.2.4	Hot-wire probes	58
4.3	Mean flow	59
4.4	FWH Computation	67
4.5	Cove Dynamics	69
4.6	Similar simulations	75
4.6.1	Simulation with wind tunnel geometry and lateral side walls included	75
4.6.2	Simulation with rectangular lateral plates only	77
4.6.3	Simulation with a reduced span and periodic boundary conditions	80
4.6.4	Reduced Re Sim	80
4.7	Streamline Curvature	81
4.8	Acoustics	88
4.9	Spanwise Trends	91
4.9.1	Hot-Wire Probes	93
4.10	Cove bursting as a modulating mechanism	97
4.11	Conclusion	100
5	Design of Experiments	102
5.1	Introduction	102
5.2	Bayes' Theorem	103
5.3	Gaussian Processes	104
5.4	Bayesian GP	105
5.5	Noise Surrogate	109
5.6	Initial dataset	111
5.7	Active Learning	112
5.8	Uncertainty Propagation	114
5.9	Acquisition Function	116
5.10	Results	118
5.10.1	Feature Extraction	118
5.10.2	Surrogate model	119
5.11	Conclusions	123
6	Cove Vortex Dynamics	125
6.1	Introduction	125
6.2	Mean Shear Layer Shape	127
6.3	Far-field Spectra	128
6.4	Shear Layer Curvature	130
6.5	Curvature Richardson	133
6.6	Spanwise Modes	136
6.7	Conclusions	142
7	Conclusions and Future Perspectives	146

A Flow and Acoustic computation details	164
A.1 Acoustic Pulse Propagation	164
A.1.1 Wave Propagation according to Linearized Navier-Stokes	164
A.1.2 Temporal Analysis	165
A.1.3 Spatial Analysis	165
A.1.4 Gaster Transformation	165
A.1.5 Useful approximation for Isothermal Adiabatic Pulse Propagation	165
A.2 FWH Surface Tests	166
A.2.0.1 Oval Surfaces	166
A.3 Wind Tunnel Simulation:	167
A.4 Auxiliary data	171
B Dataset	176
B.1 Description	176
B.2 All simulations and results	177
B.2.1 Auxiliary results	178
B.2.1.1 Shear layer and recirculation bubble shapes	178
B.2.2 Far-field Noise spectra	179
B.2.3 Shear Layer Curvature Profiles	179
B.2.4 Curvature Richardson Numbers	179
B.2.5 Spanwise Cells	179
B.2.6 Spanwise Variation of Spanwise-Velocity Spectra	185

List of Figures

1.1	An Airbus A310-300 wing with slat and flaps deployed. Photo Credit: By Adrian Pingstone (2007), from public domain.[1]	15
1.2	Comparison of standardized HLD geometries	16
1.3	Schematic showing the potential noise sources in turbulent flow of a leading edge slat cove	17
1.4	Schematic of a typical slat noise spectrum showing the broadband component, tones, and high frequency hump	18
3.1	A simple Gaussian pulse in spatial, temporal, and frequency domains	36
3.2	Time history of the propagating pulse at positions downstream of the right traveling pulse using <i>ProLB</i> simulation	37
3.3	The dissipation and dispersion results for an initial acoustic Gaussian pulse - ProLB	38
3.4	The dissipation and dispersion results for an initial acoustic Gaussian pulse - PowerFlow	38
3.5	FWH surface placement along with the HLD geometry put into perspective	42
3.6	FWH surface test case using a pulsating spherical source	44
3.7	Results for pulsating pressure source test case for TurbAcAn showing signals obtained at various probe coordinates	47
3.8	Schematic of the domain, boundary conditions, and the slat-airfoil configuration.	48
3.9	LBM mesh sizes in the domain and around the HLD geometry	50
3.10	Left: The HLD mockup geometry installed on the wind tunnel using lateral sides plates. Right: A drawing of the dimensions of the wind tunnel nozzle exit.	52
3.11	The simulation domain of the wind tunnel geometry with the tunnel and HLD installed	53
4.1	Unsteady data monitored to check convergence of dynamics in the LBM simulation	55
4.2	Pressure Coefficient $-C_p$ over the surface of HLD obtained using the LBM simulation is compared against the experimental data	56
4.3	Wallpressure PSD inside the slat cove compared between the simulation in free stream, simulation with wind tunnel, and the experimental data	57
4.4	Velocity magnitude data compared between the simulation with and without the wind tunnel geometry included in the LBM setup, against the VALIANT experimental data	58
4.5	Pressure Coefficient contours in and around the slat cove	59
4.6	The time-averaged velocity field in the slat cove identifying the shear layer shape and regions of peak velocity components.	60
4.7	Time-averaged spanwise velocity field in the slat cove	60
4.8	Spanwise velocity visualized on a cutplane parallel to the spanwise Z axis inside the cove region	61
4.9	Contours of spanwise velocity showing the cell formation inside the cove region	61

4.10 Spanwise cell formations: Different positions along the mean shear layer (left) is used to place visualizations planes PL1, PL2, and PL3, and are used to show the spatial modulations of the time averaged spanwise velocity component (right) along the spanwise direction inside the slat cove.	62
4.11 Spanwise modulations of the time averaged spanwise velocity on a visualization plane in between PL1 and PL2	62
4.12 Image of the eigen mode demonstrating the spanwise instability mode for flow over a backward facing step from the work of Barkley et al. [2]. The original caption read: “Three-dimensional flow structure of the critical eigenmode at $Re = 750$ and $\beta = 0.9$. Contours indicate the strength of the streamwise velocity component and vectors show the (v, w) flow pattern in each cross-sectional plane: $x = 1.2, 6.2$ and 12.2 .”	63
4.13 The spanwise modes in a rectangular cavity with periodic spanwise conditions from the work of Brès and Colonius [3]. The original caption read: “Visualization of the three-dimensional flow for run 2M0325-3D at six different times (a–f) corresponding to approximately one-sixth phase intervals of a half-period of the three-dimensional instability. The iso-surfaces represent the spanwise velocity levels $w/U = -0.01$ and $w/U = 0.01$. The whole spanwise extent of the cavity is shown and the wavelength $\lambda/D = 1$ of the instability can clearly be observed. The velocity vectors in the streamwise cross-section at $z = 0$ are shown inside the cavity and once in the free-stream for comparison.”	65
4.14 C-shaped FWH Surface and the dilatation field around the HLD	68
4.15 Numerical microphones relative to the FWH surface	69
4.16 Sound pressure data obtained at select numerical microphones using FWH approach	70
4.17 Sound pressure data computed at numerical microphones using FWH approach for the free stream configuration	71
4.18 Iso-surfaces of Q-Criterion, $\frac{Q}{M} = 10^9$ where $M = 0.14$, is the flow Mach number. The region of sparsity for the small scale recirculating structure is demarcated with the yellow line	72
4.19 Iso-surfaces of Q-Criterion, $\frac{Q}{M} = [10^9, 1.4 \times 10^8]$, where $M = 0.14$ is the flow Mach number	73
4.20 Streamwise vortices ejected from the slat gap	74
4.21 Streamwise counter rotating vortex pairs at the slat gap visualized using a diverging colourmap based on the streamwise vorticity	75
4.22 The unsteady aerodynamic pressure field in the slat cove identifying the trajectory of the spanwise coherent structure along the curved shear layer	76
4.23 The unsteady velocity field in the slat cove visualized using a narrow colorbar corresponding to velocity values $U = \pm 20$ m/s. The freestream velocity is 50 m/s.	77
4.24 Time-averaged spanwise velocity on spanwise planes at different locations in the slat cove region for simulation which includes the spanwise plates and wind tunnel geometry	78
4.25 Schematic of the flow simulation setup. For frame coordinate system, the incoming flow is along the X axis and spanwise direction is along the Z axis.	79
4.26 The flow separates possibly due to disproportionate interference from turbulence due to the side walls and plate corner.	79
4.27 Spanwise cell formation is still noticeable although the cove shape is distorted. Spanwise direction is along the Z axis and the visualization plane is akin to 4.24a.	80
4.28 Time-averaged velocity magnitude field for simulation using reduced span	81
4.29 Time-averaged spanwise velocity field for simulation using reduced span	82
4.30 Spanwise cells formed near the early shear layer for the case of downscaled geometry	83

4.31	The streamline obtained using Runge-Kutta integration of the velocity field from a source point near the slat cusp	83
4.32	Local curvature along a streamline in the shear layer	84
4.33	Local deceleration and location of the impingement within the flow field	85
4.34	Local curvature along a streamline in the shear layer	87
4.35	Dilatation field over the HLD from the unsteady data	88
4.36	The unsteady dilatation field is visualized using the normalized time derivative of the density, $-\frac{1}{\rho} \frac{d\rho}{dt}$. This representation is strictly valid only in the absence of mean convective flow, where the material derivative reduces to the temporal derivative.	89
4.37	The Fourier filtered pressure fields at a select frequencies corresponding to the peaks in farfield spectra	90
4.38	Wall pressure probe locations and their spanwise replications with respect to the slat geometry.	91
4.39	Wall pressure spectra from spanwise replicas of probes on spanwise center plane showing variation of spectra along the span	92
4.40	Hot-wire probe locations used for point recordings in the simulation	93
4.41	Time-averaged velocity and components from the SL probe file placed near slat cusp	94
4.42	Unsteady velocity spectra from spanwise replicas of probes close to slat cusp	95
4.43	Unsteady velocity spectra from spanwise replicas of probes close to slat cusp	96
4.44	The farfield spectra from experimental study of Jawahar et al. for the 30P30N HLD geometry.	98
4.45	The cove bursting near the mid-span diverging plane at time stamps separated by 0.005s corresponding to the 200Hz peak in the numerical hot-wire probe data	99
5.1	A sampling of the space of three slat positional variables using canonical LHS (left) and with LHS-MDU	111
5.2	A scatter plot of the initial samples drawn from the domain to create the initial dataset using LHS-MDU	112
5.3	Feature extraction for the spectra using Guo's shape function and Lorentzian peaks, showcasing few cases from the dataset	118
5.4	Scatter plots of the input targets against the 17 predicted target variables used in regression, over datapoints in the training set of first 18 simulations	120
5.5	Spectra predicted using the Gaussian Process Surrogate model	121
5.6	Maximum Coefficient of Variation in the test domain after the last step of active learning executed with total number of simulations at 18.	122
5.7	Progressions during the Bayesian Active Learning	122
5.8	Parametric predictions using the surrogate model by varying the slat overlap (SOL)	123
5.9	Parametric predictions using surrogate model by varying the slat gap (SGP)	124
6.1	Top: The mean shear layer trajectory at mid-span plane for select cases with a strong distortion of the shear layer. Bottom: Corresponding far-field noise spectrum at 90° observer angle showing the variation of tone frequencies as shear layer shape is varied.	129
6.2	Top: The mean shear layer trajectory at mid-span plane for select cases which has a positive slat overlap. Bottom: Corresponding far-field noise spectrum at 90° observer angle showing a different selection of tone frequencies according to shear layer shape variation at same spanwise simulation domain.	129
6.3	Streamline curvature contour obtained under the inviscid assumption for Case 22 demonstrating the identification of impingement location	131

6.4	Curvature distribution along the shear layer for Cases 22 and 26 computed using Eq.6.3, along with the corresponding shear layer shapes and farfield noise spectra.	132
6.5	Comparison of shear layer shape, Curvature Richardson number profile and far-field noise of select cases	134
6.6	Comparison of shear layer shape, Curvature Richardson number profile and far-field noise of select cases	135
6.7	Comparison of the shear layer shape, curvature profile, and the spanwise modulations in three cases with initial curvature lower than Case 22.	137
6.8	Comparison of shear layer shape, curvature profile, and spanwise velocity modulations of three cases with initial curvature higher than Case 22	138
6.9	Power spectral density of spanwise velocity component as a function of spanwise location for cases which has spanwise mode formations	139
6.10	Power spectral density of spanwise velocity component as a function of spanwise location. The low frequency oscillations spanwise homogeneous.	140
6.11	Spanwise variation of low frequency components of the spanwise velocity for Case 4.	141
6.12	Streamline extracted from the mean flow profile for Case 5 suggest that the recirculation in the cove maintains a frequency of 210Hz.	142
6.13	Streamline extracted from the mean flow profile for Case 11 suggest that the recirculation in the cove maintains a frequency of 170Hz	143
6.14	Streamline extracted from the mean flow profile for Case 22 suggest that the recirculation in the cove maintains a frequency of 190Hz	144
6.15	Streamline extracted from the mean flow profile for Case 29 suggest that the recirculation in the cove maintains a frequency of 190Hz	145
7.1	Schematic of the suggested mechanism that explains the intermittency of slat tones observed by Jawahar et al. [4]. The non-dimensional frequency of the bursting has also been established as the recirculation frequency of the cove flow using VALIANT geometry.	147
A.1	Oval FWH surface geometry and placement	166
A.2	Density gradient (temporal) on the oval FWH surface	167
A.4	Flow visualization to demonstrate the low vorticity structures crossing the upper side of FWH surface	167
A.3	Farfield spectra obtained using the oval FWH surface compared to 1) a simulation of the same HLD while simulated by including the wind tunnel geometry and 2) the experimental data from VALIANT program	168
A.5	Wind tunnel simulation setup in ProLB	169
A.6	Coefficient of pressure $-C_p$ over the surface of HLD obtained using the LBM simulations with and without wind-tunnel setup included are compared against the experimental data	170
A.7	The sound pressure spectra computed using simulation run by Airbus using ProLB and FWH approach for the full wind-tunnel installation	172
A.8	Wall pressure spectra for select probes on the slat wall placed along the spanwise center plane	173
A.9	Wall pressure spectra for select probes on the main element wall and on spanwise center plane - set 1	174
A.10	Wall pressure spectra for select probes on the main element wall and on spanwise center plane - set 2	175

B.1	The shear layer trajectory at mid-span plane obtained using time integration of the mean velocity field for parametric cases in the dataset.	180
B.2	Farfield noise spectra for parametric cases obtained using the LBM-FWH computation. Observer location is at 90°to the airfoil at the pressure side.	181
B.3	Curvature profiles along the mean shear layer for parametric cases in the dataset	182
B.4	Curvature Richardson Number profiles along the mean shear layer for all cases in the dataset	183
B.5	Spanwise cells of spanwise velocity demonstrated using 3D isocontours of the same for all cases in the dataset.	184
B.6	Power spectral density of spanwise velocity component as a function of spanwise location	185
B.7	Power spectral density of spanwise velocity component as a function of spanwise location	186
B.8	Power spectral density of spanwise velocity component as a function of spanwise location	187

Nomenclature

Acronyms

- **AOA** – Angle of Attack
- **BGK** – Bhatnagar–Gross–Krook collision model
- **CAA** – Computational Aeroacoustics
- **CFD** – Computational Fluid Dynamics
- **CFL** – Courant–Friedrichs–Lowy condition
- **ECL** – École Centrale de Lyon
- **FFT** – Fast Fourier Transform
- **FWH** – Ffowcs Williams & Hawkings
- **HLD** – High-Lift Device
- **LBM** – Lattice Boltzmann Method
- **LES** – Large Eddy Simulation
- **LHS** – Latin Hypercube Sampling
- **MDU** – Multi-Dimensional Uniformity
- **MRT** – Multi-Relaxation-Time
- **NFFT** – No.of points in FFT window
- **PDF** – Probability Density Function
- **PIV** – Particle Image Velocimetry
- **POD** – Proper Orthogonal Decomposition
- **PPW** – Points Per Wavelength
- **ProLB** – Industrial LBM solver
- **PSD** – Power Spectral Density
- **RSM** – Reynolds Stress Model
- **SDA** – Slat Deflection Angle
- **SGP** – Slat Gap
- **SOL** – Slat Overlap
- **SPL** – Sound Pressure Level
- **TBL** – Turbulent Boundary Layer
- **TE** – Trailing Edge
- **UCB** – Upper Confidence Bound
- **VALIANT** – Experimental program referenced for validation

Symbols

- α_S – Spatial attenuation coeff.
- α_T – Temporal attenuation coeff.
- c – Speed of sound
- c_0 – Ambient speed of sound
- c_S – Spatial phase speed
- c_T – Temporal phase speed
- C_g – Group velocity
- C_p – Pressure coeff.
- Δf – Frequency resolution
- $\Delta\rho$ – Density fluctuation
- f – Frequency
- G – Free-space Green's function [$G = \delta(g)/r$]
- $H(f)$ – Heaviside function
- \hat{A} – Complex amplitude
- \hat{k} – Complex wavenumber
- $\hat{\omega}$ – Complex angular frequency
- $\text{Im}(\cdot)$ – Imaginary part
- k – Real wavenumber
- L – Characteristic length
- L_i – Loading term in FWH
- M – Mach number
- n_j – Component of outward unit normal on surface
- ∇, ∇^2 – Gradient, Laplacian
- P' – Acoustic pressure fluctuation
- P_0 – Reference/mean pressure
- P_{ij} – Stress term on surface
- Q – Thickness term in FWH
- Q_c – Hunt's Q -criterion threshold
- r – Distance between receiver and source
- $\text{Re}(\cdot)$ – Real part
- ρ – Density
- ρ_0 – Ambient density
- ρ_∞ – Free-stream density
- t – Time
- τ – Emission/retarded time
- τ_s – Viscous relaxation time
- T_{ij} – Lighthill stress tensor
- U_∞ – Free-stream velocity
- u_i, u_j – Velocity components
- u_j^Σ – Velocity of the control surface
- ω – Angular frequency
- x – Receiver position vector
- y – Source position vector
- x, y, z – Spatial coordinates
- $\partial/\partial t$ – Time derivative operator
- ε – Gaussian noise in regression
- \mathcal{D} – Dataset of paired observations
- \mathbf{x} – Feature vector (regression)
- \mathbf{w} – Regression weights
- σ_n – Standard deviation of observation noise
- μ – Dynamic viscosity
- μ_B – Bulk (dynamic) viscosity
- ν – Kinematic viscosity
- ν_B – Kinematic bulk viscosity

Chapter 1

Introduction

High-Lift Devices (HLDs) were conceived and tested as an apparatus to improve airplane lift performance as early as the 1940s[5]. They primarily enabled aircrafts to take off from shorter runways as in the case of military requirements and as the jet engine designs were adapted for high-speed cruise, the high-lift wings became necessary to enable take offs and landings with heavy payloads. HLDs also delayed the stall of the airfoil as well as reduced the required angle of attack during take-off allowing better flight controls and enhanced visibility over the main-body leading edge. The aeroacoustics of HLDs became an active area of research slightly later when the airframe noise was identified as a major contributor to aircraft noise[1979]. This was an effect of the rising popularity of high-bypass turbofan engine designs in the 1970s implicitly leading to a sharp reduction in engine noise, making them comparable to noise from landing-gears and HLDs. The latter two, conveniently called the airframe noise, is to date the next engineering bottleneck towards quieter aircraft designs fit for modern aviation[7]. In light of these developments, renewed efforts in airframe noise research were promoted by major economies and set the target for noise reduction efforts by atleast -10 dB on average per aircraft operation (operations near airport) for the year 2020[8]. In the European vision for aviation towards 2050, [9] published in 2011, the long-term target was officially declared as to reduce the noise by “atleast 65%” from that of aircraft technologies in the 2000s – which in quantitative terms is by -15 dB, a representation of the urgency for quieter civil aviation in view of a more sustainable aviation [8, 10, 11]. This also is the fuel behind our current activity and our primary focus is on further detailed characterization of HLD noise sources using advanced computational methods. In this process we also develop tools which enable rapid and data-driven aeroacoustic characterization of such complex engineering flows attempting to bypass the complexity of its numerical modelling.

HLDs typically includes two additional components on a standard wing aerofoil, namely the leading edge slat and the trailing edge flap as shown in Fig.1.1. Both slats and flaps are commonly deployed in tandem during take-off and landing and are thus active noise sources for operation near airports. Among them the leading edge slat cavity has been identified as the dominant noise source for low and mid-frequency characteristics and the trailing edge flap for high frequency noise respectively[12]. In general, a wing with HLD generate 10dB of additional noise than a normal wing [11]. However a complete analysis of its noise mechanisms are hindered when it is part of a larger set of noise sources including the airframe cavity noise, landing gear noise, and installation effects. Hence as part of efforts to isolate behavior of HLD noise sources, standardized sub-scale geometries were created as part of BANC workshops[13]. The popular configuration is the 30P30N where the slat and flap are deflected at 30 degrees from the main element. A schematic of the same is shown in Fig.1.2a. Now, although both the slats and flaps contribute significantly to the total noise, the mechanisms behind the mid-frequency noise generation in the leading edge slat cavity are particularly elusive to engineers due to the complex cove flow dynamics. Hence on



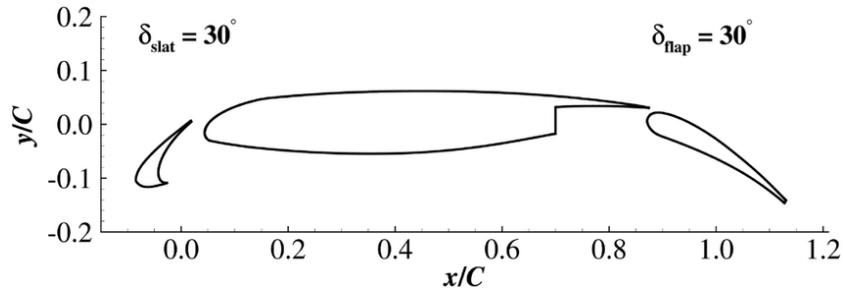
Figure 1.1: An Airbus A310-300 wing with slat and flaps deployed. Photo Credit: By Adrian Pingstone (2007), from public domain.[\[1\]](#)

further sophistication of the investigations, the slat only configuration had to be isolated and studied in detail. For the same, Terracol et al. [14], as part of the recent VALIANT initiative^[15], generated an optimized 2 element configuration with only the slat and main element. Here the flap was replaced with a sharp trailing edge for which the exact shape was determined via numerical optimization – the objective being minimizing numerical difference between the CFD solutions of cove flow between an optimized 2 element geometry and the original 3-element one^[15]. A drawing of the resulting 2 element airfoil is shown in Fig.1.2b.

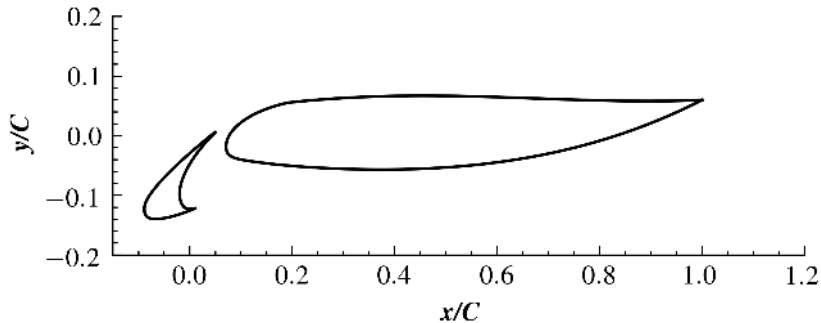
Our study is primarily intended to investigate the slat-only noise phenomena. It includes the cove flow dynamics and the noise generation mechanisms arising from such dynamics. Hence we use the 2 element geometry provided by Terracol et al. [14] and refer to the same as the VALIANT HLD. The positioning of the slat with respect to the main element in this configuration, as shown in Fig.1.2b, will be referred to as the standard geometry as well in contrast to the cases where we change this positioning. It must be emphasized that, since the noise associated with the trailing edge are not of interest, and given that there are no suspected interactions between this trailing edge and the cove flow dynamics via their acoustics, the trailing edge of the wing geometry is also not of practical relevance. Additionally, the removal of the trailing edge flap has an important advantage in enabling experimental studies. The 3 element HLD by design generates a strong lift resulting in a significant deflection of the incoming jet while mounted in the wind tunnel. The deflection necessitates that the wind tunnel installations must be adapted to allow this

deflection. In the 2 element case, the deflection is now reduced due to removal of the deflection by the flap and therefore generates less lift and less deflection. The wind tunnel setup is thus simplified. Given these features VALIANT HLD is adopted for our study.

The activities reported in this thesis was conducted within the MAMBO project at the Laboratory of Fluid Mechanics and Acoustics (LMFA). The laboratory, hosted by Ecole Centrale de Lyon (ECL), has a long standing tradition in computational and experimental aeroacoustics, with many prior experimental studies on slat noise as early as 1998. Ones that deserve special mention are the early experimental studies of slat noise by Perennes and Roger [16], and its modelling attempts by Molin and Roger [17]. The computing facility of ECL, named Newton, and the Irene national supercomputing facility was used to obtain the results presented in our work. A contemporary experimental campaign was also completed during the progress of this thesis which is however not included in the current thesis, but the geometry of the latter which is a subscaled ($x/3$) version of the VALIANT geometry is used for a few exploratory simulations, as will be discussed appropriately.



(a) The 30P30N high-lift airfoil is the three-element standard geometry for experimental and numerical campaigns



(b) The VALIANT two-element geometry numerically optimized to reduce the effect of flap removal upon cove flow dynamics. The chord size C used for the current activity is 0.3m

Figure 1.2: Comparison of standardized HLD geometries

That being the context of our research, to re-investigate slat noise phenomena, it is important to understand the current state of knowledge. We will summarize the current known features here with an extended account of the same and some closely related phenomena in the upcoming chapter.

The slat-only noise phenomena has been extensively documented, although with incomplete explanation, through both experimental campaigns and computational efforts since 1990s[12, 18, 19, 20, 15, 14, 21, 22, 23]. Dobrzynski et al. [12] were among the early researchers to initiate large scale experiments to investigate this phenomena and showed that the leading edge slat has a tonal noise signature. These tones reaching upto 80 dB were first explained to vanish in case of tripped turbulence at the slat's pressure side cusp but additional studies showed that they are persistent irrespective of turbulence conditions[24, 25]. They are typically below 10kHz in frequency range and are identified as mid-frequency tones[26]. A set

of five or more of these tones are supported by a broadband noise component which scales with approximately fifth power of the free stream Mach number[27]. As the wind tunnel facilities improved, in the recent years, an additional tone which appears to be the fundamental of the main evident ones were also identified. It is referred to as the low frequency hump since this component has a broadband and stochastic nature compared to the other tones[28, 29]. An additional broadband peak at very high frequency of 20kHz is also reported and is attributed to the vortex shedding from the thick trailing edge of the slat[30]. A typical slat-only noise spectrum showing these major components are shown in Fig.1.3.

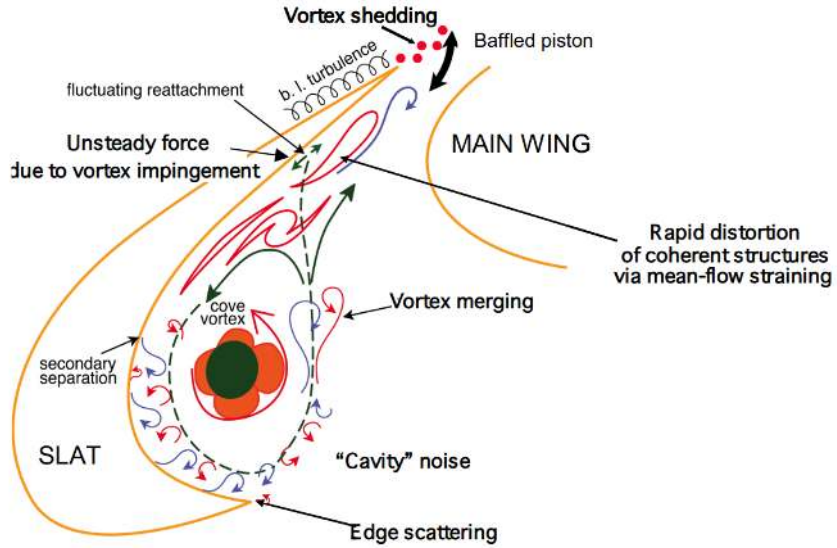


Figure 1.3: Schematic showing the potential noise sources in turbulent flow of a leading edge slat cove, reproduced from the work of Choudhari and Khorrami [31]

The study, or in particular the reasoning on mechanisms underlying slat tones, is but incomplete in the literature. The tonal noise is largely explained based on the feedback mechanism typical in a cavity flow and is called the Rossiter modes[32]. The flow develops strong turbulence as it encounters the pressure side cusp of the slat since there occurs strong shearing of flow between the two sides of the cusp. The phenomena can be explained based on Kelvin-Helmholtz (K-H) instability and leads to periodic shedding of vortices[14, 15]. Since the mean flow after the cusp deviates from free stream to pass through the slat cove, the vortices are also convected through the slat gap. See Fig.1.3 for a schematic. The nozzle effect due to constriction between the slat and main element accelerates the flow and hence the vortices are also accelerated as distorted before ejection. At low angle of attacks, these accelerated vortices impinges on inner wall of the slat trailing edge leading to strong momentum fluctuations near the trailing edge. The flow then splits where one part enters the recirculation in the cove while the other part is ejected out of the slat gap. The impinged vortices generate acoustic waves due to momentum fluctuations and these waves, both the original ones and those amplified by the trailing edge scattering, travel back to the pressure side cusp, influencing the periodicity of vortex shedding at the cusp. Thus the periodic vortex shedding and resulting influence from acoustic waves due to its impingement leads to a resonant cycle in the cove region leading to selection of discrete frequencies and the resulting pressure fluctuations emanate as acoustic waves towards farfield[33, 14]. These tonal waves manifest as narrow band peaks in the noise spectrum.

The broadband components in the spectrum has an alternative explanation although incomplete. It is suggested that the mid-frequency hump (See Fig.1.4) is generated due to the high speed turbulence ejection

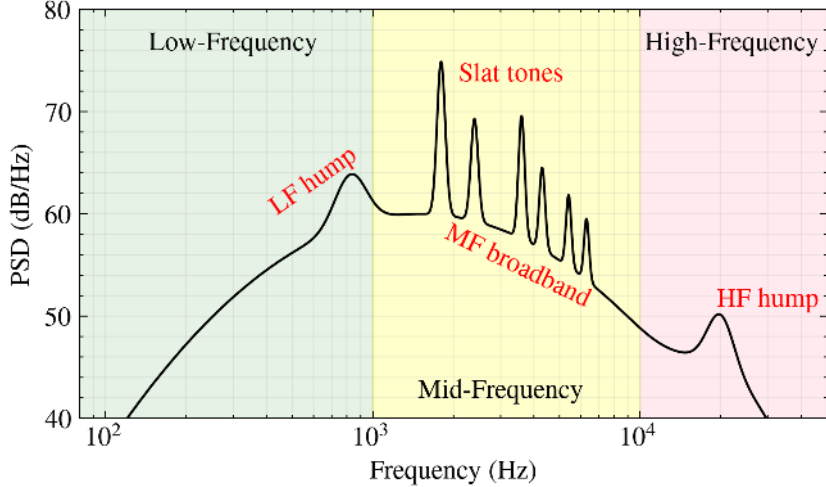


Figure 1.4: Schematic of a typical slat noise spectrum showing the broadband component, tones, and high frequency hump

from the slat gap with a particular influence from the high-amplitude low-frequency fluctuations due to vortex impingement in the upstream. Imamura et al. [34] showed that PSD of turbulence fluctuations downstream of the trailing edge have strong correlation with frequencies of the mid-frequency hump in far-field spectrum. Regarding the high frequency hump, Bolivar [35] showed that frequency of this hump increases with decreasing trailing edge thickness. Imamura et al. [34] also showed that the frequency of this hump have a high energy content in the PSD of ejected turbulence. Hence, it can be assumed that both mid-frequency and high frequency broadband humps are directly related to the turbulence ejection at trailing edge. It is worthy to note that there may exist additional high frequency tones in experimental data due to periodic vortex shedding at the trailing edge but this is not observed in flight conditions[36, 25]. Additionally, more recent advances based on advanced signal processing methods like that of Jawahar et al. [4] has shed light on the intermittent characteristic of the tones and the low frequency broadband hump thus shedding more light into their possible mechanisms. A detailed picture of these dynamics as known in the existing literature are presented in Chapter 2 and further insights from our investigations are presented in Chapter 4.

At the current juncture of this research, it must be acknowledged that the technical tool set available for scientific computing and computational aeroacoustics are also undergoing a rapid expansion. In a recent review on computational aeroacoustics, Moreau [37] has promptly underlined the importance of advanced CFD methods including the Lattice Boltzmann Method (LBM) simulations. On par with expensive high-order schemes for Navier-Stokes equations designed to obtain high fidelity data of the flow dynamics, LBMs enable fast turnaround simulations and bring in additional features such as adaptability to complicated geometries using Cartesian meshes by deploying Immersed Boundary Methods together with a high level of parallelism[38, 39, 40, 41]. Such advancements have lead to considerable reduction in the engineering effort required to unravel complex flow scenarios such as for those in real world aeroacoustic applications including slat noise[28, 42]. Popular LBM solvers like PowerFLOW have also already been demonstrated to have the capability to accurately capture both noise generation mechanisms and propagation in slat noise simulations enabling direct computation of their noise signatures[23, 43, 44]. Well in line with these developments, we also deploy the LBM simulations, to investigate the HLD noise using a newly released LBM solver *ProLB*. This solver is under active development during the work on this thesis, and although our work is not directly involved in the source code development, Ecole Centrale de Lyon's partnership in the solver development as been leveraged to obtain the necessary technical capabilities and

expertise. Consequently, we also take maximal effort to test and validate the solver for our applications. As for contributions from this thesis towards this development, we put forward a cost effective simulation framework using *ProLB* coupling it with an independent in-house acoustic analogy module based on the method of Ffowcs Williams-Hawkins[45, 46]. Details and technical aspects of these implementations are presented in Chapter 3 of this thesis.

A second advancement pertinent to modern aeroacoustics also comes from the data-driven paradigm[47]. In this perspective, reduced order models for flow and acoustics computations are possible by leveraging on the high-quality datasets available from both simulations and laboratory experiments. Their applications in aeroacoustics are still in its infancy and hence a few curious experimentation are also undertaken as part of this work. In particular we deploy a statistical inference method based on Bayesian Active Learning to enable an automated inference procedure regarding the nature of the far-field sound spectrum with respect to the position of the slat. Using this framework and by committing the required high-performance compute resources, we enabled an extensive data generation campaign collecting more than 30 high-fidelity slat noise simulations. The details of its development and associated theoretical specifications are presented in Chapter 5. Finally in Chapter 6, we utilize the data generated from these simulations to obtain new insights into the cove dynamics thereby facilitating advancement in the fundamental understanding of its phenomenology. All further details on the technical specifications and intermediate results that facilitated our progress are also included in the Appendices for completeness and to enable future investigators.

Finally, the single objective of this thesis is to advance the current state of the art in slat noise investigation. Due to renewed global research interest, this field was also evolving fast during the course of our investigation. All contemporary developments are also included in discussion and citations to as much as our resources permitted.

Chapter 2

Literature Review

This chapter aims to review the existing literature necessary to facilitate the study of slat noise. Given that the aeroacoustic mechanism in slat noise is a composite of fluid dynamic interactions arising from its shear layer behavior, trailing edge scattering, and aeroacoustic resonance, and that the three are simultaneously active under the setting of a cavity flow, we start by presenting these fundamental processes separately before presenting the actual slat noise literature. Thanks to the very recent revitalization of research interest in aeroacoustics, many of these topics have been thoroughly reviewed on their historic context and developments to until as late as the previous year. Hence we do not reproduce such extensive versions here but only present their summaries with a perspective pertinent to our intended study.

2.1 Trailing Edge Noise

Trailing edge noise or the turbulent boundary layer trailing-edge noise (TBL-TE) is an elementary noise source in the aeroacoustics of solid bodies[48]. The flow past a trailing edge convects the turbulent structures who themselves behave as quadrupole like sources[49]. The resulting fluctuations in the immediate vicinity of a sharp trailing edge are then scattered by the edge and results in a dipole like source centered at the edge. Although a debated topic, this effect was suggested to be largely independent of the unsteady Kutta condition except for high frequency noise and non-linear effects in the directivities[50, 51, 52, 53]. The farfield sound intensity is proportional to M^5 , where M is the free stream Mach number[48]. Compared to the noise of free turbulence which scales with M^8 , and that of unsteady surface fluctuations which scale with M^6 , the trailing edge scattering serves as a dominant mechanism when flow speeds are sufficiently low.

For the intensity of the farfield noise, the trailing edge scattering efficiency is dependent on the spanwise coherence length[54]. This is due to the fact that when the structures are spanwise oriented – with respect to the largely two dimensional flow – the input pressure fluctuations at the TE will also be coherent along the spanwise edge length leading to their strong radiation by scattering. According to Williams and Hall [48], if the distance between the passing eddy and the TE is increased such that the Helmholtz number $kr_0^- \gg 1$, where r_0^- is the distance of the passing eddy from the edge and k is the wavenumber of the radiated acoustic wave of interest, the trailing edge noise efficiency decreases. But within the proximity of $kr_0^- < 0.5$, the noise level increases by a factor of $kr_0^-^{-3}$. This partially can be attributed to the effective coherence of the incident fluctuations which also is inversely proportional to r_0^- .

The incident fluctuations at the trailing edge can thus be used as the input to model far-field TE noise as in the work of Amiet [50]. His model uses the pressure fluctuations at a location slightly upstream of the trailing edge together with an infinite chord assumption. This then by the Schwarzschild technique

for the wave equation of the acoustic potential enables calculating the pressure variation across the sharp trailing edge which then act as a distribution of acoustic sources at the TE. Then the radiation can be propagated to the farfield by calculating noise using the canonical Green's function. This method thus provides a physically valid method of calculation of the TE scattering phenomena and also validated the theory. An extension to the TE noise theory for engineering application was also given by Roger and Moreau [55] where the possible backscattering from the leading edge of a finite chord blade was taken in to account for the calculation.

In addition to classical theory and explanations, more recent and advanced post processing methods have been used to further TE noise studies via numerics[56, 57, 58, 59, 60]. Sano et al. [58] studied the data from large eddy simulation and used Spectral Proper Orthogonal Decomposition (SPOD) to isolate the dominant structures that are responsible for the pressure fluctuations at the trailing edge. Their analysis suggested that the largest eigen value modes represented most part of the acoustic energy. The corresponding modes were also shown to have an extended structure spanning from the location of boundary layer detachment to the trailing edge. They hence suggested that the trailing edge noise is related to non-compact source fluctuations. They also suggested that the phase of the fluctuations also have an impact such that the maximum source efficiency occurs when the incoming perturbations are out of phase between the suction side and the pressure side.

2.2 Other mechanisms of Airfoil Self-Noise

Airfoil self-noise refers to the noise generated by a single element airfoil due to interactions with the turbulence developing along its surface[61, 62, 63]. The primary source of turbulence here is the boundary layer turbulence generated by the boundary layer flow over the walls. For subsonic speeds, the major noise source mechanism is the above mentioned TBL-TE noise phenomenon and contributes to a broadband noise in the farfield.

Apart from the TE phenomena another major noise mechanism occurs when the airfoil is stalled[62]. When it happens that the flow on the suction side of the airfoil separates prematurely, before reaching the trailing edge, large scale vortex structures are shed from the suction side of the airfoil, leading to strong generation of turbulence. In a mildly separated flow, the noise mechanism will stay similar to the trailing edge radiation but due to stronger incoming vorticity at TE. Hence a broadband increase by about 10 dB over TBL-TE in the low frequency range – typically $St \in [0.02, 0.03]$ where the Strouhal number is defined in terms of the projected width obstructing the flow – is the characteristic development[64]. As the angle of attack increases, the flow separation point moves towards the leading edge and the noise progressively shifts to a lower frequency range. During deep stall, the airfoil operates as a bluff body and the noise is generated from the full surface of the chord and the low frequency component are diminished together with the development of narrow band peaks in same Strouhal range. These are attributed to the periodic shedding of large scale vortices and their interaction with the leading and trailing edges[65]. The sharpness of transition from mild stall noise to deep stall noise is also determined by the thickness of the airfoil. The stall noise is a dominant component of the total noise when present but however is less prevalent in high-lift applications. It is so since the high-lift device (HLD) primarily delays the stall on the main body, i.e. an HLD allows the airfoil to operate at a higher angles of attack without initiating stall due to the secondary turbulent flow generated by the leading edge slat. The large scale periodic vortex shedding from the suction side wall on an airfoil is hence replaced by the reattachment of a periodically oscillating shear layer from the slat trailing edge for the HLD. The only related possible mechanism in HLDs is thus of a mild-stall condition on its main element with strongly turbulent inflow conditions due to presence of upstream cove flow. This can potentially explain mid-frequency broadband components.

A third noise mechanism for airfoils arise from the vortex shedding from a low Reynolds number laminar boundary layer on the airfoil wall. Arbey and Bataille [66] were the early experimenters to show that an airfoil placed in a uniform laminar flow generated broadband noise with dominant tonal components and the tone frequencies followed a ladder-type evolution with the flow velocity. The laminar boundary layers at low Reynolds numbers without pressure gradients are stable according to the Rayleigh criteria. However, any slight incoming perturbation can excite the boundary layer (BL) instabilities. The most unstable modes in a viscous laminar parallel flat 2D BL flow are known as the Tollmien-Schlichting (T-S) waves[67]. These pressure and velocity perturbations, when excited at a source location on the airfoil surface by external factors, grow along the streamwise direction until their amplitude saturates non-linearly into turbulence generating vortices which are then convected past the trailing edge[68]. The trailing edge scattering then generates acoustic waves that travel back to the location of the T-S wave onset to enhance their excitation, thereby completing an aeroacoustic loop[69]. This mode of resonance thus destabilizes a laminar boundary layer on an airfoil even when there is no adverse pressure gradient along the wall. Since the T-S instability is receptive to a broadband range of incoming perturbations, the presence of the turbulent boundary layer on one side of the airfoil is sufficient to excite the instability on both sides, given the angle of attack and Reynolds numbers. The resulting noise spectra will also have quasi-tones related to the shedding rates at the trailing edge[70].

A fourth mechanism for airfoil self-noise arises from the trailing edge shape. A blunt trailing edge can facilitate shedding of vorticity if the edge thickness is comparatively larger than the boundary layer thicknesses. The vortex shedding is certain if the ratio of TE thickness to boundary layer displacement thickness is larger than 2.0[71]. The pressure fluctuations associated with the vortices shed, which form a von Karman street downstream of the TE, are scattered by the edges resulting in an efficient noise source. The associated far-field noise is typically a tone in the high frequency range. A similarity of the spectra was obtained when plotted as function of Strouhal numbers based on the TE thickness and the displacement thicknesses of the incoming boundary layer[72]. The St of the tones are in the range of $St = [0.2, 0.3]$ while the vortex shedding frequency based on the TE thickness are widely agreed to be at $St \approx 0.21$ for the Reynolds numbers of interest[73, 74]. Prediction methods for this noise component have also been shown to have high fidelity while taking into account the lateral fluctuation pressure frequency and the spanwise coherence length of incoming vortices at the edge[75].

This feature of a blunt trailing edge tonal noise is important for slat aeroacoustics. The trailing edge of the slat geometry in the reference configuration of VALIANT, introduced in the previous chapter, has a thickness of 1 mm. The peak velocity of the ejected flow from the slat gap rises to approximately 2 times the ambient speed and hence a velocity of 100 m/s can be taken as an estimate. Consequently the resulting trailing edge shedding frequency will be around 20 kHz and hence can explain the high frequency hump typical for slat noise spectra. However, as shown by Roger et al. [75], the coherence of the eddies along the slat trailing edge will be an important factor determining the source efficiency. In the slat cove flow, this source will hence be weakened by the vorticity dynamics in the cove which favors a disintegration of the spanwise coherent vorticity from the cusp while being convected towards the trailing edge. Moreover, given that for the high speed ejection at the slat gap, the vortex shedding noise is at the very high frequency range of 20 kHz, it does not interact directly with the characteristic resonance mechanisms that occur at much lower frequencies.

2.3 Cavity Noise

Cavity noise is another fundamental phenomenon of aeroacoustics which is of importance for the slat noise. The recent view of Hamilton Smith et al. [76], presents most of the significant developments. The

canonical cavity flow addressed in fluid dynamics is a regular shaped rectangular cavity under a grazing flow, where a turbulent shear layer develops over the open side. The shear layer at the upstream edge of the open side develops the canonical K-H instability and leads to vortex shedding. These vortices then impinge on the downstream edge of the cavity leading to partial convection of the flow past the edge and partial recirculation of the reminiscent flow within the volume of the cavity. The resulting oscillatory motion at the slat trailing edge leads to periodic variations of the static pressure inside the cavity which then leads to periodic oscillation of the shear layer itself. The perturbations that reach back to the leading edge then provide the trigger for the K-H instability. The combination of vortex shedding and acoustic waves form and aeroacoustic feedback loop that leads to the formation and impingement of strongly coherent large vorticity structures thereby generating acoustic waves at the frequency corresponding to the acoustic wave propagation time. These oscillations were understood early on by Strouhal [77] to be primarily determined by the incoming velocity and associated length scales which led him to formulate the non-dimensional characteristic frequency referred to as the Strouhal number. The shear layer oscillations and the impinging vortices were theorized and studied later as an aeroacoustic resonance by Rossiter [33] where he demonstrated, using shadowgraphs, that the regular impingement of vortices at the trailing edge and their time of shedding were synchronized, resulting in amplification of the pressure perturbations.

The flow dynamics developed in a cavity is largely dependent on the geometric proportions of the cavity. For the rectangular shape, the streamwise flow types are generally categorized into open and closed[78]. The configuration is referred to as open if the streamwise length to depth ratio, L/D is less than 5 [76]. In this configuration the shear layer reattaches the downstream of the trailing edge and hence causes large shear layer oscillations to occur which are excited by the internal recirculation. Both deep cavity tones are produced together with Rossiter modes in this case. On the contrary, the flow is treated as closed when $L/D > 12$. In this case, the streamwise length of the cavity is sufficiently high such that shear layer from the leading edge curves inwards to reattach with the cavity floor before separating again at upstream of the trailing edge. This case hence produces significant drag due to the stagnation of the flow inside the cavity[79].

It is between these two extremes that the cavity flow is called transitional. When closer to the open configuration with $5 < L/D < 7$, the flow is predominantly open with the shear layer impinging at close proximity to the trailing edge. The flow often transition here between a closed mode or open mode depending on the incoming flow velocities. The transition here is also affected by the development of the flow in the third dimension which depend on L/W where W is the cross flow width as shown by Stallings and Wilcox [80]. In view of their acoustics, Jacob et al. [81] showed that shallow cavities exceeding $L/D > 7$ predominantly behave as acoustically independent steps, i.e. a one forward facing and the other backward facing[81, 82, 83, 84], in their contribution to the total noise. This is attributed to the fact that the distance between the steps tends to obstruct the aeroacoustic loop.

The geometry of the cavity and their arrangement has also been observed to be important in view of the turbulence generated and noise characteristic. Marsden et al. [85] studied the behavior of cylindrical cavities in its interaction with the boundary layer and found that cylindrical cavities also generated Rossiter like tones linked to the cavity depth. For a staggered arrangement of the cavities on a flat plate, the local turbulence characteristics were shown to shift towards the case with wall-normal blowing by Scarano et al. [86, 87, 79].

The three dimensionality in cavity flows, as will be shown later, is an important aspect to understand the slat cove flow. In the rectangular cavity configuration, the cavity is referred to as wide $2D$, if the width of the cavity is sufficiently high, typically $L/W \ll 1$. This is also the case of an spanwise infinite flow where the spanwise features of the flow dynamics are dispersed into the infinite domain. In contrast, for the case referred to as the Narrow $3D$ case, the spanwise width is limited by the presence of a wall

constraining the domain such that $L/W > 1$. In this case the three dimensional dynamics are retained locally within the flow resulting in their influence on the larger $2D$ flow. This is often the scenario if experimental investigation of the slat noise is carried out in a wind tunnel where the spanwise spacing of the lateral supporting plates is not sufficiently large.

For the cove flow generated in a generic case, we know from the literature that the recirculation bubble roughly has a depth similar to the slat chord. For an experimental setup which has a slat chord of $C_s = 0.039\text{ m}$ [14], the cove diameter can also be taken to be the same from rough geometrical estimates. Hence the cavity length to depth ratio approximates as close to 1 and hence falls in the transitional-open regime. This motivated, in our belief, the investigators this far in the literature to treat the slat cove dynamics to be a wide $2D$ flow phenomena. However, note that this comparison is widely inaccurate on the details since for a rectangular cavity, the cavity shape is a regular rectangle whereas in the cove flow, the cavity has the shape of the inner slat wall, which itself approximates as circular. More importantly, the shear layer in an open cavity flow bridges the open side in a dominantly linear path. In contrast the slat cove shear layer undergoes a curved path whose curvature itself lies in the linearly unstable regime. This is one perspective that we wish to study and to highlight to the community through our work.

2.4 Slat Cove Dynamics and Noise

As mentioned in the introduction, the slat cove dynamics and noise mechanisms are understood largely in terms of the elementary mechanisms discussed above. Historically, in the very early developments on slat related noise studies, Fink [6] noted that its broadband noise contributes as high as 11 dB to the Overall Sound Power Level (OASPL). This component which was observed in the flight data did not have specific tones. Consequently, the early slat noise model for flight conditions by Guo [88] also focused on modelling the broadband component and followed the hypothesis that the trailing edge noise mechanism is dominant. Following this, as the first of its kind, Dobrzynski et al. [12] and Perennes and Roger [16] in 1998 separately conducted dedicated experiments to study high lift device noise isolated from the rest of the airframe noise sources by using a laboratory scale test model. In these experiments, the high lift devices were found to have narrow band tones in addition to the broadband spectra.

2.4.1 Slat Noise Mechanisms

Khorrami et al. [89] first hypothesized that these tones can originate from the vortex shedding of the blunt trailing edge but later reported that attempts to directly correlate the vortex shedding frequency to the thickness of the blunt trailing edge were not successful. Subsequently efforts were made to correlate the tone frequencies with the boundary layer displacement thickness which also did not bear fruit[89]. In 2001, Tam and Pastouchenko [90] reported the discovery of “Gap tones” and suggested that in both the slat cove and in case of jet shear layers, an aeroacoustic mechanism can explain the generation of acoustic tones. The frequency of the tones were also shown to be predictable by using only kinematic considerations, i.e. the time lag between the vortex shedding and the acoustic generation due to their interaction with the wall or the flow itself. This was the first suggestion that the slat tones could possibly be explained by an aeroacoustic resonance. Subsequent developments can be noted to be informed of both the tonal and broadband nature of slat noise with the broadband noise being the main focus for modelling flight test datasets[91], and the tones curiously being a prominent feature in experimental investigations on lab-scale models[25]. The computational campaigns that followed then showed that the broadband noise predictions using modelled turbulence statistics in the slat cove can provide a good agreement with the far-field acoustics [92, 93, 94, 95].

In the same direction Imamura et al. [34] also showed that the PSD of turbulence fluctuations downstream of the slat TE have strong correlation with the mid-frequencies in the far-field spectra while Kaepernick et al. [95] showed that the tones have mode switching processes suggesting that they are associated with resonant processes. The broadband noise was also shown to have a fifth power dependence with the free stream Mach number based on the dimensional analysis by Guo [27] and subsequently such a model was found to have reasonable agreements with their slat noise datasets from flight tests. However, in his work this correspondence of the scaling law was reported to be only nominal, derived from dimensional analysis, and the total slat noise behavior deviates to have a Mach number power dependency of 5.3 to obtain a better agreement with observations, as first suggested by Perennes and Roger [16]. This also lies in between the noise efficiency of a classical trailing edge source (M^5) and that of a simple airfoil in a turbulent field (M^6) and the difference can be attributed to the propagation effects which is determined by the presence and complex nature of the flow on the slat-airfoil configuration. The farfield directivity of slat noise also reproduces largely a dipole shaped radiation centered at the trailing edge of the slat as shown in the work of Lockard and Choudhari [19], providing further evidence that the trailing edge mechanism is the driver of the broadband noise.

The explanations for broadband and tonal noise are thus mostly satisfactory for their source mechanisms. Accordingly, modern investigations of slat noise attempt to capture the farfield noise quantitatively and engineering efforts attempt to reduce the noise by using geometrical interventions. Khorrami and Lockard [96] and König et al. [97] showed that the strength of the shear layer vorticity determines the strength of the radiated noise. The former used a blade seal to reduce the strength of the shed vorticity while the latter showed that the perturbations near the slat gap are correlated to the broadband noise in the farfield.

Following a reinvigorated research interest, the standardized geometry of the 30P30N configuration was adopted as part of the Benchmark problems for Airframe Noise Computations (BANC)[98, 99]. For this geometry, the Mach number dependence of slat related OASPL was found to be $M^{4.5}$ in the experiments by Pascioni and Cattafesta [21]. They also reported that the tonal components had a Strouhal number which depended on the angle of attack. In their suggestion, this was reasoned to be an effect of the variation of the shear layer length where a longer vortex trajectory would cause a longer travel times for the eddies and thus a reduction of the resonant Strouhal numbers. A new standardized 2 element geometry was also put forward in the VALIANT project by Manoha et al. [15] to isolate the slat only phenomena from that of a trailing edge flap which can possibly interact with the leading edge slat. Our project follows the VALIANT project in using the same 2 element generic geometry. For this configuration, the frequencies of cavity resonance were investigated by Terracol et al. [14] who deduced that the resonance follows the same phenomenology as the aforementioned Rossiter mechanism. The resulting formula based on kinematic considerations use the vortex shedding location as the slat cusp and the trailing edge as the location of impingement of the trailing edge. The travel time for the spanwise coherent vortices shed from the cusp then provides the major time delay and, together with the feedback time for the acoustic wave from the trailing edge to reach back at the cusp, it provides the total time period for the resonant oscillation. The formula for the slat's Rossiter modes according to Terracol et al. [14] then writes

$$f_n = n \frac{U_\infty}{L_a} \frac{1}{M + \frac{\alpha_l}{\kappa_\nu}} \quad (2.1)$$

where $\kappa_\nu = U_\nu/U_\infty$ is the non-dimensional vortex convection velocity, $\alpha_l = L_\nu/L_a$ is the ratio of shear layer length to the acoustic path, and M is the Mach number. This formula assumes that the slat tones are harmonics of a fundamental which is determined by the longest possible resonance loop when $n = 1$. It however needs to be reevaluated since the tones can indeed deviate from harmonic behavior and give in

to non-linear interactions[100, 101]. These non-linear interactions can lead to transfer of energy between the modes and also to secondary frequencies. However, the formula for most cases provides a satisfactory estimate of the resonant frequencies[102, 26, 103].

The most recent advancements in slat noise investigations focused on utilizing advanced post processing and measurement methodologies. Jawahar et al. [4] conducted experiments of the 30P30N configuration to uncover the stochastic character of the slat tones. It was shown using wavelet analysis that the slat tones are not a steady radiation but the leading energy modes had quasi-periodic disruptions. Wei and Liu [101] performed synchronized measurements of the far-field noise, wall pressure sensors, and hot wire probes in 30P30N experiment and confirmed that the slat tones show non-linear interactions i.e. the fundamental mode tends to be unsteady in its amplitude and transfers energy to the first and second harmonic causing a mode switching effect.

To conclude our understanding of the literature, let us briefly underline the current state of the art of slat noise modelling. In the last section we delineate Guo's model and Souza's most recent corrected formula for the tonal frequency prediction. Also note that in the literature we reviewed, we only included the efforts directed towards computational modelling and omitted those aimed to study the various slat noise reduction techniques although such improvements also have attracted well deserved engineering research interests[103, 104].

2.4.2 Current State of the Art for Slat Noise Modelling

As mentioned, among the early slat noise prediction models that are restricted to the broadband component, the one developed by Guo [27] is to date the only one dedicated to this source. The theoretical model of noise generation from turbulence, its propagation through mean flow gradients, and acoustic scattering effects were used in his approach to derive an approximate analytical form for the slat noise spectra. The model has its footing in the physics of noise generation, propagation effects, and scattering effects by rigid walls, and the final equation is inexpensive to evaluate. The proposed equation for far-field PSD reads

$$\Pi = \rho_0^2 c_0^2 A_G A_F W(M) F(f, M) D(\theta, \phi) \frac{c_s b}{r^2} \quad (2.2)$$

where ρ_0 is the air density, c_0 the speed of sound, A_G the geometry dependent amplification factor, A_F the flow-dependent amplification factor, $W(M)$ the Mach number dependent weighting function, $F(f, M)$ the spectral shape function, $D(\theta, \phi)$ the directivity function in terms of polar and azimuthal angles, c_s the slat chord length, b the wing span, and r the source to observer distance. The spectral shape function is then defined as

$$F(f, M) = \frac{M^2 c_s}{c_0} \frac{\text{St}_c^2}{\left(1 + \mu_0^2 \text{St}_c^2\right) \left(1 + \mu_1^2 (1+M)^2 \text{St}_c^2\right)} \times \frac{1}{\left(1 + \mu_2^2 M^2 \text{St}_c^2\right) \left(1 + \mu_3 M \text{St}_c\right)} \quad (2.3)$$

where the terms μ_0, μ_1, μ_2 , and μ_3 , in Eq.2.3 capture the dependency of the PSD on various case parameters including the dependency on the Green's function, spatial and temporal coherence of the sources and geometric characteristic length. These parameters together with A_G and A_F in Eq.2.2 dictate the levels and shape of the spectral prediction. The functions for directivity function $D(\theta, \phi)$, and the Mach number based weighting function $W(M)$ are paramount to its actual usage and are to be inferred in a data-driven manner, either manually or by method of numerical deduction. Nevertheless, we omit these since they are not directly used in the course of our work which only adopts the shape function to enable a data-driven

approach.

For tonal noise, Terracol et al. [14]’s formula based on the path length and free-stream velocity enables quick calculation of tonal frequencies and is in active use to-date. An example is the experimental investigations including that of Kamliya Jawahar et al. [104]. In a recent modification, Souza et al. [28] have shown that an additional constant offset of the phase by 90 degrees helps in improving the previous result, especially for the higher tones. The final formula was thus given as

$$\text{St}_n = \left(n + \frac{1}{4} \right) \times \frac{U_\infty}{L_a} \frac{1}{M + \frac{\alpha_l}{\kappa_\nu}} \quad (2.4)$$

The additional factor of 1/4 captures the phase shift between the vorticity impingement and acoustic generation at the trailing edge. The same authors also suggested that Spectral Proper Orthogonal Decomposition (SPOD) for the turbulence data reveals the major flow fluctuations in the cove region and how the modes display this phase shift of 90 degrees [105]. The results for different flow cases such as one from the standard geometry and other with a flow stopper in the slat wall leading to a separated bubble were tested and yielded satisfactory results.

Regarding data-driven modelling of broadband noise, Bolivar et al. [26] used a Lattice Boltzmann Method based commercial solver, PowerFLOW, to conduct a parametric study of slat generated noise. The CFD solver has a well documented literature for its low dissipation and dispersion properties [106, 23]. It is hence well suited for the simulation of turbulence induced acoustics. Detailed notions of why this is relevant is provided in the next chapter. Their resulting data was then used to deduce approximate analytical forms for the parameters in Guo’s model by using a least square fitting, thereby connecting Guo’s model parameters to trends in the flow solution. An alternative LBM based solver ProLB is also in active development showing promise towards reliable acoustic predictions [107, 44, 37]. The solver has been the subject of detailed study and development in the doctoral thesis of Astoul [44]. Their acoustic studies for the standardized landing gear case LAGOON 2 and LAGOON 3 using ProLB solver has shown satisfactory agreement with experiment.

2.5 Conclusion

A review of the basic phenomena related to slat noise, namely the TE noise, airfoil self noise, and cavity noise, are reviewed in this chapter together with the current state of art of leading edge slat noise. These phenomena in our understanding is necessary to form a full picture of the flow dynamics and noise generation in the airfoil configuration. With the conclusion that there are sound advancements in both analytical modeling of tonal noise and data-driven methods using LBM, we now choose the data-driven paradigm as the basis of this work. This aligns with our objective of obtaining a fast-turn around aeroacoustic prediction tool that can be used at a design engineers desk during design optimizations. For this, we deploy the commercial LBM solver ProLB, together with a Ffowcs Williams-Hawkins acoustic analogy method to develop an acoustic prediction framework. The data is first used to investigate the slat noise phenomena in relation to the above mentioned basic mechanisms of noise generation and then to put forward a data-driven framework that enables to bypass the expensive LBM or acoustic analogy methods to obtain a noise estimate. This latter choice is primarily motivated by the aim to develop a slat noise prediction framework that is agnostic to the geometrical complexities.

Chapter 3

Lattice Boltzmann Method for Computational Aeroacoustics

3.1 Introduction

The first objective of this thesis is to concoct a suitable framework that will enable the investigation of slat noise phenomena numerically. Due to the inherent complexity of accelerated shear flow along the curved path through slat gap and the impingement of the flow past the sharp edges of both the slat cusp and the trailing edge, the flow itself necessitates a high-fidelity simulation that can capture unsteady evolution of shear layer and its dynamic interactions. The three dimensional aspect of flow has also not been investigated in detail so far, although the flow features are acknowledged to have strong three dimensionality from early studies[108, 31, 15]. This is due to the fact that the spanwise homogeneity is assumed to be sufficient in explaining the major phenomena of the 2D shear layer evolution and related Rossiter mechanism[76]. However, the observed far-field sound clearly suggests that there can be unexplored mechanisms arising possibly from the three dimensionality underlying the stochastic nature of its tones[4]. Moreover, any estimation of the farfield sound using time-averaged computation of the flow will also introduce modelling errors that will prevent a deeper investigation of the flow dynamics. Hence our first choice is to obtain a three-dimensional compressible unsteady simulation framework that will enable direct simulation of the source mechanisms.

A detailed investigation of flow and acoustics within the slat cavity will also need a parametric variation of the slat positioning. Since the vortices from the shear layer and their evolution along their trajectory in the cove plays the major role in the acoustic generation mechanism[14], variation of the shear layer shape with respect to the slat positioning has to be documented in order to form a deeper understanding. To enable this, the first difficulty is in generating meshes inside the cove geometry. The mesh has to be adapted in case of parametric slat positions and hence an extensive exploration is not possible unless automatic mesh generation is enabled. Additionally, the noise generation in the slat cove needs to be captured with high fidelity in all cases computed and needs to be propagated without numerical loss and artifacts to a far-field observer. This requires that the mesh choices must enable accurate source modelling together with wave propagation with low numerical dissipation and dispersion, and at minimal computational cost.

Among a few advanced techniques in modern CFD, this case thus falls under the scope of a wall-modelled Large Eddy Simulation (WMLES). It utilises a wall-modeling approach for the boundary layer near the walls and deploys a well resolved mesh that can capture the scales of interest for the slat cove

while modelling the sub-grid scale behaviors. This has been shown to be an effective approach for detailed investigation of slat noise for a select geometrical configuration, and complicated meshing procedures were surmounted by manual effort[20]. This is also the same scenario if a Direct Numerical Simulation (DNS) has to be deployed but only with much larger computational costs which, however, will provide the same level of fidelity regarding the noise phenomena[37]. Hence the canonical wall-resolved LES and DNS are not viable in our study which aims to obtain an extensive dataset by variation of slat position.

A more advanced technique has been deployed in the recent years which uses the Lattice Boltzmann framework to obtain an equivalent WMLES. It has been demonstrated that this method sufficiently captures the noise mechanisms and the propagation effects. Here, Very Large Eddy Simulations (VLES) were introduced for slat noise simulations by Satti et al. [39] and was taken further into high-fidelity simulations in the work of Souza et al. [28]. They deployed the commercial Lattice Boltzmann software PowerFLOW to demonstrate that this class of simulations indeed enabled simulations of the slat noise phenomena to a high level of accuracy. These LBM frameworks natively uses a Cartesian mesh necessitated by the voxel based discretisation together with an Immersed Boundary model[44, 109]. Using this technique, the wall geometry is placed in a volume discretized using cubic elements and the wall model is used to estimate the conditions at the first cell. With a sufficient resolution specified to the region near the boundary, the meshing procedure is thus fully automated while varying the slat positions. This enables to eliminate inconsistencies arising from the manual meshing of the geometries and allows a coherent analysis. Another factor that advocates for the LBM approach for aeroacoustics is its low numerical and dissipation characteristics. The LBM formalism implicitly generates a scheme which has a low numerical dissipation and can be finely controlled using its modelling parameters. This enables accurate propagation of the generated acoustics to far-field observer.

Hence the expedited meshing procedure and low numerical dissipation characteristics of LBM places the same as a niche technique to be useful in a detailed study of slat aeroacoustics. It was thus chosen for the progress of our work. We now look into a detailed view of the LBM framework for its theoretical developments before delineating the methods that we use to adapt a commercial LBM software *ProLB* for our slat noise investigation.

3.2 A brief overview of the Lattice Boltzmann method

The Lattice Boltzmann Method (LBM) arises from the fundamental idea of a Lattice Gas Automata, where behavior of a fluid medium is modeled as a cellular automation at the kinetic level[110]. In this perspective, the fluid consist of particles – not exactly the physical idea of molecules, which would have been called a molecular level description of the fluid – that can interact with each other to exchange momentum such that their aggregate behavior is consistent with the kinetic theory of gases[111]. This intermediate scale of momentum interactions are referred to as the mesoscopic scale and is the domain where LBM is formulated. The fluidic behavior is then modeled on a discrete lattice in space by time-stepping the properties of the lattices depending on its current state and the state of its immediate neighbors. This means that by a suitable choice of the state variables and a physically consistent model for interaction of the cells, the macroscopic behavior of a fluid medium can be simulated. Since evolution of each lattice is driven by its own state and those of its immediate neighbors, the heaviest calculations are local and the method can be designed to be massively parallel with limited overhead due to transfer of data between parallel processors[112]. This resonates well with the burgeoning of high-performance computing architectures and Graphics Processing Units (GPUs) available in modern scientific computing especially in the field of Computational Fluid Dynamics (CFD) in application to High-Fidelity (Hi-Fi) simulation of turbulence. Its applications are hence growing in a wide range of topics including aeronautics

research, multi-phase flows, and medical hemodynamics.

Looking at it more formally, the total number of particles in a fluidic medium located at a position x with a microscopic particle velocity ξ at a time instant t can be written as

$$dN = f_N(x, \xi, t) dx d\xi \quad (3.1)$$

where $f_N(x, \xi, t)$ denotes the particle density probability distribution as a function of x , ξ , and t , and dx is a mesoscopic spatial volume around the position x . If the particles have identical mass m , then the mass density distribution becomes mf_N . Using such a probability density function, the local fluid density can be represented as its zeroth order statistical moment. Similarly the higher order moments lead to momentum density $\rho\mathbf{u}(x, t)$ and total energy density $\rho E(x, t)$. These can be written as

$$\rho(x, t) = \int_{\mathbb{R}^D} f(x, \xi, t) d\xi \quad (3.2)$$

$$\rho\mathbf{u}(x, t) = \int_{\mathbb{R}^D} \xi f(x, \xi, t) d\xi \quad (3.3)$$

$$\rho E(x, t) = \int_{\mathbb{R}^D} \frac{|\xi|^2}{2} f(x, \xi, t) d\xi \quad (3.4)$$

The total energy of a kinetic gas, $\rho E(x, t)$, is the sum of its internal energy, $\rho e(x, t)$, and its kinetic energy, $\frac{1}{2}\rho|\mathbf{u}(x, t)|^2$, and the former is linked to the variance of the velocity distribution providing the formula for the thermodynamic temperature of the fluid as

$$T(x, t) = \frac{e(x, t)}{c_v} = \frac{1}{\rho c_v} \int_{\mathbb{R}^D} \frac{|\xi - u|^2}{2} f(x, \xi, t) d\xi \quad (3.5)$$

where c_v is the isochoric specific heat capacity. The fluid pressure can now be obtained from the perfect gas law as

$$p(x, t) = \rho(x, t) r_g T(x, t) \quad (3.6)$$

where r_g is the thermodynamic gas constant in accordance with the kinetic theory of gases. The discrete particle velocity distribution function in a lattice is hence sufficient to retrieve the macroscopic quantities of the fluid. The interaction of the particle velocity distribution function, f , between the lattices needs to be modeled in such a way that the macroscopic fluid behavior is in accordance with the Navier-Stokes equations. This is achieved by utilizing the Boltzmann equation and the collision operator therein. The Boltzmann equation itself determining the time evolution of the particle distribution function is written as

$$\frac{\partial f}{\partial t} + \xi \cdot \frac{\partial f}{\partial x} = \Omega(f) \quad (3.7)$$

where the left hand side is a convection equation for the particle velocity distribution whereas the right-hand term $\Omega(f)$, the collision operator, is the term driving the convection of these probabilities. On constraining the collision process model such that the mass, momentum, and total energy, of the fluid is conserved during such a process, Bhatnagar et al. [113] showed that the primal effect of the collision operator is to shift the state of particle velocity distribution to that of the thermodynamic equilibrium of the fluid i.e. the Boltzmann equation in each time step operates on the particle velocity distribution to relax it towards the thermodynamic equilibrium. A linearisation of the collision operator was made possible by simplifying the collision process as a direct and simpler form of ‘relaxation’ of a given particle

density function to its thermodynamic equilibrium. This relaxation step using a single timestep for the Bhatnagar-Gross-Krook (BGK) model writes

$$\Omega^{BGK}(\mathbf{x}, t) = -\frac{1}{\tau} (f(\mathbf{x}, t) - f^{(0)}(\mathbf{x}, t)) \quad (3.8)$$

where τ is the relaxation time, and $f_i^{(0)}$ is the thermodynamic equilibrium distribution function given by Maxwell-Boltzmann distribution

$$f^{(0)} = \frac{\rho}{(2\pi r_g T)^{D/2}} \exp\left(-\frac{\|\xi - u\|^2}{2r_g T}\right) \quad (3.9)$$

As such, such an equilibrium function depends on the local density, temperature, and the macroscopic velocity. The equilibrium function can hence be computed based on the current local state of the particle distribution f , but however not completely. On analyzing $f^{(0)}$, it can be obtained that

$$\int_{\mathbb{R}^D} f^{(0)} d\xi = \rho(x, t) \quad (3.10)$$

$$\int_{\mathbb{R}^D} \xi f^{(0)} d\xi = \rho \mathbf{u}(x, t) \quad (3.11)$$

$$\frac{1}{2} \int_{\mathbb{R}^D} |\xi|^2 f^{(0)} d\xi = \rho E(x, t) = \frac{D}{2} \rho r_g T(x, t) + \frac{1}{2} \rho |u(x, t)|^2 \quad (3.12)$$

i.e. zeroth order moment, first order moment, and the trace of the second order moments, of the equilibrium distributions are exactly the same as that of the local particle velocity distribution f . However, only the trace of the latter, i.e. the total energy obeys this conformity as written in Eq. 3.12. The deviatoric part of the energy tensor, linked to the internal energy, and subsequently all higher order moments of the equilibrium distribution are not accurately recoverable from the local particle velocity distribution only. This means that an approximation of the equilibrium distribution based solely on the non-equilibrium distribution will introduce an error to the deviatoric part of the energy equation, although the total energy conservation will still be valid. This necessitates a modelling approach in such a way that a model for the equilibrium distribution will enable exact recovery of the full Navier-Stokes.

As a step towards the formalism to approximate the equilibrium distribution based solely on the current particle distribution function, Hilbert introduced an asymptotic expansion of the latter around the former, i.e.

$$f = f^{(0)} + \epsilon f^{(1)} + \epsilon^2 f^{(2)} + \dots = \sum_{k=0}^{k=\infty} \epsilon^k f^{(k)} \quad (3.13)$$

where ϵ denotes the Knudsen number. The Knudsen number denotes the spatial rarity of the fluid particles and formally has the definition as a dimensionless number being the ratio of the mean free path of the particles to a characteristic length scale l_0 . It can typically be translated into a ratio of corresponding time scales as,

$$\epsilon = \frac{\mathcal{L}}{l_0} = \frac{\tau_0 \sqrt{r_g T_0}}{l_0} = \frac{\tau_0}{t_0} \quad (3.14)$$

where $\mathcal{L} = \tau_0 \sqrt{r_g T_0}$ is the mean free path since $\sqrt{r_g T_0}$ is the isothermal sound speed at a reference temperature T_0 , τ_0 is the mean time between collisions, and t_0 is some characteristic time of the flow.

Chapman and Enskog independently developed this approximation further under the constraint that

the particle distribution f depends solely on the macroscopic moments. They also proposed an expansion of the time derivative based on the order of Knudsen number, written as

$$\frac{\partial}{\partial t} = \sum_{k=0}^{k=\infty} \epsilon^k \frac{\partial}{\partial t^{(k)}} \quad (3.15)$$

Now that an approximate relation between the non-equilibrium and equilibrium distribution is available, it is possible to analyze the behavior of the Lattice Boltzmann Equation in its fidelity to the Navier-Stokes behavior. For this, the asymptotic expansion in Eq.3.13 is substituted to the Boltzmann equation 3.7. We omit the actual algebra here further for sake of brevity. The zeroth, first, and second order moments, of the resulting equation will then correspond to the mass continuity, momentum conservation, and the energy equations, respectively. Here, different choices of the truncation of the expansion of equilibrium distribution based on the order for Knudsen number leads to different set of equations. When the expansion is truncated after first order for the Knudsen number, the exact Navier-Stokes equations can be retrieved. If only the expansion is truncated at zeroth order of ϵ , the inviscid Euler equation is obtained. Hence at low Knudsen number, typically $\epsilon < 10^{-2}$, which is true for widely most cases of practical application including aeronautics and aeroacoustics, the Boltzmann equation retrieves the Navier-Stokes behavior while using the BGK collision model.

Additionally, in order to recover the Navier-Stokes behavior, it is necessary to use the expansion of the non-equilibrium distribution upto first order in Knudsen number. Then to obtain the energy equation, the second order moment of the equation needs to be recovered which means that the first order moment of the non-equilibrium distribution and the fourth order moment of the equilibrium distribution will be necessary. Moments of the particle velocity distribution are typically computed using numerical quadratures in order to obtain the exact integral. Here typically, LBM utilizes the Gauss-Hermite quadratures for this purpose. Hence, since a fourth order moment of the equilibrium distribution has to be computed using the Gauss-Hermite quadrature over the discrete space of the particle velocity vector, this will impose conditions for sufficient discretisation of the velocity vector in a lattice. In the language of Gauss-Hermite quadrature, to obtain exact integrals for the fourth order moment of a distribution, a quadrature of accuracy of order 9 needs to be employed. Such quadratures require a minimum of 103 discrete velocities in a 3D lattice. Each discrete velocity equation will require one equation to be solved and hence will require 103 equations to be solved per lattice per time step to advance the time step alone. This is computationally expensive although the calculation is local and can hence be parallelized. To find a compromise and design fast-LB schemes, the heat equation in the Navier-Stokes is ignored assuming that the simulated case is athermal. In this case, only the third order moment of the equilibrium distribution is necessary to recover the exact formulations of the momentum equations alone. Thus from the relaxed requirement for the computation of the quadratures, a lower number of discrete velocities is required. Here the minimum number of discrete velocities is 39 for the 3D lattice and is more affordable than the previous case. A detailed comparison of the schemes and formulations can be found in the doctoral thesis of Astoul [44].

A further compromise that can be made is that a reasonable error in the Navier-Stokes momentum equation can be tolerated. In this setting, the computation of moments of the equilibrium distribution upto second order is shown to generate an error term in the recovered momentum equation that is of $\mathcal{O}(M^3)$. Second order moments can be calculated on a 3D lattice using the Gauss-Hermite quadratures using a minimum of 19 discrete velocities and results in a quadrature with an order of accuracy of 5. This leads to the most popular lattice used in the LBM solvers, namely the D3Q19, and also to the hydrodynamic limits for the computation using fast LBM solvers as for those with low Mach numbers, typically $M < 0.4$ [111].

3.3 Discrete LBM solvers and Aeroacoustics

LBM also has specific advantages in view of aeroacoustics. Marié et al. [38] studied in detail the wave dispersion and dissipation of LBM schemes in comparison with canonical schemes used for isothermal Navier-Stokes equation. Their work suggested that lattice Boltzmann schemes, which including the Bhatnagar-Gross-Krook (BGK) and Multi-Relaxation Time (MRT) collision models, have better dissipation performance when compared to high-order discretisation schemes typically used for Navier-Stokes, i.e. for propagating waves through the fluidic medium using a discrete mesh. LBM schemes better preserve the wave energy across the discretised medium than Navier-Stokes solvers for a comparable grid size. In this regard, LBM models with the MRT scheme were also shown to be more dissipative than with the BGK model. Conversely, LBM schemes experience a larger dispersion. In their work, Marié et al. [38] compared the dispersion performance of LBM schemes to that of a second order finite difference scheme with a 3-step Runge-Kutta algorithm. However, the degree of parallelism and the speed of calculation enabled by LBM schemes are higher than high-order schemes for a given dispersion error. Moreover, with their lower dissipation, LBM schemes are much more stable than Navier-Stokes solvers with high order optimized schemes. These properties related to wave propagation makes LBM-CFD a prudent choice for aeroacoustic applications[37].

That being said, to use LBM for practical applications involving complex geometries, one bottleneck to overcome is the high number of nodes driven by the shape constraint of the lattice. In LBM, the lattices are so far required to have an aspect ratio of 1 to maintain integrity of its theoretical guarantees. This means that to resolve the boundary layer of the fluid over a given solid wall surface, the near wall cells also needs to be cubical. In conventional CFD, the near wall elements are made to have a very high aspect ratio such that the resolution in the normal direction to the wall is sufficiently high, while that parallel to the wall is maintained low, enabling a significant reduction of the total number of nodes in the mesh. The assumptions of the boundary layer allow this geometric shortcut without reducing the fidelity of the simulation as well. However this method cannot be utilized in the LBM simulations and in cases where the boundary layer behavior are important, the number of nodes in the simulation grows rapidly.

Such a limitation introduces the requirement of mesh coarsening in practical LBM solvers much like in conventional solvers. The strategy is to contain the region of high resolution close to the wall geometry and to allow the mesh to be coarsened depending on the distance. In LBM, this coarsening is done by a factor of 2 in each direction where a larger mesh cell adjacent to a finer cell will have twice the side length, thus maintaining the cubic shape in both blocks. The cell nodes that are adjacent can be made to be congruent at the coarsening interface or an interpolation scheme can be used to use hanging nodes, which would be placed on a cell edge rather than being a common node between the cells. The latter introduces more flexibility but introduces an additional source of error due to the accuracy for the interpolations. In the solver used for our work, ***ProLB***, the mesh coarsening technique used is the first one, i.e. with common nodes between adjacent cells on either side of a coarsening interface. However, the collision model in LBM utilizes information from the adjacent cells in its computation. This means that a change in cell size introduces errors into the simulation, with a strong detrimental effect onto the acoustic field due to the fact that acoustic perturbations are of similar amplitude as the mesh coarsening errors. The problem is exacerbated by the low dissipative nature of the LBM scheme as spurious fluctuations propagate through the domain without being dissipated near its sources. The mesh coarsening interfaces are hence thought of as sources of 'spurious noise' in the language of aeroacoustics.

These errors in the *ProLB* framework were studied in detail in the work of Astoul et al. [107]. According to their work, the problem fundamentally arises from the fact that the constraints applied to LBM equations to recover the hydrodynamic behavior is not sufficient to obtain the equilibrium distri-

butions corresponding to all the elements of the discrete velocity space. The dynamics of the additional unconstrained degrees of freedoms are not directly connected to the hydrodynamic behavior through the derivation of Navier-Stokes from Lattice Boltzmann Equation. This feeds the so called non-hydrodynamic modes, or ghost modes [114, 115], and can generate fluctuations which can be amplified by numerical errors arising from discretisation. These modes need to be adequately modelled. Hence accumulation of their errors eventually pollute the numerical solution with spurious vorticity and acoustic-like modes at grid refinements. In the work of Astoul et al. [107], these modes were detected and particularly identified using sensors in the LBM simulation. They were then systematically suppressed using improvements in the collision model formulation and the resulting Hybrid-Recursive Regularization (HRR) scheme was then used to replace the MRT scheme in the solver *ProLB*. This method hence guaranteed a reduction of such spurious noise generation in the versions of *ProLB* used in our work.

3.4 Acoustic Test Case using an Unsteady Compressible Perturbation

As a pilot study to test the effective numerical performance of *ProLB*, a classical test to assess the dissipation and dispersion performance was done using a planar Gaussian pulse. For this, a one dimensional Gaussian pulse with a pressure amplitude of 100Pa was initialized over an otherwise quiescent initial state. *ProLB* was then used to advance the solution in time to propagate the pulse for a distance of 1m. Analysis of the pulse in the Fourier domain then allows estimating the dissipation and dispersion effects for relevant Fourier components. To quantitatively study this case, we follow the analysis by Bres et al. [106] and consider the propagation of a plane wave in a viscous medium. The analytical solution of a plane wave propagating according to the linearized NS equation is described in Appendix A, showing the effect of viscosity on the wave's dissipation and dispersion. When the associated propagation equation is solved on a discretized mesh, the effective dissipation and dispersion is accounted for by an additional numerical viscosity. The solution for a plane wave pulse propagating into a direction x is described hereafter along with the numerical dissipation and dispersion.

3.4.1 Quantifying Numerical Rate of Dissipation and Dispersion

The temporal Fourier transform of a selected pulse can be used to characterize the dispersion and dissipation. For this the pressure time history at an arbitrary location can be expanded into Fourier integrals as

$$P'(x,t) = \frac{1}{\sqrt{2\pi}} \int_{-\infty}^{+\infty} \hat{P}'(x,\omega) e^{-i\omega t} d\omega \quad (3.16)$$

From the Fourier transform of the arbitrary solution in Eq.(A.9), the propagated wave will have a local Fourier transform given by

$$\hat{P}'(x,\omega) = \hat{P}'(0,\omega) \exp \left[-(\alpha_S + \alpha_S^{\text{num}}) x \right] \exp \left[i\omega \frac{x}{c_S + c_s^{\text{num}}} \right] \quad (3.17)$$

which allows to determine the numerical dissipation rate α_S^{num} and sound speed c_s^{num} . Here, by taking the amplitude on both sides we obtain

$$|\hat{P}'(x,\omega)| = |\hat{P}'(0,\omega)| \exp \left[-(\alpha_S + \alpha_S^{\text{num}}) x \right] \quad (3.18)$$

or

$$\alpha_S^{\text{num}}(\omega, x) = -\frac{1}{x} \ln \left| \frac{\hat{P}'(x, \omega)}{\hat{P}'(0, \omega)} \right| - \alpha_S \quad (3.19)$$

and by taking complex argument on both sides of Eq.(3.17) we have,

$$\text{Arg}(\hat{P}'(x, \omega)) = \text{Arg}(\hat{P}'(0, \omega)) + \frac{\omega x}{c_S + c_s^{\text{num}}} \quad (3.20)$$

or

$$c_s^{\text{num}}(\omega, x) = \omega x \left(\text{Arg} \left(\frac{\hat{P}'(x, \omega)}{\hat{P}'(0, \omega)} \right) \right)^{-1} - c_S \quad (3.21)$$

where $\alpha_S = \omega^2 \nu / c_0^2$ and $c_s = c_0$ are obtained as described in Appendix A. The above equations to calculate the effective numerical dispersion and dissipation as a function of position enable us to characterize the wave propagation performance of our LBM solver and thereby choose a sufficient simulation parameter setting, particularly the required mesh resolutions to enable aeroacoustic calculations.

3.4.2 Simulation Details

Choice of initial pulse

The Gaussian pulse propagated for the simulation should contain the frequencies of interest, i.e. the bandwidth of the signal should be at least 10 kHz in frequency or $10^4 / 343 = 30 \text{ m}^{-1}$ in the spatial wavenumber domain. This is adjusted by choosing a sufficiently small pulse width. Here the Fourier bandwidth of a Gaussian pulse varies inversely as pulse width with bandwidth of a Dirac Delta function being infinite. The selected pulse in spatial domain is plotted in Fig.3.1b.

Following Brès et al. [106], we then use the initial pulse at origin with the form

$$P'(x, y, z, 0) = 10^{-3} P_0 \exp \left(-\ln(2) \frac{x^2}{\sigma^2} \right) \quad (3.22)$$

where $\sigma = 0.01 \text{ m}$ is the pulse width which contains wave numbers upto 50 m^{-1} and corresponding maximum time-frequency of 17 kHz, which is sufficient in view of slat noise since the interesting frequencies are below 10 kHz.

Choice of discretisation

To study the effect of numerical dissipation with respect to mesh sizing and to make a choice for the simulation of the slat-airfoil cases, we test *ProLB* on three relevant cell sizes, i.e. for $\Delta x \in [0.001, 0.002, 0.004] \text{ m}$. This variation then allows to study dispersion sensitivity with respect to the number of points per wavelength (N_{ppw}) given by

$$N_{ppw} = \frac{\lambda}{\Delta x} = \frac{1}{k \Delta x} \quad (3.23)$$

where k is the wave number $\frac{1}{\lambda}$.

Hence the performance of the code with respect to the wave of wavenumber of 50 m^{-1} for the case of a resolution of 0.001 m corresponds to its performance at 20 points per wavelength. The wave propagation and its numerical effects are linear in the frequency domain – being captured by the linearized Navier-Stokes – and hence the behavior of the pulse in the frequency domain is an adequate indicator of the

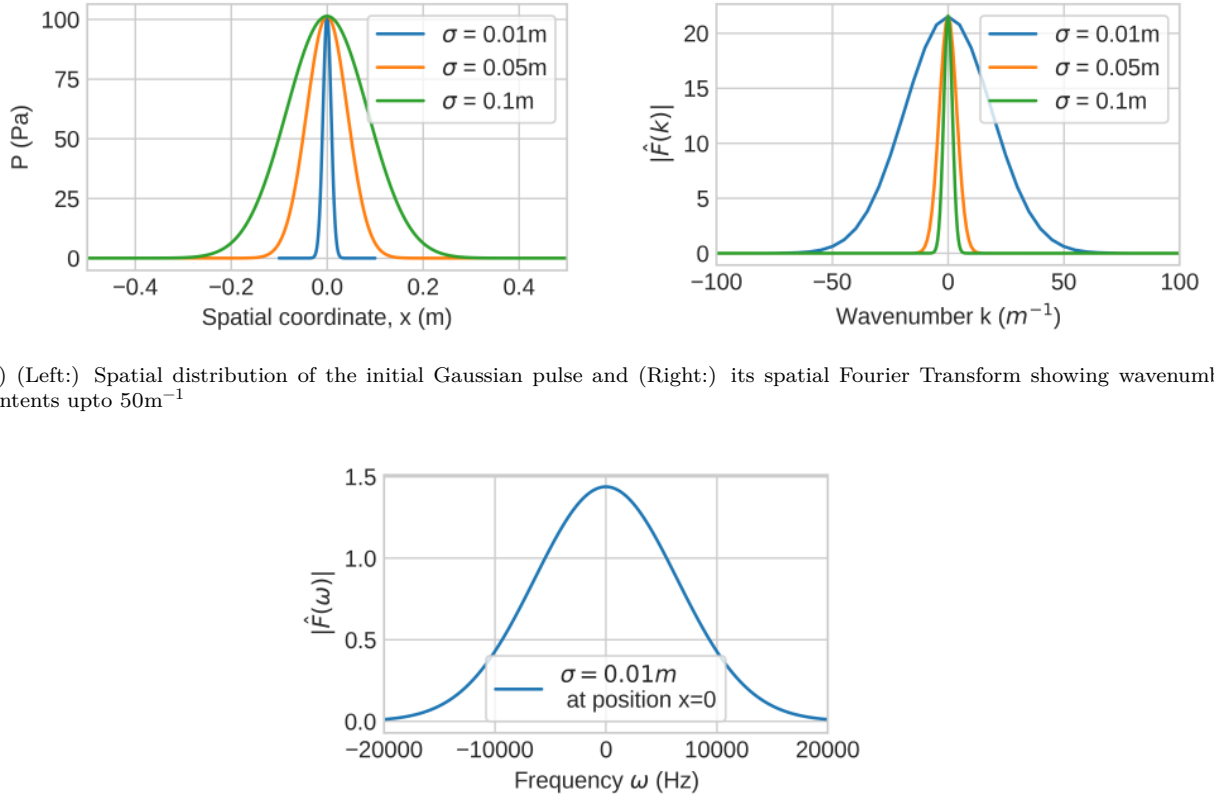


Figure 3.1: A simple Gaussian pulse in spatial, temporal, and frequency domains

LBM code response for each of its Fourier components. Thus the same for acoustic waves in an actual simulation when linear acoustics are considered to be dominant.

3.4.3 Simulation Results

LBM simulations of the above described acoustic pulse propagation are performed using the *ProLB* solver and the results are compared with the cases simulated using PowerFLOW as reported in the work of Brès et al. [106]. The propagation of the pulse, starting at the initial position $x=0$, as a time series at different probe locations of the domain, $x = [0.1, 0.6, 1.1]\text{m}$ are shown in Fig.3.2. The propagated pulse shows evident dispersion and dissipation for the coarse mesh cases $\Delta x = 0.002\text{m}$ and 0.004m . But the propagation is apparently efficient for the case $\Delta x = 0.001\text{m}$ where the loss in amplitude and dispersion effects are low upto 1m distance as we studied. A comparison of the cases are shown in Fig.3.2.

$\downarrow k \Delta x \rightarrow$	0.001m	0.002m	0.004m	
50 m^{-1}	20	10	5	17150 Hz
25 m^{-1}	40	20	10	8575 Hz
1 m^{-1}	1000	500	200	343 Hz
	$3 \times 10^{-6}\text{ s}$	$6 \times 10^{-6}\text{s}$	$1.2 \times 10^{-5}\text{ s}$	$\leftarrow \Delta t \omega \uparrow$

Table 3.1: Number of Points Per Wavelength (PPW) for relevant values of wavenumbers and cell sizes. Corresponding temporal frequencies and timestep sizes for $CFL = 1$ also shown

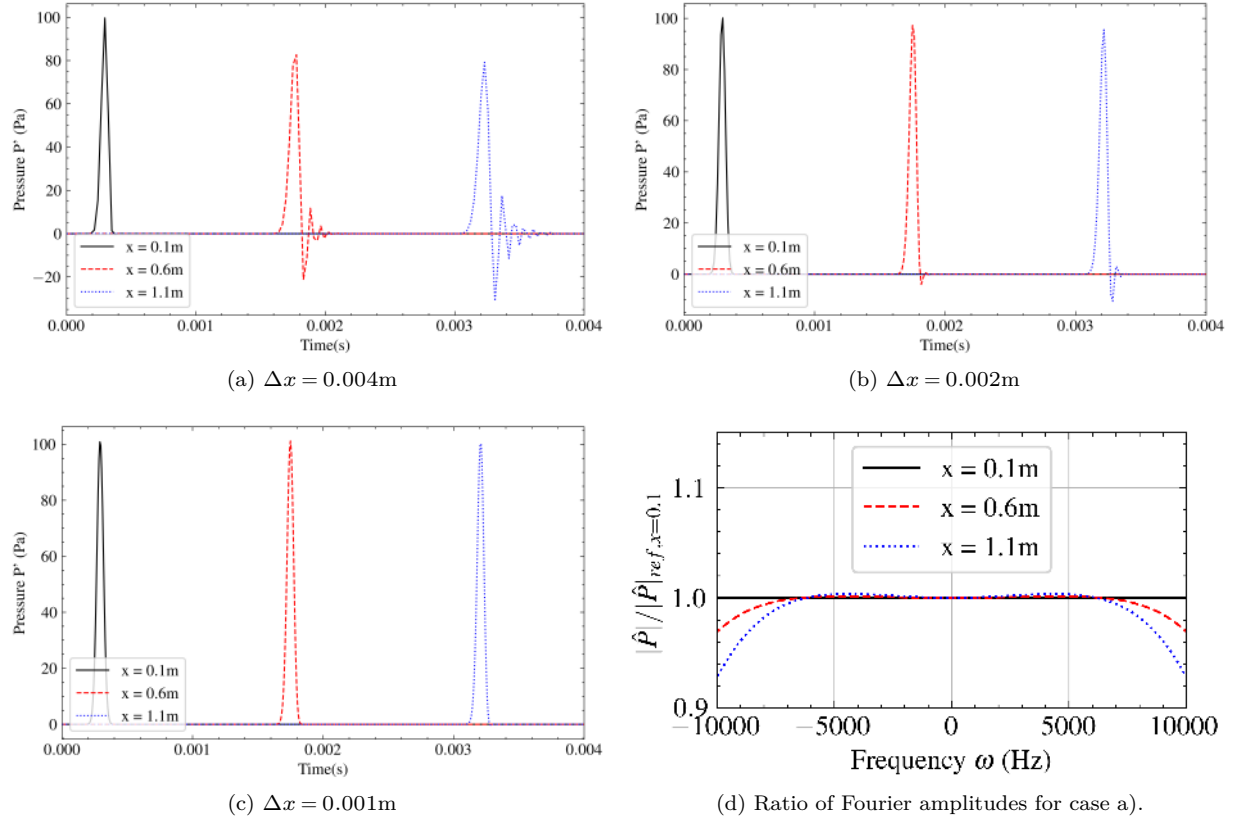


Figure 3.2: Time history of the propagating pulse at positions downstream of the right traveling pulse using *ProLB* simulation with resolution a) $\Delta x = 0.004\text{m}$, b) $\Delta x = 0.002\text{m}$, c) $\Delta x = 0.001\text{m}$. The variation of the Fourier transform with respect to propagation distances for case a) is shown in d) using the amplitudes of FT as a ratio of its initial value.

The numerical dissipation coefficient is a function of the frequency or the wave number and higher frequencies suffer higher dissipation. The inverse is true for dispersion where the higher wave number components suffer more from a loss of phase speed. Variation of the pulse in the frequency domain as it propagates through the mesh illustrates this and is shown in Figure 3.2. The same is shown as a ratio of amplitude of a propagated wave and the original wave in Fig.3.2d. The distribution of rate of dissipation α_S^{num} arising from numerical discretisation as obtained according to the spatial analysis in Section A.1.3 is shown in Fig.3.3. As expected, the obtained values follow the trend as described by Brès et al. [106] which is shown in Fig.3.4. Nevertheless, for the *ProLB* result, the slight amplification of the mid-high frequencies are also notable as the negative value of α_S^{num} . This means that the waves of these frequencies will show a growth in amplitude during the propagation and those at higher frequencies will dissipate, both effects amplified when the mesh is coarsened. However, we do not notice such growth of amplitude leading to an instability in the test case and is thought to be counterbalanced by the viscosity at a higher amplitude range. Additionally, the cell size chosen for the simulation is close to the finest grid in the test which does not exhibit such amplification. Finally, from Figure 3.3, for our frequencies of interest which is less than 10kHz, it is deduced that a cell size of 0.002m will give a system able to propagate the acoustic waves with a loss of approximately 0.01Np/m. This translates to $\approx 0.09\text{dB}$ reduction in the amplitude of the acoustic wave while propagated through a distance of 1m.

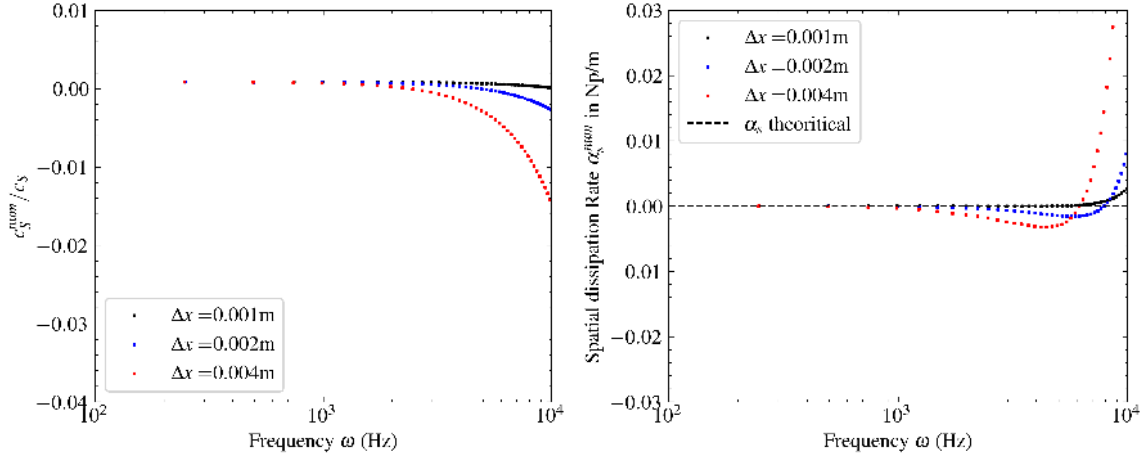


Figure 3.3: The dispersion(left) and dissipation(right) results for an initial acoustic Gaussian pulse of amplitude 100Pa, (above mean pressure, SPL: 134dB) for propagation over 1m using *ProLB*. Multiple plots are for multiple minimal voxel sizes of the mesh.

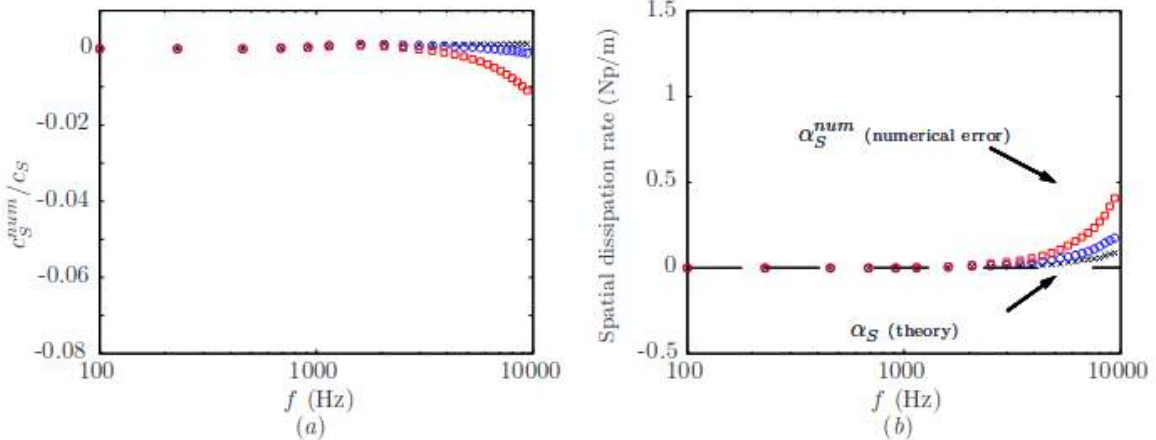


Figure 3.4: The dispersion(left) and dissipation(right) results for the same case using PowerFLOW from the work of Brès et al. [106]

3.5 Ffowcs Williams-Hawkins Analogy for Far-field Noise

As deduced from the direct pulse propagation test case, a mesh size of approximately 0.002m meets the criteria for near lossless propagation of the acoustic waves upto 10 kHz. Nevertheless, the number of voxels in the Cartesian mesh used for LBM simulations scales with $(\Delta x)^3$ and hence direct noise computation remains expensive. Here, a Ffowcs Williams–Hawkins (FWH) analogy[45, 116] is used instead for the far-field propagation. Being an exact rearrangement of the Navier-Stokes equation in the form of a wave equation and by using the free space Green’s function to obtain an analytic integral formula for the far field sound, FWH analogy enables fast computation of sound at a farfield location. For our work, the calculation is coded in the TurbAcAn solver, developed at Ecole Centrale de Lyon, based on the advanced time formulation by Casalino [46]. The solver has previously been tested alongside URANS[117] and LES[118] applications. In the present work, the solver is interfaced with *ProLB* to process the flow recordings a posteriori and simple test cases were performed which are detailed in this section. Before delineating the Ffowcs Williams-Hawkins implementation, we briefly summarize the basic theory first.

The Ffowcs Williams-Hawkins equation is an exact formulation derived from the Navier-Stokes equa-

tions in the presence of a stationary or moving body in a fluid medium. It is obtained using the same approach as for Lighthill's equation in free flow, extended to the presence of solid bodies. In addition, the variables are defined over the whole space by means of the Heaviside function and a characteristic function f that is positive in the flow domain, negative inside the solid and zero on the solid boundary. The generalized Lighthill's equation thus obtained will have two new source terms in addition to the Lighthill's stress tensor. The resulting equation is the general Ffowcs Williams-Hawkins equation. It takes the form

$$\left\{ \frac{\partial^2}{\partial t^2} - c_0^2 \Delta \right\} [\rho_a H(f)] = \frac{\partial^2}{\partial x_i \partial x_j} [T_{ij} H(f)] - \frac{\partial}{\partial x_i} [L_i \delta(f)] + \frac{\partial}{\partial t} [Q \delta(f)]$$

Here, $H(f)$ is the Heaviside function vanishing inside the solid body and experiencing a jump across the solid surface, $\delta(f)$ is the Dirac Delta function capturing the solid body surface. The first term on the right-hand side contains T_{ij} which is the Lighthill's stress tensor written as

$$T_{ij} = \rho u_i u_j + p_{ij} - c^2 (\rho - \rho_0) \delta_{ij}$$

where i and j are the directional indices and $p_{ij} = p \delta_{ij} + \tau_{ij}$ is the fluid stress tensor. Due to the second order derivative, this term represents a quadrupole source.

The formulation has two additional sources on the right-hand side than the canonical form of the wave equation due to the treatment of the variables using the Heaviside function. The first of these, $\frac{\partial}{\partial x_i} [L_i \delta(f)]$, is called the loading noise term. It involves a first order spatial derivative over the surface and is hence a dipole source term. The term L_i can be obtained as

$$L_i = [\rho u_i (u_j - u_j^\Sigma) + P_{ij}] n_j$$

where n_j is the surface unit normal vector, u^Σ is the velocity vector of the surface in case of a moving surface, and P_{ij} is same as the stress tensor p_{ij} . The difference of notation between P_{ij} and p_{ij} is canonically used to differentiate the context of source integration, where p_{ij} contributes as a volume stress tensor in the Lighthill term while P_{ij} contributes only as the surface stress or traction via $P_{ij} n_j$ in the loading noise term. In the inviscid case, both p_{ij} and P_{ij} reduce to $p \delta_{ij}$, and the surface traction simplifies to $P_{ij} n_j = p n_i$, i.e. the wall-normal pressure component.

The second additional term, $\frac{\partial}{\partial t} [Q \delta(f)]$, is called the thickness noise and captures the mass flow rate fluctuation on the surface. It is omnidirectional (time derivative) and thus described as a monopole term. Here Q can be obtained as

$$Q = [\rho (u_j - u_j^\Sigma) + \rho_\infty u_j^\Sigma] n_j$$

The FWH equation presented here represents the generalized FWH sources. When applied to a real solid surface, the wall normal flow velocity u_j vanishes and if the solid body is at rest, u^Σ also vanishes. This means that when applied to a solid body surface at rest, the loading noise term reduces to $L_i = P_{ij} n_j$, which under the inviscid assumption further reduces to the wall normal pressure loading $p n_i$, i.e. the fluctuating wall-normal pressure load.

Extension to arbitrary control surfaces

Both of these sources arise as a mathematical consequence of truncating the propagation domain by multiplying with a Heaviside function. Differentiation of the Heaviside function generates delta-function terms supported on the truncation surface, thereby converting volumetric contributions into equivalent surface

terms. This operation is analogous to Gauss's divergence theorem, in which the effect of a distributed quantity within a volume can be represented as a flux through its boundary. In the present context, this means that the presence of distributed sources inside a volume where acoustic perturbations propagate towards the boundary is equivalent to having surface sources on that boundary. The best outcome of this technique is that for both loading and thickness noise terms, mathematically, there is no direct contribution from inside of the control volume since $H(f)$ vanishes inside. Thus, instead of calculating the propagation of the sound from the exact source point, it is sufficient to have the recordings of their emanating wavefronts while they are incident on the chosen surface, and can then be used to model the equivalent surface sources for further propagation to the farfield. This enables to compute the noise generated by turbulence in complex flows by recording the emanated wave on an exterior surface surrounding the source region which are strongly perturbed by the turbulence in the interior.

Another consequence of the formalism is that the canonical Lighthill's source term, $\frac{\partial^2}{\partial x_i \partial x_j} [T_{ij} H(f)]$, is only dominant in the region of turbulent flows leading to the quadrupole source. But this source term is vanishing outside the region of active turbulence. If thought of as being computed on an imaginary surface enclosing a volume region which is first placed inside the turbulent region and then expanded towards outside of the active source region, the source energies associated with quadrupole source terms inside the volume gets progressively transferred to the other two terms by nature of the conservation of momentum itself that is causal for the sound radiation.

Solution for the FWH equation

To obtain a direct formula for the sound propagated to a farfield observer from the chosen recording surface, a free space Green's function, typically of the form $G = \frac{\delta(g)}{r}$, where $\delta(g)$ is the Dirac function at a source location, $g = t - \tau - r/c$ and $r = |x - y|$, where x is the receiver position, y is the source position, and τ is the time of emission, is used to convolve with the source term. Completing the integral in time along with the properties of δ -function support on the imaginary surface, the sound received at a particular observer location y is obtained as

$$4\pi p' = \frac{\partial^2}{\partial x_i \partial x_j} \int_{f>0} \left[\frac{T_{ij}}{r(1-M_r)} \right]_{ret} dV - \frac{\partial}{\partial x_i} \int_{f=0} \left[\frac{L_i}{r(1-M_r)} \right]_{ret} dS + \frac{\partial}{\partial t} \int_{f=0} \left[\frac{Q}{r(1-M_r)} \right]_{ret} dS \quad (3.24)$$

where $[.]_{ret}$ denotes the quantities at a retarded time, which is related to current time t as

$$\tau_{ret} = t - \frac{|x - y(\tau_{ret})|}{c}$$

where $y(\tau_{ret})$ is the source position at the retarded time τ_{ret} .

The integration then leads to the retarded time formulation of the FWH analogy called the Farassat's 1A formulation[119] with the final form for the thickness noise and loading noise terms as

$$4\pi p'_Q(\mathbf{x}, t) = \int_{f=0} \left[\frac{\rho_0 (\dot{U}_n + U_{\dot{n}})}{r(1-M_r)^2} \right]_{ret} dS + \int_{f=0} \left[\frac{\rho_0 U_n (r\dot{M}_r + c(M_r - M^2))}{r^2(1-M_r)^3} \right]_{ret} dS \quad (3.25)$$

and

$$4\pi p'_L(\mathbf{x}, t) = \frac{1}{c} \int_{f=0} \left[\frac{\dot{L}_r}{r(1-M_r)^2} \right]_{ret} dS + \int_{f=0} \left[\frac{L_r - L_M}{r^2(1-M_r)^2} \right]_{ret} dS + \frac{1}{c} \int_{f=0} \left[\frac{L_r (r\dot{M}_r + c(M_r - M^2))}{r^2(1-M_r)^3} \right]_{ret} dS \quad (3.26)$$

The quadrupole term remains an integral over the volume and cannot be reduced to a surface integral. This term is often omitted in practice on the condition that the Mach number is low, although this assumption is still under debate. This requirement is met if there is no active turbulence where the surface is placed.

This method leads to the calculation of the sound received by each observer at each time step as an integral on the recording surface. The calculation thus uses the data on the surface locations at a time of emission which coincides with the condition that a source emitting sound at a particular time will have the wave reaching the observer at the particular observer time step, or precisely, the computation time step is the observer's time step or the reception time step. This retarded time formulation leads the calculation on the surface to be done at different source emission times for the same observer time step and hence is cumbersome although calculation a posteriori on the recorded data has been widely used and proven robust. Casalino [46] gave the alternative definition that improved the numerical efficiency of this calculation. In his formulation, called the Advanced Time formulation, the calculation is instead done for each time step of the data available on the surface. Thus the computation time is now the emission time step. For this, the relation between reception time, now called the Advanced Time, and the emission time is calculated as

$$t_{adv} = t + \mathcal{T}$$

where

$$\mathcal{T} = \frac{|\mathbf{x}(t+\mathcal{T}) - \mathbf{y}(t)|}{c} \quad (3.27)$$

is the time lag between the emission time and the reception time between a source at location \mathbf{y} and an observer at location \mathbf{x} .

Using this relation, the farfield sound due the fluctuation on the surface from each time step is distributed over the full time domain of listening for the observer. This enables simpler calculation since the data on surface is now accessed sequentially and only the listener time steps need to be calculated for each mesh point. Also, the data on the surface now requires only to be recorded at the resolution of the observer time step, whereas in retarded time formulation, the requirement of source terms at differ-

ent emission times implies that the resolution of the flow recording had to be higher than the acoustic resolution for the observer to avoid errors due to discretisation of the emission times. However, in the Advanced Time approach, the distribution of the radiated sound on to discrete time steps for listener means that the calculated time lag from the source cell to the listener may not always coincide with the available discrete time step. This will necessitate an interpolation of the received sound. Nevertheless, a linear interpolation between two time steps was demonstrated to give satisfactory result in the original work of Casalino [46].

As mentioned, for practical application, Casalino's Advanced Time formulation [46] also retain the volume integrals for the quadrupole source terms causing a restriction on the placement of the FWH surface. In our simulations of the high-lift airfoil, the surface is chosen to surround the acoustic sources in the vicinity of the airfoil and is kept far enough from the airfoil suction side to avoid strong vortices ejected from the slat cove. Nevertheless, it is impossible to have a surface that encloses the airfoil and does not lead to intersecting wake region downstream of the airfoil. Therefore, the surface is kept open downstream of the airfoil, so that no vorticity fluctuations are convected through the surface. An alternative approach to keeping an open surface is by using averaging surfaces in the downstream region where vortices are convected through[120]. We do not choose this approach since our placement of the surface sufficiently far from the airfoil and extended downstream is shown to be able to recover the slat noise signature with a good agreement with the experiment in our validation test. The integration surface used for recording unsteady data is shown in Figure 3.5a and the truncated surface used for surface integral calculation is shown in Figure 3.5b. It must be mentioned that some large-size low-vorticity structures still approach the upper side of the surface but the generated spurious sound sources are negligible.

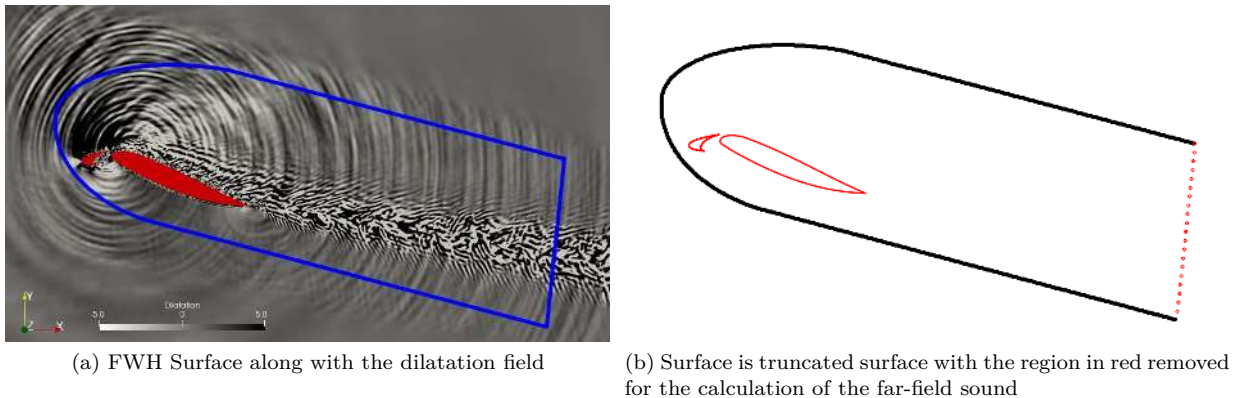


Figure 3.5: FWH surface placement along with the HLD geometry put into perspective

3.5.1 Monopole Test case for TurbAcAn

For using FWH analogy and enable far-field noise calculation from the LBM simulation data, we used an in-house solver named TurbAcAn. The routine written in FORTRAN utilizes a structured Cartesian grid for the calculation of the surface integrals mentioned in Eq. 3.25 and 3.26. Nevertheless, this routine needed to be adapted to read data saved from *ProLB* solver and we chose to use the XDMF format for the data input pipeline. An XDMF file reader was designed to read the data iteratively from memory for each time step of the recording and was used to compute the farfield sound. The following test case was then used to check the accuracy of the code and the new file reader.

For the first test case, we chose to simulate an acoustic monopole using the LBM solver *ProLB*. For this, a time varying pressure was applied to a spherical geometry of suitable size resulting in the radiation

of a sound field. A spherical FWH surface was then used to record the field at some distance around the source. The FWH module TurbAcAn was then used to calculate the sound at observer positions farther away from the source. The radiated field was found in good agreement with the analytical solution and also with the recorded field at observer positions by Direct Noise Computation (DNC).

3.5.1.1 Analytical solution

For an acoustic Monopole in an otherwise quiescent medium, the pressure and velocity perturbations at a distance R from the surface, assuming farfield, are given by the equation

$$p(r, t) = \left(\frac{Q_s}{r} \right) \sin(k(ct - r)) = \left(\frac{Q_s}{r} \right) \sin(\omega(t - r/c)) \quad (3.28)$$

$$u(r, t) = \left(\frac{Q_s}{\rho c r} \right) \sin(\omega(t - r/c)) \quad (3.29)$$

where Q_s is the strength of the so called Monopole source.

This solution can be used as a forcing agent for the LBM simulation to mimic the behavior of a Monopole source. But since the flow solver only enables specification of either velocity or pressure distribution, we choose the pressure as time varying forcing. This also limits the specification of source only as a farfield solution since in the near field of a Monopole source, the pressure and velocity fluctuations are out of phase, and hence both pressure and velocity need to be specified. On the other hand, in the farfield, the pressure and velocity oscillations are approximately in-phase, and hence a specification of pressure only as forcing term leads to velocity fluctuations that are approximately in-phase. For the given source frequency of 5000Hz, corresponding Helmholtz number is $He = \frac{2\pi f}{c} r$. A source surface of radius 0.025 m is chosen such that the Helmholtz number of the source surface $He_s = \frac{2\pi f}{c} r = \frac{2\pi \times 5000}{c} \times 0.025 = 2.29 > 1.0$. This source surface is shown in red in Fig.3.6a.

Following Eq.3.28, the effect of point Monopole source at the center of a spherical surface of radius $r = 0.025$ m leads to pressure distribution on the surface given by

$$p(0.025, t) = \left(\frac{Q_s}{0.025} \right) \sin(2\pi \times 5000 \times (t - 0.025/c)) \quad (3.30)$$

Since the pressure on the surface is specified in the *ProLB* solver with the time coordinate $t_s = t - t_0$, where t is the time coordinate of imaginary monopole source and $t_0 = 0.025/c$ is the time at which the wave reaches the source surface in simulation. This surface was used as the forcing surface for a harmonic wave of 5000Hz and amplitude of 100Pa which can be written as

$$p(0.025, t_s) = 100 \sin(2\pi \times 5000 \times t_s) \quad (3.31)$$

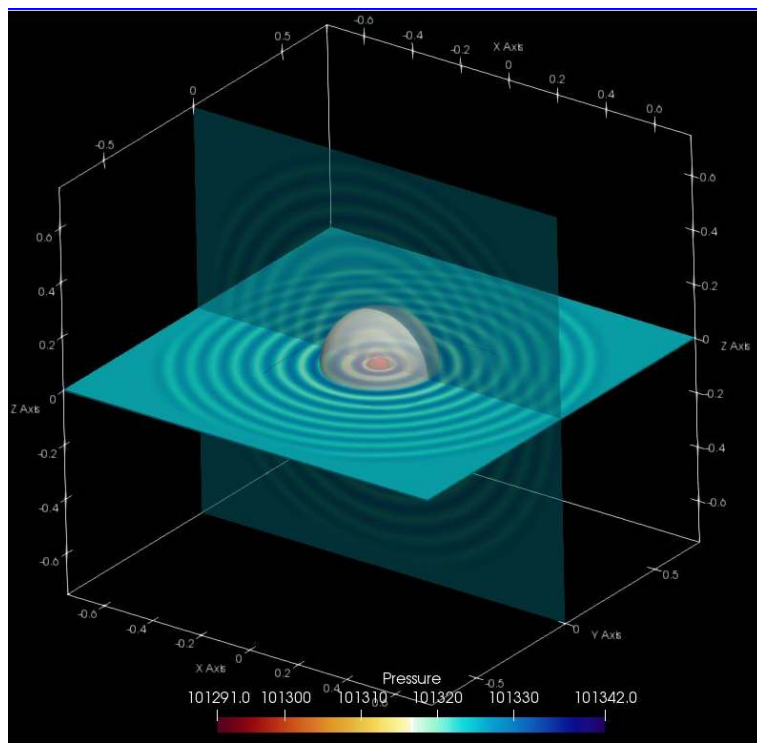
On comparing Eq.3.30 and Eq.3.31, we obtain equivalent monopole source amplitude

$$\frac{Q_s}{0.025} = 100 \implies Q_s = 0.025 \times 100 = 2.5 \text{ Pa.m} \quad (3.32)$$

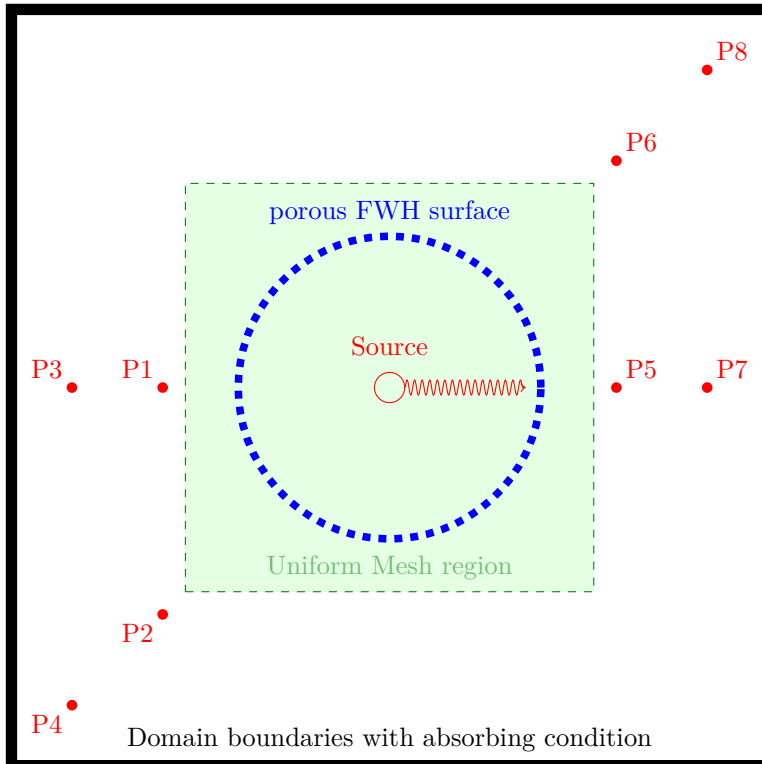
Using this value of equivalent monopole strength in Eq.3.28 to estimate the amplitude on the FWH surface with radius $r = 0.2$ m, we get

$$P(0.2, t_s) \approx \left(\frac{2.5}{0.2} \right) \sin \left[2\pi \times 5000 \times \left(t_s - \frac{0.2}{c} \right) \right] = 12.5 \sin \left[2\pi \times 5000 \times \left(t_s - \frac{0.2}{c} \right) \right] \quad (3.33)$$

However, this amplitude of 12.5Pa is not recovered on the FWH surface during the simulation and observed waves tend to have a lower amplitude. This owes to the fact that the simulated harmonic pressure



(a) Pulsating source surface (red) simulation showing the spherical wave propagation and FWH surface (grey) used for recording flow variables.



(b) A 2D schematic of the test case for FWH module TurbAcAn showing the probe locations. Even numbered probes are not in the same 2D plane during recording and exact coordinates are given in Fig. 3.7

Figure 3.6: FWH surface test case using a pulsating spherical source

source efficiency is lower than that of an actual Monopole since the specified boundary conditions in the LBM setting does not involve specification of the macro-variables but that of the particle population densities. The latter introduces additional complexity, as mentioned while discussing on Eq. 34 in the work of Wissocq et al. [121]. Hence for the purpose of expediency towards study of acoustics, instead of using the explicitly specified source amplitude, the simulated amplitude available at the FWH surface is used to estimate the equivalent Monopole strength. Simulated pressure amplitude on the FWH surface is obtained as 6 Pa on the spherical surface having a radius $r = 0.2\text{m}$. i.e.

$$P(0.2, t_s) \approx \left(\frac{Q_s}{0.2}\right) \sin \left[2\pi \times 5000 \times \left(t_s - \frac{0.2}{c}\right) \right] = 6 \sin \left[2\pi \times 5000 \times \left(t_s - \frac{0.2}{c}\right) \right] \quad (3.34)$$

Hence,

$$\left(\frac{Q_s}{0.2}\right) = 6 \implies Q_s = 1.2 \text{Pa.m} \quad (3.35)$$

Following Eq.3.28, corresponding analytical solution for farfield observer at radial distance R_{obs} then writes

$$P(R_{obs}, t_s) \approx \left(\frac{1.2}{R_{obs}}\right) \sin [2\pi \times 5000 \times t_s]$$

This result is used as the analytical solution for comparison in Fig.3.7.

3.5.1.2 Choice of time stepping and cell size

According to Casalino [46], the FWH scheme shows phase shifting depending on the time stepping used. Accordingly, a timestep corresponding to 75 points per time period of the wave is chosen for the first case study. Hence for the simulation, a time step $\Delta t = 2.66 \times 10^{-6}\text{s}$, corresponding to 75 points for a wave with frequency 5000Hz is used.

Cell size corresponding to the time step is obtained by setting the cell Courant number to 1, which is default for the LBM scheme in *ProLB* , leading to

$$\Delta x = c\Delta t\sqrt{3} = 343.2 \times 2.66 \times 10^{-6}\sqrt{3} = 1.58 \times 10^{-3}\text{m} \approx 1.6\text{mm} \quad (3.36)$$

The number of points per wavelength for minimal dissipation and dispersion in *ProLB* was identified in a previous section. Considering that maximum frequency of interest is 10 kHz, a cell size of 0.002m was satisfactory. This corresponds to a value of 17 points per wavelength. The cell size used in current simulation is 1.6mm, and for a frequency of 5000Hz of the source, this correspond to 34 points per wavelength.

3.5.1.3 Results

The spherical wave test case results from the FWH computation were compared with the analytical result. As shown in Figure 3.7, the FWH routine implementation provides an accurate computation. Here the odd numbered probes are placed in the same 2D center plane as the source and the even numbered probes are placed on a diagonal line and out of the center plane. For all probes, the wave shape, frequency, amplitude, and delay times, for different observer locations are found to be in good agreement. The computation using the FWH surface are also compared with noise obtained at observer positions by direct recording, which is a Direct Noise Computation (DNC). For the DNC, the recordings shows deviations in the even numbered probes placed on the diagonals and also have notable phase variations. This is expected since, as shown in Figure 3.7, the probes are placed outside the first level of refinement and the corner nodes at the coarsening distort the propagation of waves as discussed in Section 3.3. This suggests

that the propagation of waves through mesh refinements in the *ProLB* solver has room for improvement, particularly at the corner nodes of refinement interfaces.

3.6 Validation Case Setup

With the aim of running a parametric study on the HLD geometry of slat-airfoil configuration, we concocted a template based case setup for the LBM simulation. The voxel meshing combined with the immersed boundary method used for the *ProLB* software enables meshing of the complicated flow domain in the slat cove with almost no user intervention during mesh generation and is thus very convenient for such a parameterisation. In this section, we first explain the choice of parameters that we selected for the template, which are the parameters of the LBM case setup for all simulations described in this thesis. The acoustic computation using FWH is also made part of this template since the surface placement can be chosen such that no case specific adjustments or repositioning is necessary. Following this case setup and injection of the geometries of the airfoil and slat, the complete simulation case files are compiled, where the relative position of the slat with respect to the main element are varied. The latter is then documented and post-processed in the following chapter.

3.6.1 Base template

To create the base template for the simulation, we utilize the pre-processing module LBPre available with *ProLB* suite. Following best practices from previous works on HLD using LBM solvers [105, 28, 39], a square domain is selected with an extent of $25C$, where $C = 0.3\text{m}$ is the stowed chord length of the VALIANT airfoil. The boundaries are then supplied with appropriate macro flow variables as inlet and outlet boundaries. The inlet velocity is $50,\text{m/s}$ for all parametric simulations planned. For the outlet and farfield boundaries, a constant Pressure condition of 101325 Pa is supplied. The domain boundaries are then supplanted with 2m of absorbing region with conditions to avoid reflection of the perturbations from the boundary. The absorbing boundary layers available in *ProLB* provide relaxation parameters to enable compatibility with different boundary conditions. The relaxation parameters allow the macro-variables to be maintained or attenuated by altering the underlying particle populations[121]. In the case of the inlet velocity boundary, the velocity relaxation targets are fixed to the inlet velocity value so that the absorbing layer does not attenuate the incoming velocity into the domain. To avoid reflection of the pressure waves, the pressure relaxation target is set to be Dynamic. In the Dynamic setting, the Pressure is relaxed towards the mean thermodynamic equilibrium pressure by only attenuating the fluctuating pressure waves. This enables a clean and steady inlet velocity boundary condition. For the case of three other boundaries, i.e. the outlet plane and farfield planes at the pressure and suction side of the airfoil, the Pressure value is set to the atmospheric pressure. This Dirichlet condition requires that the Pressure field in the absorbing region needs to be relaxed to a fixed Pressure. Since the outflow is unconstrained, the velocity target is set to be Free, meaning that the relaxation of velocity is not performed. In the spanwise direction, periodic boundary conditions are applied.

3.6.2 Spanwise Periodic conditions

On using periodic conditions for the flow, perturbations in the spanwise domain are known for their tendency to foster spatially periodic patterns scaling on the span extent and multiples of the associated wave number $2\pi n/L$ to maintain spanwise correlation as well as to make the flow homogeneous over the span avoiding the spontaneous decorrelation of the flow. This artificially induced coherence needs to be avoided, particularly in view of the aeroacoustic mechanisms involving the role of spanwise coherent eddies

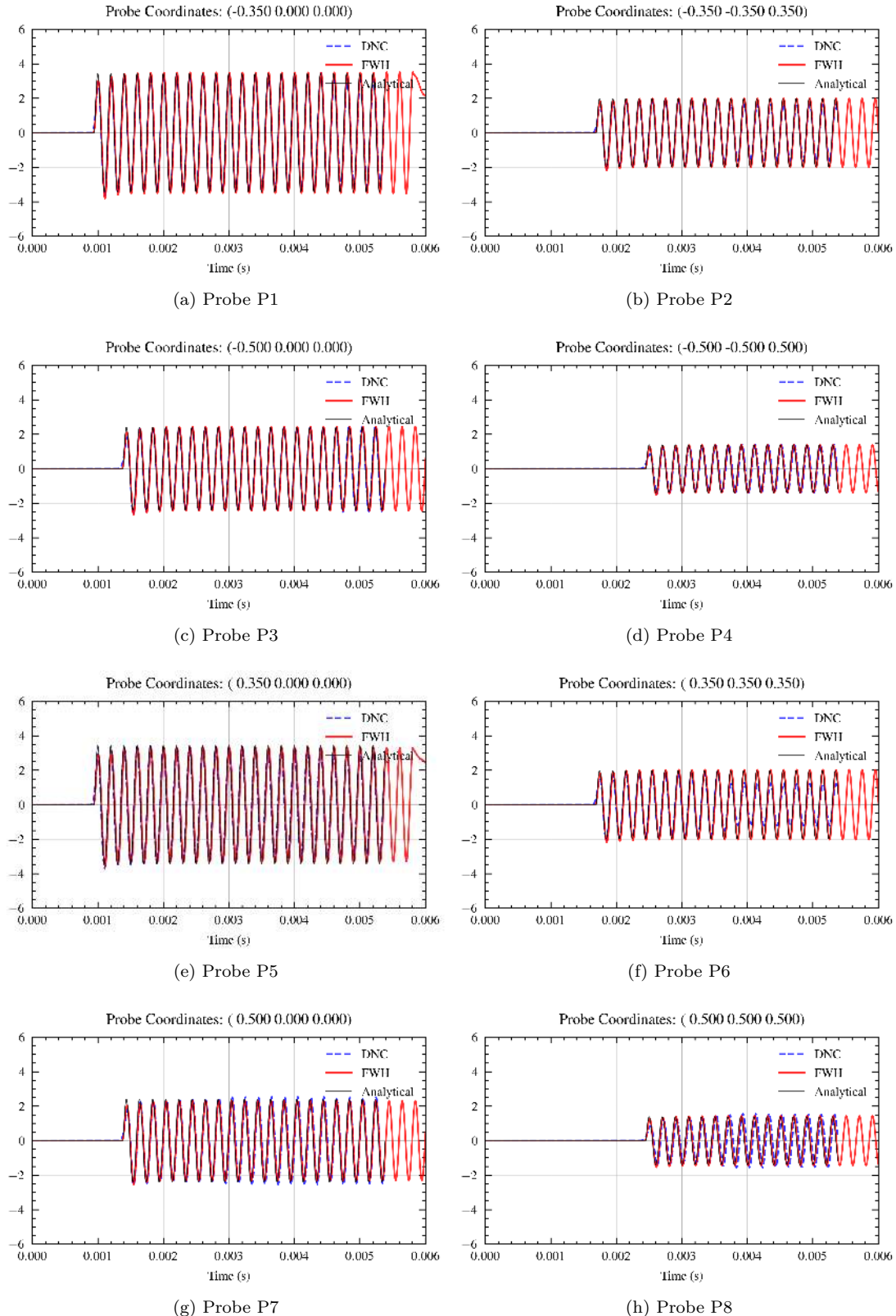
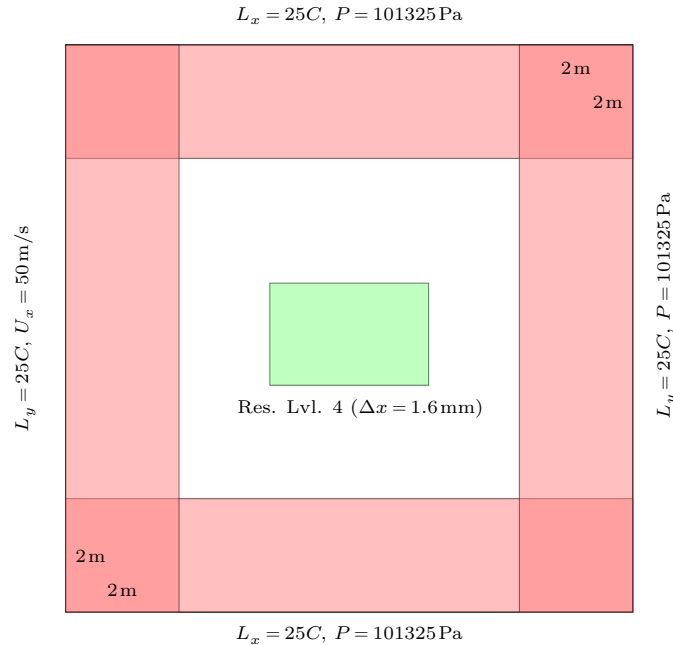
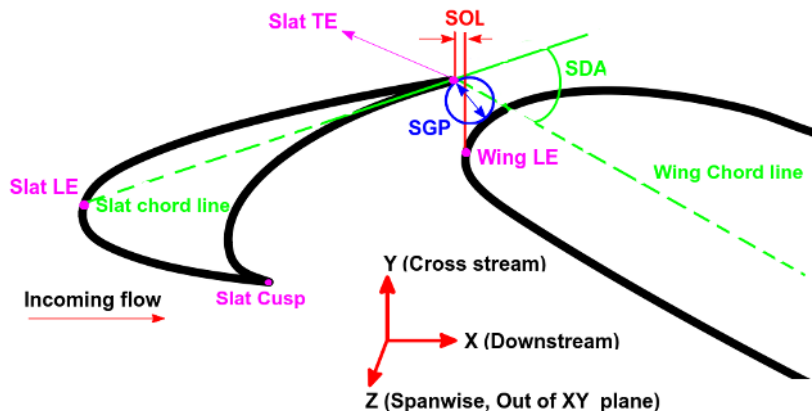


Figure 3.7: Results for pulsating pressure source test case for *TurbAcAn* showing signals obtained at various probe coordinates. The inaccuracies arising from propagation of waves by DNC across mesh coarsening can be noted to be larger when the probe is in coarse mesh region. FWII recording is done inside the first refinement level and hence remain accurate in all cases. All coordinates are in meters.



(a) The schematic of full domain which has fixed a spanwise extend and includes 1)square sponge regions (pink stripe), restricted domain where the refinement is at level 4 or finer (green rectangle), and mesh coarsening beyond sound propagation limit (white stripe).



(b) A schematic of the slat-airfoil geometry showing the slat positioning system relative to the main element denoted as the Slat Gap (SGP), Slat Overlap (SOL), and Slat Deflection Angle (SDA). The coordinate axes used for the simulation are also shown with marking of the downstream, cross stream and spanwise directions.

Figure 3.8: Schematic of the domain, boundary conditions, and the slat-airfoil configuration.

Boundary	Absorbing Layer width	Type	Mean values	Relaxation Targets
Inlet	2m	Velocity	50 m/s	Velocity: Fixed Pressure: Dynamic
Outlet	2m	Pressure	101325 Pa	Velocity: Free Pressure: Fixed
Top	2m	Pressure	101325 Pa	Velocity: Free Pressure: Fixed
Bottom	2m	Pressure	101325 Pa	Velocity: Free Pressure: Fixed
Spanwise	0	Periodic	All variables equated	

Table 3.2: Boundary conditions applied for the simulation domain

in the slat cove, by using sufficiently long span length: we choose $L_z = 0.7C$ which is significantly higher than that suggested in the work of Choudhari et al. [20]. A template setup consisting of the boundary conditions and refinement regions was first generated as shown in Fig. 3.8 and the slat-airfoil geometry was defined to allow for parameter variations. Additionally, all flow boundary conditions are coupled with appropriate absorbing boundary conditions with a region of influence of about $7C$ (2 m). The boundaries and applied absorbing layer settings are collected in Table 3.2.

For generating the mesh layout, prudence is given to minimize the number of nodes in order to minimize the cost of simulations. This enables exploring the parameter space extensively. Hence, the meshing is initiated from the domain boundaries with the minimum possible cell size, i.e. same as spanwise domain length of $L_z = 0.2\text{m} = 0.66C$. In previous sections, it was shown that to obtain a lossless propagation of the acoustics generated by the flow, we need to maintain a resolution of 17 points per wavelength and corresponding to the frequencies of interest upto 10 kHz, this corresponds to a cell size of approximately 1.6mm. Hence, a sub-region of the domain, marked as Resolution Level 4 in the Figure 3.8, is maintained at this cell-size to enable propagation of the generated noise. The FWH surface is also placed inside this region to record the perturbations so that the input to the FWH calculation does not involve spurious effects due to propagation on an unresolved grid. The airfoil geometry is then positioned inside the FWH surface.

3.6.3 Coordinate System

The coordinate system of the airfoil for the simulation is chosen such that for variation of the angle of attack of the airfoil, the positioning of the FWH surface and the meshing on the airfoil does not necessarily change. For this we choose to keep the airfoil and FWH in steady position and update region of boundary conditions (together with absorbing regions) to reflect the change in the flow direction. Hence inlet velocity is specified using its vectorial components calculated from the required angle of attack with respect to the main element.

3.6.4 Meshing

The boundary layer resolution required to simulate the flow is determined by the flow Reynolds number. For the case simulated in our work, the chord based Reynolds number is around 10^6 . Based on the slat chord, this corresponds to a Reynolds number of 1.3×10^5 , and hence from the wall y^+ based on friction velocity, to maintain $y^+ < 50$, a cell size of 0.0003m is required. The LES-LBM using *ProLB* utilizes a wall-model based on the logarithmic wall law[122, 123]. When a wall boundary is present with no-slip

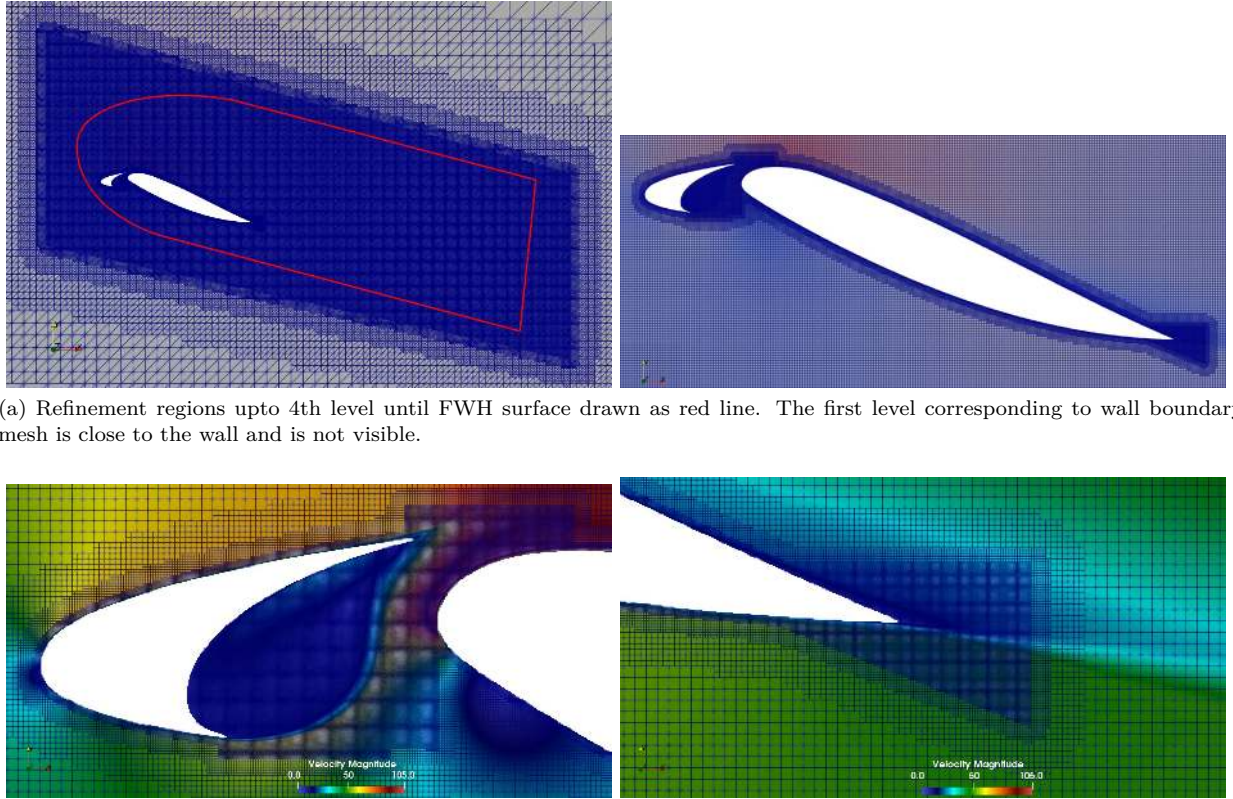


Figure 3.9: LBM mesh sizes in the domain and around the HLD geometry

condition, the boundary nodes are provided with additional fictitious particles such that the momentum of the particles that would otherwise exit the domain is supplied back into the domain. This condition is called the bounce back condition[124]. Although it requires a few additional manipulations, it has shown to be sufficient to recover the Navier-Stokes behavior in the boundary layer. Additionally, with a Cartesian grid, the wall y^+ distribution cannot be definitively controlled in an LBM simulation. Hence a choice for the case is made by keeping the y^+ close to 50, where a boundary layer cell size of 2×10^{-4} m is chosen resulting in an effective y^+ of 35. This is based on the expectation that the boundary layer development happens along the wall within a length of 0.039m, which is the slat chord length.

With the specification of the near-wall cell size, this property is then attributed to the wall geometry. The Cartesian meshing algorithm then maintains this cell size in the region surrounding the wall and does the same until a few layers of the mesh away from the wall. The number of layers for our case is set to 6. This leads to having 6 layers of the cell size attributed to the solid wall around it and then automatic coarsening by factors of two following every 6 layers of the cells. The blocks of meshes with same sizes thus formed are the so called mesh Refinement Levels. Starting with the boundary cell size of 0.0002m as Refinement Level 1, and coarsening by factor of 2, the resolution as required by the acoustic propagation is obtained in Level 4. Hence, within the region of Level 4, as shown in the Figure 3.8, the mesh has 3 sub-levels, the exact shapes of which are primarily dictated by the shape of the wall geometry.

To capture the aeroacoustic phenomena accurately, the slat cove flow has to be well resolved since the spanwise coherence of the vortical structures and their convection by the mean flow needs adequate fidelity as well as the sound back-propagating from the slat trailing edge to its cusp. To aid in accurate visualization of the vortices, and to obtain a smooth averaging of the flow, we choose to keep the boundary layer cell size constant throughout the slat cove. The same is also applied to a region downstream of the

slat trailing edge and also downstream of the main element's trailing edge. The resulting mesh around the airfoil is shown in Figure 3.9a and the mesh in the slat cove is shown in Figure 3.9b. The mesh for the current standard positioning of the slat is obtained with 99 million nodes.

3.6.5 Temporal scales

LBM simulation time steps are primarily determined by the cell sizing. This is due to the fact that a fixed Courant–Friedrichs–Lowy (CFL) number, is maintained in cell calculation. This means that during the timestepping, the time step calculated for each Refinement Levels are different corresponding to its cell size. The smallest time step corresponds to the Level 1 cells whose timestep is calculated as

$$CFL = \frac{\Delta x}{c\Delta t\sqrt{3}} = 1 \implies \Delta t_{L1} = \frac{\Delta x_{L1}}{c\sqrt{3}} = 3.46 \times 10^{-7} \text{ s} \quad (3.37)$$

where c is the sound speed calculated at the reference temperature of 276.48K. For higher Resolution levels whose cells size grows by a factor of 2, the timestep also grows by a factor of 2 and hence the time stepping for n^{th} resolution level is given by $\Delta t|_{Ln} = \Delta t_{L1} \times 2^{n-1}$. The total number of time steps required for the simulation is dictated by the acoustic measurement requirements. For the reference wind tunnel experiment, the spectral resolution obtained is 1Hz. However this resolution is impossible to simulate since the number of time steps are prohibitively high. A good compromise is made when the resolution is decreased to 22Hz. For this resolution, the number of time steps required is given by the discrete Fourier transform theory by

$$N_{FFT} = \frac{f_s}{\Delta f} \quad (3.38)$$

where N_{FFT} is the number of time steps per averaging window of the Welsch method, and f_s is the sampling frequency. The sampling frequency is determined by the Nyquist-Shannon criterion, whereby the sampling rate of the signal must be at least twice the bandwidth of interest for the signal. This means that for slat noise spectra upto 20kHz, the sampling rate must be atleast 40kHz. To avoid the high frequency edge effects close to the edges of the band, it is common practice to maintain at least four times the sampling rate according to the Nyquist-Shannon criterion. In the current case, the FWH propagation region at Refinement Level 4 is maintained at the required resolution of 1.6mm. The corresponding time step is hence $2^{4-1} = 8$ times the simulation timestep and hence the recordings are done with $\Delta t_{FWH} = 2.77 \times 10^{-6}$ s and the corresponding frequency is ≈ 360 kHz. However, to obtain a good trade-off between the length of the signal and the resolution, we choose to sample the FWH surface at half of this frequency, i.e. $f_{s-FWH} \approx 180$ kHz. The number of time steps then follows as $N_{FFT} \approx 8200$ time steps.

This combined with an averaging requirement for the Welsch algorithm of 7 averages leads to a total of $8200 \times 7 = 57400$ timesteps for recording the flow at Refinement Level 4. The number of timesteps at Level 1 then translates to $57400 \times 2^3 = 459200$. An additional transient time is required to remove the initial transients in the simulation due to a non-physical initialization of the near wall flow. The resulting spurious waves need to be allowed to leave the domain to reach a converged flow state. Moreover, the flow characteristics leading to the acoustics are established once the macro-flow converges to steady oscillatory behavior. Hence an initial transient of 290000 iterations, equivalent of a physical time of approximately 0.1s (or more than 16 chord pass times for a stowed chord of 0.3m in a flow at 50m/s) are run before starting the recordings for post processing including FWH. This together with the recording timesteps demands a total of 874200 timesteps at Refinement level 1 for a simulation.

Additionally, to accelerate the convergence, we utilize the two-step initialization feature available with

ProLB. Accordingly, the simulation initiates without fully resolving the mesh but only until Level 2. The simulation is then run until a physical time of 0.2 seconds corresponding to 144324 iterations at the time step of Refinement Level 2. The solver then fully resolves the mesh until Refinement Level 1 and interpolates the solution from Level 2 to Level 1, where necessary, to initialise the actual simulation.

3.7 Simulation with the Wind Tunnel Installations

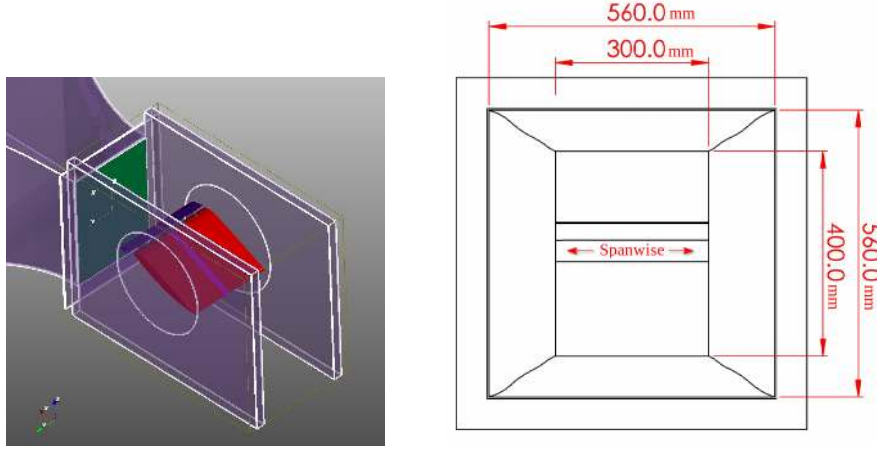


Figure 3.10: Left: The HLD mockup geometry installed on the wind tunnel using lateral sides plates. Right: A drawing of the dimensions of the wind tunnel nozzle exit.

The complete configuration of the wind tunnel setup of the original VALIANT experiment, which includes the converging duct and the lateral support plates, were simulated using the same simulation parameters of the free stream simulation. This simulation was setup by Airbus engineers (Dr. Maxime Itasse and Dr. Florian Guiho) and was reproduced at the ECL facility for the purpose of testing the version of the code for producing reference data. Schematics of the simulation domain and the lateral side plates of the same are given in Fig. 3.11 and 3.10. The total physical time of the simulation in our standard free stream configuration is 0.2s in comparison to 0.078s in the current one and is driven by the necessity of computer resources while including the wind tunnel geometry meshes. With a reduced signal length, the computation leads to spectra with lower resolution also. The FWH surface was placed inside the cavity covered by the shear layer from the nozzle lip, to avoid shear layer vortices crossing the FWH surface. The two main differences between a free-stream simulation and a wind-tunnel case are that while a spanwise periodic condition is used in the free-stream case, a wall boundary is applied in the wind tunnel case mimicking the experimental setup, and that the free-stream case is not in a jet but a uniform flow. Consequently, for spanwise periodic condition, the spanwise acoustic domain is theoretically infinite. However, the periodic condition numerically copies the data between the spanwise boundaries thereby enforcing congruence of the flow variables at both boundaries. Hence, although the domain is infinite for acoustic propagation, it may trigger spurious periodic behaviors in the flow with wavelengths that confer to the domain length, i.e a standing pressure wave based on the spanwise periodicity might arise in the free stream case even if this is not the case in the actual wind-tunnel. Another effect of the spanwise periodic condition is that it tends to exert spanwise homogeneity in the flow if the spanwise domain length is smaller than that which would allow three dimensionality to develop. This has been investigated in previous works for the same geometry as that used in the present simulations[14] and

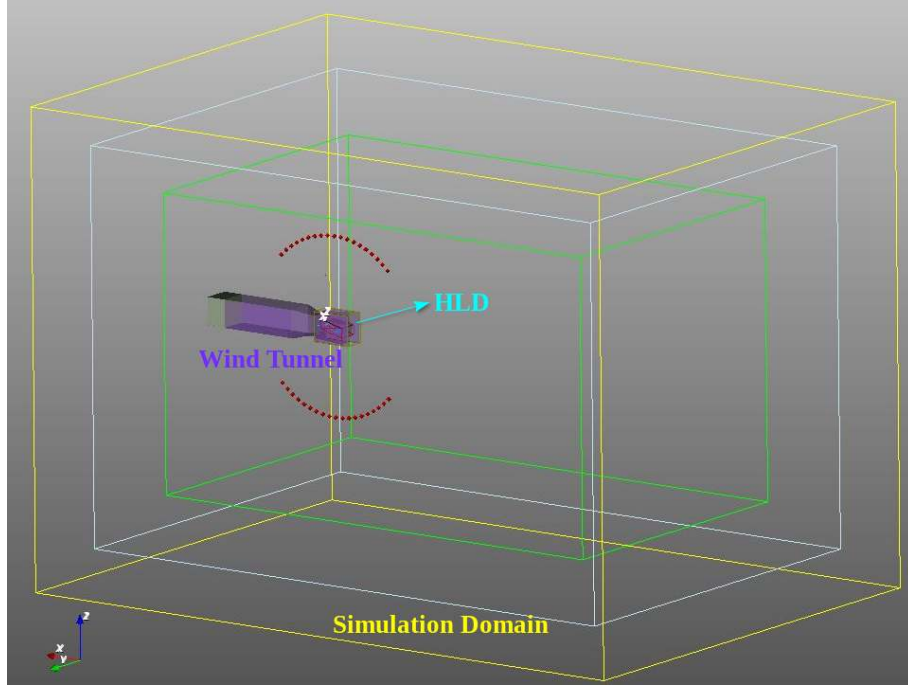


Figure 3.11: The simulation domain of the wind tunnel geometry with the tunnel and HLD installed

also for other HLD configurations[31, 20, 98, 125, 126]. Lockard and Choudhari [19] showed that for the development of three-dimensionality of the coherent structures in the cove region, a spanwise extend of $0.75c_s$, where c_s is the slat chord is necessary. For the current case simulated, this corresponds to a length of 0.0312m while the actual simulated span length is 0.2m corresponding to more than 6 times the suggested value. Hence this factor is not expected to affect the features of the flow simulated in our case and the three dimensionality is expected to develop unhindered.

That being the differences between the two cases, the wind tunnel installation effects are necessary to explain a few of the disparities between our standard free stream simulation and the reference experiment. As will be demonstrated in the following chapter, the simulation tends to obtain a better agreement with the experiment if the installations are included, particularly for the broadband levels and the strength of the first tone.

3.8 Conclusion

This chapter in its early development details the Lattice Boltzmann method and the basis of its suitability for the aeroacoustic simulations. The low dissipation and dispersion characteristics that are implicitly available in the LBM schemes are then put to test in the commercial solver *ProLB* and a quantitative but empirical characterization of the dissipation performance is obtained. Guided by this development, a further reduction of the computation cost for noise calculation is achieved by deploying an in-house Ffowcs Williams-Hawkins module *Turb'AcAn*. The software was then successfully tested for its accuracy on a Gaussian pulse propagation test case. In the later part of the chapter, the simulation setup designed to enable slat noise investigations using the same framework is detailed. The simulation parameters are obtained based on the data available from the test cases mentioned and necessary compromises are made to enable computationally affordable simulations.

Chapter 4

Detailed Study of Nominal Slat Configuration

4.1 Introduction

The 3D Lattice Boltzmann Method can provide a high fidelity description of sound-flow interactions and will therefore be applied to an in-depth analysis of the slat noise mechanisms. The ProLB solver with its advanced functionalities enable the recording of the flow field to sufficient resolution such that the turbulent structures and their dynamics in the cove can be visualized with great detail. Hence this chapter is dedicated to our investigation of the cove flow phenomena using the data collected during our simulation of a well documented experiment carried out in the European project VALIANT. This data is used to optimize the simulation and to validate it. The configuration is that of a 2 element geometry designed by Terracol et al. [14] as detailed in Chapter 1, here with only the standard positioning of the slat with respect to the main element. This configuration has the slat coordinates [Angle of Attack - $AOA = 18.0^\circ$, Slat Deflection Angle - $SDA = 35.2\text{mm}$, Slat Gap - $SGP = 7.94\text{mm}$, Slat Overlap - $SOL = -6.36\text{mm}$] and will be referred to as the reference configuration.

To begin, we first validate the simulation framework for aeroacoustic computations by comparing its accuracy against experimental data using a standard geometry in a free-stream configuration. This serves as the baseline for the validation process. Next, we examine a case that includes the full installation effects and explain the differences observed in the results. Additionally, we present further simulation results based on variations of the same geometry, including one where the inlet velocity is reduced and another where the spanwise length of the simulation domain is shortened.

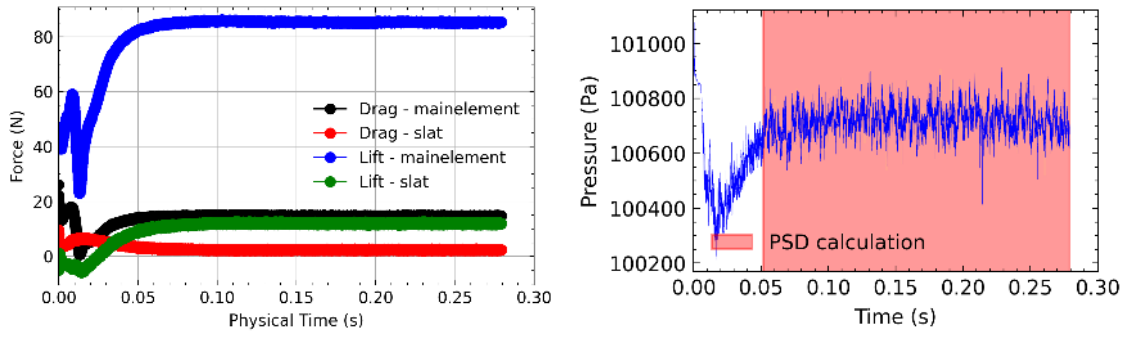
4.2 Validation of standard case simulation

The results from validation case study detailed in the previous chapter based on the free stream conditions are detailed in this section. The convergence of the unsteady dynamics and mean wall pressure distributions are canonical measures of fidelity for the simulation and are discussed first. Subsequently, the probe data recordings are analyzed and finally the FWH computations are discussed to validate the aeroacoustic capabilities of the solver.

4.2.1 Convergence

In LBM simulations the convergence is checked primarily by using the unsteady data recorded using numerical probes in the simulation. This is due to the fact that unlike conventional solvers, the LBM approach calculates a simulation time step without iterative procedures[111]. Hence a useful monitor for the stationarity of the simulated aerodynamics is the unsteady forces on the solid geometries. ProLB enable users to integrate the surface forces over the solid wall geometries using native functions and is deployed to extract the results. The force components which are in the direction of the X coordinate axis are taken to be the drag force and the one in Y direction is taken to be the lift force. This directionality are not exactly accurate since the angle of attack of the main element is not aligned with the coordinate axes. Nevertheless, for convergence monitoring the directionality is not relevant. The recordings obtained are shown in Fig.4.1a. The unsteady loading show satisfactory convergence after a total physical time of 0.05s and the mean values are steady after 0.075s.

A second monitor is the unsteady data from critical locations of the flow. Here the slat cove dynamics can be monitored using the wall pressure sensor data. Raw data from a sensor placed inside the slat cove is shown in Fig.4.1b. The same also shows good agreement with the unsteady loading and the flow dynamics show stationarity after 0.05s of physical time.



(a) Surface integrated forces of drag and lift on the geometry walls.

(b) Raw wall pressure probe data inside the cove from the free-stream simulation for Probe 6 (See Fig.4.3a). Timesteps used for calculation of the PSD is highlighted.

Figure 4.1: Unsteady data monitored to check convergence of dynamics in the LBM simulation

4.2.2 Mean wall pressure distributions

The mean wall pressure data from the simulation is compared against the experimental values in Fig.4.2. As can be noted, there is a general agreement of the $-C_p$ distribution. However, the suction pressure on the slat is slightly higher in the simulation whereas it is lower for the main element as compared to experiment. This difference owes to the fact that in the experiment the wind-tunnel installation has additional features including the finite width jet. The static pressure over the airfoil also causes a potential effect which interferes with the wind tunnel jet exit to modify the exit pressure distribution.

The difference of angle of attack for the experiment and the simulation is also a factor affecting the pressure distribution. For the experiment, the airfoil is kept at 25° to the jet exit direction and for the corresponding simulation in free stream condition, the angle of attack is reduced to 18° . This is a method to correct the change in effective deflection. The equivalent angle of attack between the free stream case and the wind tunnel case was obtained empirically by matching the shape of C_p distributions from the free stream RANS simulations and actual experimental values, done by Terracol et al. [14]. The VALIANT

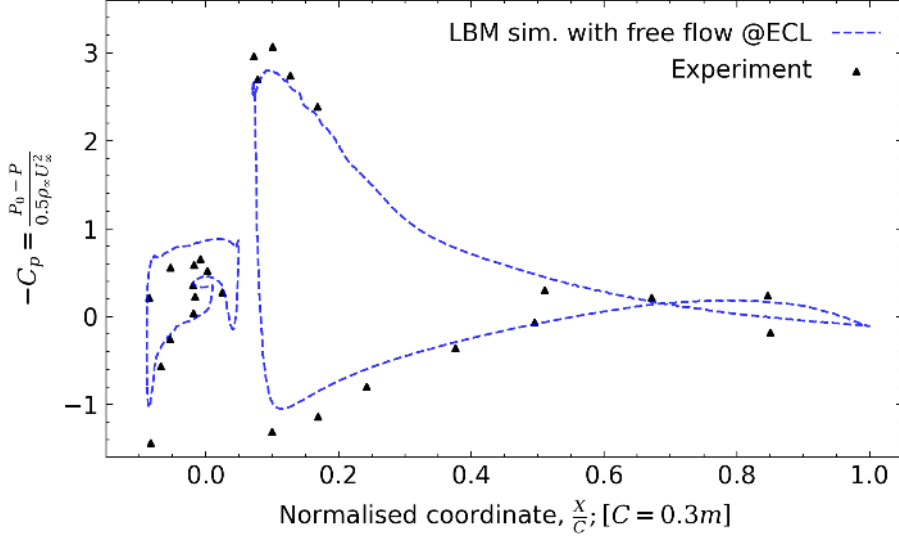


Figure 4.2: Pressure Coefficient $-C_p$ over the surface of HLD obtained using the LBM simulation is compared against the experimental data

HLD geometry was also obtained by replacing the flap of the base three-element configuration with a sharp trailing edge by keeping this equivalence of the shape of C_p distribution. Hence the same angle of attack of 18° with the free stream is maintained for our comparison with the experiment as well.

The discrepancies related to difference of configurations are alleviated to a good extend if the simulation setup includes the full wind tunnel installation geometries. Such a simulation, together with a few additional cases varying the angle of attacks for free stream simulation, are detailed in the Appendix A Section A.3.

The pressure on the main-element also shows a spatially local sharp peak which owes to the acceleration of the flow in the nozzle like shape of the slat gap. This feature is more prominent in the simulation since continuous data over the airfoil wall is available. This acceleration is responsible for the high velocity ejection of the slat turbulence from the slat trailing edge and hence is likely to drive both the characteristic low frequency broadband noise and the high frequency noise.

4.2.3 Unsteady Wall pressure data

The wall pressure data inside the cove represents the dynamics of pressure field inside the cove. This includes both the hydrodynamic and the acoustic perturbations, where the hydrodynamic fluctuations usually dominate. Hence it captures both large scale fluctuations due to the vortex behaviors and the acoustics including resonances. The PSD is calculated over a total time of 0.23s with a sampling frequency of 180405Hz. The total number of time steps allow a Welsh averaging window of 8200 time steps and 5 averaging windows with 50% overlap resulting in a spectral resolution of 22Hz. The PSD is calculated using the routines provided by Python package “matplotlib.mlab” and a detrending using a linear fit for the mean value is also used for each window together with smoothing of the window edges using Hann window. For the free-stream simulation, the data is collected over the full length of the simulation to monitor the convergence and is shown in Fig.4.1b. The comparison of the wall pressure spectra obtained in the free-stream and wind tunnel simulation are shown in Fig.4.3. (Details of the latter are provided in Appendix A).

It can be noted that both cases show a reasonable agreement with the experiment regarding the tonal frequencies. For the SPL, the first tone at 1771Hz tends to be better captured by the wind tunnel

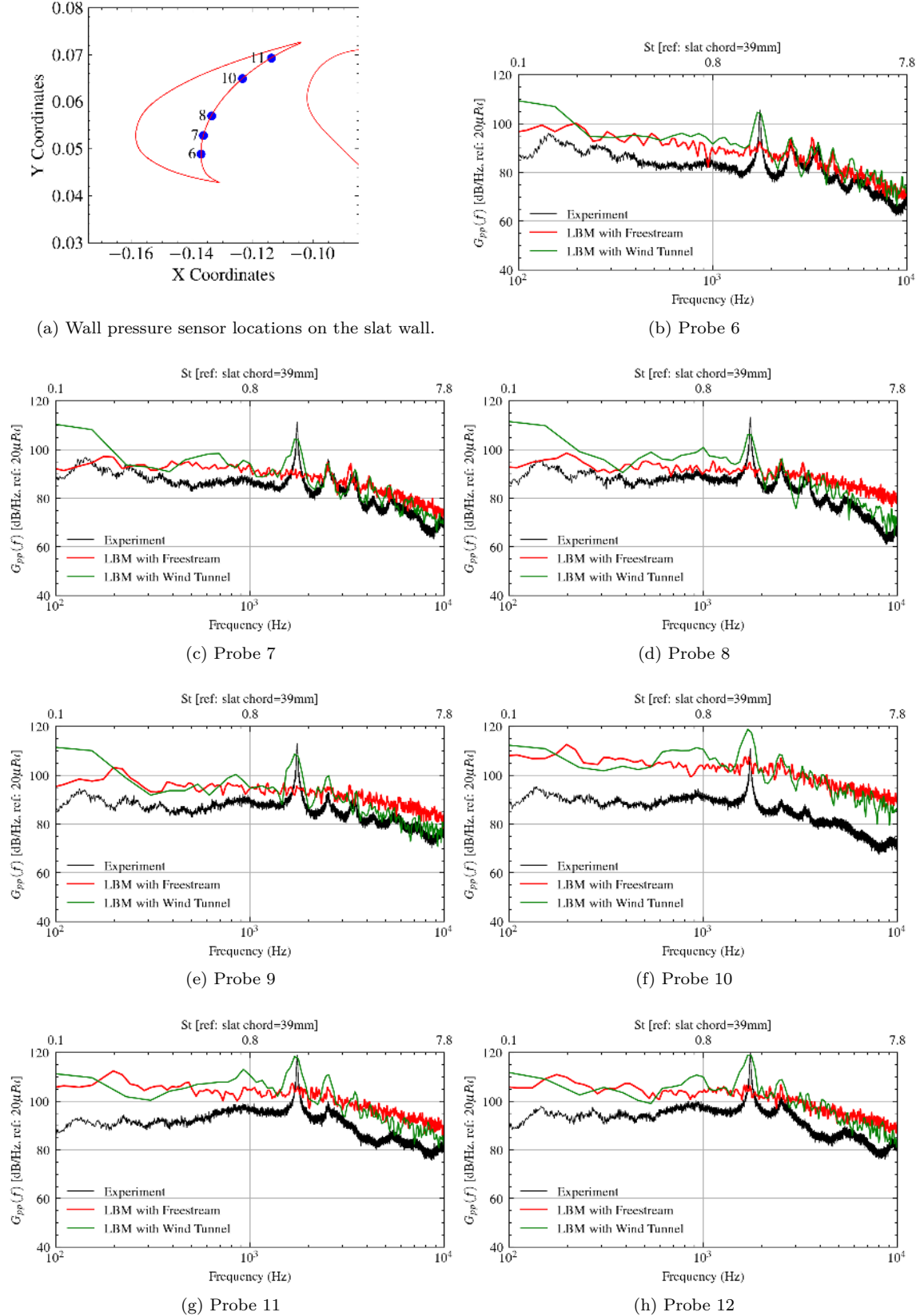


Figure 4.3: Wallpressure PSD inside the slat cove compared between the simulation in free stream, simulation with wind tunnel, and the experimental data

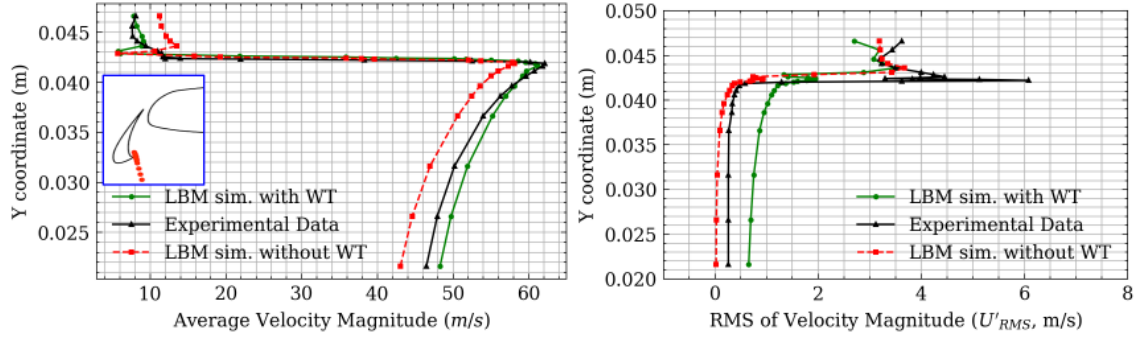


Figure 4.4: Velocity magnitude data compared between the simulation with and without the wind tunnel geometry included in the LBM setup, against the VALIANT experimental data for probe file SL placed across the initial shear layer near the slat cusp

simulation whereas it is almost vanishing in most free stream curves. A good agreement can be seen in general for all higher frequency tones (not all harmonics) along with consistently higher broadband SPL in simulations. A higher SPL suggests that the pressure fluctuations in the cove are more energetic in the simulations than the experiment.

4.2.4 Hot-wire probes

The hot-wire probe provides velocity data in flow-critical locations allowing comparison of the fidelity of the simulation. A plot comparing the velocity magnitude across the nascent shear layer is shown in Fig.4.4. The experiment and simulation which includes the wind tunnel installation geometries tend to have a better agreement of the average velocity data. In both cases, the velocity recovers the free stream velocity of 50 m/s and shows a mean recirculation velocity of 8 m/s on the cove side. In comparison, the flow in free stream simulation tends to develop a slightly weaker shear layer, with the free stream velocity recovering to 43 m/s and the inner cove recirculation to 12 m/s. The velocity ratio between the inner and outer flows, $\frac{U_i}{U_o}$, is thus 0.16 and 0.27 for wind-tunnel and free stream simulation respectively. This suggests that a perfect capturing of the shear layer thickness and strength requires the presence of the full installation.

A few factors can explain this disparity. In the free stream simulation, the incoming flow is homogeneous and laminar. Hence the boundary layer and the turbulence therein are developed locally and spontaneous. On the contrary, the incoming flow in the experimental setup and its simulation has multiple sources of turbulence upstream of the HLD, i.e. the shear layer of the nozzle generates a shedding of vorticity and spanwise plates that support the HLD develops a fully turbulent boundary layer upstream of the HLD.

The velocity ratio across the shear layer has an important role in determining the dynamics of the flow especially the acoustics. Among many, the primary effect is that it determines the strength of the Rossiter mechanism. The shed vorticity from the cusp leads to the generation of the spanwise coherent eddies which excite the resonance and hence a reduction of the shear strength will weaken the generated vorticity, eventually weakening the resonance. As will be shown next, this can be one influential factor leading to the diminished strength of the first tone in the free stream simulation as compared to the experiment.

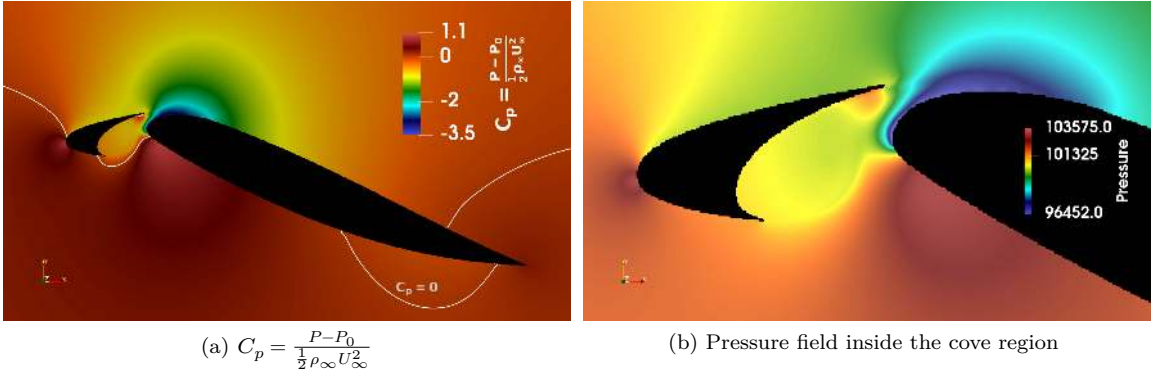


Figure 4.5: a) Pressure Coefficient, $C_p = \frac{P - P_0}{\frac{1}{2} \rho_\infty U_\infty^2}$, where $P_0 = 101325 \text{ Pa}$, is the ambient pressure, $U_\infty = 50 \text{ m/s}$, and $\rho_\infty = 1.225 \text{ kg.m}^{-3}$, are the free stream density and velocity respectively. White line indicates the contour $C_p = 0$. b) Time-averaged pressure field in the slat cove. Both averaging is done for 5 chord pass times ($C = 0.3 \text{ m}$ and $U_\infty = 50 \text{ m/s}$) corresponding to a physical time of 0.03 s.

4.3 Mean flow fields

Given that the unsteady dynamics has many features worthy of further exploration, it is important to understand the time-averaged fields in tandem. The mean flow field convects the fluid and its vortices to establish the macro-flow features like the accelerated flow through the slat gap and the recirculation region. Within this configuration, the unsteadiness can be thought to be introduced by the generation of vorticity due to the presence of slat cusp or the shear layer. These vortices then develop unsteady dynamics which leads to the aeroacoustics. Hence the vortex dynamics itself is intrinsically first determined by the established mean flow.

The mean pressure field around the HLD is shown in the Fig.4.5a in terms of the Pressure Coefficient, C_p . The mean pressure, as can be noted, drops significantly near and downstream of the slat gap leading to a negative spike. This suction peak enhances the lift performance of the wing. Looking more closely on to the slat cove, the visualization is made in terms of the primitive variables with a tailored color map in Fig.4.5b. The region of impingement is distinctly identifiable as a region of high pressure due to the partial stagnation of the flow and hence the reduction in the flow area through the slat gap. It is also evident that the low pressure core of the cove due to recirculation is not exactly at the center of recirculation itself but shifted nearer to the shear layer. See Fig. 4.6.

The mean velocity fields also largely agree with the understanding of the cove flow as inspected in the mid-span plane, as shown in Fig.4.6. The mean center of the recirculation can be identified in Fig.4.6a and the fact that the peak mean velocity magnitude occurs on the suction side of the main element which is also the region of reattachment of the flow from the slat TE with the main element. The peak locations of U_X and U_Y also agree with the geometrical redirection of the flow towards the slat gap. However, the spanwise mean velocity in Fig.4.6d using the same colormap leads to the erroneous inference of its insignificance due to the comparatively lower magnitudes. An alternative colormap restricted to $U_Z \in [-5, 5] \text{ m/s}$ as shown in Fig.4.7 reveals the formation of cells of spanwise velocity inside the cove region. The recirculation tends to have alternating signs for the spanwise velocity component in the upper and lower regions of the cove. The contour of velocity ratio $R_{U_Z} = \frac{U_Z}{\sqrt{U_X^2 + U_Y^2}}$ in Fig.4.7a, as well as the raw U_z for the mean field, shows lower magnitudes than themselves obtained while using the unsteady fields as shown in Fig.4.23a and Fig.4.23d. This suggests that the cell formation or the spanwise dynamics may possibly be a periodic phenomena which are being numerically averaged out in time but with a lower frequency than one which

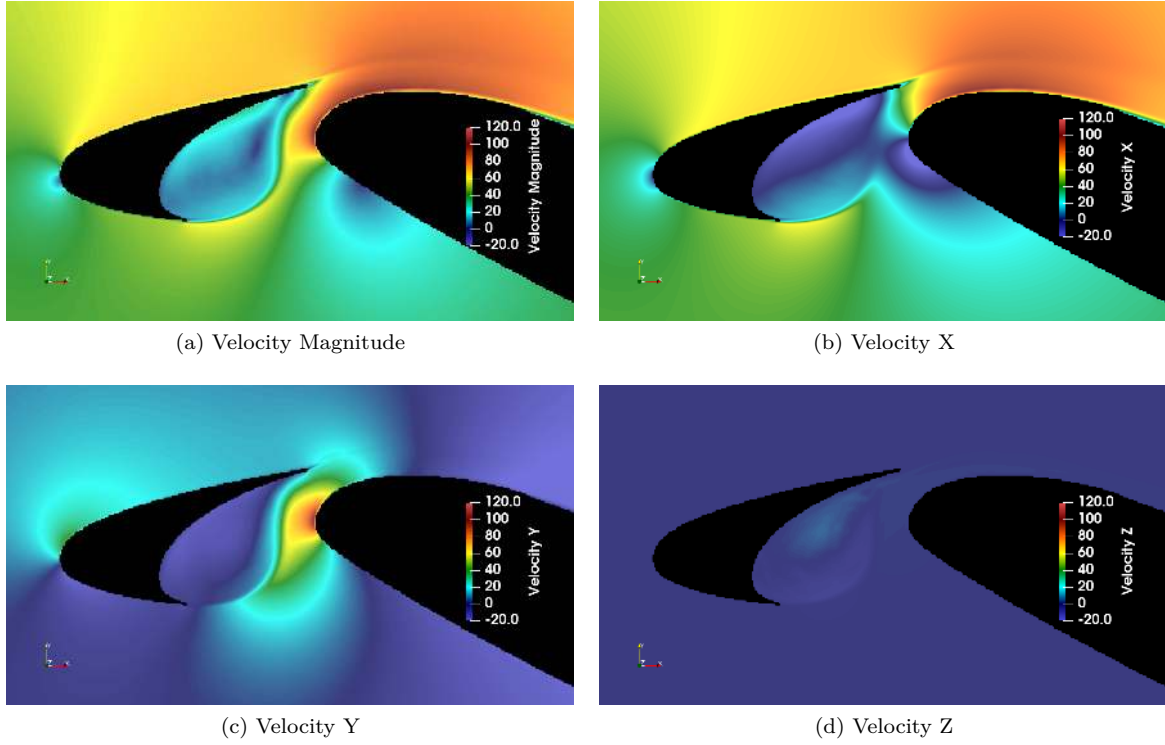


Figure 4.6: The time-averaged velocity field in the slat cove identifying the shear layer shape and regions of peak velocity components.

cannot be sufficiently averaged out within 5 chord pass times.

To generate the spanwise planes, a slice is made parallel to the spanwise axis as shown in Fig.4.8. The spanwise velocity is then visualized on this plane with suitable color map to identify the local sign of spanwise velocity. As can be observed, the ‘spanwise cells’, as we like to refer to the region of same velocity direction, appear to be stacked periodically with alternating signs. The magnitude of mean spanwise velocity is close to 5m/s, which is upto 10 times smaller than of the free stream velocity, $U = 50\text{ m/s}$. These cells are also of length scales of the same order of the spanwise domain length, which for the current case of standard slat positioning generate a total of 6 cells, or 3 pairs of alternating signs. Their average spanwise wavelength is hence $\lambda_z = L_{span}/3 = 0.2/3 = 0.066\text{ m}$. An exact measurement of the length of center cells are shown in Fig.4.9 and is approximately 0.0696 m thereby giving a slat chord

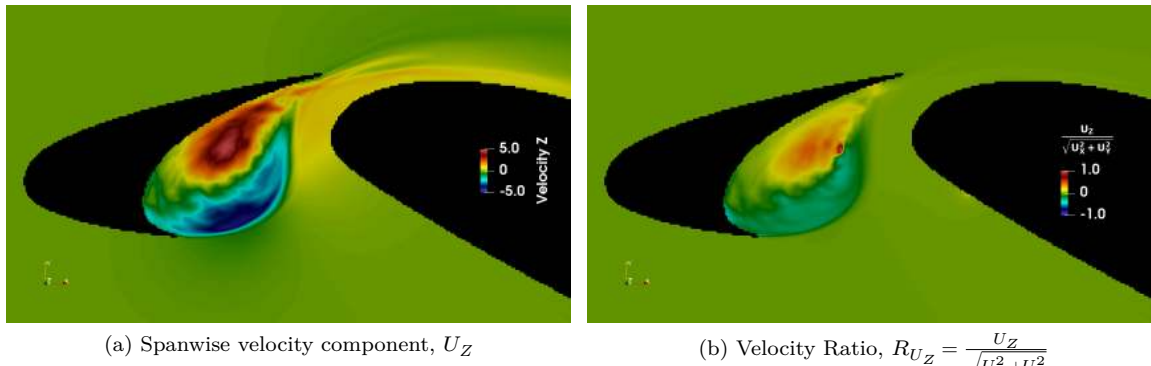


Figure 4.7: Time-averaged spanwise velocity field in the slat cove

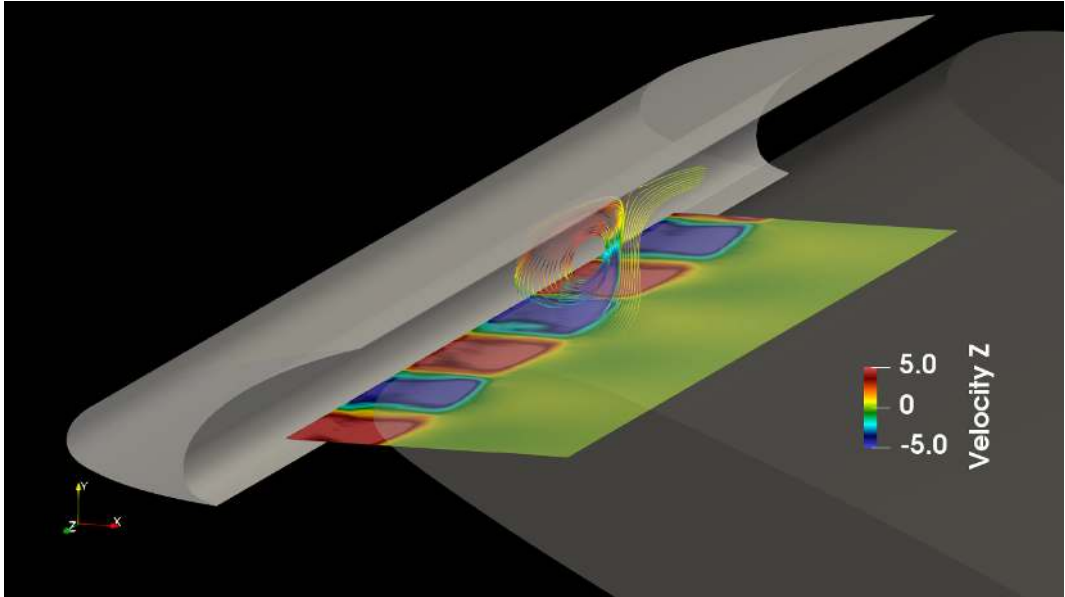


Figure 4.8: Spanwise velocity, U_Z , visualized on a cutplane parallel to the spanwise Z axis inside the cove region. The stream tracers are used in the mid-span plane to show the recirculation path in the mid-plane

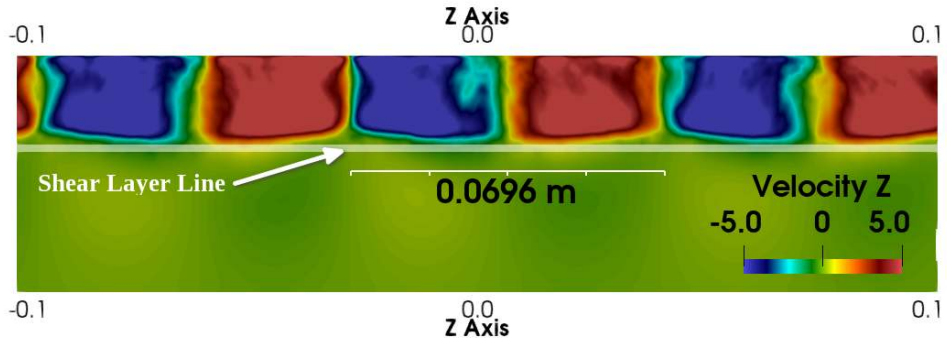


Figure 4.9: Contours of spanwise velocity, U_Z , showing the cell formation inside the cove region. The cut line denoted the approximate position of the shear layer passing through the visualization plane

based non-dimensional wavelength as $\Lambda_z = \lambda_z/C_s = 1.785$, where $C_s = 0.039\text{ m}$.

The cell formations tend to maintain approximately the same cells size along the spanwise direction. However, the cells are not only modulated in the spanwise direction but are arranged into two layers along the length of the shear layer path. The spanwise plane visualizations, on multiple spanwise planes marked PL1, PL2, and PL3, at varying Y coordinates as shown in Fig.4.10, suggest that the stacking of cells again also form an alternating arrangement for the sign of the spanwise velocity, i.e. along the shear layer length, the arrangement of the cells are such that they oppose in signs between the cells attached to early shear layer and later shear layer. Visualizing on a fourth plane which lies between PL1 and PL2 as shown in Fig.4.11 also show this arrangement as they transition from the early shear layer to the later stage.

The spanwise modulations and their obscurity in slat noise literature lead us to many interesting thoughts of which the following three are worthy of mention:

1. First is that the alternating time-averaged spanwise velocity cells means that there exist static nodal planes towards which the flow can converge and diverge from. Those planes whose both sides have

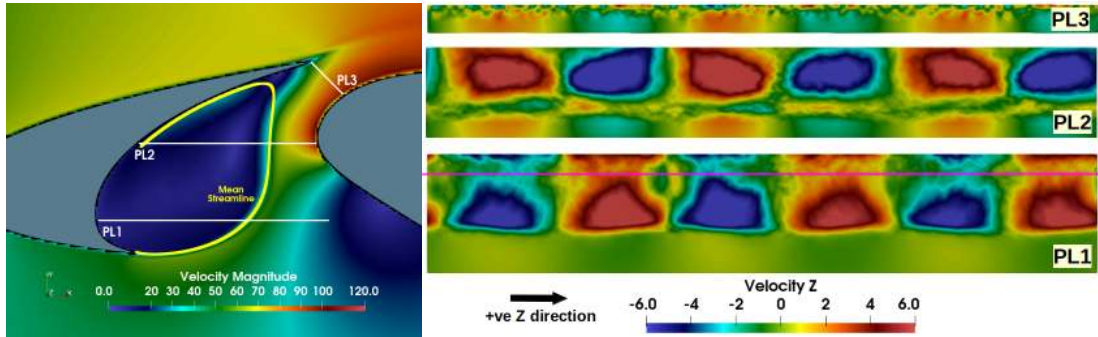


Figure 4.10: Spanwise cell formations: Different positions along the mean shear layer (left) is used to place visualizations planes PL1, PL2, and PL3, and are used to show the spatial modulations of the time averaged spanwise velocity component (right) along the spanwise direction inside the slat cove.

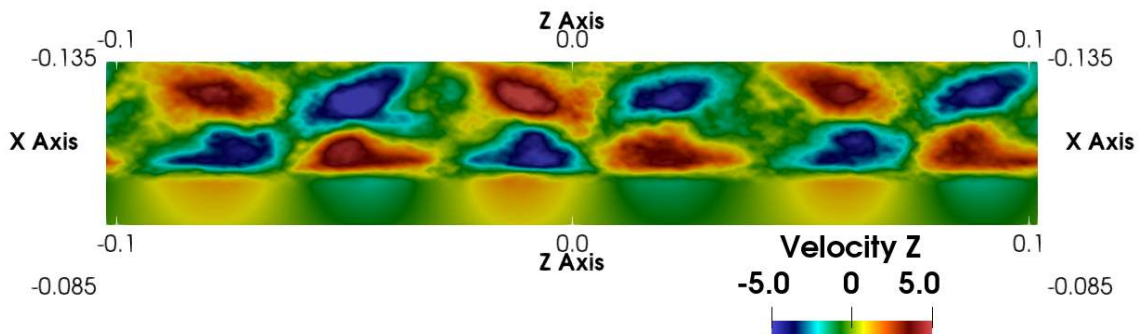


Figure 4.11: Spanwise modulations of the time averaged spanwise velocity on a visualization plane in between PL1 and PL2

spanwise velocity such that it decreases from positive to negative along the spanwise direction and hence have the flow directed towards the plane will be referred to as the ‘converging plane’. The other type of planes where the spanwise velocity increases from negative to positive necessitating the flow to diverge from the plane are the ‘diverging planes’. Since these planes act as sources and sinks for the spanwise dynamics, they must facilitate the interaction of the spanwise dynamics with the 2-dimensional dynamics in the streamwise direction.

2. Second is that if such nodal planes exist, it is necessary that there must exist a mechanism to redistribute the fluid from the converging planes and to replenish the diverging planes continuously to establish a steady dynamics. Here, we have already seen that the recirculating small scale streamwise vortices are absorbed into the shear layer in regions near the mid trajectory. This suggests that for a converging plane, the mechanism to redistribute the fluid is by entrainment of the flow along with the streamwise structures into the shear layer, which must also lead to higher concentration (spanwise) of streamwise structures at the locations of the converging planes. There must also be a lower concentration of the streamwise structures in the diverging planes. Nevertheless, this may not be a phenomena easily observed in a largely turbulent state at $Re = 10^6$ with constant generation, distortion, and redistribution of vorticity, as in the slat cove.
3. The driving factor for the spanwise modulations should be the result of a dynamic instability either due to the shear layer geometry or due to the recirculating flow. Similar spanwise modulations are documented for flow over a backward facing step by Barkley et al. [2]. An image from their original work is displayed in Fig.4.12. Their work demonstrated the existence of large scale spanwise modulations in the shear layer due to the presence of a backward facing step, and argues that the

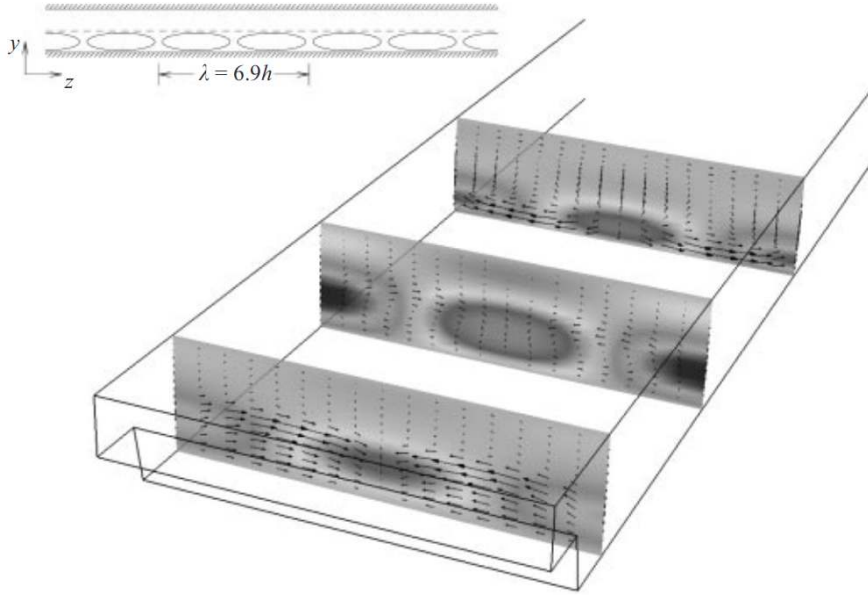


Figure 4.12: Image of the eigen mode demonstrating the spanwise instability mode for flow over a backward facing step from the work of Barkley et al. [2]. The original caption read: “Three-dimensional flow structure of the critical eigenmode at $Re = 750$ and $\beta = 0.9$. Contours indicate the strength of the streamwise velocity component and vectors show the (v, w) flow pattern in each cross-sectional plane: $x = 1.2, 6.2$ and 12.2 .”

spanwise modulations are the result of an absolute convective instability owing to the closed loop streamline in the recirculation bubble leading to generation of steady spanwise modes. The eigen functions identified in their work using the linear stability analysis of a simplified flow configuration predicts the spanwise wavelength with same order as that of the cavity depth. This is consistent with the observation that the spanwise cells in the slat cove have a wavelength with same order as the slat chord. On comparing the rectangular flow cavity with the slat cove, the cavity depth is analogous to the diameter of the recirculating cove flow, and this diameter is approximately the slat chord. Their study also suggest a critical Reynolds number, although at a low range of $Re_c = 748$, from which the spanwise modulations are dominant and this critical Reynolds number is also argued to be decreased when a lateral side wall is present. In the case of simulations with spanwise periodic conditions mimicking an infinite spanwise domain, the critical Reynolds number is also increased. The case of slat cove dynamics is at a Reynolds number of 10^6 based on the mean flow and if considering the flow inside the cove region, taking the mean velocity to be 20 m/s, and the characteristic length scale to be the slat chord, $C_s = 0.039$ m, corresponding Reynolds number is at 54000. This regime is still two orders of magnitude higher than that required to trigger the convective instability[2]. The presence of spanwise walls are also of much importance for the slat cove flow as well, since, in our simulations we employ periodic conditions, and in experimental studies the lateral side walls are necessary to support the HLD mockup in the wind tunnel. Hence, drawing parallels between the fact that the flow over a backward facing step is much similar to the cove flow, particularly due to the fact that both cases have one side bounded by a shear layer and both have a recirculation bubble in which the spanwise modes tend to dominate, we suspect the same mechanism is also in action in the slat cove dynamics.

4. Similarly, Neary and Stephanoff [127] studied open rectangular cavity flows and the same was studied more analytically using Linear Stability arguments by Brès and Colonius [3]. For the work

of Neary and Stephanoff [127], three regimes of flow for an open rectangular cavity based on the Reynold's number was identified. In the first, there is a strong interaction of the shear layer with the recirculating vortex inside the cavity. In a second regime of higher Reynolds number, the interaction leads to intermittent behavior leading to a bursting phenomena where the recirculating vortex tends to oscillate in size leading to it bursting through the shear layer to release vorticity. While doing so, the flow is said to be strongly turbulent. In the third regime typically at $Re = 33500$, (for our low speed cove recirculation, $Re = 54000$), the bursting oscillations and associated pressure oscillations become more frequent but irregular.

5. In the later work of Brès and Colonius [3], the rectangular cavities were further analyzed using three-dimensional global instability analysis to show that the spanwise instability wavelength scales are proportional to the cavity depth. An image of the spanwise modulated velocity fields from their original work are shown in Fig.4.13. The resulting spanwise modulated flow also develop oscillations that can induce a low frequency pulsation of the recirculating vortex. This frequency was deduced to have one order of magnitude lower than the Rossiter oscillations. The dependence of the growth rate of the spanwise modes with Reynolds number was also identified along with a critical value that would trigger the formation of the spanwise modes. However, the most interesting argument made by Brès and Colonius [3] was that the spanwise instability was a result of the curvature of the flow, i.e. the curved streamline of the recirculating vortices in the cavity would lead to a centrifugal instability that is different from the Rossiter oscillations and the Görtler type instability that occurs on curved boundary walls. This argument finds its strength from the fact that the location of the strongest spanwise modulation is in the region of strong curvature of the recirculation bubble on the downstream corner of the cavity. The spanwise modulated recirculation vortex would develop also a low frequency oscillation, and this additional oscillations can interfere with the Rossiter modes to modulate both its frequency and peak amplitudes.
1. That being noted on the spanwise mode formations, the same argument, along with the fact that for both the shear layer on a backward facing step and the recirculation streamline in open cavity flows have, in common, a curved streamline with one side bounded by a shear layer, we choose to investigate the case of slat cove dynamics in terms of its peculiarities arising from curved streamline path of its shear layer. In line with this hypothesis, the behavior of a curved shear layer was also studied by Liou [128]. His work studied the linear inviscid hydrodynamic stability of a slightly curved free shear layer. The study compared the cases of a stably curved and unstably curved shear layer identifying sensitivity of the flow to the addition of curvature to an already present shear layer. The formation of Görtler vortices was identified as a possible reason for the generation of streamwise oriented counter rotating vortex pairs while the unstably curved regime is present. The work also provides a non-dimensional parameter, the curvature Richardson number, to quantify the effect of an accelerated generation of streamwise vortices and will be used for comparison in our study as well.

From the above-mentioned array of ideas, we tend to theorize that the slat cove dynamics at the current Reynolds number has the following features and explanations:

The slat shear layer formed due to the difference of velocity between the free-stream and the recirculation vortex leads to the canonical Kelvin-Helmholtz (K-H) instability as well identified in the literature[14, 28]. The saturation of K-H instability leads to the generation of 2-dimensional spanwise coherent structures being shed periodically from the cusp. If these vortices were to be convected in a straight line path, their behavior would only have the peculiarities of a vortex convected through an accelerated flow.

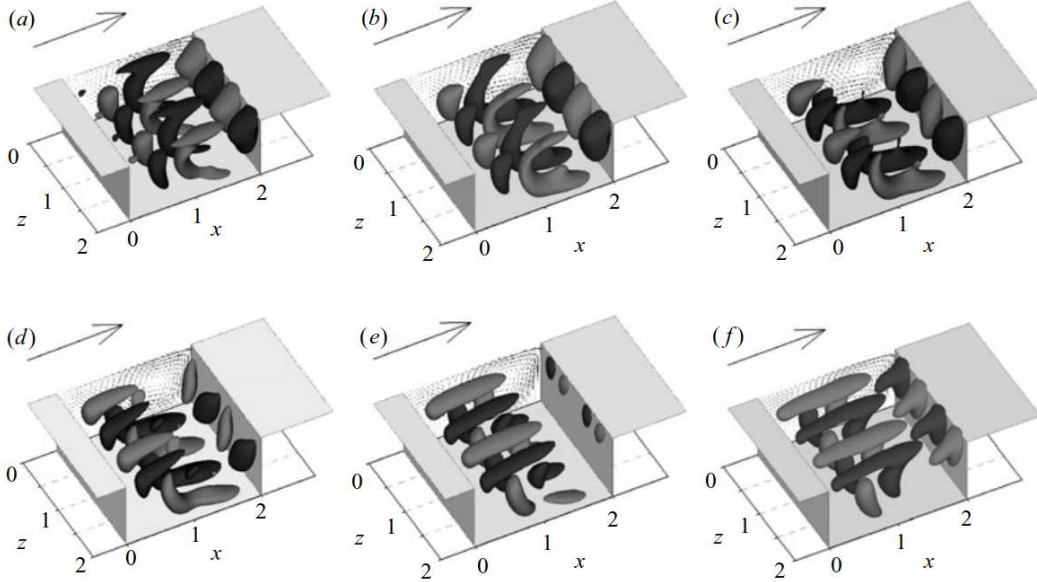


Figure 4.13: The spanwise modes in a rectangular cavity with periodic spanwise conditions from the work of Brès and Colonius [3]. The original caption read: “Visualization of the three-dimensional flow for run 2M0325-3D at six different times (a–f) corresponding to approximately one-sixth phase intervals of a half-period of the three-dimensional instability. The iso-surfaces represent the spanwise velocity levels $w/U = -0.01$ and $w/U = 0.01$. The whole spanwise extent of the cavity is shown and the wavelength $\lambda/D = 1$ of the instability can clearly be observed. The velocity vectors in the streamwise cross-section at $z = 0$ are shown inside the cavity and once in the free-stream for comparison.”

However, since the established mean flow is such that the streamlines are curved along with the shear layer to facilitate flow through the slat gap, the vortices also follow a curved trajectory. This curvature of the streamline necessarily have a mean diameter of curvature similar in magnitude to the slat chord length. The spanwise coherent vortices which undergo such strong curvature experience an additional centrifugal force. Here, the pressure distribution inside the slat cove is lower than the pressure outside the cove region due to the fact that the region outside the slat cove is at the pressure side of the main element and is affected by presence of stagnation point on the main-element. Hence, the normal pressure gradient along the shear layer is positive along a radius of curvature of the shear layer with center of rotation inside the cove. This radial pressure gradient opposes the centrifugal force thereby requiring a balancing of these forces to enable a stable flow. This is the classical requirement for a dynamic instability to occur where two opposing forces which are supposed to be balanced are, in reality, not exactly and dynamically balanced, thereby leading to large growth rate for certain class of perturbations. The curved shear layer is hence susceptible to the curvature instability leading to the typical steady spanwise modes primarily attached to the shear layer as described by Barkley et al. [2].

Considering the mean velocity distribution as shown in Fig.4.6a, it can be noticed that for the early part of the shear layer, the lower velocity flow is on the concave side of the shear layer curvature. This is a stable curvature since according to Rayleigh criteria the equilibrium is stable against curvature instability if the angular momentum decreases radially outward[129]. In early shear layer, the streamline velocity is increasing radially outward from the cove center and hence the curvature instability is stabilized. Furthermore, as inferred by Liou [128], the initial K-H instability may also be stabilized partially leading to a reduced growth rate of the streamwise perturbations suggesting a delayed spanwise vortex generation due to the effect of curvature. Hence, in this regime, the major noticeable dynamics are a delayed generation of K-H vortices as suggested by Liou [128] together with the large spanwise modulations

arising from the convective instability of the recirculation from the suggestion of Barkley et al. [2].

As the flow progresses downstream, the shear layer weakens due to its spreading and growth of spanwise vortices. Simultaneously, the radius of curvature also decreases to eventually reverse its sign. Once the sign of curvature reverses and re-strengthen near the vicinity of the slat trailing edge region, i.e., the streamlines curve such that the low pressure area of the suction peak on the main element is again on the concave side of the streamlines near the slat gap, and the high pressure region generated due to the impingement of the shear layer on the slat trailing edge is on its convex side. This reversed configuration of pressure gradient is again opposing the centrifugal acceleration facilitating curvature instability again. However, unlike the early shear layer, the velocity field can be noticed to have the high velocity stream on the concave side of the curvature. This according to Liou [128] is the unstably curved configuration and satisfy the Rayleigh criterion to have a radially decreasing angular momentum. Hence the shear layer now develops a strong centrifugal instability leading to the generation of streamwise oriented counter rotating vortex pairs. This generation of small scale structures are strongly accelerated by the presence of the ingested vortices from the recirculation region. It must be clearly noted that the regime of flow near the slat trailing edge is the asymptotic case for the linear stability analyzed by Liou [128] whose conclusions are only directly valid for a curved free shear layer with small curvatures. The effective range of curvature Richardson numbers for their analysis is of the order of 10^{-3} where for the slat shear layer, these are on average two orders of magnitude higher as we will show in the upcoming session. Hence, for the later part of the shear layer near the impingement location and flow through the slat gap, the major phenomena is the curvature instability driven by a considerably lower radius of curvature with a mean velocity distribution enabling a fully unstable configuration. The only noticeable effect is hence the generation of streamwise oriented counter rotating vortex pairs which assimilate into larger streamwise vortices on the slat trailing edge and are elongated and ejected through the slat gap. The terminology used in the recent literature[130, 131] that these are ‘Görtler like’ transition is hence logically valid, although there is no curved boundary layer as in the case of the canonical Görtler transition that leads to small scale streamwise oriented structures. Note that since this is a purely centrifugal instability, meaning that this generation of streamwise structures would happen even if there was no supply of spanwise coherent vortices in the impinging shear layer, as reported by Wang and Wang [131]. Their work demonstrates that at low enough Reynolds numbers, the periodic vortex shedding from the slat cusp is suppressed, possibly due to the combined effect of the stabilization of K-H instability due to curvature and the low Reynolds number, and the only noticeable turbulence generation is that of the streamwise vortices near the trailing edge.

Finally, inside the recirculation, the flow developing spanwise modulation was previously unidentified in the literature although it was noticed early that the vorticity ejected from the slat gap had spanwise modulations. The flow in the cove region was largely analyzed under the assumption that it is spanwise homogeneous, and at this point of understanding the cove dynamics, it is striking why the prediction of cove flow and related acoustics remained elusive from a perfectly predictive modelling [42]. This we suggest is due to the fact that the three dimensionality of the flow due to the spanwise modulation would induce additional oscillations, suggestively with frequency one order of magnitude lower than the first Rossiter tone, which can modulate the tonal frequencies and the amplitude of the peaks as suggested by Brès and Colonius [3]. This tone, or more precisely a broadband hump in the low frequency was clearly identified in the work of Jawahar et al. [4], who characterized the same as having a different source mechanism compared to other tones. The broadening of a purely tonal wave while propagating though a strongly turbulent region like that of the slat cove and flow around the airfoil [132], together with the fact that the intermittent bursting phenomena associated with oscillation of the recirculation vortex can both significantly broaden the frequency bandwidth of fluctuations effected by this mechanism on a

far-field microphone. This broadband hump is also in the low frequency range which is dominated by the measurement noise from the experimental setup and noise from the shear layer of the open jet wind tunnel adding to their elusiveness. Thus when tonal character of slat noise was rightly identified as those related to the Rossiter mechanism by Terracol et al. [14], their modulation mechanism was overlooked due to the assumption of the spanwise homogeneity and thereby wrongly advising the choice of methodology for both experimentation and numerical studies so far.

Before a further analysis of this newly observed spanwise feature, let us complete the validation of the simulations using the predicted and experimental noise signatures.

4.4 Ffowcs Williams-Hawkins Computation

The placement of FWH surfaces requires careful consideration for reasons detailed in the previous chapter. The primary challenge is the positioning the surface to allow vortical structures to exit the computational region without crossing it. However, utilizing an open surface inherently reduces predicted pressure levels, as acoustic wave fronts from internal sources interact with the entire surface area, albeit with varying timing and amplitudes. This challenge is mitigated by spherical spreading, where wave amplitudes decay with increasing distance from the source. Consequently, surface regions far from the source contribute less significantly to the far-field observer measurements. This physical behavior allows positioning of the open part of the surface sufficiently downstream from the main element while maintaining acceptable accuracy Giret et al. [133], Jacob et al. [134], Casalino et al. [117].

To optimize surface placement and evaluate far-field sound contributions, we conducted multiple test cases. Our investigation began with an oval surface positioned close to the airfoil, which was progressively modified into a C-shape and enlarged to contain the ejected cove vorticity within the airfoil's suction side, thereby preventing spurious effects. While results from the oval surface testing are presented in Appendix A1, we focus here on the optimal C-shaped surface configuration here.

C-shaped surfaces, characterized by one rounded side and one open side, are widely adopted in airfoil FWH computations [133, 135]. Their primary utility is in the open ended shape which allows the convected vortices to exit through the open side and since the open side can be kept sufficiently far, the radiation of the downstream eddies is expected to have a negligible effect onto the sound field regions that are upstream of the surface open end. In our case they also allow to avoid large size low vorticity structures on the suction side by careful placement. They also provide sufficient space to be confidently deployed to parametric case simulations such that when the slat positioning is varied, the increase or decrease of ejected flow will not necessarily cross the upper part of the surface, thereby enabling easier parameterisation. The C-surface placement plotted against the dilatation field around the airfoil is shown in Fig.4.14 and the numerical microphones are placed at coordinates as shown in Fig.4.15.

The sound signals obtained for selected probes are shown in Fig.4.16. All microphones show a steady mean-pressure that corresponds to the local flow pressure as the microphones places in the non-turbulent region. The mean pressure is however not same across the probes and a constant pressure at the ambient is subtracted from the total pressure for the FWH calculation. The residual value of pressure reflects as the non-zero mean value of the microphone recording, but does not affect the calculations of farfield sound since only the time derivative of pressure is used in the FWH formulation and not the absolute values. Accordingly, to avoid the DC component in the spectra computed using Welsh's method, a constant local mean subtraction is also enabled for each of the averaging windows.

The resulting spectra for corresponding probes are shown in Fig.4.17 where they are compared with the spectra from the VALIANT experiment (WT experiment). The comparison of results show a good performance of the numerical framework in capturing the far-field tones and the broadband characteristic

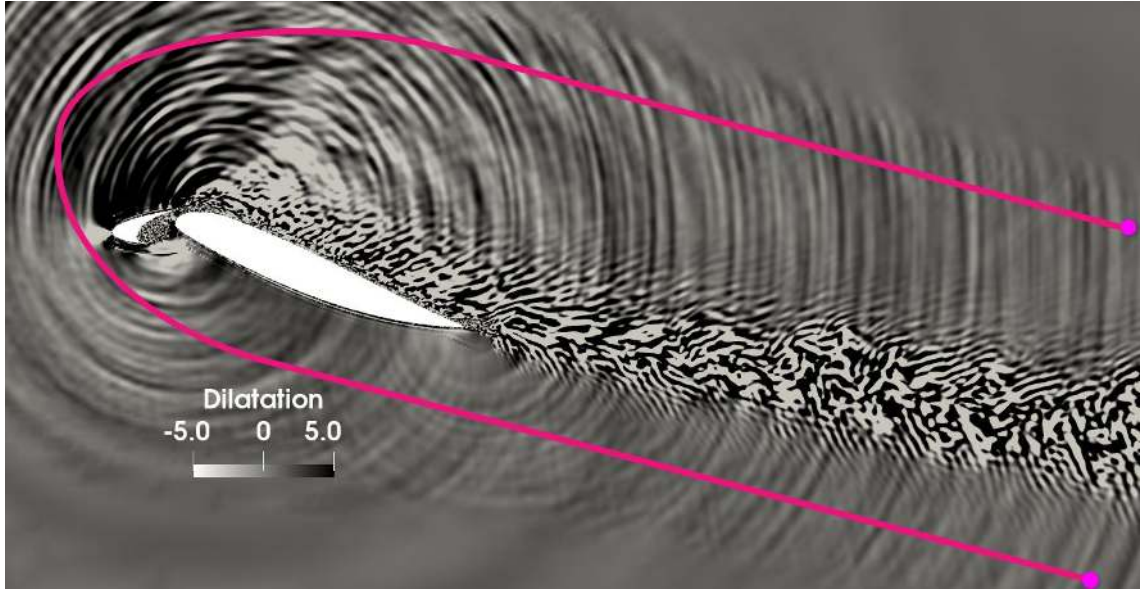


Figure 4.14: C-shaped FWH Surface and the dilatation field around the HLD

slat noise. For an observer at -90° at the pressure side of the airfoil, the prediction obtains the peak at 1771Hz, and the higher harmonics of the fundamental which is at 885Hz corresponding to the first Rossiter tone for this case according to Terracol et al. [14]. For the fundamental tone at 885Hz, the experimental spectrum also misses the first tone primarily due to the fact that at frequencies of 800Hz and below, the installation noise dominates the acoustic field in the experimental setup. In addition, the fundamental tone has a lower SPL component that hardly peaks out of the main spectrum as a small hump. This suggests that the source radiation might be strongly distorted by the local large eddies resulting in a flattening and broadening of the associated peak[132]. Nevertheless, the hump is visible at the upstream microphone on the pressure side, corresponding to Probe 9 at observer angle 135° as seen in Fig.4.17f. Furthermore, we demonstrate in a subsequent chapter using a slightly adjusted position of the slat that this first peak can in fact be captured with stronger power levels in the same simulation setup and installation effects.

For the first main tone at 1771Hz, which is the second Rossiter tone, the simulation faithfully reproduces the experimental frequency. However, the measured sound level is considerably higher at this frequency, which is not captured by the free stream simulation. A separate simulation including the installation geometries was also performed (see Appendix A.3), which showed better agreement at 1771 Hz. This suggests that the amplification of this tone can be due to the effect of the lateral side plates. Indeed, a spanwise resonance can be reasonably suspected to be present in the experiment. The experiment was designed with a span-to-chord ratio of 1, leading to separation between the plates to be 0.3m. The fundamental tone for resonance between the plates is thus $f_{S0} = 572\text{Hz}$ whose second harmonic is at 1716Hz. This is close to the 1771Hz, i.e. the first harmonic of the cavity resonance. Furthermore, while comparing with the simulation that included the spanwise lateral plates, both wall pressure recording and the farfield spectra show that the first tone obtained in the installed case is amplified with respect to the free stream configuration and hence reaches better agreement with the experiment. This supports the assumption that the disparity of the first tone is not an inaccuracy due to the simulation methodology but has a physical background.

For higher frequencies, the spectra downstream of the airfoil on pressure side, i.e. Probe 0 (see Fig4.15), shows good agreement. The obtained agreement between the simulation in free flow condition and wind

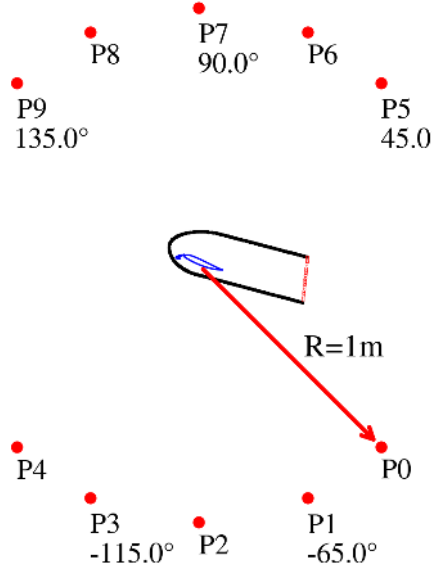


Figure 4.15: Numerical microphones relative to the FWH surface

tunnel experiment is hence reasonable. In contrast, microphones facing the suction side (which are not shown) registered higher levels for the frequencies above 10kHz and are possibly due to sources on the suction side of the HLD. Both turbulence ejection from the slat and its impingement on to the suction side of the airfoil leads to generation of high frequency noise. Since this is not of particular interest for the cove related noise, it is not investigated in our work.

Additionally, as mentioned, the spanwise extent of airfoil is not the same in both experiment and simulation. For the experiment, the distance between lateral side plates is kept as 1 chord length, i.e. $C = 0.3\text{ m}$. On the other hand the simulation uses a chord length of $0.66C = 0.2\text{ m}$. Theoretically, the experiment is designed to isolate a region between the plates which is unaffected by the boundary layer and the corner flow formed at the junction of side plates and the airfoil. But an exact estimation of what length along the span is effectively free from this disturbance and hence acoustically effective is not possible from the available data. Hence a correction of the sound level corresponding to the spanwise length difference can not be considered.

4.5 Unsteady Data and Cove Dynamics

To study unsteady dynamics of the cove for the noise-validated standard geometry case, we used the Q-criterion visualization [136] to first isolate the vortices. The Q-criterion is defined as

$$Q = \frac{1}{2} ((\nabla \cdot \mathbf{u})^2 + |\boldsymbol{\Omega}|_2^2 - |\mathbf{S}|_2^2)$$

where \mathbf{u} is the instantaneous velocity vector, \mathbf{S} is the strain rate tensor or symmetric part of the velocity gradient $\nabla \mathbf{u}$, $\boldsymbol{\Omega}$ is the vorticity tensor or the anti-symmetric part of $\nabla \mathbf{u}$, and $|\cdot|_2$ is the Frobenius norm. The Q-criterion serves as a scalar which represents relative magnitude of the vorticity component as opposed to the strain rate. In the volume occupied by a vortex, the vortex core has a strong vorticity component with minimal strain (hence a larger Q-value) and vice-versa on the exterior. Hence, by choosing a suitable Q-criteria and obtaining the isocontours of the same, vortex structures can be identified given the 3D

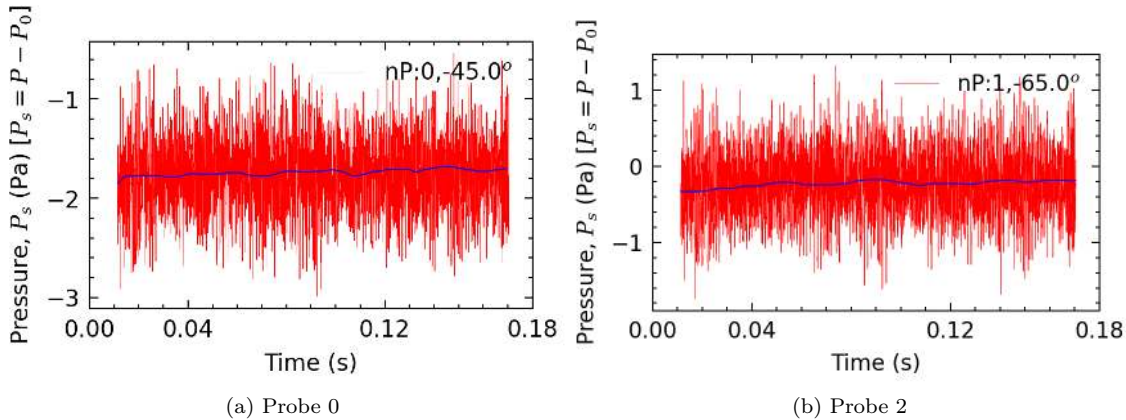


Figure 4.16: Sound pressure data obtained at select numerical microphones using FWH approach. The offset of mean pressure arises due to the usage of uniform standard pressure of 101325Pa as reference across the FWH surface, instead of locally averaged value. This steady offset nevertheless does not contribute to the spectral calculations.

unsteady velocity field. To use the same, we use the internal calculator of the ProLB solver to record the Q-values along with the unsteady velocity field and extract the isocontours using the visualization software ParaView.

The selection of Q-criterion depends on the application and a good visualization is obtained by iterative refinement. For our application, the Q-value of 1.4×10^8 was found to isolate the vortices in the flow as shown in Fig.4.18. As an additional aid in visualization, we also use one additional Q-value which is 70 higher. This allows to visualize the exterior of the spanwise rollers in addition to their inner vortex core. The coloring of the isosurface aids in identification of dynamics associated with the vortex. Here we color the same using the vorticity value which aids in identifying the core from the exterior surface. The spanwise vorticity behavior can then be isolated by setting the transparency settings in order to selectively highlight the structure based on the vorticity component on the iso-contours. By using the spanwise vorticity as the coloring criteria and for transparency, the spanwise rollers shed from the slat cusp can be clearly identified as shown in Fig.4.19a. As expected, the spanrollers can be noted to have a strong spanwise coherent vorticity in the vicinity of the slat cusp with progressive dispersion until the mid shear layer where the sense of curvature of the shear layer reverses. By sense of curvature we refer to the fact that the low speed recirculation region is on the concave side of the mean shear layer. Once the sign of curvature changes, i.e. the low speed flow is on the convex side of the curvature, the spanwise vortices can be noticed to disintegrate strongly by generation of smaller streamwise vortices primarily formed from the periphery of the spanwise structures, leading to the ejection of majorly streamwise vortices through the slat gap as shown in Fig.4.19b. A close up visualization of the vortex structures ejected from the slat trailing edge are shown in Fig.4.20. It must be mentioned that in addition to the streamwise vortices, this case also has comparatively similar, although less amount of residual spanwise vorticity that passes through the slat gap. This residual spanwise vorticity is a necessary component for the generation of the aeroacoustic phenomena since the streamwise vortices are far less efficient than spanwise coherent vortices to generate acoustic waves due to trailing edge scattering[55].

The unsteady visualizations of Fig. 4.19, made available as the supplementary document to this thesis, reveal that the process of generation of the streamwise vortices in the current case is particularly near and after the region where the curvature of the mean shear layer switches signs. This fact however does not allow us to clearly state that the transition of vorticity is definitively due to the effect of curvature. This is due to the fact that the region near the slat gap is a region of both streamwise acceleration and

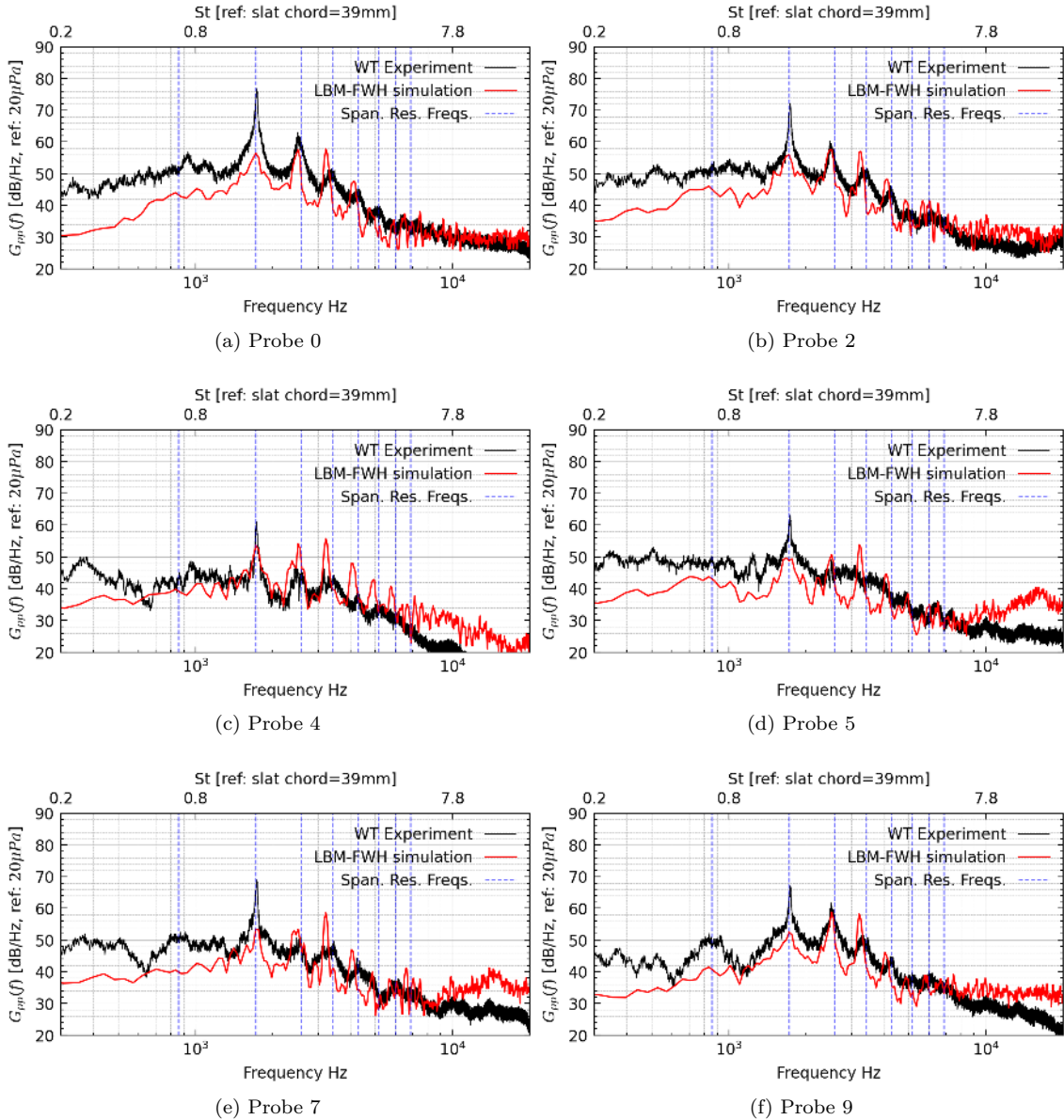


Figure 4.17: Sound pressure data computed at numerical microphones using FWH approach for the free stream configuration. The resonance frequencies corresponding to a flat plate resonance for plate separation 0.2m are also marked. Signal spectra parameters: Total time = 0.2s, NFFT= 8100, Sampling Freq.= 180405Hz, N.Avg.= 6 and $\Delta f = 22$ Hz

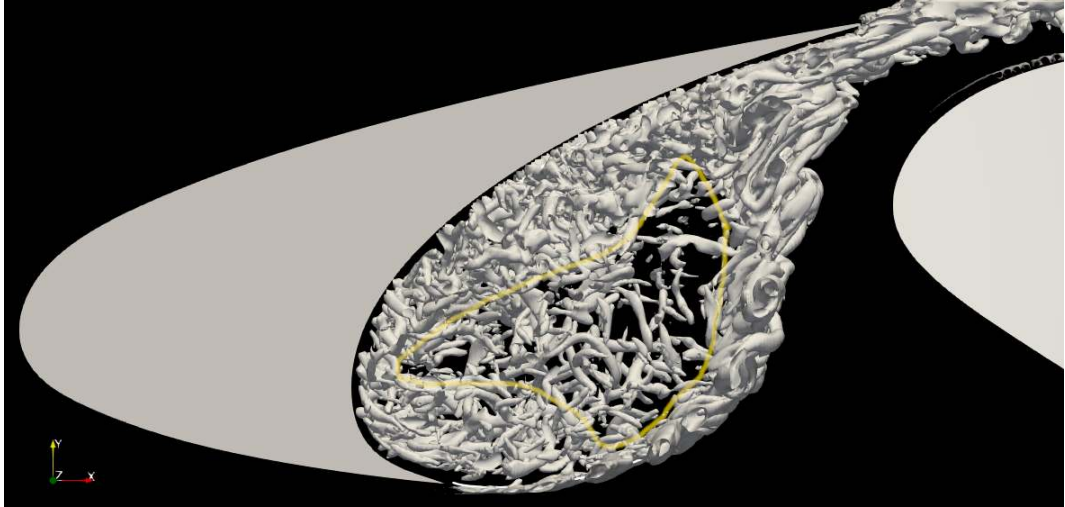


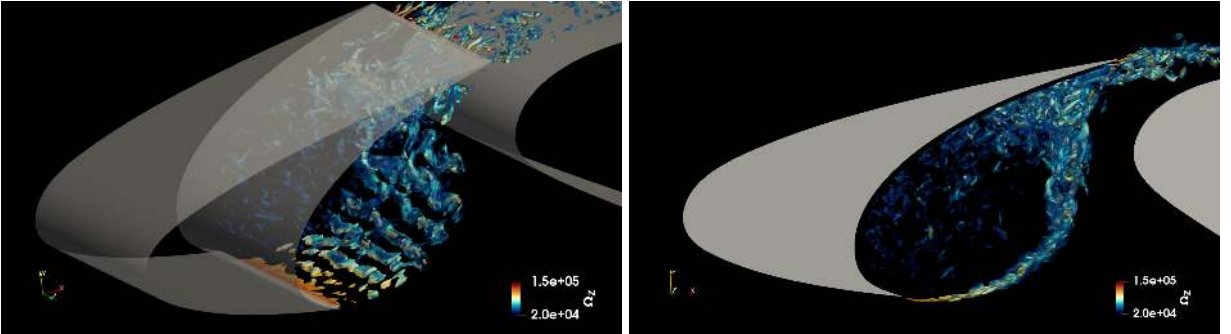
Figure 4.18: Iso-surfaces of Q-Criterion, $\frac{Q}{M} = 10^9$ where $M = 0.14$, is the flow Mach number. The region of sparsity for the small scale recirculating structure is demarcated with the yellow line

deceleration of the mean flow. The acceleration is due to the nozzle like shape of the region leading to the slat gap while the deceleration is caused by the stagnation region due to the impingement. The area of impingement region generates a zone of stagnation for the mean flow which further reduces the area available for the flow to exit, aggravating the nozzle effect of the geometry further. This complex interaction of the dynamic forces of the fluid hence makes it difficult to state that the vorticity transition is definitively driven by the curvature effect alone. Nevertheless, it is clear that the major source of the streamwise vortices is by the transition from the spanwise coherent structures along the later stages of the curved shear layer. Additionally, the curved wall of the inner slat is susceptible to the well-known Görtler instability of concavely curved boundary layers [137, 138], and are potentially contributing to the generation of streamwise structures in the recirculation particularly close to the slat cusp whose inner wall has a strong curvature.

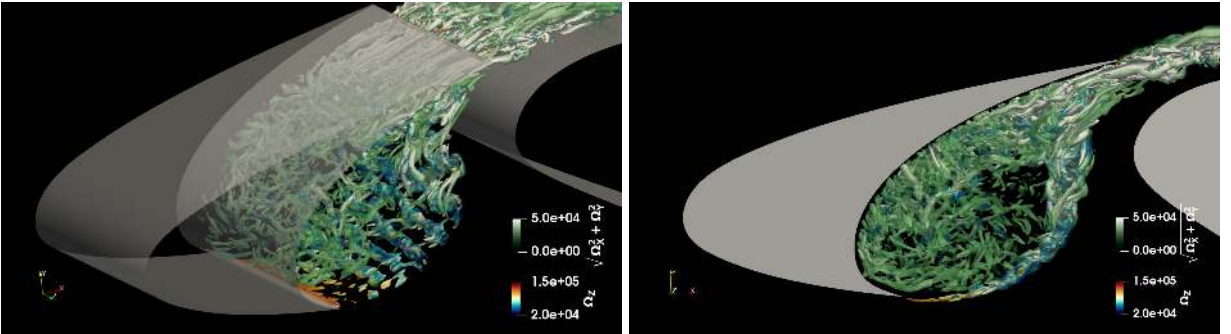
Another notable feature of the unsteady flow is the uneven distribution of the recirculation vortices inside the cove region as seen in both Fig.4.18 and 4.19b. The streamwise vortices which are more populous tend to be sparse in the region close to the mid trajectory of shear layer and at the center of recirculation whereas the density is higher along the curved inner wall of the slat. The streamwise vortices that reach the impingement location are inevitably stretched along the wall due to the streamwise accelerated ejection and the stretched vortices disintegrate into smaller vortices as they enter the recirculation. These smaller vortices then move along the wall and experience the centrifugal force due to the curved streamline of the recirculation. The centrifugal force hence explains the tendency of the vortices to stay in the outer periphery of the cove recirculation causing sparsity near the centre of recirculation.

The recirculating streamwise structures also reach the slat cusp by moving along the inner slat wall. These structures can be noted to interfere with the shear layer in the region near the slat cusp and also in the early shear layer. The structures then interfere with the spanwise vortices accelerating the generation of more streamwise vortices in the process. This also aggravates the fact that the streamwise vortices are sparser in the mid-region of the slat shear layer since a major portion of the recirculated streamwise vortices are entrained into the shear layer.

The vortex stretching happening at the trailing edge is also worthy of further mention. The impinging vortices in the shear layer is a mix of streamwise and spanwise vortices with streamwise vortices in larger proportion. The latter majorly wind around and form ladder structures together with the spanwise



(a) Vortices visualized by setting transparency of iso-surfaces using the spanwise vorticity component Ω_z , isolating the streamwise coherent structures shed from the slat cusp. The streamwise vortices in the inner circulation region are now set to low visibility due to their low spanwise vorticity.



(b) Vortices visualized by using both the spanwise vorticity component Ω_z , and the residual in-plane component, $\sqrt{\Omega_x^2 + \Omega_y^2}$, on separate colourmaps to highlight the streamwise structures inside the recirculation region against spanwise coherent structures.

Figure 4.19: Iso-surfaces of Q-Criterion, $\frac{Q}{M} = [10^9, 1.4 \times 10^8]$, where $M = 0.14$ is the flow Mach number

structures. Near the wall at impingement, the streamwise vortices become stronger and assimilate to larger structures, and, as they impinge, the streamwise structures are elongated in both the forward and backward directions, towards the ejected and recirculated directions respectively. Here the stretching is stronger in the downstream direction through the slat gap. The streamwise vortices in the slat wall are also continuously replenished by incoming vortices and as they interact with the wall as they tend to roll along wall in the spanwise direction. This leads to counter rotating vortices coalescing to form large counter-rotating vortex pairs. These counter rotating vortex pairs can be visualized by using a diverging colourmap that highlights the streamwise vorticity in opposing directions as shown in Fig.4.21. The ejected counter rotating vortices and residual smaller streamwise vortices are then flushed on to the suction side of the main element. The counter rotating pairs often undergo further instability to form helical structures before impinging with the suction side wall on main element and can be noticed in Fig.4.21.

The mean streamlines ejected from the trailing edge location need not necessarily directly graze the main element. However, in the unsteady dynamics, the ejected vortices tend to have an unsteady oscillation which redirects the ejected vortices to have a flapping motion towards and away from the main element suction wall. This low frequency oscillation also leads to oscillation of the reattachment point of the ejected streamwise vortices on the main element.

The local unsteady component of pressure, $P' = P - P_0$, is shown in Fig.4.22. As expected, P' exhibits quasi-periodic fluctuations along the shear layer trajectory, reflecting the convection of vortices periodically shed from the cusp. These vortices impinge on the wall near the trailing edge, thus generating an oscillating pressure field that extends its influence to the leading edge of the main element as well. Consequently, the aerodynamic pressure within the whole of slat gap has periodic fluctuations that are synchronized with

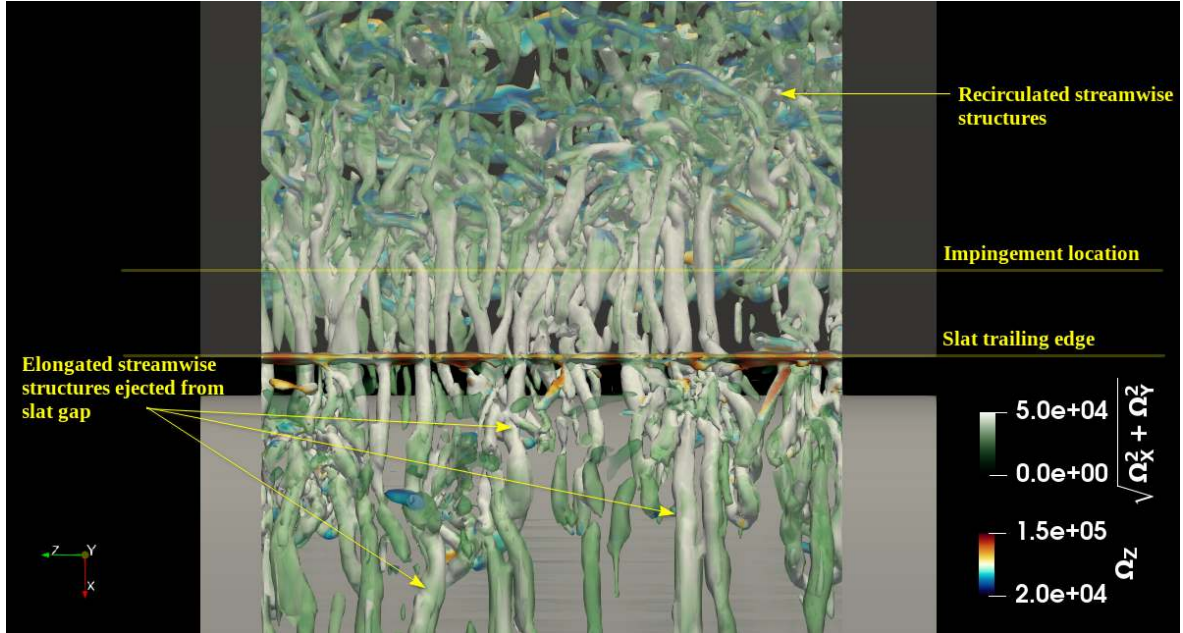


Figure 4.20: Streamwise vortices ejected from the slat gap. The slat wall is set to be partially transparent to inspect the dynamics of the impinging vortices. Q-criterion is set to $\frac{Q}{M} = [10^9, 1.4 \times 10^8]$, where $M = 0.14$ is the flow Mach number.

the pressure variations induced by the convected vortices.

Another prominent feature to be noticed is in the velocity components. In Fig.4.23b and 4.23c, it can be noticed that the major unsteadiness is confined to a region close to the slat TE while the larger area of the slat gap maintains a steady flow. This suggests that the ejected vortices, which are understood to be majorly streamwise structures, tend to primarily graze the surface of the slat trailing edge and the leading edge wall of the main element experience a smoother flow. The unsteady velocity components also tend to suggest uneven distribution inside the slat cove and are generally consistent with the effects of flow redirection through slat gap from the pressure side. This can be noticed in the broader distribution of U_X inside the cove region and the same for U_Y around the mid-length of the shear layer.

To further highlight the spanwise of flow inside the cove region, the colormap is further restricted to a smaller range of $U \in [-20, 20]$ m/s in Fig.4.23. Here the 3D-feature is more prominent and hence a velocity ratio capturing relative out-of-plane velocity U_z against the residual planar velocity $\sqrt{U_X^2 + U_Y^2}$ is used. By definition, $R_{U_z} = \frac{U_z}{\sqrt{U_X^2 + U_Y^2}}$, serves to quantify the significance of the spanwise component. It can be noted in Fig.4.23a that the R_{U_z} is majorly positive in the lower part of the cove and have an opposite sign in the upper region. By nature of R_{U_z} , this indicates that both U_z is significant compared to the inplane velocity and that its direction reverses in different regions of the cove. This feature is however slightly vitiated by the unsteadiness of the recirculating scale vortices but is a clearly demonstrable one with a sharp boundary for the sign reversal while analyzing the time-averaged fields as shown in Fig.4.7.

Additionally, we note that the point of stagnation on the pressure side of main element's leading edge only have a weak local spike in value of R_{U_z} since at this point the flow is majorly redirected within the plane with no significant mean flow in the spanwise directions. This contrasts with the effect inside the cove where there is no region with $R_{U_z} \approx 0$, thus suggesting that the 3-dimensionality is a result of the re-circulatory flow within the slat cove. The spanwise velocity field U_z has a maximum of upto $U_z = 10$ m/s inside the cove, i.e. upto 20 of the free stream velocity.

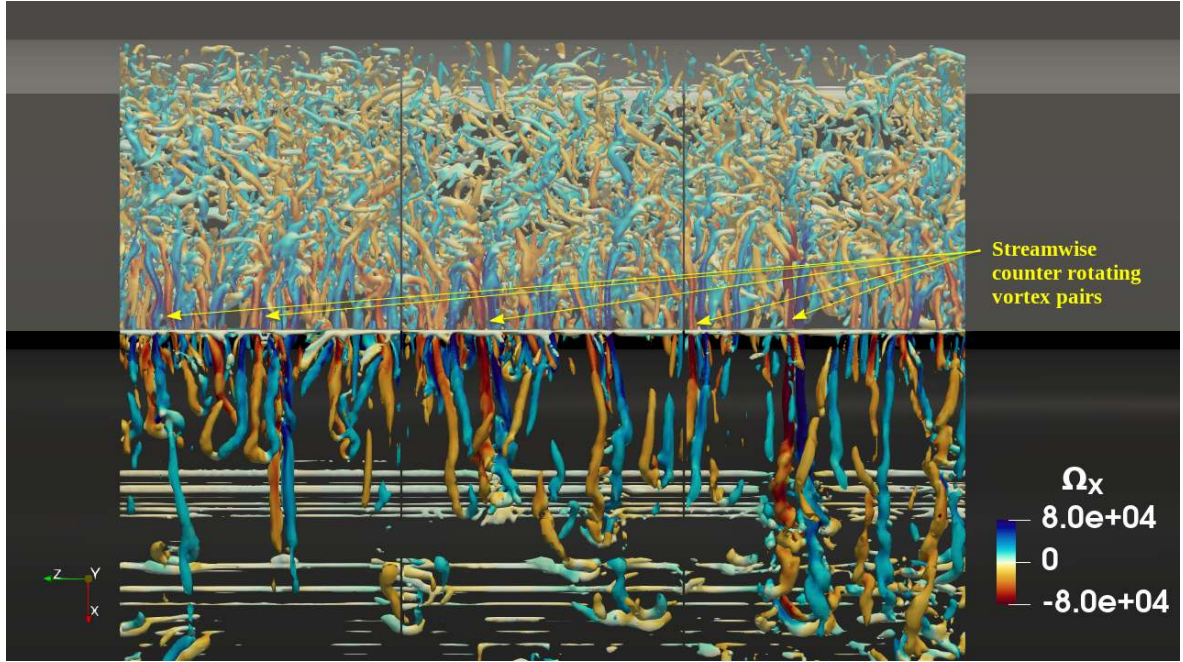


Figure 4.21: Streamwise counter rotating vortex pairs at the slat gap visualized using a diverging colourmap based on the streamwise vorticity Ω_X . The Q-criterion is set to $\frac{Q}{M^2} = [10^9, 7 \times 10^9]$, where $M = 0.14$ is the flow Mach number. The assimilation of streamwise vorticity below the slat trailing edge then leads to rolling of the vortices along the wall and pairing up of counter rotating vortices. These are then stretched and ejected on to the suction side of the main element often leading to helical structures.

4.6 Similar simulations confirming the spanwise modulation in cove flow

To demonstrate that the formation of spanwise modes is not an artifact of the simulation or the spanwise boundary condition applied, we discuss a few simulations which have a slightly varied configurations. For this first we take the case of simulation of VALIANT HLD geometry which has the wind tunnel geometry and the supporting lateral sidewalls included in the simulation. Then we discuss the simulations where the spanwise length of the domain is reduced by a factor of 0.5, and then a case with only two rectangular plates included to use reflecting boundary conditions in the spanwise boundaries as opposed to periodic conditions used in the standard simulations. All these cases are shown to develop the spanwise cells for the time-averaged spanwise velocity field.

4.6.1 Simulation with wind tunnel geometry and lateral side walls included

For sake of brevity, only the mean flow results of this simulation are discussed here and a detailed account of the same given in the Appendix A Section A.3. The mean velocity field obtained at multiple vertical planes across the span in the cove region is shown in Fig.4.24.

The time-averaged mean flow fields are computed from the simulation data by averaging over 5 chord pass times same as the standard procedure. As can be noted, the cell formation due to the previously mentioned curvature instability is notable in the spanwise velocity distribution near the central plane away from the lateral walls. However, closer to the walls, the velocity field is more strongly modulated with stronger amplitudes than near the center planes. Such effects were also noted in the presence of

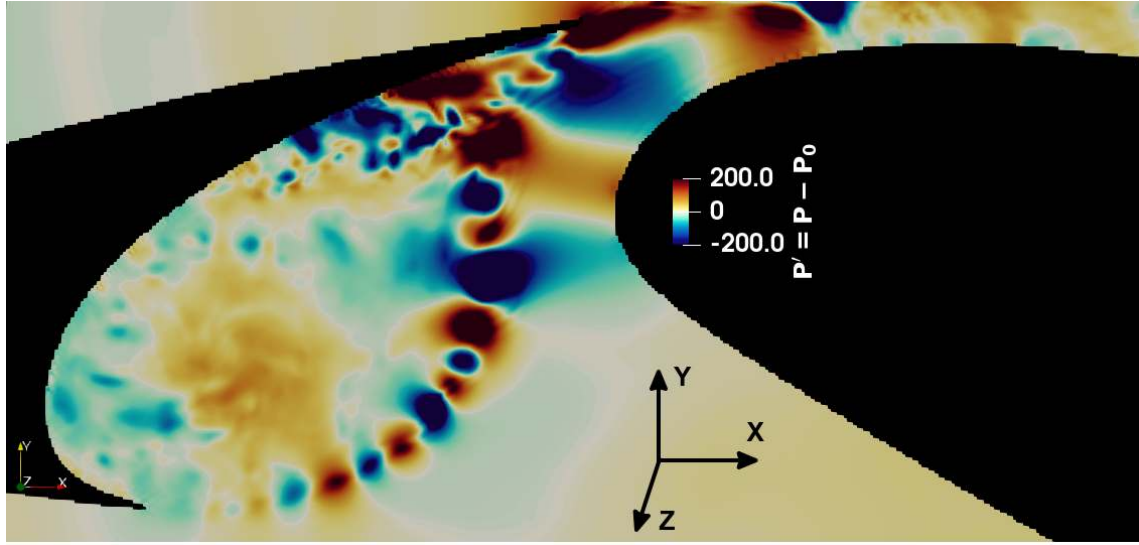


Figure 4.22: The unsteady aerodynamic pressure field ($\pm 200 \text{ Pa}$) in the slat cove identifying the trajectory of the spanwise coherent structure along the curved shear layer

the backward facing steps where lateral side walls generate strong three dimensionality for flow adjacent to the walls [2]. However these can be thought to be a separate phenomenon since the lateral walls of the airfoil also generate additional dynamics due to the problem of corner separation for the turbulent boundary layer.

The cells near the center plane appear to have the same properties as those formed in the free flow simulation. The modulations are largely attached to the shear layer, and as the shear layer developed downstream, the cells inside the recirculation region tend to remain attached to the shear layer. A separate arrangement of cells with phase inversion is seen to then occupy the interior of the cove nearer to the curved inner wall of the slat. This new arrangement then develops stronger towards the slat gap but is noticeably more distorted due to the end wall effects. The nodal planes leading to converging and diverging planes are noticeable which suggests that the pulsating mechanism related to the low frequency broadband peak can be present.

The extent of the effect of lateral walls into the interior of the cavity in spanwise direction is significant. Current simulation suggests that more than 80% of the spanwise extent is affected by the distortion and the curvature related flow structure is limited to only 20% of the length. This means that curvature related low frequency pulse is considerably weaker in the experimental spectra and hence is also not notable. It is hence possible that the experiment also has reduced effect of the spanwise modulation leading to a reduced modulation of the tonal frequencies.

Another factor worthy of mention is that in comparison with the VALIANT experiment which uses a spanwise length of 1 chord length, i.e. 0.3m as the distance between the spanwise plates, the setup for a different experiment on the 30P30N HLD geometry by Kamliya Jawahar et al. [29] used a spanwise length of 0.5m. In terms of the chord to span ratio, VALIANT experiment kept $\frac{L_s}{C_s} = 1$, whereas in Jawahar et al. [4]'s work, a ratio of $\frac{L_s}{C_s} = 1.42$ was kept. The latter also was designed at a chord based Reynolds number of $Re = 70000$. The experiment was conducted at the wind tunnel facility at University of Bristol and lead to observation of the prominent low frequency hump in the spectra corresponding to the first Rossiter mode, and particularly with strong intermittency and stochastic character. From the influence of the lateral side wall plates that is shown to disrupt the spanwise mode formation due to centrifugal instability and the nature of its suspected low frequency oscillation, we conjecture that the strength of the low frequency hump in the noise spectra will be correlated with the availability of

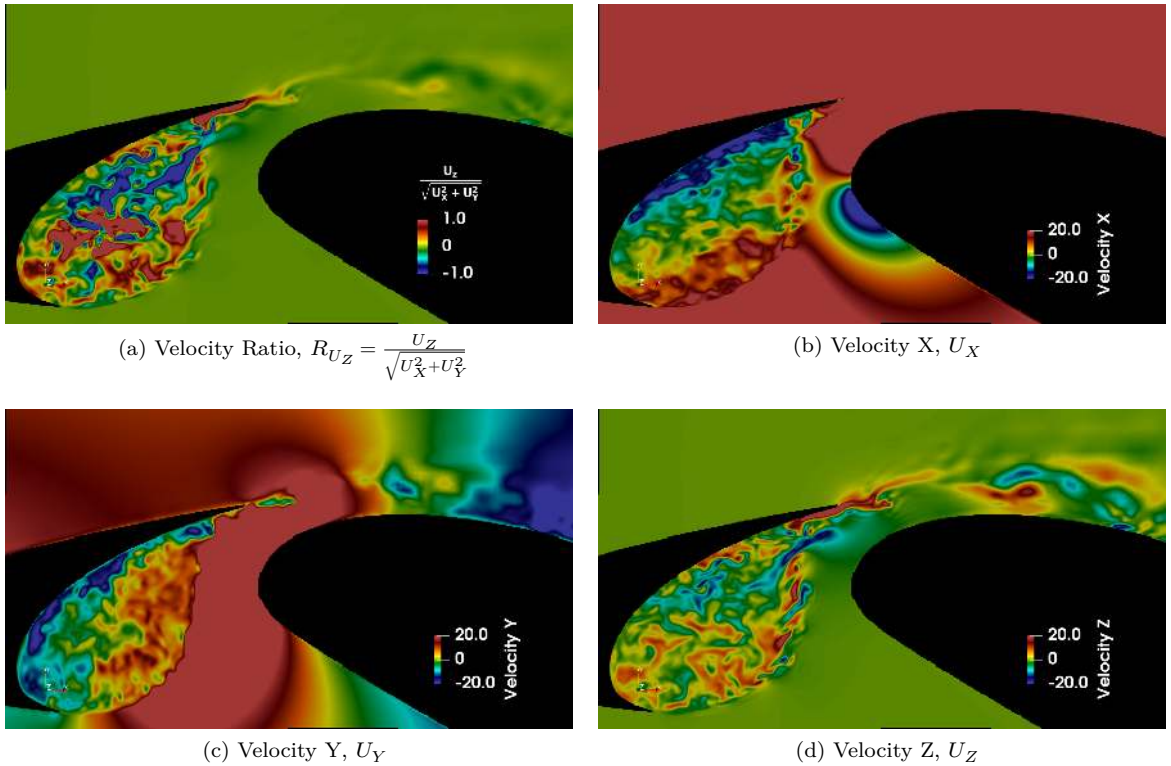


Figure 4.23: The unsteady velocity field in the slat cove visualized using a narrow colorbar corresponding to velocity values $U = \pm 20$ m/s. The freestream velocity is 50 m/s.

sufficient space between spanwise holding plates. This can also influence the strength of the tones and can be suspected to be the reason for the variation of strength for the alternating narrow bands peaks in their far-field observation. It is however the general experimenter's wisdom that keeping the spanwise distance as high as possible would reduce the three dimensional effect of the side wall boundary layer thereby recovering the spanwise homogeneous 2D flow in the spanwise central plane. This is expected from the behavior of wide span cavities as well[76]. But counter-intuitively, this is only disrupting the development of the three dimensionality due to the centrifugal instability for the slate cove case. Furthermore, the measurement of the turbulent intensity and wall pressure spectrum will also be misinformed in the case of similar experiments with insufficient spanwise margin since the existence of a nodal plane at the spanwise central plane can lead to erroneous observation of either excessive or reduced turbulence intensity due to the converging or diverging motion of spanwise structures in the cove recirculation region. The spanwise modes and their possible oscillations hence provide a reasonable explanation for the intrigue upon the quasi-periodic behavior of the Rossiter tones in the study by Jawahar et al. [4].

4.6.2 Simulation with rectangular lateral plates only

To investigate the effect of spanwise boundary condition for the slat cove region, a similar simulation was setup where the span boundaries were supplanted with a plate. The wall of the plate provides a no-slip condition similar to the simulation of the wind-tunnel case and hence avoids the additional artifacts of using a spanwise periodic domain. A schematic of the arrangement is shown in Fig.4.25 and the mean flow across the span length inside the slat cove is shown in Fig.4.26 and 4.27.

The mean flow around the airfoil in this case shows a strong deviation from the standard case results. Here the flow separates early from the leading edge of the main element and is hence stalled. The shape of

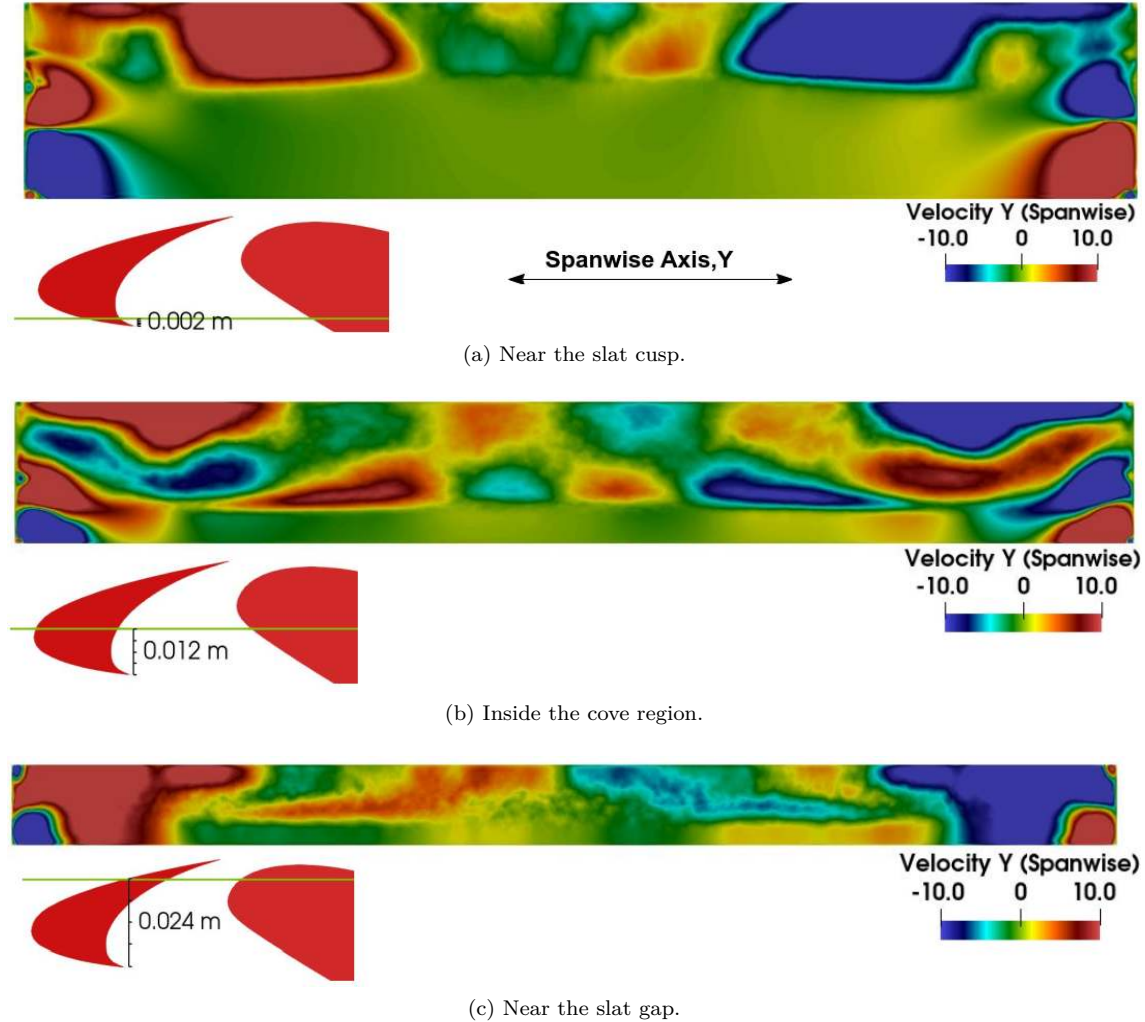


Figure 4.24: Time-averaged spanwise velocity on spanwise planes at different locations in the slat cove region for simulation which includes the spanwise plates and wind tunnel geometry. Note that only for this particular simulation, the coordinate system is such that the spanwise direction is along the Y direction. The modulation of the spanwise velocity is noticeable with cell formation similar to the free flow simulation without spanwise plates. The edge effects distorting the cells are also evident on the sides which is due to the presence of lateral side walls and the boundary layer and associated vorticity generation

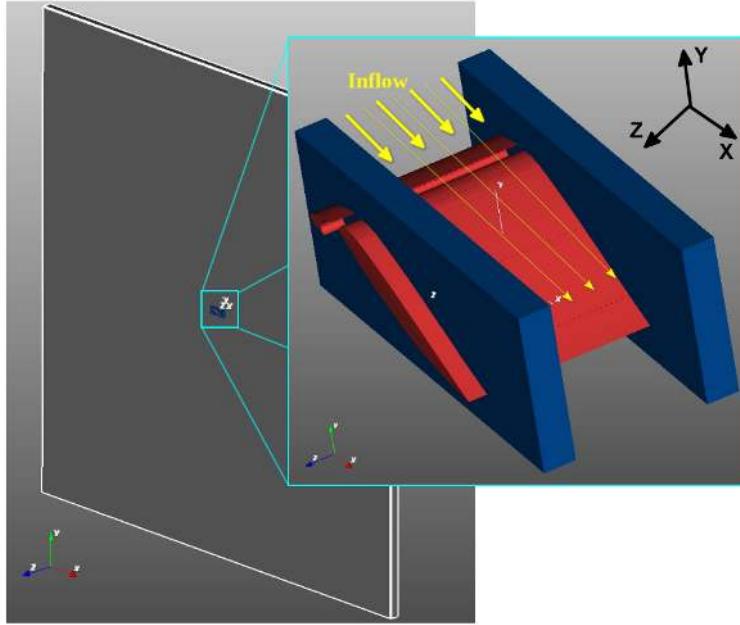


Figure 4.25: Schematic of the flow simulation setup. For frame coordinate system, the incoming flow is along the X axis and spanwise direction is along the Z axis.



Figure 4.26: The flow separates possibly due to disproportionate interference from turbulence due to the side walls and plate corner.

the cove flow is also strongly distorted such that shear layer is elongated with a reduced initial curvature near the slat cusp. Hence this case is not successful simulation of the aerodynamics in view of its fidelity against the experiment, but however is still valid to be inspected for the effect of the spanwise condition inside the slat cove.

As can be seen in Fig.4.27, the spanwise cut plane across the span still retains the spanwise periodic cell formation. Here the region inside of the cove region can be seen to have the spanwise cells while the region outside of the shear layer region is strongly affected by the presence of the wall. The spanwise velocity near the spanwise walls are strongly perturbed by the boundary layer to have a mean distribution as to direct the flow towards the span center.

The outcome of this simulation is two fold: one is that the presence of spanwise cells are demonstrated to be independent of the spanwise boundary conditions in the simulation for the slat cove region; the second is that this cell formations are possible even if there is a strong incoming turbulence intensity. For the incoming turbulence, it can modify the flow such that airfoil stalls at an early angle of attack and also alter the shear layer shape. Nevertheless, the recirculation flow generates the centrifugal instability

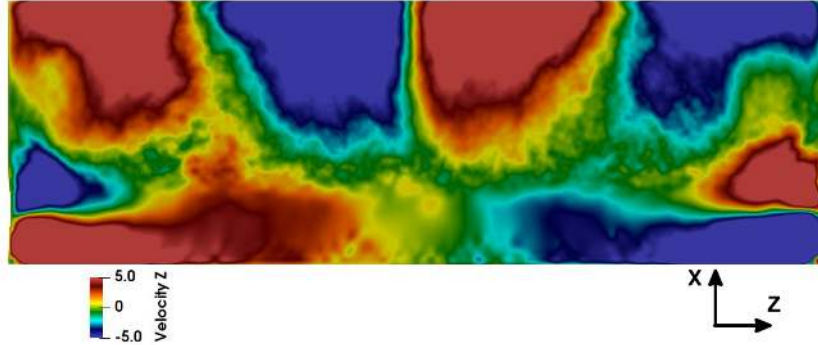


Figure 4.27: Spanwise cell formation is still noticeable although the cove shape is distorted. Spanwise direction is along the Z axis and the visualization plane is akin to 4.24a.

inside the cove and hence the spanwise cells are still present.

4.6.3 Simulation with a reduced span and periodic boundary conditions

Another case for inspecting spanwise cell formation was one with a reduced span of one-half of the original length. All other simulation parameters are kept the same as the standard simulation. Here, as shown in Fig.4.28, the velocity distribution shows little difference in the larger two dimensional features of the flow in the mid-span plane. However, the three dimensionality of the cove flow and the formation of spanwise cells seems to be attenuated in this case. As shown in Fig.4.29, the spanwise cells are formed in the early part of the shear layer as expected from the full span simulation. However, for the region corresponding to the later part of the shear layer, the spanwise modulation seems to have weakened leading to more homogeneity in the flow and reduced spanwise velocity component. This induced homogeneity of the flow due to spanwise condition is recognized in literature and have served as a criterion to determine the lower bound for the spanwise length of simulation domain for numerical studies[19, 14]. Terracol et al. [14] have already studied the VALIANT geometry using different spanwise extent to demonstrate the same phenomena. For the current case, spanwise length of 0.1m is hence inferred as insufficient to reproduce the full three dimensionality of the flow. This leads to the partial formation of the spanwise modulations in the early part of the shear layer due to strong curvature of the flow and a largely homogeneous spanwise distribution in the rest of the cove region.

The partial presence of the spanwise cells in a reduced span simulation also hints at the fact that the spanwise boundary condition acts only so as to induce homogeneity. The persistent formation of cell structures in the region of early shear layer with strong curvature again suggests that the 3-dimensionality is predominantly a centrifugal effect. This centrifugal flow is primarily driven by the concave curvature of the inner wall of the slat cusp together with the redirection of the flow by the incoming ambient flow from upstream. The persistence of the spanwise modulation at this region, while induced homogeneity dominating in the downstream locations, suggests that the amplification of the spanwise mode instability is higher in the region of early shear layer compared to other regions in the cove.

4.6.4 Simulation at lower Reynolds number using geometry scaling

The spanwise mode formation is tested again in the case of a reduced chord length. For this we scale the geometry by a factor of $\frac{2}{3} = 0.66$. The new stowed chord of the HLD is $C = 0.2\text{m}$. All the simulation parameters are kept same as the free flow standard simulation, including the spanwise length which is at $L_s = 0.2\text{m}$.

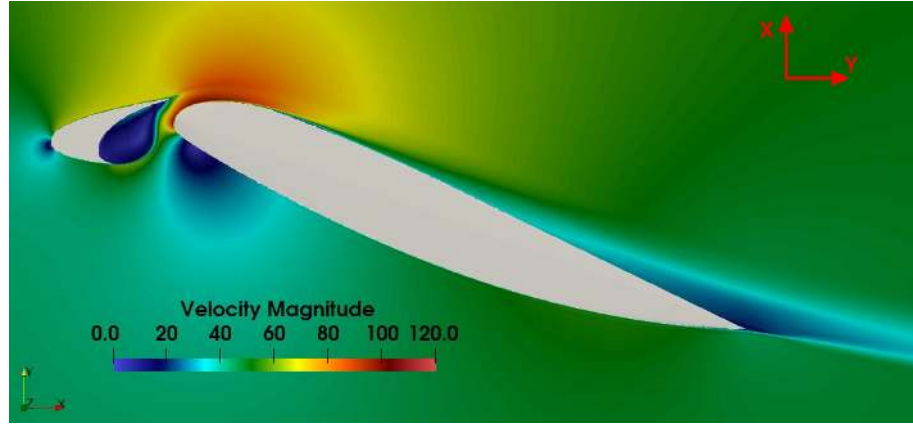


Figure 4.28: Time-averaged velocity magnitude field for simulation using reduced span of 0.1m. Major flow features are not altered as compared to span length of standard simulation at 0.2m

The time-averaged spanwise velocity fields are visualized for this case in Fig.4.30. The spanwise cells can be noted to have similar arrangement as in the standard case. However, the spanwise wavelength has been reduced by a factor of 0.56. This is consistent with the fact that cells are formed by mechanism similar to the backward facing step studied by Barkley et al. [2] where the spanwise wavelength is of the same order as that of the cavity depth. Here the scaling of the slat chord, and hence the cavity depth, is also by a factor of $\frac{2}{3}$ with respect to the standard geometry, and hence is now 0.026m. Correspondingly, the spanwise wavelength also undergoes down scaling. By a linear factor of $\frac{2}{3}$, the new wavelength would be expected at 0.0464m corresponding to 4.3 cells. However the observed configuration forms a total of 5 cells with a wavelength of 0.039m.

The Reynolds number of the flow is also scaled by a factor of $\frac{2}{3}$ due to the scaling of characteristic length. However, the inlet velocity is maintained at 50m/s and hence the flow along the shear layer maintains a similar velocity profile. Here the magnitude of curvature is amplified by a factor $\frac{3}{2}$ and hence higher the effect of centrifugal destabilization. For this case the observed spanwise wavelength 0.039m and shown in Fig.4.30 and therefore the slat-chord based non-dimensional wavelength $\Lambda_z = \lambda_z/C_s^* = 1.5$ where C_s^* is the new slat chord. Note that for the full span case, it maintained $\Lambda_z = 1.785$. Nevertheless, the final selection of wave number is constrained by the fact that the spanwise boundaries have a periodic conditions thereby necessitating a whole number of cells in the total span length. Counting this in, the given cases validates the suggestion of Brès and Colonius [3] that the spanwise wavelength is proportional to the cavity depth and also that the mode formation is primarily driven by the centrifugal instability mechanism similar to cavity flows. Since this phenomenon was only discovered during the exercise of this thesis, we did not conduct a parametric study to understand the variation of the span length, along with spanwise domain length. Such an investigation and also a model for the prediction of cell formation in the particular case of slat cove flow by using linear stability analysis can be an interesting avenue for further investigation.

4.7 Analyzing Streamline Curvature of the Shear Layer

The analysis of the mean flow inside the cove region and drawing parallels from the literature, particularly from that on the spanwise modulation of curved flows in cases of flow past a backward facing step, open cavity flows, and lid-driven cavity flows, it suggests to investigate the effect of i) the three dimensionality and ii) streamline curvature in the shear layer and recirculation region. The curvature of the streamline in the shear layer may also trigger a ‘Görtler’ like transition leading to the generation of counter-rotating

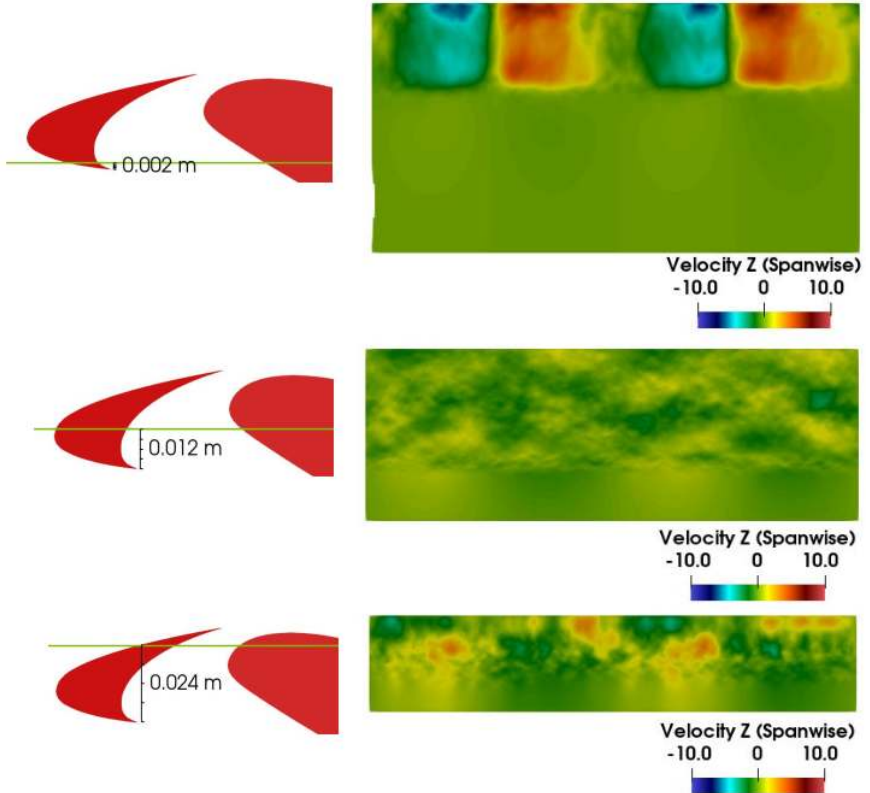


Figure 4.29: Time-averaged spanwise velocity field for simulation using reduced span of 0.1m. The spanwise cell formation is seen to remain only in the early part of the shear layer whereas the rest of the cove region seems to develop spanwise homogeneity arising from the effect of periodic boundary conditions applied in the spanwise boundaries

small-scale streamwise structures. Both these effects are fundamental to the slat noise generation mechanism whose tonal characteristics are necessarily influenced by the coherence of the impinging spanwise coherent vortices. Hence, to understand the curvature effects more thoroughly and to quantitatively understand its implications on the shear layer development, we attempt to characterize the mean streamlines by utilizing the mean field recording available from the LBM simulations.

The mean streamlines can be obtained from the time-averaged velocity field. For our purpose, we use a constant time stepping and the mean 2-dimensional velocity as the gradient field as inputs to a Runge-Kutta integrator. Here, since we assume that the flow features in the spanwise direction are primarily driven by the streamline curvature in the mid-span 2D plane, the streamwise and cross-flow component of the velocity field is used to study the streamline in their 2D plane and omit the contribution of spanwise velocity component. For the Runge-Kutta integrator, we use the classical fourth order RK4 formulation.

The mean flow data is obtained on the Cartesian grid of the simulation. However, this grid is not suitable to obtain a continuous streamline and hence the velocity field need to be interpolated in order to obtain the velocity value at a given query point for the RK integrator. For this interpolation we use the Clough-Tocher interpolation scheme provided with the scientific computing package SciPy. The interpolation scheme finds the three neighboring points of the query point and uses a piece-wise interpolating Bezier polynomial with order of accuracy upto third degree. Since the procedure is computationally inexpensive and over resolution is used by setting the time stepping to $2 \times 10^{-7}s$.

The streamline can thus be recovered for any selection of the source point in the flow field. However, to select a suitable point that would allow capturing the mean trajectory of the spanwise coherent vortices,

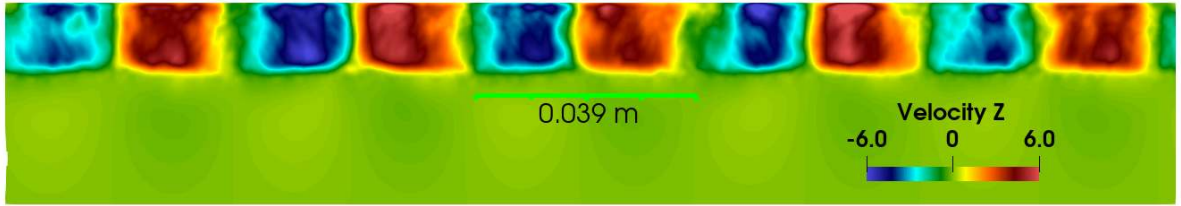


Figure 4.30: Spanwise cells formed near the early shear layer (for location see plane PL1 in Fig.4.10) for the case of downscaled geometry. The downscaling factor of $\frac{2}{3}$ also affect the wavelength of the cells. However the selection of wave number is constrained by the fact that the spanwise length requires a whole number multiple of the wavelength

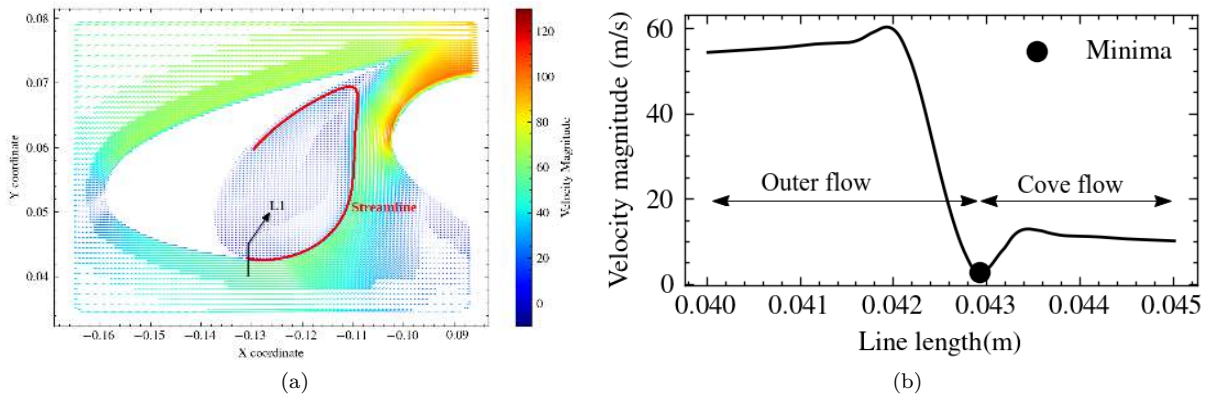


Figure 4.31: a) The streamline obtained using Runge-Kutta integration of the velocity field from a source point near the slat cusp. The initial line across the shear layer used to obtain the streamline source point is shown as L1. b) The velocity magnitude obtained along the line L1 with the minima denoting the location of the line crossing the immediate vicinity of the slat cusp is marked with a dot

the mean velocity magnitude distribution on a straight line across the shear layer near the slat cusp is used as shown in Fig.4.31b. The point at the bottom of the dip in velocity magnitude correspond to the point immediately downstream of the slat cusp and this point is selected as the source point for the streamline integrator. The obtained streamline is then used to quantitatively analyze the streamline curvature. Geometrically, the local curvature of a streamline is defined as the rate of variation of a unit tangent vector direction with respect to the arc-length. This definition allows to calculate the Radius of curvature in different forms as

$$R = \frac{\left\| \frac{d\vec{T}}{ds} \right\|}{\left[1 + \left(\frac{dy}{dx} \right)^2 \right]^{\frac{3}{2}}}$$

where R is the Radius of Curvature, which is the reciprocal of the measure of curvature, $C = \frac{1}{R}$, and s is the path length. Here, since we obtained the coordinates of the points of the streamline path, we choose the formula

$$R = \left[\left(\frac{\partial^2 x}{\partial s^2} \right)^2 + \left(\frac{\partial^2 y}{\partial s^2} \right)^2 \right]^{-\frac{1}{2}}$$

where ds is the differential arc length computed as the first order gradient of flow path-length obtained by cumulative sum of the individual Runge-Kutta integrated steps for the path-length. The numerical computation of the local Radius of Curvature as a function of the streamwise location on the shear layer for the standard geometry is shown in Fig.4.32. The calculation of gradients is particularly noisy for the calculation of the second order derivative along the streamline due to the interpolation and hence an additional averaging is applied using a moving window for the calculation of curvature. This averaging, with a window size of 100 points, reduces the numerical noise and delivers a smoother calculation in the early shear layer and also in the downstream where the mean velocity field is less converged due to the low frequency oscillations of the cove flow. For calculations using the second order gradient we report only the smoothed version of the obtained quantities.

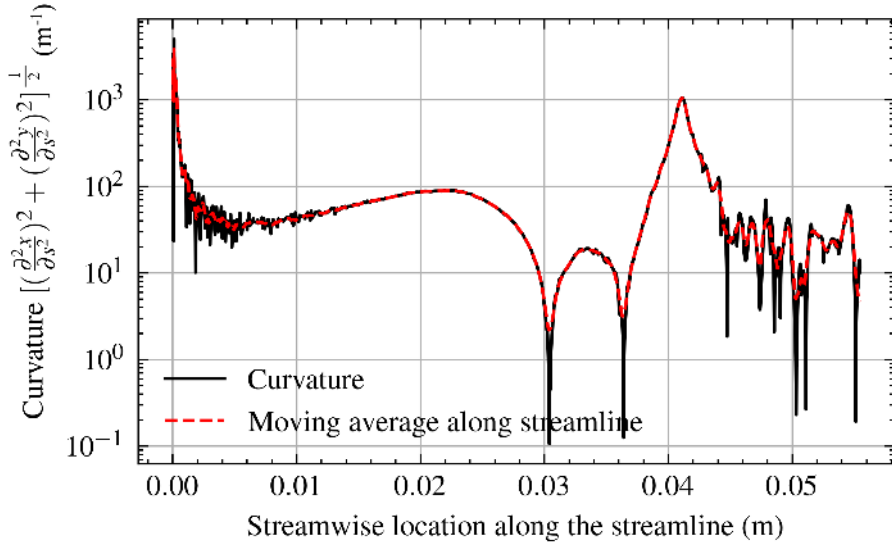


Figure 4.32: Local curvature along a streamline in the shear layer

The measure of curvature is the inverse of the Radius of Curvature, R . The shear layer shape necessarily follows a path whose mean curvature is of the same order as that of the slat chord thereby suggesting a mean curvature around $2/C_s = 51.28 m^{-1}$ or higher.

At the impingement location, the mean streamline can have two trajectories, one into the recirculation zone, and the other towards the ejection through slat gap. The streamline which enters the recirculation zone is sharply curved as seen in Fig.4.31a and is the region of highest curvature. The streamline that exits through the slat gap has a smaller curvature than the other.

To investigate the streamline for related parameters, the first parameter of interest is the time-averaged streamwise deceleration. This can be computed from the mean velocity field along the streamline as

$$D = -U \frac{dU}{ds}$$

where U is the streamwise velocity magnitude. Here the velocity magnitude is taken to be $U = \sqrt{U_X^2 + U_Y^2}$ where X and Y are the in-plane velocity components for the streamline.

As shown in Fig.4.33, the deceleration on the streamline is far from uniform. The flow is first accelerated along the streamline in the initial region of the vortex shedding and as the streamline curvature decreases in the intermediate region, the flow is accelerated. Before the impingement near the wall, the stagnation causes a region of strong deceleration. This stagnation of the mean flow generates the neces-

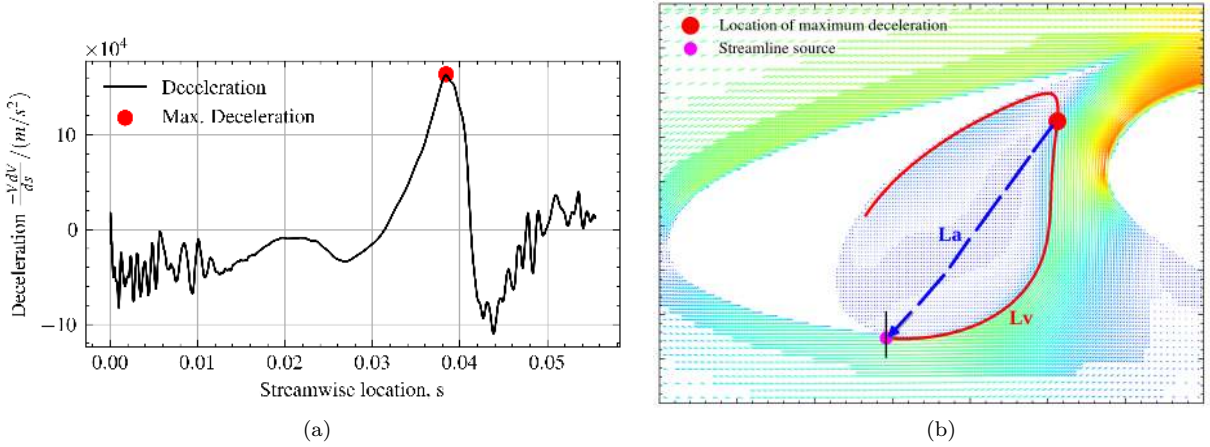


Figure 4.33: a) Local deceleration along a streamline in the shear layer and the location of its maximum. The numerical noise in the early and later regions arise from the numerical differentiation of the interpolated velocity field. Local fluctuations are also present in the velocity field due to the effect of low frequency oscillations not sufficiently averaged out within 5 chord pass times. b) Location of the impingement location within the flow field. A representative color map is used to indicate the background flow velocity

sary pressure gradient required to counter act the centrifugal force generated by the curvature of the flow. However, when the angular momentum decreases radially across the streamlines, the centrifugal force can be in excess of the established pressure gradient. This imbalance is the cause for the centrifugal instability. These perturbations then allow exchange of momentum along the radial direction by the transport of fluid thereby balancing the deficit in the pressure gradient to counteract the centrifugal force. This rapid generation of streamwise vortices is also enhanced by the degeneration of spanwise coherent vortices which have already entrained a portion of the recirculating streamwise vortices.

The location of maximum deceleration relative to the flow geometry is marked in Fig. 4.33b. The position is not exactly on the slat trailing edge but slightly upstream, the exact location being dependent on the choice of streamline. Nevertheless, the marked position is the location of the maximum deceleration experienced by a fluid particle moving along the streamline and is hence the location of maximum momentum transfer. In view of the theory that impingement of vortices is responsible for the generation of acoustic waves that modulate the K-H shedding frequency at the cusp and thereby select the tonal noise frequency, this location must correspond to the length of the shear layer that predicts the tonal noise frequency. To understand this further we look at the actual velocity distribution along the streamline and compute the time of travel.

The time required for the spanwise eddy to reach the location of maximum deceleration can be obtained as $t_S = \int^S \frac{ds}{V(s)}$. The total time is then obtained as sum of t_S and the acoustic propagation time from the location of impingement to the source point of the streamline. This calculation leads to total time of 1.213 ms corresponding to a frequency of 824 Hz.

To compare this frequency to the theoretical model, the tone prediction formula of Terracol et al. [14] has the simplified form

$$f_n = n \frac{U_\infty}{L_a} \cdot \frac{1}{\mathcal{M} + \frac{\alpha_l}{\kappa_v}}$$

where L_a is the acoustic path length, α_l is the ratio of length of the shear layer to the acoustic path between the impingement location and the cusp and κ_v is the ratio of vortex convection velocity of

vortices along the shear layer to the free stream velocity. Here, the vortex convection velocity is not calculable from a mean flow solution and for our study we resort to the value obtained for the same case by Terracol et al., i.e. $\kappa_v = 0.79$. Based on the location of maximum deceleration, the acoustic path length is obtained as $L_a = 0.0326\text{ m}$, and the vortex path length along the shear layer as $L_v = 0.0387\text{ m}$, leading to $\alpha_l = 1.187$. The resulting fundamental tone corresponding to $n = 1$, is then at $f_1 = 928\text{ Hz}$ and the multiples being [1856, 2784, 3712, 4640, and 5568] Hz. These frequencies are higher than the experimental tone frequencies [1771, 2655, 3540, 4425, and 5310], and hence suggest that the location of maximum deceleration is a location slightly too early than the actual location of the acoustic generation. However, Terracol et al. [14]’s formula is highly sensitive to the computation of the shear layer path length, and hence on the location of the acoustic generation, lending high level of uncertainty in the tone calculation using this method. Moreover, for the same calculation, a correction of the convection velocity factor to $\kappa_v = 0.75$ can lead to a more accurate prediction of the frequencies.

Now we inspect the curvature of the streamline further, more in line with work of Bradshaw [139]. His analogy of the streamline curvature with a stratified flow under the effect of buoyancy led to formulation of representative parameters. One of these, pertinent to interpretation of the slat shear layer, is the flux Richardson number. By the analogy, for flow along a curved streamline, it is the ratio of turbulent kinetic energy production between the radial direction and the streamwise direction, i.e.

$$R_f = - \frac{\text{extra } v^2 \text{ production}}{\text{sum of } u \text{ and } w^2 \text{ production}}$$

where \bar{u} is conventionally the streamwise velocity, \bar{v} is the velocity in the cross-stream direction across the streamlines, and \bar{w} is the spanwise velocity. Bradshaw and Young [140] obtain a form of the flux Richardson number inspired from the work of Wyngaard [141], as

$$R_f = \frac{2\frac{U}{R}}{\frac{\partial U}{\partial R} + \frac{U}{R}} = \frac{2U}{\frac{\partial}{\partial R}(UR)} \quad (4.1)$$

This form was then re-derived later by Liou [128] while studying the stability of curved free shear layers in small curvature regime. The generation of vorticity in the streamwise direction, in their perspective, is an effect of the diffusion of the turbulent velocity perturbation into the streamwise direction led by the effect of the centrifugal force and hence arises from the requirement of inviscid stability. The flux Richardson number aids in quantifying the effect of this imposed vorticity transfer by taking into account the effect of the centrifugal force acting on the flow and also the local vorticity thickness by incorporating the radial streamwise-velocity gradient $\frac{\partial U}{\partial n}$. In this regard, we extrapolate the existing perspective as follows:

It is well understood from the literature that the streamline curvature along a shear layer can lead to additional instability arising from the centrifugal effects. This leads to the generation of streamwise vortices across a wide range of Reynolds numbers. The effect of curvature is such that there is a generation of streamwise vorticity which is cumulative in the sense that this accumulation of streamwise vorticity happens as long as the Rayleigh criteria holds, i.e. with a reduction of the angular momentum radially outward from the center of curvature. The cumulative effect of this curvature can be captured by the total transfer of momentum due to the additional centrifugal force in action, or as the work done by the same. The instantaneous momentum transfer, M_c , effected by the centrifugal force while the fluid traverses a curved path ds with a local radius of curvature R , traversing with a streamwise velocity U , is equivalent to

$$d\Theta_c = \frac{U^2}{R} \frac{ds}{U} = \frac{U}{R} ds$$

where U is the velocity component along the streamline, and in the vectorial sense of the centrifugal force, the direction of this momentum transfer is invariant as the direction radially outward from the center of curvature. The resulting term $\frac{U}{R}$ is hence the effective density of total momentum transfer due to the centrifugal force along the path length. Thus the curvature Richardson number of the form in Eq.4.1 effectively capture the effect of the centrifugal force in its momentum transfer leading to the generation of streamwise vorticity. The same term is used in the curvature Richardson number together with the cross-stream velocity gradient, $\frac{\partial U}{\partial R}$. In case that the shear layer has a strong velocity gradient such that $\frac{\partial U}{\partial R} \gg \frac{U}{R}$, as in the early part of the slat shear layer, or in the case of a plane shear layer, the curvature Richardson number approaches zero. However, in the region where the shear layer weakens, and the curvature is finite such that $\frac{\partial U}{\partial R} \ll \frac{U}{R}$, the curvature Richardson number will tend to increase and saturate at 2. For the case of applying the linearized equations to study effects of a slightly curved free shear layers, Liou [128] used a Richardson number of the order of 10^{-2} . However, for the case of slat shear layer, the curvatures are at least two order of magnitude higher and hence is expected to be highly non-linear in its dynamics.

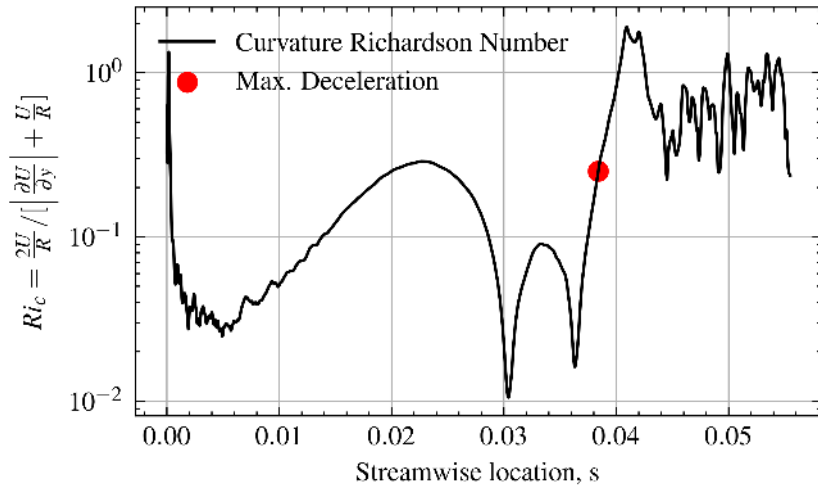


Figure 4.34: Local curvature along a streamline in the shear layer

The local curvature Richardson number along the streamline is shown in Fig.4.34. The Richardson number can be seen to have a low value in the early shear layer due to the high value for the strain rate. As the shear layer spreads, the curvature Richardson number tends to increase, suggesting the strong momentum transfer due to the centrifugal force. In the mid-region, the curvature reduces as the shear layer inverts its direction of the curvature towards the unstable configuration, and the Richardson number hence drops. Afterwards, the curvature Richardson number increases as the shear layer spreads due to growth of the spanwise eddies along with entertainment of streamwise vortices. The curvature Richardson number then tend to saturate towards 2 in the region immediately downstream of the location of maximum deceleration, owing to the large value of curvature.

The case considered here is the standard geometry with standard position of the slat with respect to the airfoil. This configuration showed strong presence of the broadband acoustic spectra and tonal noise owing to the fact that the spanwise coherence of the shed vortices from slat cusp is not fully disintegrated by the time of their travel towards the trailing edge. This owes to the fact that the curvature Richardson number rises to a strong value only near and downstream of the location of maximum deceleration suggesting that the flow did not accrue a large enough effect of the centrifugal destabilization, as it would have been the case if the flow developed a larger curvature Richardson number further upstream of the impingement

location. This means that although the effect of centrifugal instability is substantial in generating the streamwise turbulence, it is not sufficient to cause a complete degeneration of spanwise coherence to disable the aeroacoustic resonance.

4.8 Acoustics

Acoustic perturbations are essentially perturbations of the pressure field arising from compressibility and translate to equivalent density perturbations. By the continuity equation, the density perturbation can be written in terms of the divergence of the velocity field as

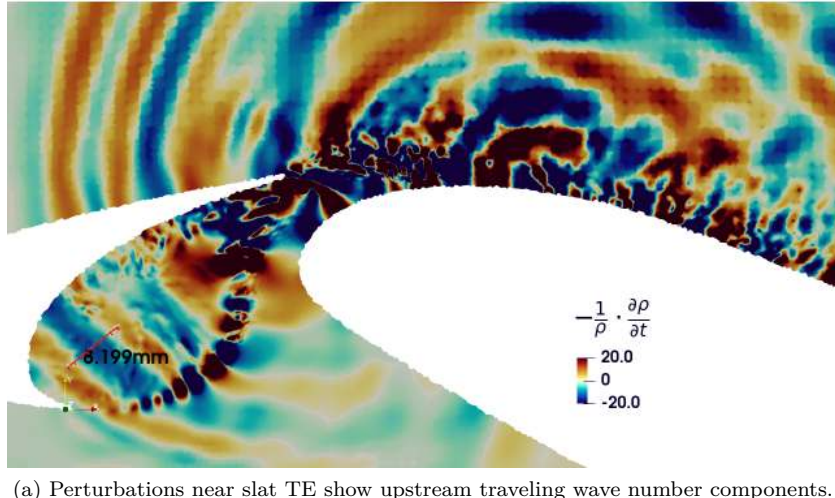
$$\Theta = -\frac{1}{\bar{\rho}} \frac{D\rho}{Dt} = \nabla \cdot \mathbf{u}$$

where $\frac{D}{Dt} = \frac{\partial}{\partial t} + \mathbf{u} \cdot \nabla$ represents the material derivative and Θ is called the dilatation field[142]. Within turbulent flows, the dilatation field has two components due to the hydrodynamic and acoustic fluctuations. The former are large magnitude perturbations that witness slight hydrodynamic compressibility that might contribute or not to sound radiation whereas the latter are small magnitude perturbations that represents the propagation of sound. Although vastly differing in their order of magnitudes, separating the two is still a non-trivial procedure[143]. But the emanating acoustic wave fronts can be identified in the region outside the turbulent region where sound generation is absent. The typical dilatation field around the HLD as obtained from the unsteady simulation is shown on the snapshot of Fig.4.35. The wave fronts emitted from the slat cove are identifiable from the dilatation field towards both the suction side and the pressure side, latter being towards the ground observer. The major acoustic source region can be identified as the slat cove and the trailing edge of the main-element. The trailing edge of this HLD, must be recalled, is obtained by replacing a TE flap in order to reduce lift[14]. Hence the noise generation from the trailing edge is not covered in our study since it is found to have no interference with the slat cove acoustics.



Figure 4.35: Dilatation field over the HLD from the unsteady data

The slat cove radiation can be noticed to have characteristic directivity[98]. The radiation towards the pressure side is seen to radiate from the region close to the slat gap, and for the radiation to the



(a) Perturbations near slat TE show upstream traveling wave number components.

Figure 4.36: The unsteady dilatation field is visualized using the normalized time derivative of the density, $-\frac{1}{\rho_0} \frac{d\rho}{dt}$. This representation is strictly valid only in the absence of mean convective flow, where the material derivative reduces to the temporal derivative.

suction side, the source appears to be located within the slat cove. There also exist a region with acoustic shadow in the upstream of the slat since the geometry shadows the radiation unless the wave number is small enough to enable diffraction.

The dilatation field also has drawbacks visualizing data on the grids with refinement interfaces. At the refinement interface, the calculation of derivative introduces numerical errors, which are not necessarily unsteady. Hence the errors does not necessarily lead to generation of spurious acoustics but vitiates the acoustic field visualization. An improvement in this regard is hence possible by using an alternative definition for dilatation as the density rate. For isentropic fluctuations of small amplitudes in an otherwise quiescent media, the dilatation can be expressed as the rate of pressure fluctuation as

$$\Theta = -\frac{1}{\rho_0} \frac{\partial P}{\partial t}$$

where ρ_0 is the ambient mean density. The pressure rate being a temporal derivative also removes its local steady component. A visualization of the density rate field in the slat cove vicinity is shown in Fig. 4.36a. The acoustic field thus visualized shows majorly high frequency wavefronts which have an approximate wavelength of $\lambda = 0.008$ m. This corresponds to acoustic waves of frequency higher than 50kHz . It hence suggests that the wavefronts visible in this visualization are also strongly vitiated by the high frequency numerical noise which are amplified by the temporal derivative.

Filtered pressure fields

To study the acoustic modes of particular frequency, the unsteady pressure fields can be bandpassed to extract relevant frequencies only. For this we choose to apply the filter for the pressure field on a 2D plane recording around the slat cove region for frequencies corresponding to the broadband hump at the 885Hz, and the tonal peaks at 1771, 2655, and 3540Hz. The Fourier transform and corresponding inverse transform at single frequencies were done using the python package NumPy. The visualization of the filtered fields are shown in Fig.4.37. The left side plots highlight the hydrodynamic pressure fluctuation at the select frequency inside the cove region, and right side plots highlight the acoustic field around the HLD over a larger domain. A better separation of the flow fields are not possible using FFT related tools available at the moment.

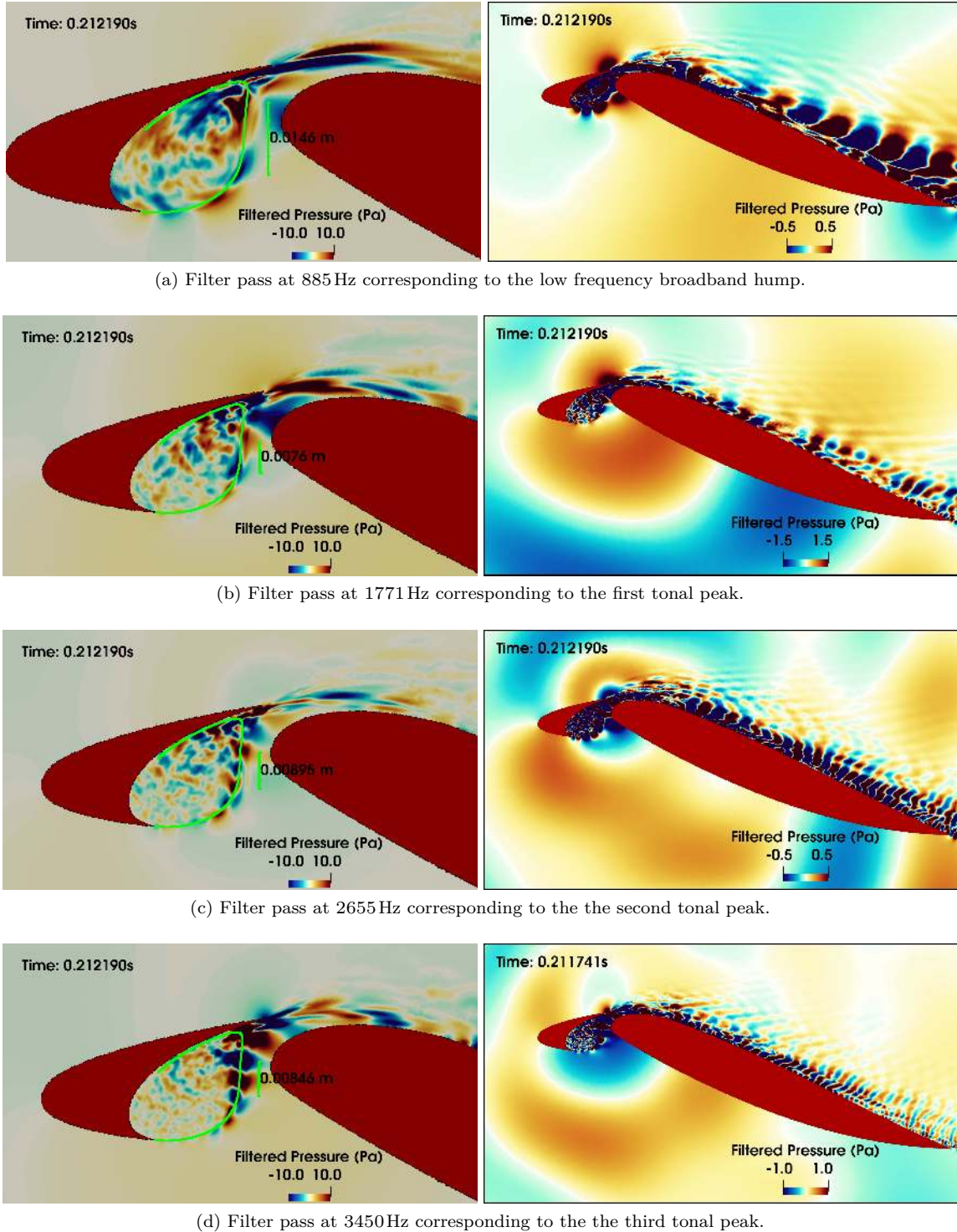


Figure 4.37: The Fourier filtered pressure fields at a select frequencies corresponding to the peaks in farfield spectra. The visualization is for a spanwise central plane, and the streamline along which the vortex path is extracted from mean flow is shown as green line and corresponding wavelengths for the traveling waves are also annotated

From observing the dynamics of the filtered fields, the following observations can be made:

1. The hydrodynamic pressure in the slat cove for all tone frequencies of 1771 Hz and above extracted shows a spatially growing wave along the shear layer. These waves represent the pressure fluctuation induced by the convected vorticity of spanwise coherent structures generated near the cusp. The mode structures convect at the corresponding phase velocity.
2. The hydrodynamic oscillation at the slat TE for 885 Hz shows persistent elongated lobes along the shedding direction. These lobes represent pressure fluctuations that due to the vortex shedding and is responsible for the flapping motion of the shear layer at the slat TE.
3. The acoustic fields show that a dipole like source can be safely assumed on the slat trailing edge. The radiated field can be clearly identified to have opposing phase centered at the slat TE. The axis of the dipole is also observed to be aligned with the local normal to the slat TE wall at the edge. The radiation towards the suction side can be identified to have dipole like radiation pattern, but the pressure side lobe is strongly distorted by the shape of the cove. The hydrodynamic component present at the TE also mask the acoustic radiation at the slat TE at the inner side making clearer discernment difficult.

4.9 Spanwise Trends in Wall Pressure Data

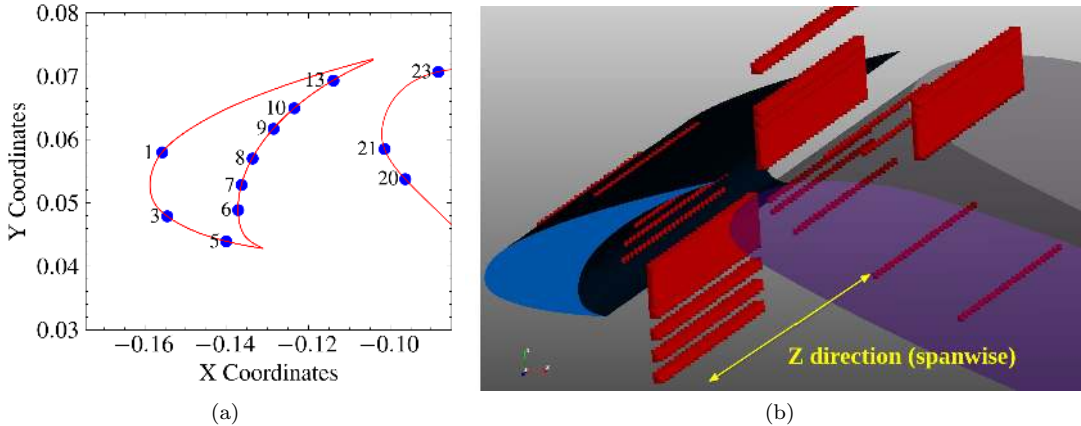


Figure 4.38: a) Select wall pressure probe coordinates on the slat. b) Spanwise replicated numerical probes and the slat geometry.

The wall pressure probes used to record the unsteady pressure fields in the simulation are analyzed next with the particular aim to study their spanwise behavior. The very low frequency oscillations inside the cove are suspected to be the result of the modes induced by centrifugal modes which are also accompanied by the spanwise cell formations. To understand this further, plots of the spectra along the spanwise direction is given in Fig.4.39 for probes 6, 7, 8, 9, and 10, from Fig.4.38a. Each of these probes are replicated along the spanwise direction as illustrated in Fig.4.38b and a function spectra is plotted as function of the spanwise coordinate. The mean pressure from these probes for the computed PSD are also shown on the right side to shed light on the correspondence between the spanwise trend of spectra and spanwise cell formations.

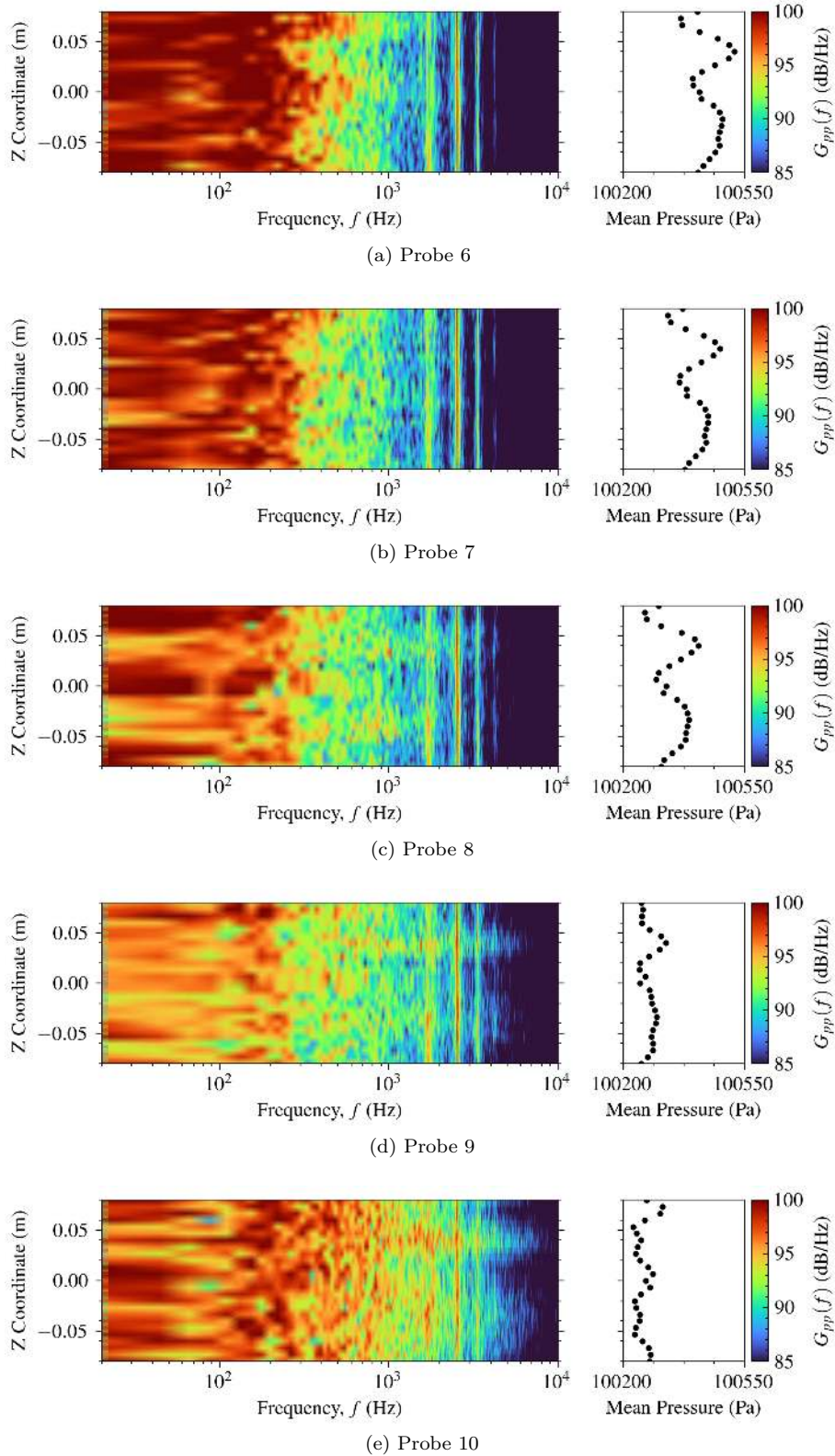


Figure 4.39: Wall pressure spectra from spanwise replicas of probes on spanwise center plane showing variation of spectra along the span. Corresponding time-averaged pressure for the probe recording is also shown to identify the spanwise cell locations

From inspection of data of Probe 6 and its replicates, as shown in Fig.4.39a, it can be noted that the spanwise modulations are reproduced in the low frequency part of the spectra particularly above 200Hz and below 1000Hz. The spectra in this region tends to have stronger levels for spanwise locations that correspond to pressure locations which are at the diverging plane of the spanwise velocity field. Probe 6 location being close to the slat cusp with spanwise modulation at low frequency verifies the hypothesis that spanwise nodal planes are stronger and driven by the initial curvature of the shear layer. It also further suggests that there are low frequency fluctuations particularly associated with such planes.

For other probes, namely Probe 7 which is adjacent to Probe 6, but deeper into the cove from the slat cusp, the spanwise modulation in the wall pressure spectra becomes less pronounced. This is expected from the shape of the spanwise velocity contours which shows that the cells near the slat cusp region is closer to the shear layer than the wall and also transition to the upper chain of cells as we move along the inner wall of the slat. The modulation again gathers strength for Probe 8 and 9, also with a lowering of the low frequency contents. As we move further towards the impingement location with Probe 10 and 13, the low frequency contents again becomes dominant due to the possible contribution from low frequency fluctuations associated with strongly curved flow at the impingement location.

Apart from the spanwise modulated behavior, the presence of the tones at 1771, 2655, and 3450Hz can be seen to be present irrespective of the spanwise location. The first tonal peak at 1771Hz however seems to be more susceptible to the spanwise modulations particularly for Probes 8, 9, and 10. For the low frequency hump at 885Hz, the wall pressure spectra is not able to provide a clear identification, although for probes outside the cove, namely Probe 3, 5, and 19, this hump is distinctly identifiable.

We now proceed to inspect the numerical hot-wire probe data.

4.9.1 Hot-Wire Probes

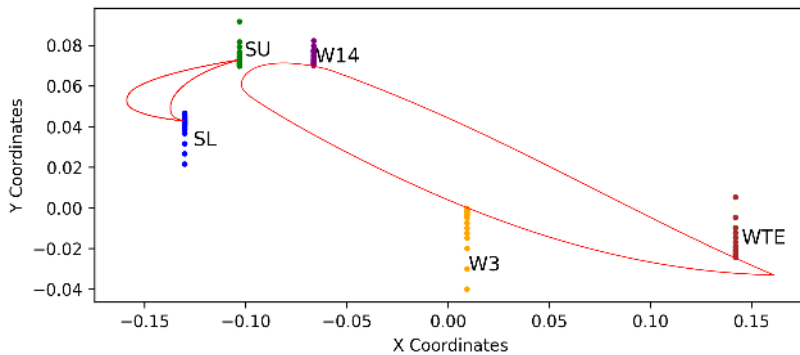


Figure 4.40: Hot-wire probe locations used for point recordings in the simulation

The hot-wire probe data allows to analyze single point time series recording of the flow velocity. The point recording captured from LBM simulation at selected nodes are hence analogous to the hot-wire measurements in the experiments and are typically used to compare the experiment and simulations. Here they are used to study spanwise variability of the flow.

Various groups of probes are used to obtain the velocity fields near the cusp, near the slat trailing edge, and on few select locations on the main element wall. We intend to call these probe groups as files and their positions are shown in Fig.4.40. Among these we first analyze the file placed near the cusp across the early shear layer, capturing the variation of turbulent velocity field from outside of the cove flow to its interior. For this, first the mean velocity magnitude is plotted as shown in Fig.4.41a. The

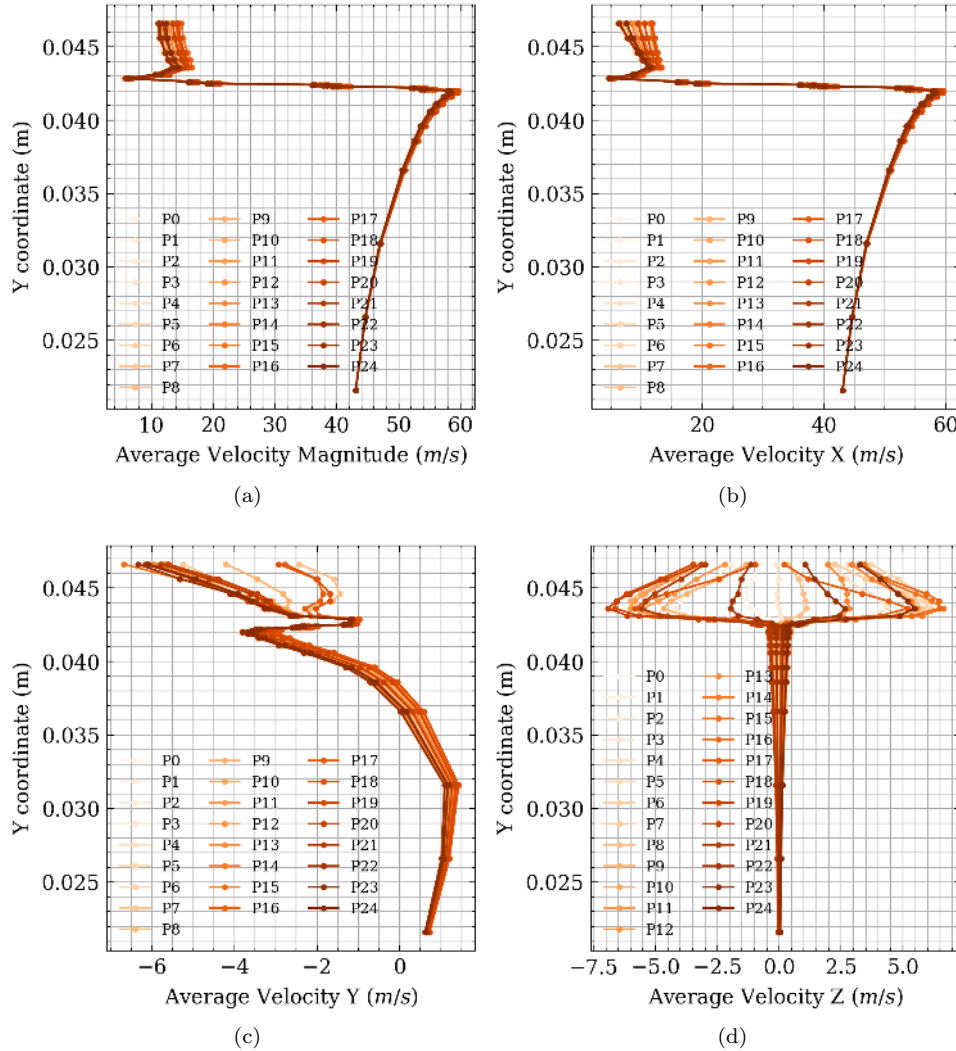


Figure 4.41: Time-averaged velocity and components from the SL probe file placed near slat cusp. P0 to P24 represent the 25 spanwise replication of the SL file and each curve represent the velocity profile as each spanwise location. a) The velocity magnitude profile is uniform along the span, b) The streamwise velocity is also uniform along the span, c) the cross-stream velocity in the 2D plane of the airfoil cross section is also largely uniform along the span, and d) the spanwise component of velocity shows uniformity along the span but has an alternating profile inside the shear with an amplitude of $\approx 15\%$ of the velocity magnitude.

time-averaged velocity magnitude profile shown in Fig.4.41a concurs with the mean inflow velocity of 50 m/s, and the deceleration due to presence of the main-element outside of the cove region. The mean recirculation velocity near the cusp is obtained as 15 m/s, which also concurs with Fig.4.31b. The velocity magnitude profiles are also largely spanwise invariant outside the cove and have a deviation of ± 5 m/s inside the recirculation.

The profiles for all velocity components are also shown. For the spanwise component shown in Fig.4.41d, the region outside the cove region shows negligible variation whereas for the region inside the cove, the velocity switched signs with a peak amplitudes of 7 m/s, suggesting that the spanwise modulation is the main contributor to total velocity modulation along the span. The alternating averaged spanwise velocities correspond to the spanwise cells previously demonstrated in Fig.4.10 and is an additional characterization uncovering their structure.

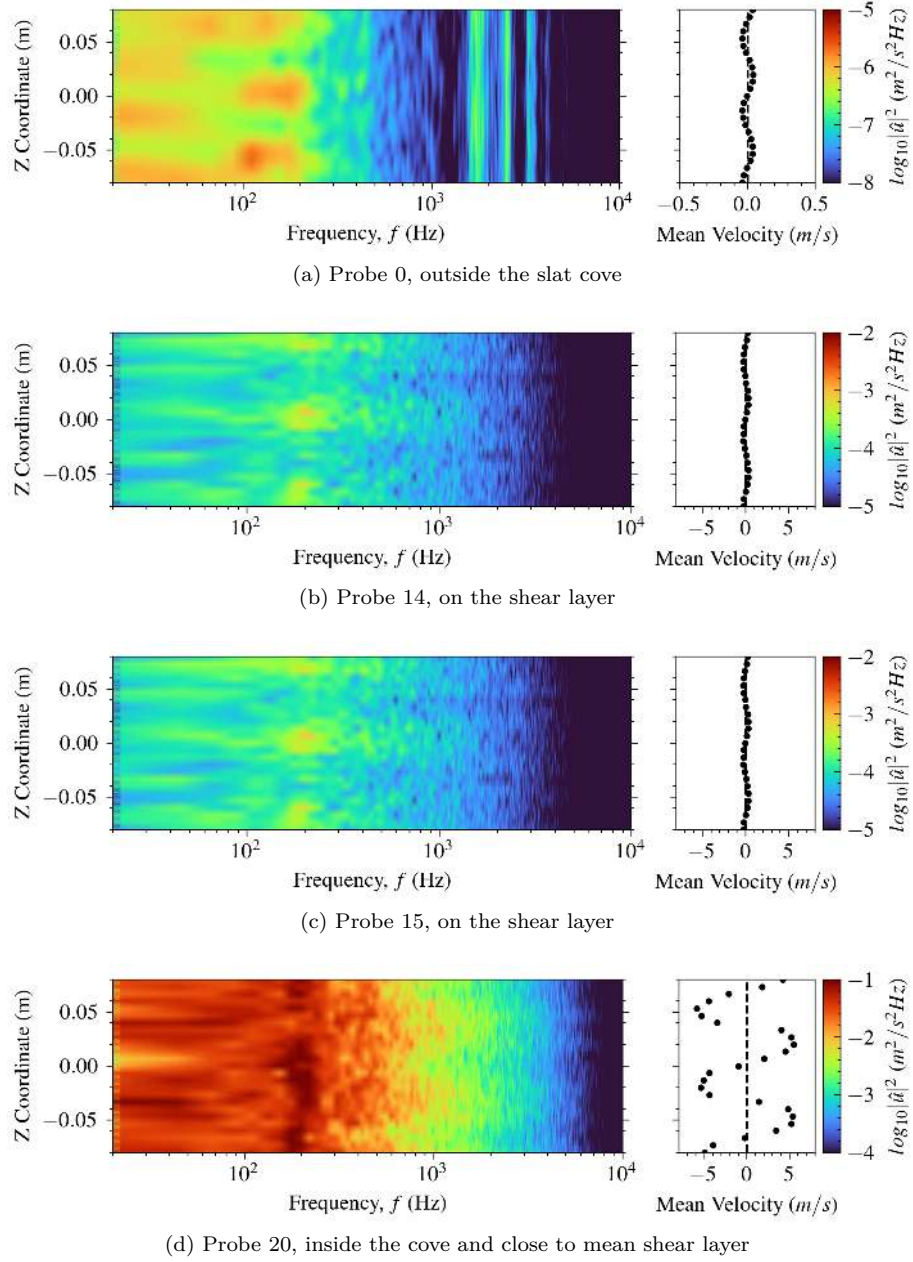


Figure 4.42: Unsteady velocity spectra from spanwise replicas of probes close to slat cusp. Corresponding time-averaged spanwise velocity for the probe recording is also shown to identify the spanwise cell locations

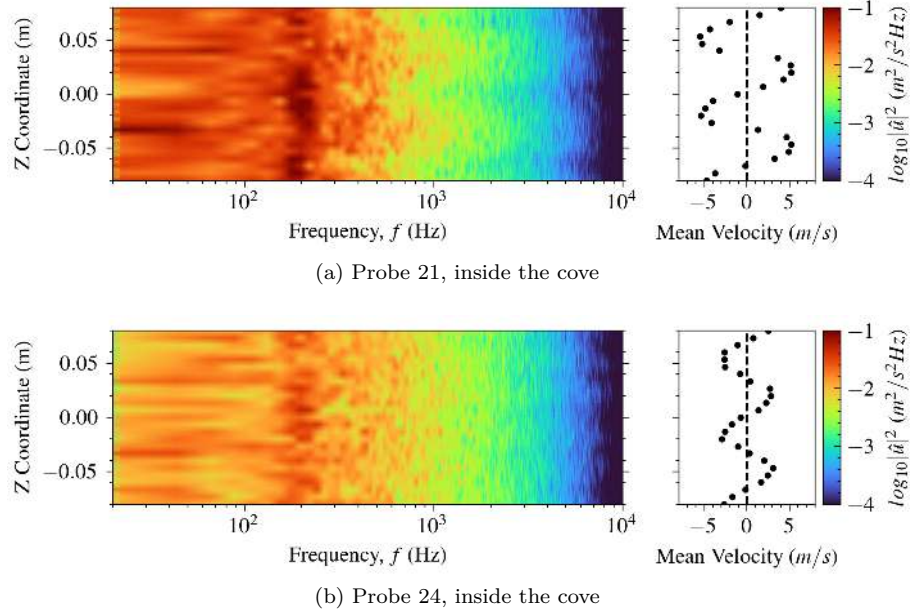


Figure 4.43: Unsteady velocity spectra from spanwise replicas of probes close to slat cusp. Corresponding time-averaged spanwise velocity for the probe recording is also shown to identify the spanwise cell locations

The modulated velocity spectra for the spanwise component U_z are shown in Fig.4.42 and 4.43. For the case of Probe 0 positioned outside the cove as shown in Fig.4.40, the fluctuation related to tonal peaks in the acoustic spectra can be identified for 1771Hz and above. The low frequency hump at 885Hz is however absent. For probes 14 and higher, it can be noted that the spanwise velocity shows a consistent oscillation between 200 – 300Hz across multiple probe locations along the span. For Probe 14 and 15, shown in Fig.4.42b and 4.42c, the peaks corresponding to acoustic frequencies are hardly distinguishable but instead hot spots for a frequency of 200Hz can be noticed. The hot spots appear strongest at spanwise location where the spanwise mean velocity switches sign from negative to positive suggesting that this location is a diverging plane. The periodic oscillations are interestingly absent in the locations of the converging planes where the fluid is removed from the spanwise motion potentially entrained by the shear layer. This suggests that redistribution mechanism arising from presence of nodal planes tend to develop a low frequency pulsating behavior with which the initial shear layer bursts periodically. This low frequency bursting is also consistent with the behavior identified by Brès and Colonius [3] in the case of rectangular cavity flows.

Such a periodic bursting if present may affect the acoustics. Since the Rossiter mechanism is driven by the impingement of spanwise coherent vortices at the slat trailing edge, the retained spanwise coherence is a necessary factor for exciting a strong resonance. The periodic disruption of the spanwise coherence of the early vortices thereby affects the resulting acoustic tones through an amplitude modulation. Furthermore, for Probe 20, which is placed deeper into the cove inside the shear layer, the spectral content shows increased activity at the same frequency of 200Hz. Here the averaged spanwise velocity modulation is also with a higher amplitude approximately 7m/s, thereby having a higher power level for the low frequency fluctuations including 200Hz. The higher energy levels at 200Hz for this location is clearly distinguishable from neighboring frequencies as shown in Fig.4.42d.

Additionally, the modulation of spanwise velocity biased towards the interior of the shear layer also agree with the hypothesis that this additional spanwise modulation and its associated low frequency fluctuations are predominantly the effect of curvature, since it is known from the work of Liou [128] that

for the case of a mildly curved shear layer, the spanwise eigen modes have predisposition to shift to the low velocity side of the shear layer. See Fig.9 in Liou [128] for further clarity. Here the lower speed side correspond to the interior of the shear layer towards the center of recirculation.

For Probes 20 and 21 shown in Fig.4.43a and 4.43b, the spanwise modulation of the frequency range between 700Hz and 1000Hz are also notable. This also suggests that there is a spanwise inhomogeneity in the hydrodynamic fluctuations at 885Hz. However, this frequency is clearly the first Rossiter mode since it matches with the theoretically calculated first mode based on the vortex and acoustic travel times.

4.10 Cove bursting as a modulating mechanism

One key ingredient in understanding the subsequent effects of such a cove bursting is in the fact that the bursting occurs at the diverging planes. Since the velocity is diverging, the generated streamwise vortices are convected either by the positive velocity or by the negative. By nature of turbulent flow, the bursting location is located more frequently at the center and hence the convection direction is selected in a stochastic manner. Consequently their location of impingement at the trailing edge of the slat also varies in the same fashion. This is precisely the phenomena noted in the recent work of Wei and Liu [144] where spanwise location of the tonal sources shows intermittent variations along the spanwise locations at the slat trailing edge. Our demonstrations hence provides a plausible explanation on what fundamentally drives this dynamics.

Moreover, the Rossiter mechanism selects the frequencies based on the number of vortices that are shed which upon impingement are able to close the aeroacoustic loop. This means that if there is a periodic disruption of spanwise coherence, select Rossiter peaks would be affected depending on the frequency of the modulating oscillation, while the vortex shedding at other frequency multiples can remain intact. One direct evidence of such a periodic disruption of spanwise coherence is that the acoustic waves formed by impinging vortices which drives the Rossiter mechanism will show an amplitude modulation in time. The amplitude modulation will then lead to non-linear transfer of energy between the tonal frequencies, and is also a popular phenomena is slat noise, though unexplained. Here the first broadband hump which corresponds to the first Rossiter tone is weaker in the sound level compared to the second tone, and is not evident in the VALIANT experiment against installation noise. This peak also shows intermittent behavior according to Jawahar et al. [4] for measurements in the wall pressure measurements. A further investigation of the farfield spectra observed by Jawahar et al. [4] shows that the low frequency broadband humps shows two symmetric shoulders on its sides, as shown in Fig.4.44, within a frequency range of approximately $\Delta St_s = 0.12$ on both side of its central frequency. We here theorize that this appearance of shoulders for the broadband low frequency hump is the result of the first Rossiter mode (corresponding to the BB hump) being amplitude modulated. The effect of amplitude modulation of a signal leading to development of additional symmetric peaks in the spectral domain corresponding to frequencies $F_{peaks} = F_c \pm F_s$ around the carrier frequency F_c by the modulating signal frequency F_s is a canonical phenomena in signal processing. Correspondingly, an estimation of the Strouhal number for modulating frequency of 200Hz for the given slat chord yields $\Delta St_s = 0.16$.

Here, the Strouhal numbers for the Rossiter tones are dependent on the shear layer path length. Following the hypothesis that the low frequency oscillation is due to the effect of mass flow disparity, the Strouhal number for the low frequency oscillation is not necessarily linked to the shear layer path length but related to the difference of velocity, $\Delta U = U_0 - U_i$, between the inner cove and the free stream and also to the length of spanwise cells λ_s . Thus, if the frequency of the cove bursting is f_B , then $f_B \propto \Delta U$ and $f_B \propto \frac{1}{\lambda_s}$, then $St_B \propto \frac{\Delta U}{\lambda_s} \times \frac{C_s}{U_\infty}$. However, the spanwise cell wavelength is proportional to the slat

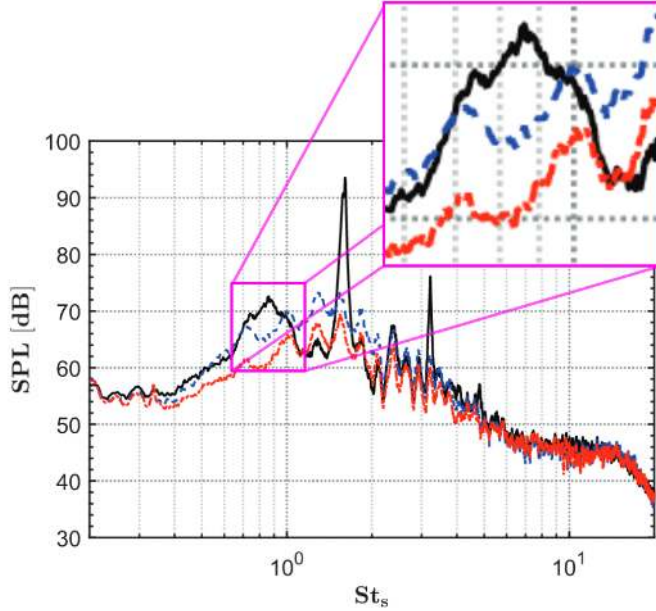


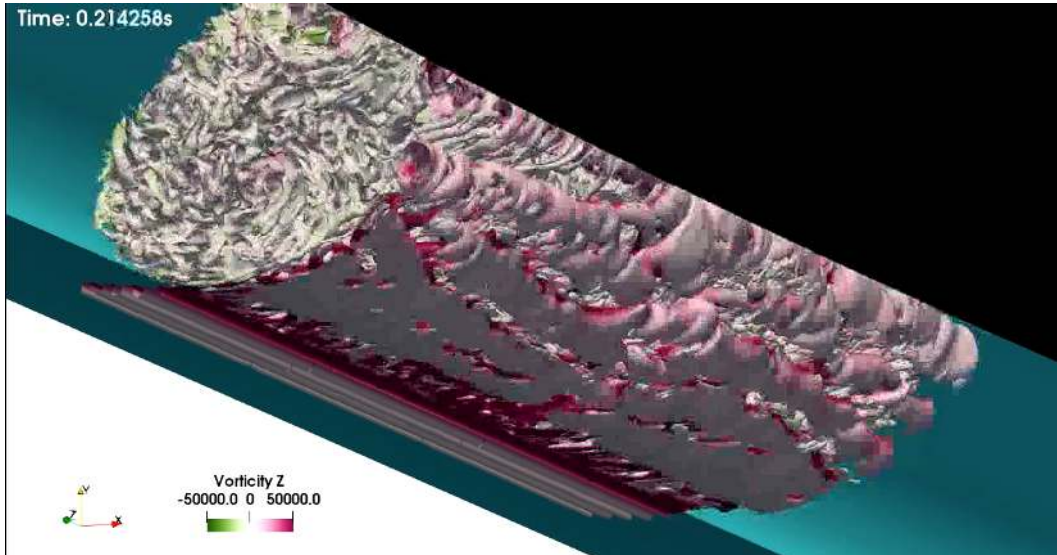
Figure 4.44: The farfield spectra from experimental study of Jawahar et al. [4] for the 30P30N HLD geometry. The experiment had a free field velocity of 30m/s, $Re = 7 \times 10^5$, and a span to chord ratio of 1.5. The low frequency broadband hump shown in the inset correspond to the first Rossiter mode and can be noted to have the shoulder frequency corresponding to $\Delta St = 0.12$. This is conjectured to arise from the low frequency modulation of the first Rossiter mode due to the spanwise mode formation and resulting low frequency bursting of the early shear layer demonstrated in this chapter

chord as suggested by Brès and Colonius [145], then St_B would reduce to

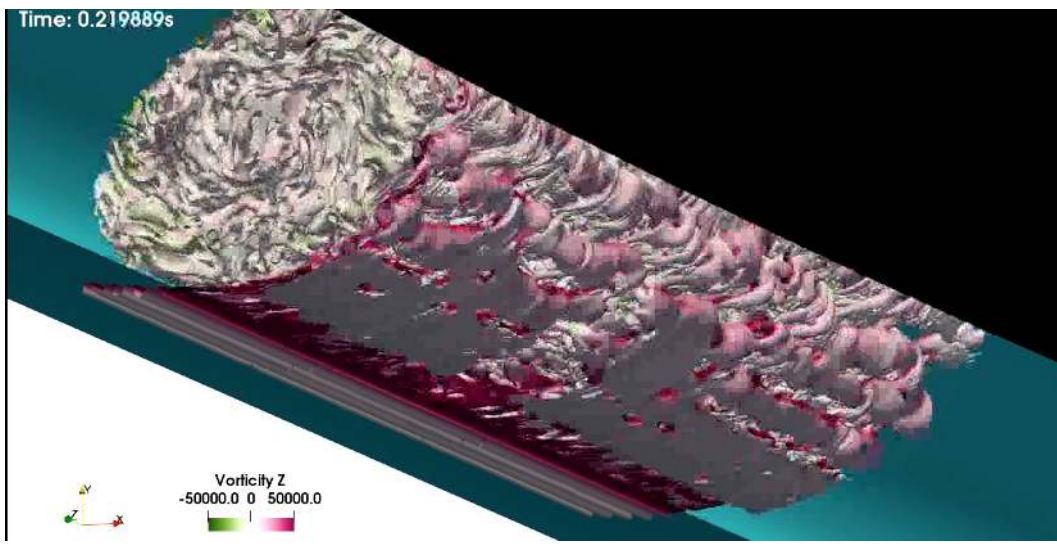
$$St_B \propto \frac{\Delta U}{U_\infty} \propto 1 - \frac{U_i}{U_\infty}$$

where U_i is the velocity of recirculation. Hence Strouhal number for the bursting phenomena can be reasonably assumed to be dependent only on ΔU , the velocity difference across the initial shear layer. Nevertheless a more rigorous approach on extracting a model for this Strouhal number requires precise knowledge of the dependence of spanwise cell size based on the slat chord.

Furthermore, from the inspection of data recorded from the high fidelity simulation, the vortex visualization enables to identify the cove bursting. For this, we increase the Q-criterion value used to obtain the iso-contours to obtain a smooth cover of the region of initial shear layer such that a bursting of this spanwise coherent isocontour, itself arising from the spanwise vorticity of the early shear layer, can be identified. Snapshots of the flow separated in time by a time interval of 0.005s corresponding to the frequency for 200Hz are shown in Fig.4.45. It can be noticed that the spanwise coherence of the shear layer is burst in a quick burst of streamwise vorticity formation which is then convected along the shear layer. The generated vortices also gain a spanwise velocity corresponding to the position of the bursting, i.e. the vortices from the bursting are carried by the positive or negative spanwise velocity depending on the proximity of such vortices to the negative or positive velocity cells in the initial stage. This suggests that the position of the bursting is only approximately static in the very early shear layer, and towards the impingement location the location of vortices from the bursting can be highly chaotic. This is only of significance if there is a sufficient difference of characteristic between the region of vortices from bursting and the slurry of streamwise vortices already present towards the impingement location.



(a) Time stamp 0.214s



(b) Time stamp 0.219s

Figure 4.45: The cove bursting near the mid-span diverging plane at time stamps separated by 0.005s corresponding to the 200Hz peak in the numerical hot-wire probe data

4.11 Conclusion

In this chapter, we presented the numerical investigation and major findings specific to cove dynamics and noise mechanisms for VALIANT geometry HLD. The airfoil was kept at an angle of attack at 18^0 against an inflow of 50m/s at a chord based Reynolds number of 10^6 [14]. The slat positioning was kept as standard.

The objective of the study was to investigate the details of data generated using unsteady 3D LBM for the slat cove flow and to revisit existing knowledge on its noise mechanism. In line with this, the unsteady visualizations of the cove vortices using Q-criterion was obtained and the behavior of spanwise coherent structures and their conversion to small scale streamwise structures were discussed. The generation of streamwise structures were shown to be possibly influenced by the curvature instability of the shear layer which augments the current understanding of their behaviors. Detailed visualizations were used to suggest that the vortices are generated from the outer periphery of the spanwise coherent structures and that a major fraction of the recirculated vortices are entrained and consumed by the spanwise coherent vortices from the early the shear layer.

On inspecting the mean flow contours of the velocity and pressure fields in the cove, the 2D flow components largely agreed with the existing knowledge of slat cove dynamics. However, the distributions of spanwise velocity rendered strong spanwise modulations which called into question the veracity of a spanwise homogeneous flow typically assumed for the configuration in both experiments and numerical simulations. The spanwise velocity modulation with amplitude upto more than 10 of the mean stream velocity was observed in the simulation which used a spanwise domain length of more than $5C_s$ and $0.66C$, where C_s is the slat chord length and C is the stowed chord of the full HLD.

To establish that the modulation is not an artifact of the simulation due to application of the periodic boundary condition, a simulation of the original wind tunnel geometry along with the lateral supporting plates were used. Here, the flow around the HLD was typically expected to be spanwise homogeneous in the region which is free from the influence of the wall in the experiment. But counter-intuitively this region was found to have a length of $0.2C$. However, the presence of spanwise modulations were also strongly disrupted by the presence of wall related turbulence for the rest of the span. Hence it is inferred that the presence of spanwise modulations is not a numerical artifact of the simulation but an effect of the centrifugal force due to the recirculating motion in the cove. To further the argument, two other simulations, one with a reduced span length by a factor of 0.5 and another with a subsized geometry with the chord scaled by a factor of $\frac{2}{3}$ are also presented. Both the cases are also shown to retain the spanwise cell formation with the latter having a higher spanwise wave number for the modulations demonstrating that the feature responds to the geometrical conditions.

On further investigation of the mean flow distributions, it was inferred that the spanwise modulation of velocity leads to generation of converging and diverging 2D planes. At these planes, if we move along the positive spanwise direction, spanwise velocity switches signs. For those which switches the velocity from negative to positive are what we refer to as the diverging planes and they act as a source of the fluid for spanwise flow. The vice-versa is true for the converging planes which act as the sinks enabling entrainment of flow into the flow exterior to the recirculation. Such a configuration was shown to distort the pressure field in the cove such that the low pressure center of recirculation (time-averaged) generated due the centrifugal effect is not spanwise homogeneous, but deflected towards the shear layer at the location of the diverging nodal planes.

The spanwise variation of the velocity spectra for the spanwise component then revealed that there exists an oscillation at 200Hz, corresponding to $St \approx 0.156$. These periodic oscillations since occurring at the diverging planes only at the early share layer can potentially affect the spanwise coherence of

the shed eddies. Moreover, the streamwise vortices generated in this oscillation are convected towards both spanwise directions from the diverging plane in a stochastic manner. The latter phenomena is thus suggested as a plausible reason for recently discovered stochastic nature of the spanwise coherence location, trailing edge turbulence characteristics, and the non-linear interaction between the slat tones.

Thus, based on the above inferences, we suggest in this chapter that the spanwise modulation of the spanwise velocity present in the slat cove have a non-trivial impact on both the cove vortex dynamics and their acoustic signature. The problem of spanwise mode generation itself is sparingly attended in the fluid dynamics literature although the same has been noted, intrigued on, and partially characterized in the works including that of Barkley et al. [2], Albensoeder et al. [146], and Brès and Colonius [145]. The low frequency oscillation mechanism connected to spanwise modes and their interaction with the recirculating 2D flow can be noticed in the recent exhaustive review of cavity flows by Hamilton Smith et al. [76]. A further investigation of these phenomena is an interesting topic of future research and can be undertaken by fundamental analysis of the behavior of the Navier-Stokes equation under the effect of strong curvature of a shear layer which bounds a region of recirculation. For its implications for slat noise, it is clear from this demonstration that experimental investigations which use 2D PIV and hotwire measurements at the spanwise center-plane will not be able to capture the spanwise mode formations. This explains why the stochasticity of slat Rossiter tones remained elusive of a reasonable explanation, and the discrepancies related to the tone frequency calculations and amplitude calculations from explanation based on Rossiter mechanism alone.

Chapter 5

Design of Experiments for Parametric Simulations

5.1 Introduction

The design of computer simulation experiments is a fundamental aspect of scientific computing. Effective simulation campaigns necessitate a strategic plan to explore a parametric space of interest, enabling accurate inference of its behavior. Although the ideal outcome is a highly detailed representation of the parametric space, the escalating costs associated with each simulation constrain the number of experiments that can be conducted within a given computational budget. The primary objective of a Design of Experiments (DOE) methodology is therefore to implement a statistically optimal sampling technique, ensuring that each costly simulation maximizes its information yield[147]. From an optimization perspective, the challenge is to develop an efficient routine that approximates the behavior of the parameter of interest with the fewest possible query points. This solution varies depending on the nature of the problem, its dimensionality, data acquisition costs, and other factors[148]. Consequently, it is imperative to devise an optimal method for sampling the parameter space, such as in the context of this study, where data on the far-field acoustic signature of a slat-airfoil configuration, focusing on the position of the leading-edge slat relative to the airfoil, is needed. Each data point acquisition involves an LBM-FWH simulation, as detailed in the previous chapter, a procedure known for its computational expense[149].

A first approach to DOE is to discretize the parameter space and query discrete points uniformly from the resulting manifold. However, the number of points grows exponentially with the number of dimensions and is hence sample inefficient. The use of factorial designs, which instead of querying all the discrete points, systematically explores all possible combinations of discrete parameter levels, obtaining a sparser representation of the manifold, reduces compute costs but is not optimal because the acquisition is still not carried out based on information availability. Strategies derived from these factorial designs, such as fractional factorial designs, Latin hypercube sampling, and adaptive sampling methods, aim to balance the trade-off between discretization size of the manifold and efficiency of acquisition. These methods are therefore theoretically optimal to sample a manifold apriori to the experiment and guarantee that the cost of simulation is the least possible against the information collected on the parameter manifold.

Surrogate Modeling(SMs) is a more recent approach to cost-effective technique to aid in the inference of the parameter space involving expensive simulations[150]. A surrogate model or a response surface is an approximate discrete representation of the behavior of a simulated variable of the given parameter domain which can be used to infer the behavior of the variable over the continuous parameter space. In

simple Response Surface Modelling (RSM)[151], the response surface is assumed to be a linear function of the parameters whose coefficients are then deduced from a few available data points, i.e. a linear fit which demands only N_D number of observations, same as the dimensionality of the problem. When it is known that the response is non-linear, an approximate polynomial order can be assumed and the corresponding coefficients can be computed. This method hence results in a fixed number of points per parameter if an approximate function can be guessed correctly.

In more recent advances, the data collected over a response surface in the first few simulations can be subjected to a more rigorous statistical data analysis and better inferences about the surface can be obtained. Such methods includes that of Kriging[152] and Active Learning methods[153] and primarily involves deploying Bayes' theorem to statistically estimate the nature of the response surface. The estimated probabilities are then used to guide the acquisition process which leads to sample efficiency. Theoretically, the data acquisition can be controlled online, i.e. the decision to make new query points are not determined apriori to the experiment but are adaptively calculated during the acquisition process. The nature of this active acquisition leads to different methods of surrogate modelling. For the purpose of this work, we adapt and deploy the Gaussian Process Surrogate model for creating a response surface of the noise characteristics of the HLD under study. The noise surrogate is then utilized to design an experiment based on the active learning strategy to acquire data and provide a fast-turn around model for noise behavior based on the slat positioning. In the rest of this chapter, we explain the details on the construction of this model.

5.2 Bayes' Theorem

Bayes' Theorem is a fundamental idea in the statistical school of thought[154] and provides a simple rule to calculate conditional probabilities. According to Bayes's rule, commonly written as

$$P(H | E)P(E) = P(E | H)P(H) \quad (5.1)$$

where $P(H | E)$ is the conditional probability of a hypothesis H being true in the light of some observed evidence E being available, and $P(E)$ and $P(H)$ are the raw probabilities of the evidence to exist and the hypothesis to be true. In effect, Bayes' rule leads us to think that for any scenario determined by the rules of probabilities, we can first form a prior belief about a hypothesis, and then numerically update the probability of that hypothesis being true according to our observation of evidences. Indeed, the prior hypothesis can be even a false one with respect to reality but can still be updated in the wake of new observations and be updated iteratively to obtain a true representation of the reality. The formula itself is a representation of how this updation of the belief must be done numerically.

Bayes' formula can be reasoned to arise from a symmetry of the probabilities, i.e. in the symmetry of argument between the probability of a hypothesis being true 'if' the evidence is present and and probability of observing evidence 'if' the hypothesis was true. The left side of the equation gives a product of the probability of a hypotheses H being true in the presence of observed evidence E , and the probability of observation of such an evidence E . Together they represent the probability of the hypothesis being true 'if' the evidences are observed. On the right hand, we have the product of the probability of the evidence being observed given that the hypothesis was true ($P(E | H)$) and the probability of the hypothesis being true ($P(H)$), and together it represent the probability of the observation of the evidence E 'if' the hypothesis is true. This symmetry leads to the objective equality of these two quantities and hence the formula.

Bayes' formula becomes a powerful tool once written as

$$P(H | E) = \frac{P(E | H)P(H)}{P(E)} \quad (5.2)$$

where $P(H | E)$ is called the posterior, since it is the probability of the hypothesis H being true after observation of evidence E . The naive probability of H being true indicated by $P(H)$ is called the prior distribution since it is the probability of H being true before the observation of evidence E . The conditional probability $P(E | H)$ is called the likelihood, being the probability of the observation of evidence given that H is true. Emphasis must be given to the fact that the formula is useful for both an iterative procedure to updating the prior to converge towards a conclusion of reality or, when a sufficient sample of the data is available already, allows direct estimation of the real nature of the hypothesis. In a Bayesian inference setting, if we are trying to estimate the true value of a variable, the Bayesian posterior will converge to the exact value if an infinite number of samples are collected. For a rigorous explanation of this fact, refer to Section 5.3 in the work of Bernardo and Smith [155]. This asymptotic behavior is however not true at every intermediate step of a Bayesian inference procedure and that difference is the core feature which differentiates a Bayesian paradigm to statistical inference from that of the Frequentist.

In a Frequentist approach to probability, the objective value of a probability is obtained by repeating an experiment infinite number of times. This means that the value of the probability is an intrinsic quantity related to the experiment and each run of the experiment is a realization of the process that functions according to the set probability. On the other hand, in the Bayesian perspective, the probability of an event is only a measure of the confidence that the event will occur and is not inherently derived from an infinite sampling. In other words, in Bayesian perspective, probability has a meaning while using a finite sample size as the representation of the confidence in a prediction for the next sample. This is while Frequentist approach cannot give a prediction of confidence in the prediction for the exact next sample, based on only the previous experiments. In fact, if the sample size is large enough, the Bayesian estimate and the Frequentist probability will converge.

Now that Bayes's formula is familiarized, let us visit the premise of how to use Bayesian inference for a regression and surrogate modelling problem.

5.3 Gaussian Processes

The Gaussian Processes (GPs) also known as Kriging or Wiener-Kolmogorov prediction, are a popular and powerful tool in the repertoire of statistical inference and regression[156]. It is a non-parametric tool for modelling complex functions that are otherwise not amenable to analytical modelling. The key advantage of GPs is that they can be used to approximate a function or response surface while the nature of the function is not explicitly known. Moreover, the function modelled is a distribution over functions meaning that the GP representation of a function is an average function along with a standard deviation function. This naturally leads to uncertainty quantification on the approximation and also enables the use of Bayesian methods for estimation of the variables. The latter property is what makes GPs well suited as a function approximator in the Bayesian regression setting.

More precisely, a Gaussian process is a function approximator of the form $y \in \{y_1, y_2, y_3, \dots, y_n\}$ in a multidimensional domain of $X \in \{x_1, x_2, x_3, \dots, x_n\}$. If we assume that these variables are independent, and have a Gaussian distribution each, then the collection of these variables into y leads it to have a jointly Gaussian distribution. The function y can then be written using the joint distribution as

$$y \approx \mathcal{N}(\mu(X), K(X, X))$$

where $\mu(X)$ is the mean function, often taken to be zero as an initial guess, and $K(X, X)$ is the co-

variance matrix. The mean function now is an average function over the domain whereas the covariance matrix determines the flexibility or expressiveness of this function. This is because, for each realization sampled for y , we obtain a function that has different values at each of the discrete points $y_1, y_2, y_3, \dots, y_n$ but their mean values are determined by corresponding $\mu_1, \mu_2, \mu_3, \dots, \mu_n$, and then their variances by the deviatoric components of $K(X, X)$. This means that the values $y_1, y_2, y_3, \dots, y_n$ are not completely independent, but are rather correlated, the correlation between each component denoted by corresponding elements of the 2D symmetric covariance matrix $K(X, X)$.

The nature of this correlation matrix can now be understood more deeply if we assume simple forms. Let us say that the correlation matrix is a banded matrix with the major diagonal as unity and adjacent elements slightly less. In this case, each of the elements will be correlated to its immediate neighbor on both sides and to none other. Thus for each realization, the sampled values of the vector y will be smoothed due to the constraint of adjacent elements by the correlation. If the bandwidth of the correlation matrix is increased, each element will then be correlated with more and more of its neighbors thus leading to stiffness of the vector y towards a homogeneous one. Thus the bandwidth of the correlation matrix directly leads to the expressiveness of the Gaussian processes.

The covariance matrix $K(X, X)$, or as often called the kernel matrix, or just the kernel, thus primarily represents the nature of the approximator given by a Gaussian process. In a detailed analysis, the covariance matrix is often subjected to the Mercer's theorem which guarantees that for a positive definite symmetric matrix such as a covariance matrix, an eigen decomposition is always possible into an infinite space of eigenvalue-eigenfunction pairs[157]. In the GP context, these eigen functions are then a set of infinite number of feature functions representing the feature space on which the GP attempts to represent a given test function. In a regression or classification problem, the projection of input datapoints and query points onto this infinite dimensional feature space is possible without the exact knowledge of the feature space itself and without explicit calculation of their infinite dimensional coordinates. This saves the computation of data transformations to latent spaces and provides straightforward computation of predictive distributions and is essentially called the 'kernel trick'.

5.4 Bayesian Regression using Gaussian Processes

In order to use Gaussian Processes for Bayesian regression and to generate a noise-surrogate of the high-lift device, we follow the theoretical framework of Rasmussen and Williams [156]. We also borrow the notation followed wherein the vector variables are denoted in bold, and a set is denoted in uppercase. Accordingly, a linear regression problem imbibes the properties of a stochastic process by assumption of an additive noise to the data representing its aleatoric uncertainty. It then follows that a linear regressor for a given dataset $\mathcal{D} = \{(x_i, y_i) | i = 1, \dots, n\}$ mapping multidimensional observations from domain X to the scalar targets Y can be written as

$$y = f(\mathbf{x}) + \varepsilon = \mathbf{x}^\top \mathbf{w} + \varepsilon \quad (5.3)$$

where $\varepsilon \sim \mathcal{N}(0, \sigma_n)$ is a normally distributed statistical noise with mean 0 and standard deviation σ_n . Consequently, the linear fitting weights also need to be expressed as a distribution that is assumed to be a Gaussian distribution as well for the ensuing mathematical necessity. The target variable also now is obtained as a statistical process, $y = \{y_1, y_2, y_3, \dots, y_i, \dots\}$. It can be noted that if a Gaussian noise is assumed together with the assumption that linear weights are also Gaussian distributed, then calculating the joint probability of the process y in the presence of the feature data X and the chosen weights w is written as $p(y | X, w)$ and its joint probability (conditional) is calculated as

$$\begin{aligned}
 p(\mathbf{y} | X, \mathbf{w}) &= \prod_{i=1}^n p(y_i | \mathbf{x}_i, \mathbf{w}) \\
 &= \prod_{i=1}^n \frac{1}{\sqrt{2\pi}\sigma_n} \exp\left(-\frac{(y_i - \mathbf{x}_i^\top \mathbf{w})^2}{2\sigma_n^2}\right) \\
 &= \frac{1}{(2\pi\sigma_n^2)^{n/2}} \exp\left(-\frac{1}{2\sigma_n^2} (\mathbf{y} - X^\top \mathbf{w})^\top (\mathbf{y} - X^\top \mathbf{w})\right) \\
 &= \mathcal{N}(X^\top \mathbf{w}, \sigma_n^2 I)
 \end{aligned} \tag{5.4}$$

Hence, the likelihood distribution, as $p(\mathbf{y} | X, \mathbf{w})$ is named, also inherits the Gaussianity with a mean distribution $X^\top \mathbf{w}$ and the covariance being $\sigma_n^2 I_n$. Hence the posterior is now essentially a Gaussian process whose mean function follows the classical linear fit on the data and with a covariance matrix directly following the assumed noise in the data.

Now, in a regression task, the goal is to obtain a set of weights for a suitable set of basis functions such that the data can be modelled, and used for predictions of unsampled data points. To enable this, we need to deduce the distribution functions that represent the weights. This is achieved by deploying Bayes' theorem over the above linear regression problem, i.e. according to Bayes' formula, the conditional probabilities can be inverted as

$$p(\mathbf{w} | \mathbf{y}, X)p(\mathbf{y} | X) = p(\mathbf{y} | X, \mathbf{w})p(\mathbf{w}) \tag{5.5}$$

Here $p(\mathbf{y} | X, \mathbf{w})$ is the likelihood, $p(\mathbf{w})$ is the assumed prior belief on the distribution of weights or simply the prior, and $p(\mathbf{w} | \mathbf{y}, X)$ is the conditional posterior distribution on the weights, conditioned on the available sample points (\mathbf{y}, X) . The second term on the left hand side is $p(\mathbf{y} | X)$ is called the marginal likelihood, being dependent only on the available data, and can be expressed as an integral over the weight distribution as

$$p(\mathbf{y} | X) = \int p(\mathbf{y} | X, \mathbf{w})p(\mathbf{w})d\mathbf{w} \tag{5.6}$$

In this perspective, the marginal likelihood is the likelihood of the dataset integrated over the space of all possible weight distributions and serves as a normalization factor. To enable the calculation of the posterior, it is also now necessary to define the prior distribution of the weights. Assuming Gaussianity such that $\mathbf{w} \sim \mathcal{N}(\mathbf{0}, \Sigma_p)$, the posterior distribution of weights $p(\mathbf{w} | \mathbf{y}, X)$ given a set of observations from the dataset \mathcal{D} , follows

$$\begin{aligned}
 p(\mathbf{w} | X, \mathbf{y}) &\propto p(\mathbf{y} | X, \mathbf{w})p(\mathbf{w}) \\
 &\propto \exp\left(-\frac{1}{2\sigma_n^2} (\mathbf{y} - X^\top \mathbf{w})^\top (\mathbf{y} - X^\top \mathbf{w})\right) \exp\left(-\frac{1}{2} \mathbf{w}^\top \Sigma_p^{-1} \mathbf{w}\right)
 \end{aligned} \tag{5.7}$$

and for sake of notational simplicity, is written as

$$p(\mathbf{w} | X, \mathbf{y}) \propto \exp\left(-\frac{1}{2} (\mathbf{w} - \bar{\mathbf{w}})^\top \left(\frac{1}{\sigma_n^2} X X^\top + \Sigma_p^{-1}\right) (\mathbf{w} - \bar{\mathbf{w}})\right) \tag{5.8}$$

$$| X, \mathbf{y}) \propto \mathcal{N}(\bar{\mathbf{w}}, A^{-1}) \tag{5.9}$$

where $\bar{\mathbf{w}} = \sigma_n^{-2} A^{-1} X \mathbf{y}$, and $A = \sigma_n^{-2} X X^\top + \Sigma_p^{-1}$. The posterior also thus inherits the Gaussianity assumed on the prior probability on the weights and the additive statistical noise.

Now that a posterior distribution of the weights conditioned by the available data can be computed,

a regression based on the Gaussian process representation of the target variable is possible. For this, the only assumption to be made is the prior probability distribution, or precisely its correlation matrix. However, in the Bayesian perspective, the prior distribution only represents the initial belief about a hypothesis, and given that Bayesian posterior enables the conditioning the prior on the available data, the initial assumption on the prior does not affect the calculation significantly. Or in other words, within Bayes' formula, the prior and the likelihood terms compete with each other to influence the posterior distribution, and by the effect of this conditioning, the posterior develops adherence to the available data. In the event that sufficient data is available to obtain a well fitted model by using the underlying basis function, the significance of the prior reduces and the posterior converges to the true distribution that can be inferred from the available data as the dataset grows. This convergence with only weak assumptions of the prior distribution of weights is what in essence makes the Bayesian regression using Gaussian process a powerful regression tool.

To obtain the predictive distribution $p(f_* | \mathbf{x}_*, X, \mathbf{y})$ for an output f_* at a query point \mathbf{x}_* , after conditioning the regression on the dataset \mathcal{D} , an averaging of all the possible predictions over the space of the linear weights can be done. Such an averaging can be written as the integral

$$\begin{aligned} p(f_* | \mathbf{x}_*, X, \mathbf{y}) &= \int p(f_* | \mathbf{x}_*, \mathbf{w}) p(\mathbf{w} | X, \mathbf{y}) d\mathbf{w} \\ &= \mathcal{N}(\sigma_n^{-2} \mathbf{x}_*^\top A^{-1} X \mathbf{y}, \mathbf{x}_*^\top A^{-1} \mathbf{x}_*) \end{aligned} \quad (5.10)$$

Note that the final predictive distribution is obtained analytically with the help of the assumption of Gaussianity on all the variables involved. The terms involved are the covariance of the assumed statistical noise, covariance of the prior distribution, and the dataset only and thus simplifies the actual calculation as opposed to the rather esoteric definition of a Gaussian process regressor itself.

That being the case, the linear regression using this Bayesian technique can be easily translated to a non-linear regression using arbitrary basis. For this the linear approximation function can be replaced as

$$y = f(\mathbf{x}) + \varepsilon = \phi(\mathbf{x})^\top \mathbf{w} \quad (5.11)$$

i.e. by replacing the raw feature space \mathbf{x} with $\phi(\mathbf{x})$, its transformation using an arbitrary non-linear basis ϕ . Note that $\phi(\mathbf{x})$ is a projection of the input vector \mathbf{x} onto the basis ϕ using the matrix product between ϕ and X , and ϕ itself is a collection of the unit column vectors or arbitrary dimensions of the feature space. Hence $\phi(\mathbf{x})^\top \Sigma_p \phi(\mathbf{x}')$ and $\phi(\mathbf{x}_*)^\top \Sigma_p \phi(\mathbf{x}_*)$, all use the same kernel $k = \phi^\top \Sigma_p \phi$ and then $k(x_1, x_2) = x_1^\top \phi^\top \Sigma_p \phi x_2$.

The previous calculations then lead to the predictive distribution as

$$f_* | \mathbf{x}_*, X, \mathbf{y} \sim \mathcal{N}(\sigma_n^{-2} \phi(\mathbf{x}_*)^\top A^{-1} \phi(X) \mathbf{y}, \phi(\mathbf{x}_*)^\top A^{-1} \phi(\mathbf{x}_*)) \quad (5.12)$$

or by eliminating A^{-1} and the making the choice that $K(x, x) = \phi^\top(x) \Sigma_p \phi(x)$

$$\begin{aligned} f_* | \mathbf{x}_*, X, \mathbf{y} &\sim \mathcal{N}(\phi(\mathbf{x}_*)^\top \Sigma_p \phi(\mathbf{x}) (K + \sigma_n^2 I)^{-1} \mathbf{y}, \\ &\quad \phi(\mathbf{x}_*)^\top \Sigma_p \phi(\mathbf{x}_*) - \phi(\mathbf{x}_*)^\top \Sigma_p \phi(X) [K + \sigma_n^2 I]^{-1} \phi(X)^\top \Sigma_p \phi(\mathbf{x}_*)) \\ &\sim \mathcal{N}(K(\mathbf{x}_*, \mathbf{x}_*) [K(X, X) + \sigma_n^2 I]^{-1} f, \\ &\quad K(\mathbf{x}_*, \mathbf{x}_*) - K(\mathbf{x}_*, X) [K(X, X) + \sigma_n^2 I]^{-1} K(X, \mathbf{x}_*)) \end{aligned} \quad (5.13)$$

Such a formulation leads us to the previously mentioned ‘‘kernel trick’’. It can be observed that in this form of the predictive distribution, the arbitrary basis ϕ always appears as part of an inner product of

the form $\phi(\mathbf{x})^\top \Sigma_p \phi(\mathbf{x})$ be it for query points as $\phi(\mathbf{x}_*)$ or datapoints as $\phi(\mathbf{x})$. However, the matrix $\phi^\top \Sigma_p \phi$ is a quadratic form, an inner product on Σ_p which is a positive definite, regardless of the assumptions on ϕ . Hence, a square root $\Sigma_p^{1/2}$ is always defined and $K(x, x') = \phi^\top(x) \Sigma_p \phi(x')$ can be represented purely as an inner product $K(x, x') = \psi(x) \cdot \psi(x')$. Thus to project the inputs to the feature space, it is indeed not necessary to transform the raw inputs to a high-dimensional input space, but instead the formulation can be used with only the kernel function in every instance of the inner product. In plain simple terms, since $\phi^\top(x)$ is a matrix product of the collection of high dimensional basis vectors of ϕ and the input vector x . Thus the kernel being representable as an inner product means that when $K(x, x') = \phi^\top(x) \Sigma_p \phi(x')$, it can be written as $K(x, x') = x^\top \phi \Sigma_p \phi x'$, where $\phi \Sigma_p \phi$ remain an inner kernel regardless of the inputs. Now, if ϕ always occurs only in the form of the inner product, then we does not need to know the actual form of ϕ but only of the finite dimensional inner product $\phi \Sigma_p \phi$. This means that one can have a theoretically infinite dimensional feature space of arbitrary functionality, but in calculation use only a simpler representation of the inner product $\phi \Sigma_p \phi$.

The predictive covariance according from Eq.5.10 has an intuitive explanation as well. The first term $\phi(\mathbf{x}_*)^\top \Sigma_p \phi(\mathbf{x}_*)$ is a quadratic form representing the variance arising from position of query point with respect to the existing prior probability distribution and is always non-zero. This hence represent the maximum possible uncertainty according to the prior at the query point \mathbf{x}_* before any observation is available at this point and is fully dependent on the prior or in the same sense the kernel choice. The second term on the other hand represent the reduction in uncertainty due to the observed data from the available dataset in the vicinity of the query point \mathbf{x}_* . If no noise is assumed in the data, which corresponds to the case of $\sigma_n = 0$, the full term reduces to $K(\mathbf{x}_*, X) K(X, X)^{-1} K(X, \mathbf{x}_*)$ which is non-zero only at a point which is not present in the dataset X . In the case $\mathbf{x}_* \in X$, then the term simplifies to $K(\mathbf{x}_*, \mathbf{x}_*)$ by property of the matrix multiplication thereby collapsing the predictive variance. This is hence the iconic behavior of the GP regression that in the absence of assumed noise in the dataset, the GP regressor captures the training points exactly and with a zero variance. However, for points which are not in the dataset, the variance is inevitably non-zero.

The input data noise assumption using the σ_n parameter this is a hyperparameter for the model. In practice, when GP is deployed on noisy observations, the data are modeled as $y = f(x) + \varepsilon$ with $\varepsilon \sim N(0, \sigma_n^2)$. This parameter is typically treated as a hyperparameter and optimized jointly with the kernel parameters by maximizing the log marginal likelihood. In practice, σ_n is often initialized to a small, non-zero value to avoid numerical instability, then adjusted during optimization. A larger estimated σ_n means the model attributes more variation to noise, making it less sensitive to small-scale fluctuations in the training data, which can improve generalization. The final optimized model balances smoothness and complexity via the kernel parameters and the tolerance to noise via σ_n .

It must also be noted that by choosing a kernel function, we are also choosing the prior distribution in the Gaussian processes since the kernel also has the term Σ_p . Hence the only actual choice to be made in the formulation of a problem for deploying this algorithm are the kernel parameters. Hence, finally obtaining the predictive distribution using the Gaussian Process regression is by a straightforward calculation written as

$$\begin{bmatrix} \mathbf{y} \\ \mathbf{f}_* \end{bmatrix} \sim \mathcal{N}\left(\mathbf{0}, \begin{bmatrix} K(X, X) + \sigma_n^2 I & K(X, \mathbf{x}_*) \\ K(\mathbf{x}_*, X) & K(\mathbf{x}_*, \mathbf{x}_*) \end{bmatrix}\right) \quad (5.14)$$

This kernel trick then involves only the selection of a suitable kernel which has a suitable family of basis functions. For an arbitrary positive semi-definite matrix, the underlying basis can be numerically obtained by calculating its eigen decomposition, where the matrix is decomposed as $M = U \Sigma U^\top$. For an analytic example, if we choose squared exponential function as a kernel, this kernel can be written as an

infinite sum of Gaussian functions since

$$\begin{aligned} k(x_p, x_q) &= \sigma_p^2 \int_{-\infty}^{\infty} \exp\left(-\frac{(x_p - c)^2}{2\ell^2}\right) \exp\left(-\frac{(x_q - c)^2}{2\ell^2}\right) dc \\ &= \sqrt{\pi} \ell \sigma_p^2 \exp\left(-\frac{(x_p - x_q)^2}{2(\sqrt{2}\ell)^2}\right) \end{aligned} \quad (5.15)$$

One particular kernel that is popular among the Machine Learning community is the Matern kernel. This takes the form

$$k_{\text{Matern}}(r) = \frac{2^{1-\nu}}{\Gamma(\nu)} \left(\frac{\sqrt{2\nu}r}{\ell}\right)^\nu K_\nu\left(\frac{\sqrt{2\nu}r}{\ell}\right) \quad (5.16)$$

where ν and ℓ are tuning parameters and K_ν is a modified Bessel function. For the values of ν , the properties of the resulting kernel are usually matched for the requirement of the problem. If we set the value $\nu = \frac{1}{2}$, the resulting function reduces to a simple exponential kernel $k(r) = \exp(-r/\ell)$. This kernel in 1D is the covariance function of the Ornstein-Uhlenbeck process that models the Brownian motion. The kernel thus gives a function that is excessively random for a smooth regression. A smoother version of the kernel is possible by choosing $\nu = \frac{3}{2}$ and $\frac{5}{2}$, commonly called Matern32 and Matern52, and allows for modelling functions for practical applications. A value of $\nu > \frac{7}{2}$ also is not generally chosen since the resulting function tends to be excessively noisy and is difficult to distinguish from slightly noisy input data [156]. For the purpose of our work, we test both Matern32 and Matern52 and chose Matern52 as it delivers a smoother model.

5.5 Feature Engineering for Noise Surrogate

This section aims to develop a noise surrogate model for farfield spectra of high lift device where the position of the slat relative to the main element is the varying parameter. The input domain is hence composed of the slat position coordinates relative to the main element, namely, Slat Gap, Slat Deflection Angle, Slat Overlap, and Angle of Attack. A 4-dimensional input domain is finely suited for the Gaussian Process Regression model, given the fact that GP methods are cost prohibitive at higher dimensions $D > 10$. In addition, the target space is the far-field noise spectra and a spectrum as such is not amenable to modelling by Gaussian processes.

The frequency range of interest for slat noise was determined to be 20 kHz. For a spectrum collected experimentally, the frequency resolution is typically 1Hz and hence results in number of bins being 20,000. For a spectrum sampled from CFD, a resolution of 40Hz is typical, and will result in 500 frequency bins. This is still cost prohibitive in terms of modelling using GP.

As a solution, the spectrum needs to be converted to an alternative low order representation. One approach to this problem is to use a spline fit and to use the parameters of the spline functions as the predicted variable. However, this removes the physics informed modelling approach that is already available from the slat noise literature. A robust model of the slat noise was already developed by Guo [88] based on the surface FWH equations on the radiating surface of the slat and is explained in Chapter 02. This is not reiterated here and instead we here design a reduced order approach for the representation of the power spectral density data.

As mentioned, Guo's model gives the representation of the spectra in terms of multiple components as

$$\Pi = \rho_0^2 c_0^2 A_G A_F W(M) F(f, M) D(\theta, \phi) \frac{c_s b}{r^2} \quad (5.17)$$

where A_G , A_F are scaling factors depending on the flow geometry and flow parameters, $W(M)$ is a weighting function dependent on the Mach number, $F(f, M)$ is the shape function, and $D(\theta, \phi)$ is the directionality function. This formula hence only contains terms which are derived from the physics of the problem and has no calibration parameters, and recovers the spectra satisfactorily for a good range of flow parameters and observer positions. However, for the purpose of extracting only the essential features of the PSD to aid simplification, we reduce the formula to the form

$$\Pi = a \times F(f, M) D(\theta, \phi) \quad (5.18)$$

Here, only the shape function and the directionality functions are retained and other factors are replaced with a single calibration parameter a . The shape function as function of Strouhal number has the definition

$$F(St, M) = \frac{M^2 L_S}{c_0} \frac{St^2}{(1 + \mu_0^2 St^2)(1 + \mu_1^2 (1 + M)^2 St^2)(1 + \mu_2^2 M^2 St^2)(1 + \mu_3 M St)} \quad (5.19)$$

Here, the coefficients $\mu_0, \mu_1, \mu_2, \mu_3$, are adjustable parameters, M is the flow Mach number, L_S is the characteristic length, taken to be the slat chord length, and St is the Strouhal number. This function captures the shape of the characteristic broadband hump of the slat at a given Mach number. Since in our experiment, the inlet velocity is kept constant, the flow Mach number is not a variable. Hence this function adds additional four calibration coefficients to fit the spectra. For the case of directivity function, we retain the function as suggested originally by Guo for the initial development and hence it does not contribute new parameters. Finally, the total parameters from Guo's functions are $y = \{a, \mu_0, \mu_1, \mu_2, \mu_3\}$

The second dominant feature of a slat noise spectra are the spectral peaks. These peaks are strongly suspected to be due to aeroacoustic resonance mechanism, but however the spacing between the peaks are not exactly homogeneous. Both peak frequencies and peak width at different frequencies are shown to have variations when the flow configurations change. Hence we choose to model them separately. For capturing the shape of the peak, we use the Lorentz pulse function form

$$L = \frac{h_n}{1 + \left(\frac{St - St_n}{w_n/2}\right)^2} \quad (5.20)$$

for which the three parameters are the pulse height h_n , the pulse width w_n , and the central frequency St_n . Here the peak width is set to constant for the easing the fit, and is thus not a variable in the dataset. The slat noise spectra typically contain five dominant peaks over the broadband range and the number vary with the positioning of the slat. We choose to keep the number of peaks modeled to six. Two parameters for each peak then leads to a total of 12 parameters for the peaks. Hence in total, the total number of parameters to represent the spectra becomes 17. This target dimensionality is suitable for a low dimensional Gaussian process regression task.

Equation 5.17 gives the spectral density in raw power units. Combining the broadband spectral shape and the Lorentzian peaks function can be done in the deciBel units. Following Eq.5.18 and assuming that the total spectral density is the product of the broadband spectrum and the 6 Lorentzian shape functions, the combined spectral density model can be written in deciBels as

$$\hat{\Pi} = \hat{a} + \hat{F}(St, M) + \hat{D}(\theta, \phi) + \sum_{n=1}^{N_p} \hat{L}(St_n, h_n, w_n) \quad (5.21)$$

where (\cdot) denotes each quantity in deciBel.

Hence finally, the dataset will be represented as an input space of the four slat positioning coordinates $\{AOA, SGP, SDA, SOL\}$, and the target space of parameters from Eq.5.21 as $\{a, \mu_0, \mu_1, \mu_2, \mu_3\} \cup \{h_i, w_i, St_i : 1 \leq i < 6\}$.

5.6 Initial dataset

To generate a Gaussian Process regression model and to enable active-learning as a sampling technique, an initial dataset is required over which a naive surrogate model has to operate. For this we choose to generate our first set of simulations using the Latin Hypercube sampling. A Latin Hypercube is an efficient method to sample points from a multi-dimensional space with the guarantee that all discrete intervals of the domain are sampled at least once. This type of sampling guarantees that the whole of the domain is covered in a fairly uniform manner obtaining a reasonable representation of the response surface, however much more sparsely than an interpretable form. Here although the canonical Latin Hypercube Sampling is widely used, the sampling algorithm can generate samples which are not most uniformly distributed in the multi-dimensional space. Deutsch and Deutsch [158] suggests a modified version of the LHS algorithm to have an improved uniformity of distribution of points in multidimensional space. They achieve the improvement by sequential elimination of samples that obtain the smallest average distance from other sampled points while generating the samples for each dimensions. The rest of the procedure remains the same as in the canonical method.

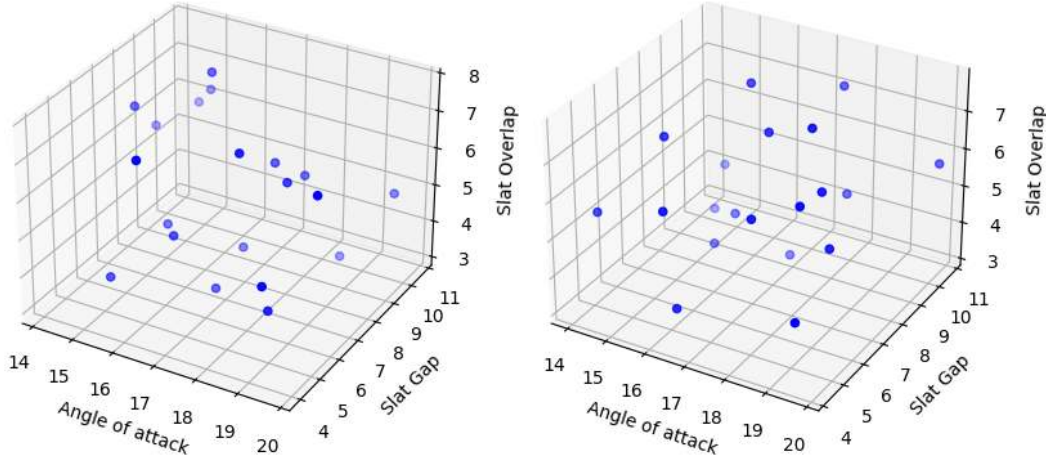


Figure 5.1: A sampling of the space of three slat positional variables using canonical LHS (left) and with LHS-MDU (right). A total of 20 samples were made to create the initial set.

To generate the initial dataset, we then use the following ranges for the variables of slat positional coordinates. These coordinates are obtained around the standard position of the slat. A total of 10 samples, number 10 being only a convenient choice, were then generated to launch the simulation. A plot comparing the sampling methods, between Latin Hypercube and Latin Hypercube with Multi-Dimensional Uniformity is shown in Fig.5.1. The final 10 samples in a reduced 3D space are shown in Fig.5.2.

It must be mentioned that in our iterations to generate the initial dataset and while facilitating the analysis of the dynamics of the cove flow, it was found that cases with positive slat overlap are particularly silent in view of characteristic slat noise. This is due to the fact that in such cases the slat is positioned too close to the leading edge of the airfoil and the resulting mean shear layer is deformed in such a way that the aeroacoustic resonance mechanism is not favored. Hence for the presentation of this surrogate

model we chose to omit the domain with positive slat overlap. The complete range of parameters used to initialize the dataset is shown in Table 5.1.

	Lower limit	Upper limit	Standard Geometry
AOA	10.0	20.0	18.0
SDA	20.0	40.0	35.5
SGP	4.0	10.0	7.94
SOL	-9.0	0.0	-6.36

Table 5.1: Table of upper and lower bounds for slat positional variables and angle of attack used to generate the initial sample using LHS-MDU . This is also the test domain used for the surrogate model.

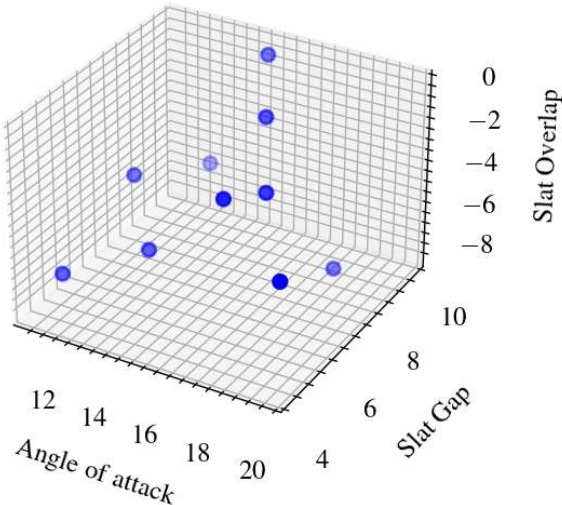


Figure 5.2: A scatter plot of the initial samples drawn from the domain to create the initial dataset using LHS-MDU

5.7 Bayesian Active Learning

By deploying LHS-MDU, the initial sample to enable the surrogate model is made. These samples were then used to run simulations using the LBM-CAA routines as described in Chapter 3. The resulting data then generates the Power Spectral Densities (PSD) of the far-field noise of the corresponding slat positions. These PSDs are then transformed into the feature space by least square fitting of the spectra onto the reduced order model according to Eq. 5.21. To reduce the least square error, we deployed the Nelder-Mead algorithm taking into account the dimensionality of the problem and the fact that the optimization is unconstrained[159]. The obtained dataset is then used to fit a Gaussian Process regression implemented using the Surrogate Modelling Toolbox developed under the name SMT [160, 161]. The surrogate model is obtained using a sample of 10 simulations over the 4D space of parameters.

To generate samples for further simulations, and to improve the surrogate model to a satisfactory accuracy, the epistemic uncertainty in the predictions of the model needs to be understood. As mentioned

in the previous section, a Bayesian regression model generates a predictive distribution for the target variables of interest. Since these distributions are essentially a Gaussian probability distribution, the mean and variance of the variable can be computed over a range of values. The surface generated by the mean values of the predicted variable is output as the mean response surface. The variance is then used to estimate the confidence of the model for the prediction of the mean value. The confidence interval is a range of values for which there is a prescribed probability, α , for the value of the prediction to fall within and can be expressed by

$$1 - \alpha = \Pr \left(\frac{|X - \mu|}{\sigma / \sqrt{n}} < z \right) \quad (5.22)$$

where X is the variable, μ is the mean, σ is the standard deviation or the square root of variance, z is the number of standard deviations from the mean, commonly called the z-score, and n is the sample size used for the estimation if it is not done on an infinite sample. Accordingly, for a Gaussian distribution, 5% confidence interval is the region where the value of the variable falls with 95% probability and the corresponding z-score is 1.96. A list of z-scores and corresponding confidence levels are given in Table 5.2.

z-score (Standard Deviations)	p-value (Probability)	Confidence level
< -1.65 or > +1.65	< 0.10	90%
< -1.96 or > +1.96	< 0.05	95%
< -2.58 or > +2.58	< 0.01	99%

Table 5.2: Table of p-value and z-score of a Gaussian distribution

The goal of the regression process is to reduce the epistemic uncertainty of the model arising from the noise in the data. But the noise that is added to the linear regressor for formulating the Gaussian Process Regression, as in Eq. 5.3, is in fact the aleatoric uncertainty assumption, i.e. the uncertainty assumed inherent in the training data due to measurement errors and inherent noise which are not reducible. The other type of uncertainty, which is the epistemic uncertainty, arises from modelling errors due to unoptimal parameters to fit the data, and due to insufficient data points. This uncertainty can be minimized by obtaining a better fit to the data through optimizing the model parameters. In the GP based Bayesian regression, the only model parameter to tune is the type of kernel and its correlation length scale. Optimising these parameters is the process of offline 'learning' in a GP regression.

The uncertainty for the model arising from lack of datapoints can only be reduced by addition of new datapoints. However, since the predicted distribution is heteroscedastic, the sampling can be adapted to ensure an uncertainty informed sampling. For each new datapoint collected or batches of datapoints, the parameters of the model can be optimized to obtain a new model with reduced epistemic uncertainty. The new model uncertainties can then be used to obtain a suggestion for sampling the next datapoint or batch of points, thereby obtaining better sampling techniques that progressively minimizes the epistemic uncertainty. This approach to reducing the model uncertainty is called the active learning approach and is attempted in our work.

For the calculation using the first 10 data points, we use the Squared Exponential kernel. A noise of 5% is assumed to enable the uncertainty calculation. This noise value is obtained by first enabling an iterative search for optimal noise value so as to obtain the best fit of the model output using least-square fitting of the predicted and available data. Then the noise value is kept fixed and the resulting predictive uncertainty is then used for the active learning. The hyperparameters of the model are the kernel parameters, namely the inverse of correlation length θ_l , using which the kernel can be written as

$$K = \prod_{l=1}^{nx} \exp \left(-\theta_l (x_l^{(i)} - x_l^{(j)})^2 \right) \quad (5.23)$$

The search bounds for this parameter is set to $\theta_l \in [0.05, 20]$ and initialized at 10. The parameter is then optimized using the gradient free optimizer COBYLA (Constrained Optimization BY Linear Approximation) available with the SMT toolbox using default parameters.

5.8 Uncertainty Propagation for the Surrogate Model

As mentioned in the previous section, we use a reduced order representation of the slat noise spectra to enable the regression. This means that predicted mean and uncertainties are in terms of the calibration variables in the model. These uncertainties then need to be propagated through the model equations in order to obtain the uncertainty of the spectra calculation and allow a quantitative understanding of the model's confidence in the predictions.

From Guo's formula, the power spectral density of far-field slat noise can be taken as a sum of the shape function and Lorentzian peaks, in deciBel units, and can be written as

$$\hat{\Pi} = \hat{a} + \hat{F}(f_d, M) + \hat{D}(\theta, \phi) + \sum_{n=1}^{N_p} \hat{L}(St_n, h, w) \quad (5.24)$$

whose uncertainty arising from individual terms can be combined using the general derivative formula for the variances, i.e.

$$\sigma_{\hat{\Pi}}^2 = \frac{\partial \hat{\Pi}}{\partial \hat{a}} \sigma_{\hat{a}}^2 + \frac{\partial \hat{\Pi}}{\partial \hat{F}} \sigma_{\hat{F}}^2 + \frac{\partial \hat{\Pi}}{\partial \hat{D}} \sigma_{\hat{D}}^2 + \sum_{n=1}^{N_p} \frac{\partial \hat{\Pi}}{\partial \hat{L}_n} \sigma_{\hat{L}_n}^2 \quad (5.25)$$

$$= \sigma_{\hat{a}}^2 + \sigma_{\hat{F}}^2 + \sigma_{\hat{D}}^2 + \sum_{n=1}^{N_p} \sigma_{\hat{L}_n}^2 \quad (5.26)$$

The shape function is taken directly from Guo's model and has the following form

$$F(St, M) = \frac{M^2 L_S}{c_0} \frac{St^2}{(1 + \mu_0^2 St^2)(1 + \mu_1^2 (1 + M)^2 St^2)(1 + \mu_2^2 M^2 St^2)(1 + \mu_3 M St^2)} \quad (5.27)$$

or by collecting the variables as

$$\begin{aligned} F_1 &= \frac{M^2 L_S}{c_0}, \\ F_2 &= \frac{1}{1 + \mu_0^2 St^2}, \\ F_3 &= \frac{1}{1 + \mu_1^2 (1 + M)^2 St^2}, \\ F_4 &= \frac{1}{1 + \mu_2^2 M^2 St^2}, \\ F_5 &= \frac{1}{1 + \mu_3 M St^2} \end{aligned}$$

we have

$$F = \frac{F_1}{F_2 F_3 F_4 F_5} St^2 \quad (5.28)$$

Here the calibrating coefficients $\mu_0, \mu_1, \mu_2, \mu_3$ were predicted by the surrogate model as a function of the slat position. Uncertainties in the calculation of these variables can be translated to the uncertainty of the predicted spectra by considering their sensitivities via the gradients, and can be written in primitive units as

i.e.

$$\sigma_F^2 = \left(\frac{\partial F}{\partial \mu_0} \right)^2 \sigma_{\mu_0}^2 + \left(\frac{\partial F}{\partial \mu_1} \right)^2 \sigma_{\mu_1}^2 + \left(\frac{\partial F}{\partial \mu_2} \right)^2 \sigma_{\mu_2}^2 + \left(\frac{\partial F}{\partial \mu_3} \right)^2 \sigma_{\mu_3}^2 \quad (5.29)$$

where the partial derivatives can be obtained as

$$\frac{\partial F}{\partial \mu_0} = \frac{F_1}{F_3 F_4 F_5} \times \frac{-2\mu_0 S t^2}{(1 + \mu_0^2 S t^2)^2} \quad (5.30)$$

$$\frac{\partial F}{\partial \mu_1} = \frac{F_1}{F_2 F_4 F_5} \times \frac{-2\mu_1 (1 + M)^2 S t^2}{(1 + \mu_1^2 (1 + M)^2 S t^2)^2} \quad (5.31)$$

$$\frac{\partial F}{\partial \mu_2} = \frac{F_1}{F_2 F_3 F_5} \times \frac{-2\mu_2 M^2 S t^2}{(1 + \mu_2^2 M^2 S t^2)^2} \quad (5.32)$$

$$\frac{\partial F}{\partial \mu_3} = \frac{F_1}{F_2 F_3 F_4} \times \frac{-M S t}{(1 + \mu_3 M S t)^2} \quad (5.33)$$

The above formulation is used to calculate the uncertainty of the broadband shape function output by the surrogate model. This gives the power spectral density and now needs to be converted to decibels.

The formula for the Lorentzian peak functions has the form

$$L_n = L(St_n, h, w) = \frac{h}{1 + \left(\frac{St - St_n}{w/2} \right)^2} \quad (5.34)$$

and where h is the height of the peak, St_n is the central frequency and w is the peak width. The uncertainty with respect to these parameters can be obtained as

$$\sigma_L^2 = \left(\frac{\partial L}{\partial St_n} \right)^2 \sigma_{St_n}^2 + \left(\frac{\partial L}{\partial h} \right)^2 \sigma_h^2 + \left(\frac{\partial L}{\partial w} \right)^2 \sigma_w^2 \quad (5.35)$$

where the partial derivatives can be obtained as

$$\frac{\partial L}{\partial St_n} = \frac{8(St - St_n) \times h}{w^2 \left(1 + 4 \left(\frac{St - St_0}{w} \right)^2 \right)^2} \quad (5.36)$$

$$\frac{\partial L}{\partial h} = \frac{1}{1 + \left(\frac{St - St_0}{w/2} \right)^2} \quad (5.37)$$

$$\frac{\partial L}{\partial w} = \frac{8h(St - St_n)^2}{w^3 \left(1 + \left(\frac{St - St_0}{w/2} \right)^2 \right)^2} \quad (5.38)$$

Since the uncertainties of the individual peaks can be taken to be independent of each other,

$$\sigma_{\sum_{n=1}^{N_p} L_n}^2 = \sum_{n=1}^{N_p} \sigma_{L_n}^2 \quad (5.39)$$

For converting the uncertainty to dB, we need the formula for error propagation in a logarithm function, i.e. if $f = \ln(z)$

then, by the gradient formula,

$$\sigma_f = \frac{\sigma_z}{z} \quad (5.40)$$

Finally, since the acoustic spectra in dB with reference to the $20\mu\text{Pa}$ level,

$$\hat{\Pi} = 10 \log_{10} \left(\frac{\Pi}{P_{ref}^2} \right) = 10 \frac{\ln \left(\frac{\Pi}{P_{ref}^2} \right)}{\ln(10)} = 10 \frac{\ln(\Pi) - \ln(P_{ref}^2)}{\ln(10)} \quad (5.41)$$

Therefore,

$$\sigma_{\hat{\Pi}} = \frac{10}{\ln(10)} \frac{\sigma_{\Pi}}{\Pi} \quad (5.42)$$

which applies to all terms which are not modeled in the decibel units. Hence, finally for the spectra computed using the surrogate model, we have the total uncertainty as

$$\sigma_{\hat{\Pi}}^2 = \sigma_a^2 + \sigma_F^2 + \sigma_D^2 + \sum_{n=1}^{N_p} \sigma_{L_n}^2 \quad (5.43)$$

$$\sigma_{\hat{\Pi}}^2 = \sigma_a^2 + \left(\frac{10}{\ln(10)} \right)^2 \left(\frac{\sigma_F^2}{F} + \frac{\sigma_D^2}{D} \right) + \sum_{n=1}^{N_p} \sigma_{L_n}^2 \quad (5.44)$$

Finally, to obtain the total uncertainty of the predicted spectra over the range of frequencies, we consider the integral of the spectral uncertainties in the dB units as appropriate, which can be written as

$$\hat{\Sigma}^2 = \int \sigma_{\hat{\Pi}}^2(f) df \quad (5.45)$$

5.9 Acquisition Function for Uncertainty Cased Sampling

Sampling the next simulation based on the current dataset is enabled in Bayesian optimization by combining the two above said techniques, i.e. by using the surrogate model and its uncertainty estimate. The straightforward approach for uncertainty based sampling is to look at points where the uncertainty is highest and sample a new point from this vicinity. Such a criteria looks only at the current state of the model and the effect of sampling on the immediate next state after the sampling. However this approach has shown to be sub-optimal when it comes to obtaining the best sample. To obtain a better estimate of the most efficient sample, a sample estimator is typically used in Bayesian optimization and is called the Acquisition function.

Many acquisition functions have been proposed in the literature, with one of the early ones being the Probability of Improvement (PI). This method is based on an estimate of the aforementioned acquisition function with the objective of minimizing a given cost function and select the sample which has the best probability. However, by nature of its formalism, it suffers from the problem of local minima. This difficulty is overcome by the Expected Improvement function in the work of Mockus et al. [162]. As elucidated by Letham et al. [163], here the a utility function was chosen such that

$$u(x) = \max(0, g' - g(x))$$

where g' is a current estimate of the minima of an arbitrary function of interest approximated by a Gaussian posterior g . The utility function $u(x)$ then collects a reward equal to the improvement $g' - g(x)$ or otherwise collects nothing. The expected improvement for acquisition for a given sample x in its formal definition is the expectation of this utility function defined as

$$\begin{aligned} a_{EI}(x) &= \mathbb{E}[u(x) | x, \mathcal{D}] \\ &= (g' - \mu(x))\Phi(g'; \mu(x), K(x, x)) + K(x, x)\mathcal{N}(g'; \mu(x), K(x, x)) \end{aligned}$$

where \mathcal{N} and Φ are the density and cumulative distributions functions of a standard normal distribution and μ and K are its mean and covariance matrix. A more rigorous account of the same is available from Zhan and Xing [164]. Here the two terms arising from this definition contribute to two different factors that control an exploratory process. One is the contribution from the mean function which biases the estimated sample to minimize the mean function leading to finding the optima. The other terms proportional to the variance will bias the function towards areas where the function has large predictive variances, leading the optimizer to explore the domain potentially away from optimas. Thus there is a competition between the exploration and exploitation of the domain. Essentially, all acquisition functions fundamentally address this tradeoff and attempts to minimize the overall uncertainty in the least number of sampling operations. In this regard, the Expected Improvement (EI) is considered the standard procedure in application to finding the optima using Bayesian Optimization.

A further improvement of the acquisition function came from the work of Hennig and Schuler [165]. Their suggestion was to use an acquisition function that minimize the uncertainty present in the location of the already computed optimal value. The method thus called the Entropy Search attempts to minimize the information entropy of the predictive distribution, but however due to the excessively complicated formalism, a closed form of the function is not derivable analytically and for applications, an approximate form is used for the computations.

An acquisition function applicable to the case of surrogate modelling with a straight forward explicit calibration of the exploitation-exploration trade off is the Upper Confidence Bound (UCB) proposed in the work of Kaufmann et al. [166]. This function uses a simple algebraic form to obtain a utility function defined as

$$a_{UCB}(x; \beta) = \mu(x) + \beta\sigma(x) \quad (5.46)$$

The two terms are the mean function $\mu(x)$ and the scaled standard deviation $\beta\sigma(x)$ and the scaling factor β serves as a control between biasing the functions towards the maxima (exploitation) or to uncertain regions of the domain (exploration). For using the UCB algorithm, two approaches can be followed. One is that the extremum of a_{UCB} can be used to pick a sample for next data acquisition step and only β needs to be adjusted in order to calibrate the acquisition process. The other is to use a_{UCB} as a probability density function and sample from the distribution. The second variant leads to the stochastic UCB algorithm and allows to maintain a distributed random sampling over the domain. Compared to the non-stochastic version, this allows to ensure that the algorithm does not tend to conservatively follow the acquisition function itself but also allows a reasonable calibrated exploration of the domain.

For the purpose of our work, we choose to use an adapted version of the stochastic UCB algorithm. For this, we use the utility function in Eq. 5.46, and use an additional thresholded distribution with 99% percent of the maximum as the threshold. The additional thresholding was found to be aiding in amplifying the PDF generated by the raw utility function a_{UCB} and hence enabled a more conservative sampling in terms of sampling efficiency. Consequently we chose to sample in batch sizes of 5 points to carry out the CAA simulation and acquire spectra from the space of slat position parameters.

5.10 Results

5.10.1 Feature Extraction

The feature extraction module was designed and implemented for our work using a Python workflow. Each of the simulated spectra was obtained at a frequency resolution of 44Hz and was then fed into a Least Square (LS) fitting algorithm using the python package SciPy. The obtained feature extraction module is observed to be of sufficient accuracy to extract the broadband and tonal characteristics of the spectra and a few select cases from the dataset after the LS fit are shown in Fig.5.3. In contrast, the true spectra has a large variance in the frequency domain, the obtained Guo's shape function fit is a smooth representation of the same. Regarding the peaks, the Lorentzian peak functions are a satisfactory fit for the actual tonal characteristics in a representative fashion. The convergence of the feature extractor to extract the central frequencies and peaks heights are also found to be satisfactory. However, from an aeroacoustic perspective, the broadening of a tonal peak has its own implications related to the convection of the waves, source effects, and effects of the presence of solid bodies which are all pertinent to the slat geometry case. In our study, this factor is not investigated and is hence not included in the design of the surrogate model. The typical broadband shape function also models the spectra such that there is a larger deviation at the lower frequencies which are considered to be the range where the background noises are prominent in a real experiment. This noise is minimal in the numerical case but the levels obtained using our simulations are still higher than modeled using the Guo's shape function.

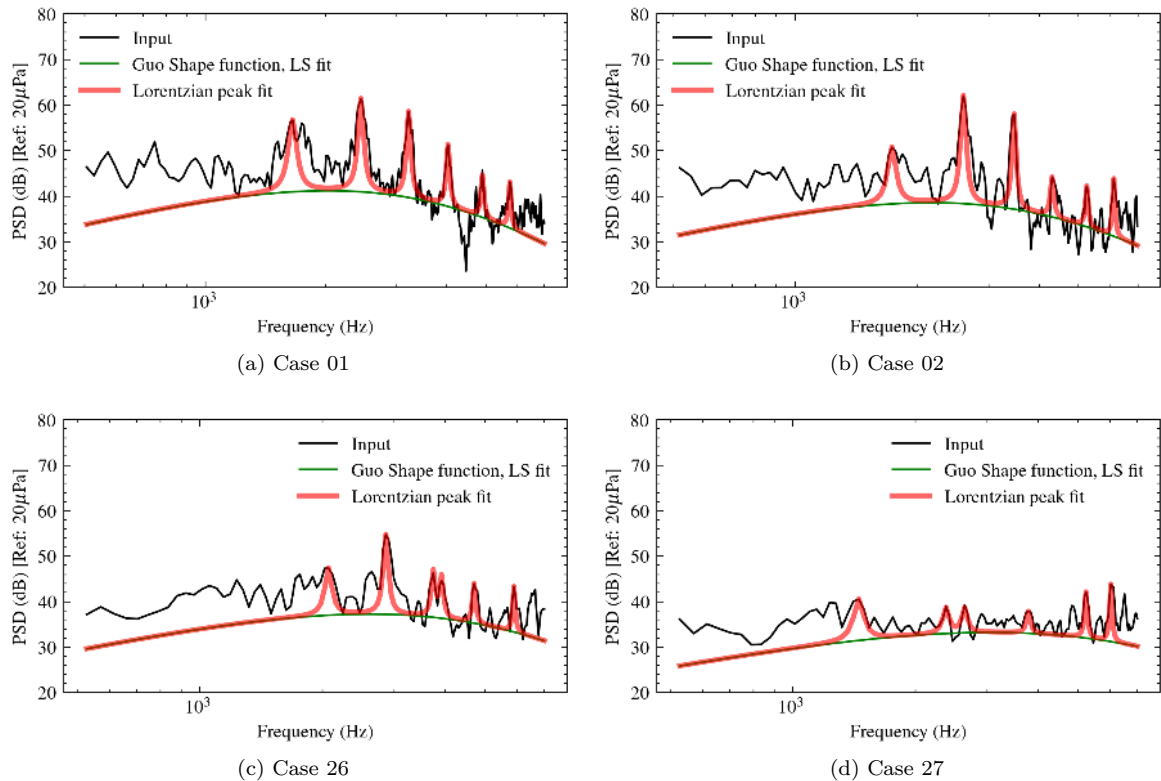


Figure 5.3: Feature extraction for the spectra using Guo's shape function and Lorentzian peaks, showcasing few cases from the dataset

5.10.2 Surrogate model

The Bayesian Surrogate model approximates a high-dimensional map from the space of 4-dimensional positional parameters of the slat to the 17-dimensional representative variables for the far-field noise spectra. A measure of the accuracy of the model is the overall uncertainty of the model integrated over the domain of experimentation. This uncertainty however is not easily calculable since it involves computing the predictive variance over the 4D domain with sufficient resolution. Hence for a direct comparison on the predictive accuracy of the targets with training data and within the domain of interest, only the quantitative measures are useful whereas the graphical representation provides a qualitative idea of the accuracy.

The Bayesian model was initialized using 10 data points from the prescribed domain as shown in Table 5.1. For a total of 18 simulations, the fitting of target variables in training dataset were visualized using a residual scatter plot in Fig. 5.4. Different target features have shown an excellent fit while using the Squared Exponential Kernel and with an initial noise parameter, $\sigma_n = 5\%$.

The predicted parameters were then used to predict the model parameters of the spectra which were then used to reconstruct the spectra in decibel units. The uncertainties of the predicted variables were also propagated to the frequency domain of the spectral predictions using the methods described in Section 5.8. With the availability of the first 10 data points, a prediction of the spectra is possible for any query point within the domain. Hence, to demonstrate the working of the model, a prediction on a randomly selected training point is shown in Fig. 5.5. The four predictions shown are obtained by varying the initial noise parameter, $\sigma_n(\%) = [50, 5, 1, 0]$ that is used to generate the model and the predicted variances are also proportional to the initial assumption according to Eq. 5.10. It can be seen in 5.5a that if the initial noise is assumed to be 0%, then the predictive variance will also collapse to null leading to the GP model having 100% confidence in the training datapoints. The predicted response surface of this model fits the training target values exactly and hence leads to an exact reconstruction of the spectra. The resulting predictive variance is then zero and hence is absent in Fig. 5.5a. As the variable σ_n is increased, the predictive variance is also amplified accordingly. As can be noticed in Fig. 5.5d, a sufficient initial noise assumption leads to a non-zero predictive variance as well as lower confidence of model in the training dataset. The non-zero variance assumption leads to a non-zero variance prediction for the response surface at the collocation points from training data and hence a slightly inaccurate prediction of the spectra. The inaccuracy is noticeable in the prediction of the central frequencies of the tones as they are visibly deviating from the original peaks in Fig. 5.5d.

The predictive variance for the broadband shape seems to have a good agreement even with a noise assumption of $\sigma_n = 5\%$. However, the uncertainty for the peaks have a higher value on both sides of the peaks. This is due to the fact that in our routines, we only extract the central frequency and the peak height while modelling the peak using the Lorentzian peak function. This leaves out the peak width parameter that is kept constant and is hence not extracted from the training data or used in the prediction. This omission leads to a difference of levels between the predicted spectra and the modeled spectra on the both sides of the peak while the zenith is rightly modeled from the peak height. This problem is infact solvable by taking into account the peak width parameter in the regression, but the feature extraction procedure needs to take into account a total of 23 features instead of 17, and was found to be unstable during the feature extraction using least square fitting. An upgradation of this feature extraction technique using advanced methods must therefore eliminate the amplified variances on the slopes of the peaks resulting in a uniform predictive variance in the spectral domain.

It must also be mentioned that the noise assumption in the input data stems from the assumption of aleatoric uncertainty in the data acquisition and processing. However, the predictive variance represents

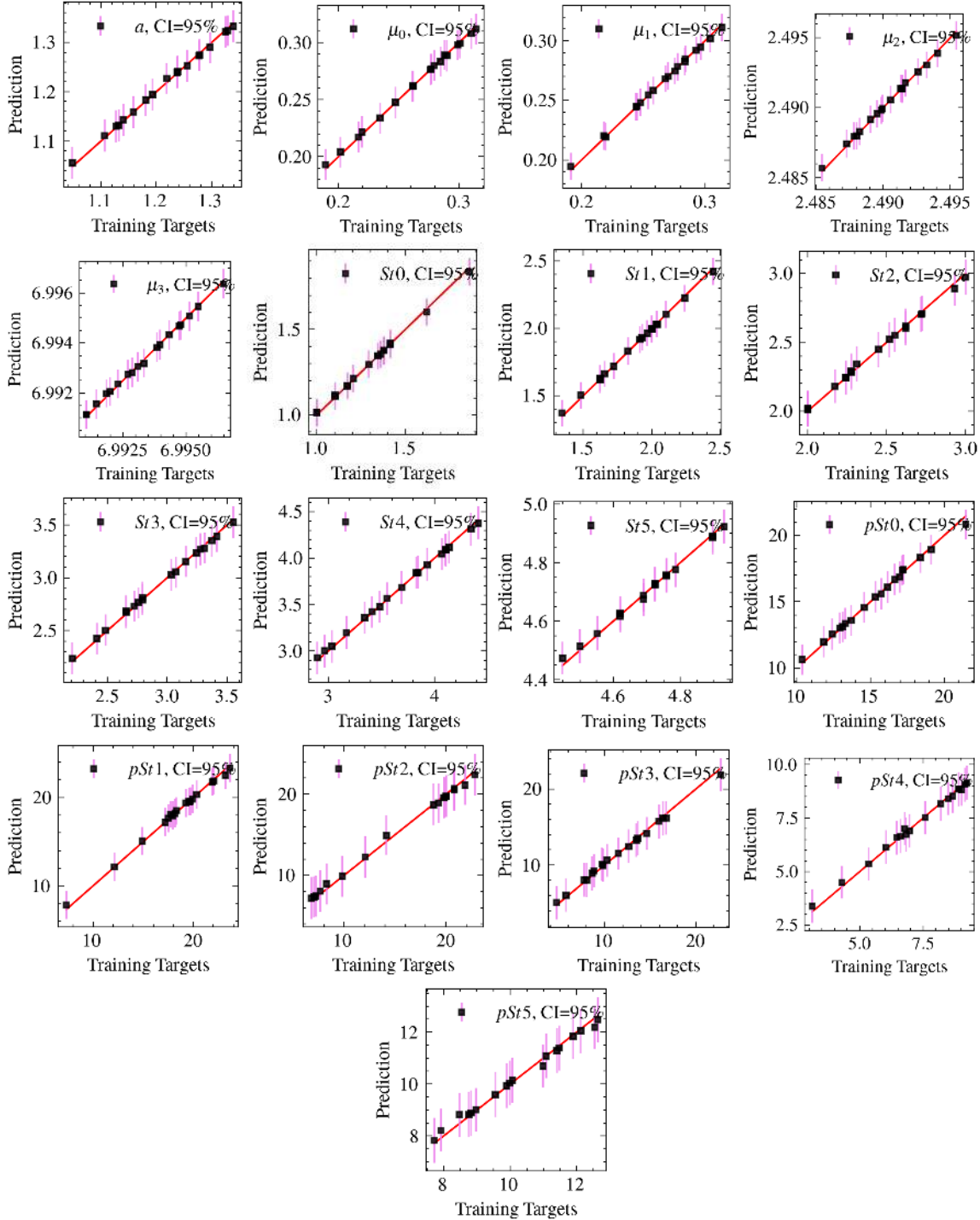


Figure 5.4: Scatter plots of the input targets against the 17 predicted target variables used in regression, over datapoints in the training set of first 18 simulations. The diagonal line $y = x$ is given for comparison representing a zero residual. For this demonstration, $\sigma_n = 5\%$.

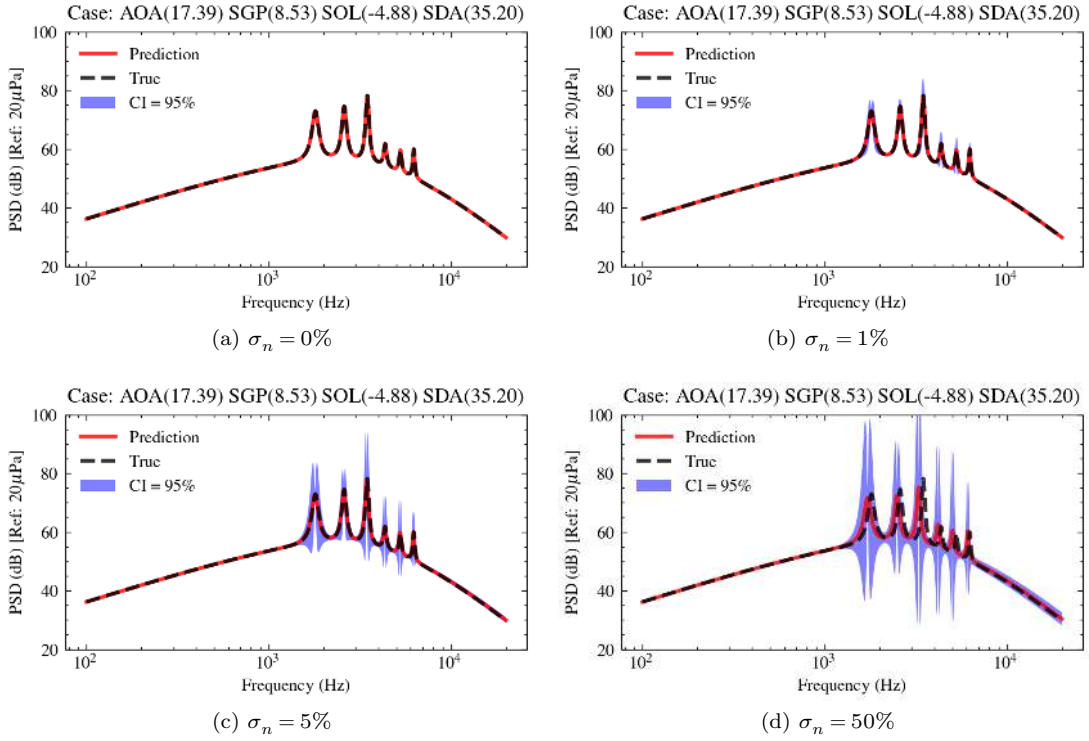


Figure 5.5: Spectra predicted using the Gaussian Process Surrogate model by using the first 10 initial samples, tested on a randomly selected datapoint ($\text{AOA} = 17.39^\circ$, $\text{SGP} = 8.53\text{mm}$, $\text{SOL} = -4.88\text{mm}$, $\text{SDA} = 35.2\text{mm}$) from the training set, and when the initial noise parameter is set to four different values are shown. The total estimate at a datapoint reduces to the aleatoric uncertainty by the nature of GP regression and hence is only sourced by the aleatoric uncertainty represented by the prior noise assumption in data through σ_n . The noise parameter is also updated at each iteration before the active learning sampling and thus does not maintain a stationary value. This parameter hence should not be misinterpreted as representing spectral level uncertainty in quantitative terms, but only as a model parameter allowing the estimation of model's statistical uncertainty.

the total uncertainty of the model prediction including the additional epistemic uncertainty arising from the Bayesian surrogate modelling. The fact that the initial noise assumption is necessary to obtain a non-zero predictive variance is due to the fact that in the Bayesian regression formalism, the predictive variance arises as a function of the initial noise assumption as seen in Eq.5.14.

Now that the inaccuracies arising from omission of peak width in the regression module and the effect of the noise parameter is understood, we choose to keep the noise parameter at 5% and assess the overall variance of the model over the chosen domain of the slat positional parameters. For this the model is used to make predictions of the target variables and the spectra is reconstructed for collocations points on a uniform grid in the 4D domain. We call this the test domain and is the same as defined by Table. 5.1. Also, for computing the total uncertainty for each spectra, we integrate the predicted variance over a range of [100, 20000]Hz, and this sum, without averaging over the frequency domain, is what we call Total Spectral Variance (TSV) as defined in Eq.5.45. This value is then obtained over the discretized test domain whose grid size is kept at 8 points within the corresponding interval for each variable. In the initial state of the model using 10 input points, the TSV is obtained at 68.84 dB.

The Total Spectral Variance distribution over the test domain is a measure of the statistical accuracy of the surrogate model, expressing the total epistemic uncertainty. Hence the Mean Total Spectral Variance (MTSV) can be used to monitor the progress of the surrogate model during the course of the active

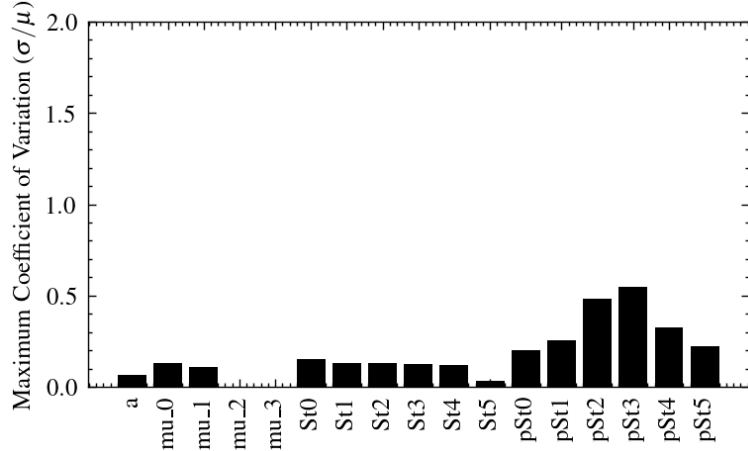


Figure 5.6: Maximum Coefficient of Variation in the test domain after the last step of active learning executed with total number of simulations at 18.

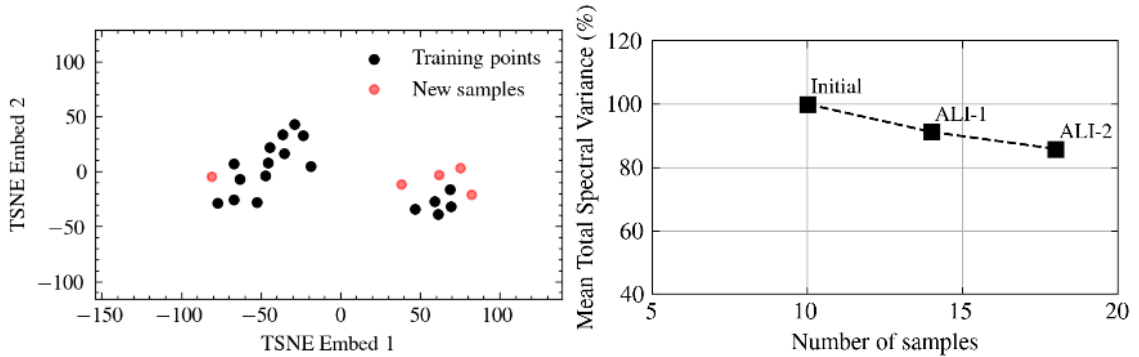


Figure 5.7: Left: A t-SNE visualization of the high dimensional feature space of the training dataset of 18 simulations together with 5 newly sampled points to be used for subsequent data acquisition. The t-SNE hyperparameter 'perplexity' is maintained at value 5. Right: MTSV over the domain for the surrogate model expressed as a percentage of the initial model (MTSV is calculated in dB), plotted as a function of the number of samples acquired during the active learning procedure.

learning procedure. The active learning model is then used to progressively update the model to obtain a reduction on the MTSV until satisfactory convergence. Here, as an experiment we choose to use a batch size of 5 simulations to sample the spectra. Note that although the sample size is set to 5 for each set, the number of successful simulations can be lesser due to technical errors and on average is maintained at 4. The evolution of the MTSV with respect to the active learning steps during the initial stages of the model development are shown in Fig. 5.7. Additionally to monitor the sampling of points, we choose to visualize the 4D domain using a dimensionality reduction using t-Stochastic Neighbor Embedding. The visualization allows to monitor the relation between the sampled points and the points in the dataset based on their Eulerian distance in the 4D domain. Here the clustering of the points represents close proximities and the sampling is monitored to generate points which maintains a compromise between conformance to the clustering (exploitation) and sufficiently balancing the different clusters (exploration).

5.11 Conclusions

A method for automating the exploration of parameter space of slat positioning with respect to the airfoil was developed for the particular application to aeroacoustic investigation. By no means we claim the optimality of the design of the current state of this approach but is an experimental step towards a more advanced application in the domain. Currently, a framework which is able to handle the spectral data – including the broadband components and the tonal peaks – as the target features and slat coordinates as the input variable is developed by appropriate feature extractions. Then a Gaussian Process Regression is used to obtain a surrogate model of the available data. Gaussian Processes being a statistical regression tool based on the Bayesian formalism, a measure of uncertainty of the model is implicitly available along with its concurrent state. This epistemic uncertainty is high during the initial phase of the exploration and the sampling process is then adapted to minimize this uncertainty. A few methods to leverage the uncertainty information and obtain an optimal sampling were attempted and finally the Upper Confidence Bound method is chosen for the current application. Consequently a roadmap for uncertainty calculations for the spectra predictions are also developed that are extensible to more complex scenarios. The algorithm is then shown to carry out exploration where the model is pinned to the most noisy configuration which is close to the standard slat positioning. The epistemic uncertainty is then shown to have a monotonic decrease.

As for demonstration of the model, a few predictions based on parametric variation of the slat overlap and slat gap is made. Variation of the spectra for the strength of the peak and the distribution of energy between the peaks can be observed. For an progressive increase of the slat overlap from extreme value of -15.0 to -4.0, the surrogate model predicts the standard spectra as the base line. For further increase from -3.0 to -2.0, a region where data is available from the dataset, the peaks show a decrease in the resonant frequency as expected. This consistent with the fact that the increase in overlap leads to additionally skewed shear layer path length which is longer in length and thus reduce the Rossiter frequencies due to higher vortex travel times. The effect is nullified and the model returns to standard spectra as the slat overlap is further increased to -1.0 where data is not available in the dataset. Note that the prediction now can be made for any continuous trajectory in the parameter space.

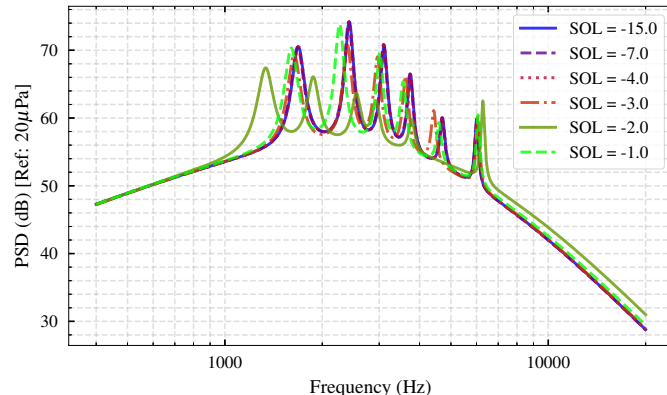


Figure 5.8: Parametric predictions using the surrogate model by varying the slat overlap (SOL). Other coordinates: AOA:18.0mm, SGP:4.0mm, SDA:35.2°

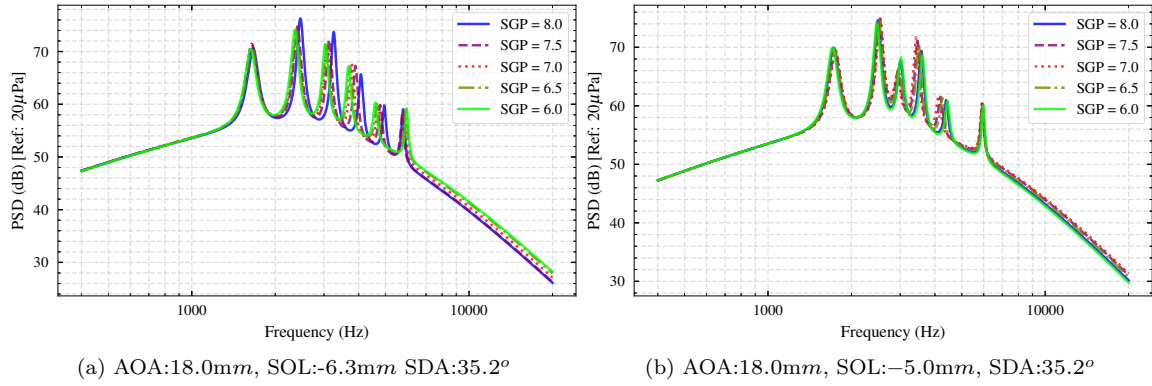


Figure 5.9: Parametric predictions using surrogate model by varying the slat gap (SGP). a) The sensitivity of SGP is higher with SOL as -6.3mm . b) The sensitivity is reduced at an increased overlap and is the same case for further increase. The slat gap parameter is most sensitive thus close to the nominal slat overlap configuration.

That being demonstrated that the model is fully viable for a data-driven noise surrogate model for industrial cases, it is imperative to delineate the limitations of the current implementation. The surrogate model currently has been fed with only few datapoints, i.e. 18 data points. This occurred due to the technical difficulties and to obtain a fully viable surrogate model, the simulation based on active learning must be continued for sufficient number of acquisitions such that the Mean Total Spectral Variance is converged to the best possible value. Further improvements can also be made in the design of acquisition function, in accordance with the evolving literature, such that the active learning methodology itself is improved leading to a higher sample efficiency. However this is beyond the scope of our work within the premise of the slat noise investigation. Thus although the surrogate model is used for exploring the parameter space utilizing the Bayesian sampling technique, the model itself is declared as requiring further accuracy before deployment for use in the HLD design setting.

Now, for the continuation of slat noise investigation, the aeroacoustic LBM simulations that we conducted were used to record pertinent information regarding the flow dynamics. These datasets thus allows for a fundamental analysis into the flow dynamics. This will be attempted in the upcoming chapter.

Chapter 6

Cove Vortex Dynamics in light of parametric LBM simulation

6.1 Introduction

The Bayesian framework together with ProLB and FWH modules explained in the previous chapter enables a computational investigation of the slat noise phenomena with unprecedented detail. The Bayesian Active Learning method is a numerical twin for a real-time experimenter who samples simulations based on the uncertainty of the noise surrogate model within any selected domain. The special application to aeroacoustics that we designed in this work approximates the acoustic data in the form of far-field spectra as a function of the position of slat with respect to the main element. A spectra is thus predicted by the model for any slat position along with a measure of its own epistemic uncertainty. A stochastic Upper Confidence Bound (UCB) algorithm then ensures that the model's exploration is always pinned to the noisiest case and hence collects data which are relevant to the noise characteristics. While this framework paves way to an optimal and automated aeroacoustic design optimization, in our current activity, we also enable data recording such that the phenomenology of cove dynamics can be investigated. This chapter is dedicated to this exploration of the dataset, with the ambition to manually elaborate on the newly found cove dynamics. For this we focus particularly on the spanwise modulations of spanwise component of velocity, their periodic bursting behaviors at diverging planes, and how they affect the slat noise characteristics, and deploy comparative analysis across cases by varying the slat positioning for the standard VALIANT 2 element geometry.

As pilot investigation, we used the case of standard positioning of the slat in Chapter 3 to demonstrate that the spanwise modulations, that are newly found in the cove flow, suggests that the recirculation bubble has a non-homogeneous distribution of both time-averaged velocity and pressure along the spanwise direction. These modulations are also shown to be attached to the curved shear layer during its early spatial development although the whole volume of the cove remains modulated by phase-inverted arrangement of these cells. The presence of periodic inversion of spanwise velocity along the span also necessitates a mechanism that allows the stability of the converging and diverging planes which acts as sources and sinks for the spanwise flow. Here, the streamwise oriented small-scale recirculating structures are entrained by the shear layer and the recirculation resupplies them back into the cove. However, in view of the 1-dimensional spanwise dynamics, the velocity with which the shear layer entrains the structures from a spanwise converging plane is approximately the free stream velocity outside shear layer, but the velocity responsible for replenishment of the diverging planes is the velocity of recirculation. The

former is higher than the latter, the difference being quantitatively captured by the velocity ratio, and hence a mass and pressure deficit develops in the diverging planes of spanwise velocity. We theorized in the Chapter 04 that this leads to the low frequency “bursting” of the cove at the diverging planes and demonstrated that this frequency corresponds to $St \approx 0.16$. This was the case when the slat position is standard without additional deformation of the shear layer by variation of the slat position with respect to main element.

To understand this low frequency oscillation and its effects, the unsteady velocity inside the cove has to be studied. Since the cove flow and the impingement location have quasi-periodic oscillatory motions[29] the time-averaged velocity field removes relevant information. Hence the unsteady velocity fluctuations need to be studied using the spanwise variation of its spectral components which can be computed using probe recordings and used to extract the behavior in parametric cases as the slat position is varied. This will be one objective of the discussions in this chapter.

Another important aspect of the cove dynamics which is related to slat acoustics is the vorticity transfer from 2D spanwise coherent structures in early shear layer to the smaller scale streamwise structures towards the slat gap. It is clear that the spanwise coherent vortex structures are responsible for driving the aeroacoustic resonance. However, this spanwise vorticity is not fully preserved as the shear layer develops towards the impingement location. The streamwise vortex structures from the recirculation interacts with the shear layer from the early development near the cusp and intertwines with spanwise structures to form a ladder structure. Towards impingement, the spanwise vorticity is thus largely converted to streamwise vorticity, the latter being a less efficient source of noise, both by driving an aeroacoustic loop or by trailing edge scattering. Extrapolating this scenario, we put forward the case that if the vorticity conversion effect is strong enough such that the reminiscent spanwise coherent vortex core that impinges the upper slat wall is weaker than that required to excite a resonance, the Rossiter tones can disappear. In between the extreme cases, it should also be possible to obtain a progressive suppression of the tones thereby obtaining a model for the strength of the tones together with already available frequency prediction using Rossiter model.

More importantly, and apart from this vortex dynamics which are clearly notable in the visualizations of simulation data, we also conjectured in this work that the fundamental driver of vorticity conversion to streamwise direction is not the interference by the entrainment of streamwise recirculating vorticity but is an effect of the shear layer curvature. In this direction, Wang et al. [167] previously showed that Görtler-like instability of the shear layer due to strong unstable curvature near the trailing edge can occur in case of low Reynolds numbers where the spanwise vortex shedding is weak. Early works of Bradshaw [139], Bradshaw and Young [140], and more recently Liou [128], have shown that a curved shear layer is linearly unstable due to the effect of curvature and can develop streamwise oriented vorticity by developing spanwise instability modes. Bradshaw also drew parallels between the case of a buoyancy driven flow under density stratification and a shear layer development under action of centrifugal force. Their studies both suggest that a formulation of the curvature Richardson number can quantitatively capture the transfer of vorticity between streamwise and spanwise directions, if the flow is within linear approximations. Nevertheless, in contrast, the length scales and flow magnitudes in the slat flow case suggests that the curvature effects in cove dynamics should be strongly non-linear and saturated. Hence, the interactions cannot be accurately captured using a simplified formulation of the Richardson number. In how much the curvature Richardson number, or a cumulative history of the same along the shear layer path, can represent the relative strength of tones is thus the second objective of discussions in this chapter.

For structuring the discussions we utilize Section 2 to discuss the mean flow fields from the dataset to understand the different flow cases and to identify a few particular cases for a more detailed analysis. In Section 3, the acoustic predictions for each of the cases are documented to understand how the far-field

noise can be related to the mean flow fields. In Section 4, we extract the shear layer shape from the mean flow for each of the cases available using methods explained in Chapter 4. In Section 5, 6, and 7, we choose 4 interesting cases and discuss the newly observed spanwise modes and their low frequency oscillations to establish the relations between the shear layer shapes and these behaviors. In Section 8, we include a few additional cases that we simulated during our investigation to improve the argument that the effect of the shear layer shape and the curvature Richardson number can explain the the variability of the tonal nature of slat noise. In Section 9, we also attempt to provide an estimation of the Strouhal number based on the details available from the dataset.

6.2 Mean Shear Layer Shape

The shape of the shear layer for all cases simulated are documented in Appendix B and a selected set of shear layer shapes and corresponding farfield spectrum is shown in Fig.6.1. For this figure we chose cases which have a strongly distorted shear layer shape compared to the rest of the dataset. The mean velocity fields at spanwise center-plane averaged over 5 chord pass times are used to generate the mean flow field. The procedure for obtaining the streamline using a Runge-Kutta integration of the velocity field and an apriori choice of an initial point near the cusp are elaborated in Chapter 4 Section 4.7. It is to be noted in particular that the mean fields are not averaged along the spanwise direction. This is due to the fact that the simulations were designed without prior knowledge of the spanwise modulations.

From the collection of shear layer shapes, the first observation is the sensitivity of shear layer shapes to the position of the slat. Clearly the shear layer shape is influenced by all three coordinates of the slat simultaneously, but it is the slat overlap which principally determine the shape of the shear layer while the slat deflection angle determines the initial curvature of the shear layer. The slat gap in contrast primarily affect the peak ejection velocity more than other characteristics and hence deemed as most important for the broadband noise level[27]. For the shear layer shape alone, the slat overlap determines the horizontal proximity of the slat to the main element and when increased with respect to standard slat position, the shear layer is forced to have a low initial curvature and stronger curvature at mid-length as the flow is redirected to flow through the slat gap. As such, the slat overlap significantly modifies the initial curvature of the shear layer and therefore the spanwise mode formations.

A particular case of high overlap is the Case 4. Here, the flow at the cusp is largely aligned with the incoming flow along the outer wall of the slat cusp and is not immediately redirected as for the standard case. Instead the curvature is minimal in the initial region with a strong curvature appearing in the mid-trajectory and closer to the main element. In Case 4, the slat gap is also particularly reduced to 4mm which reduces the ejected flow velocity to 60m/s which is a case of severe chocking when compared to the standard geometry which has an ejection speed close to 110m/s. This reduction of speed leads this case to have a strong deviation from the standard noise profile, both for the broadband levels and the Rossiter tones which is expected since the broadband noise trailing edge noise scales with M^5 .

In the same direction, Case 11 can be noted to have a less skewed shear layer shape with the impingement point closer to the trailing edge. Hence, the latter can be expected to have a slightly improved source efficiency for both broadband and tonal components. An even further improvement on the same is Case 19, which despite having a reduced initial curvature has a more evenly distributed curvature with the impingement point close to the slat trailing edge. As shown from the comparison of spectra in Fig.6.1, this significantly recovers the broadband and tonal characteristics. Note that the comparison is made by changing the shear layer shape but keeping the free-stream velocity and angle of attack constant.

A case of high initial curvature of the mean shear layer is Case 5. This high curvature is due to the fact that the slat overlap is high together with a sufficient slat gap such that the flow is strongly

redirected from the cusp towards the slat gap. Such high initial curvatures and high mean velocity along the shear layer leads to higher growth rates for the centrifugal related instability. However, in addition to this effect, the impingement point is deeper into the cove in this case as compared to the standard noisy configuration and hence the impinging vortices have a strong interaction with the turbulent region of impingement. Therefore, the spanwise coherence is significantly reduced before the flow approaches the trailing edge. This case hence have have a low efficiency source for the tonal and broadband components. Similar cases are Case [8, 9, 12, 14, 27, 28, and 30], whose impingement location is too upstream from the trailing edge to enable a strong noise source.

The cases with a strong characteristic broadband and tonal characteristics are those which are close to the standard geometry. The characteristic shear layer shape for this noisy configuration is clearly identifiable from the dataset. The main characteristics include a uniform distribution of the curvature magnitude together with a high ejection velocity, which in the standard noisy case is twice that of the free stream. Specifically, in the dataset probed by the Bayesian model, the most noisy case is Case 22. This case is acoustically similar to the standard positioning with the same angle of attack. The difference is that the slat is moved further outward from the main element due to a reduced slat overlap and also maintains a higher slat gap. The slat deflection angle is also decreased enabling the shed vortices to be convected along a moderately curved path to the the slat trailing edge. The positioning of the impingement location is also such that the vortical structures have minimal interaction with the stagnated turbulent region of the impingement by being convected directly to the trailing edge, but inevitably, the mean shear layer streamline from the cusp has incidence on the trailing edge wall. These characteristics renders Case 22 the most noisy in the dataset. This case is hence is taken as the base case for comparative analysis from here on.

To elaborate further, we must discuss the numerical calculations based on the mean shear layer and before this we take a quick detour to discuss the details of the observed acoustic characteristics in the upcoming subsection for completeness.

6.3 Far-field Spectra

The acoustic signature of three parametric cases whose broadband component is strong relative to other cases in the dataset are shown in Fig.6.2. The farfield spectra is compared against the base case, Case 22. As mentioned, this case is chosen since it both reproduces the farfield spectra from the experimental case very closely and is the loudest among the cases generated using the Active Learning approach. The spectra is calculated using the FWH approach detailed in Chapter 3 Section 3.5.

For the given VALIANT geometry and Reynolds number, the first major tone can be noticed at approximately 1771Hz for Case 22 similar to the experiment. A lower frequency hump is also suspected at $1771/2 = 885$ Hz as suggested by the first Rossiter mode calculation according to Terracol et al. [14], however not noticeable in the experiment. This hump is usually not noticeable in experimental studies since at frequencies close to and less than 800Hz, the noise from jet shear layer issued from the wall lips of the tunnel and other installation noises are prominent. This noise floor is not present in the simulations of the airfoil in free-stream and the low frequency hump is hence noticeable for most of the noisy cases.

The primary observation from the comparative analyses that can be deduced from the full dataset (see Appendix B) is that the Rossiter mode frequencies can be seen to be prominent only for cases that have an impingement location close to the slat trailing edge. For Cases [4, 5, 6, 8, 9, 28, and 30], the Rossiter modes are absent along with a significantly lower broadband component. In cases where the Rossiter tones are prominent, the frequency of modes show variations with respect to the slat positioning. Compared to the Case 22, Cases [7, 15, 16, and 17] (see Fig.6.2 and Appendix B) shows a significant shift of all the

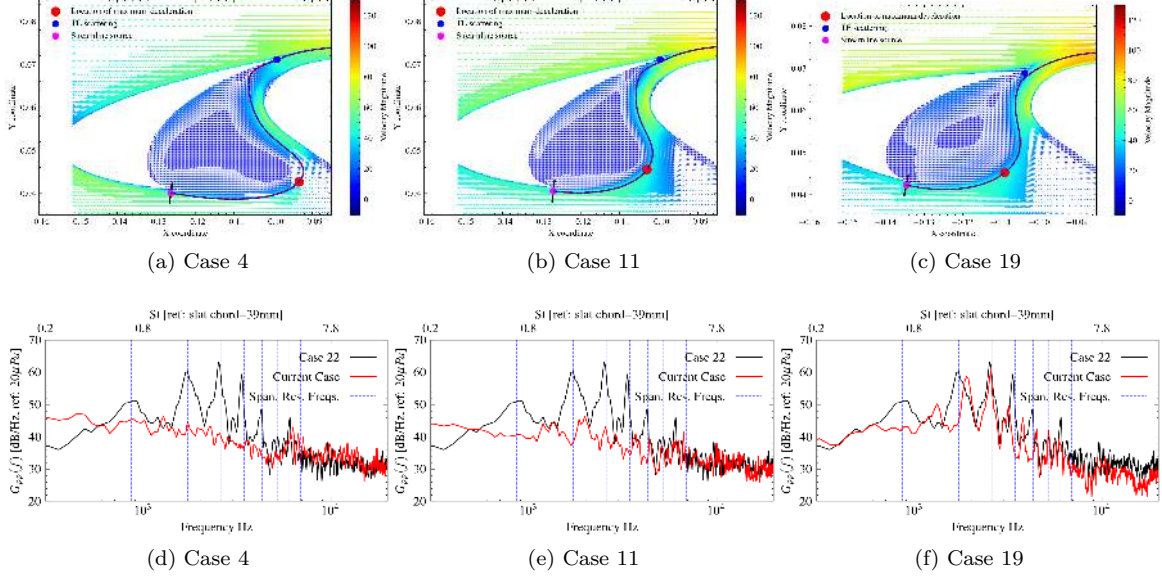


Figure 6.1: Top: The mean shear layer trajectory at mid-span plane for select cases with a strong distortion of the shear layer. Bottom: Corresponding far-field noise spectrum at 90° observer angle showing the variation of tone frequencies as shear layer shape is varied.

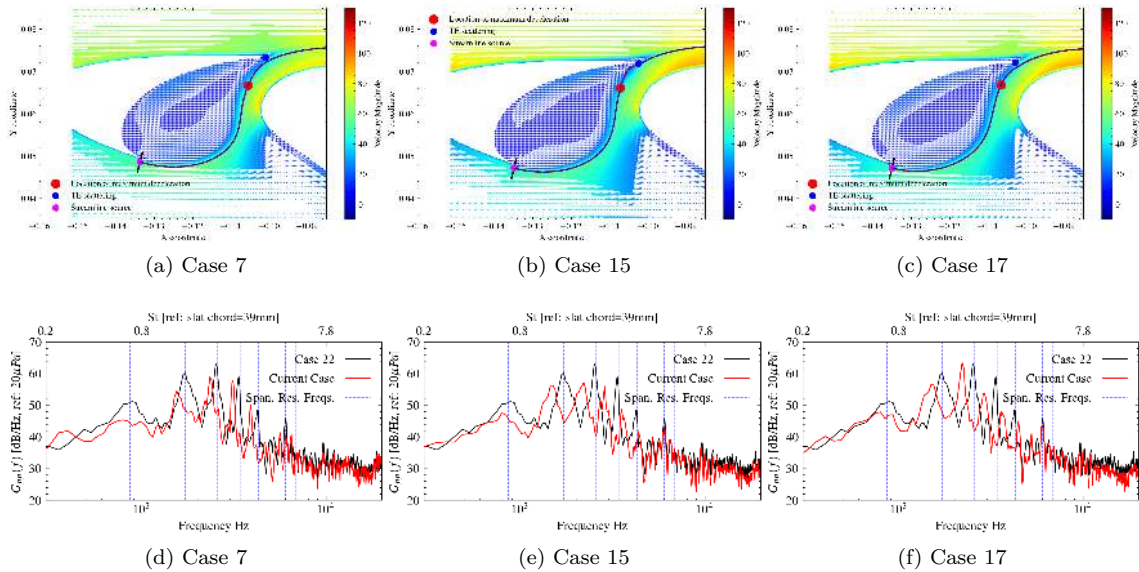


Figure 6.2: Top: The mean shear layer trajectory at mid-span plane for select cases which has a positive slat overlap. Bottom: Corresponding far-field noise spectrum at 90° observer angle showing a different selection of tone frequencies according to shear layer shape variation at same spanwise simulation domain.

tones. It can also be noted that the shift of frequency of the tones are not equal for all the tones. The first five Rossiter modes which are multiples of the fundamental at 885Hz have a higher correlation in the frequency shift than the sixth tone at approximately 6500Hz. This sixth tone also shows anomaly by being present in the cases which have a deformed shear layer as in the case of Cases [4, 12, 27, and 30], while other Rossiter tones and the broadband noise is absent. This suggest that the mechanism underlying this sixth tone is different from the aeroacoustic resonance loop. The source of this separate tone in the absence of a resonance loop is also not previously identified but is suspected as due to the oscillations at the trailing edge or possibly a spurious component arising from the trailing edge of the main element.

Another interesting observation from the spectra dataset is that our choice of spanwise length of $L_z = 0.2\text{m}$ has an implication for the predicted spectra. For an acoustic wave of this wavelength, the corresponding frequency is 1715Hz and the fundamental of this tone is at $1715/2 = 858\text{Hz}$ – only 5% lower than the Rossiter mode. The higher harmonics then follow the formula for harmonics as $f = N \frac{2c}{L_z}$, where c is the acoustic speed, and the set of frequencies corresponding to a stationary wave in the spanwise domain will be [2574, 3432, 4290, and 5148]Hz. These frequencies are marked in all plots for far-field spectra in Fig.6.2 demonstrating the fact that as the slat position is varied with respect to the airfoil, the frequencies may or may not match with these spanwise characteristics. Cases [7, 15, 16, 17, 19, 20, 26, 29] are examples in which the slat positioning leads to a different set of frequencies with the peaks maintaining the same amplitudes as for the standard case. This serves the argument that the spanwise domain size of the simulation, although possibly imposing similar characteristic frequencies, are not a reason for the existence of such tones. That being said, it is possible that most noisy configuration, Case 22, and the configuration in close proximity to the same in the slat coordinate system may tend to have a spurious numerical bias towards selection of frequencies depending on the spanwise length of the simulation. However, given that the same-span simulations with varying slat positions renders a variety of frequency selections, this is only a remote possibility and not pursued further.

6.4 Shear Layer Curvature

The shape of mean shear layer of the slat is best captured by the distribution of its local curvature. In a 2D view of the flow, this curvature can be calculated two ways: one is using the mean velocity contour to extract the streamline curvature over a given plane and second by using the mean streamline along the shear layer. To obtain the curvature on a 2D plane using only the mean velocity field, a local inviscid assumption is necessary. Under this assumption which is largely valid only for the external flow around the slat, we can assume a balance of forces along a streamline such that the pressure gradient balances the centrifugal forces generated due to curvature. Then

$$\frac{\partial p}{\partial n} = \rho \frac{U^2}{R} \quad (6.1)$$

where n is the radially outward normal to the streamline and R is the local streamline curvature. Given that the streamline normal is $\frac{-U_y \hat{i} + U_x \hat{j}}{U}$, the streamline normal pressure gradient becomes

$$\frac{\partial p}{\partial n} = \frac{U_x}{U} \frac{\partial p}{\partial y} - \frac{U_y}{U} \frac{\partial p}{\partial x}$$

thereby obtaining the local streamline curvature as

$$\frac{1}{R} = \frac{1}{\rho U^2} \left[\frac{U_x}{U} \frac{\partial p}{\partial y} - \frac{U_y}{U} \frac{\partial p}{\partial x} \right] \quad (6.2)$$

A contour plot of the calculated curvatures inside the cove flow is shown in Fig.6.3 for Case 22. As can be noted, for the region inside the shear layer, the curvature computed using Eq.6.1 computes a strong clockwise curvature. This streak of strong curvature is spurious in the calculation as, evidently from the velocity distribution, the streamline does not follow a path of the indicated curvatures. Hence the numerical values are evidently excessive of the actual curvature and is due to the fact that in the inner shear layer, the centrifugal forces are not indeed balanced by the pressure gradient but by the viscous momentum diffusion. By virtue of the latter, the balance is finally achieved by developing streamwise vorticity which convects fluid across the streamline accelerating the momentum diffusion to produce additional dynamic forces and thereby equilibrium. This hence strongly violates Eq.6.1, leading to erroneous calculation of the curvature for all cases. In simple terms, the inviscid assumption is too exacting in the case of cove flow whose shear layer undergoes a three dimensional vorticity transitions inside the recirculation. Nevertheless, the locations of impingement are clearly notable from the curvature inflection on the walls as shown in Fig.6.3.

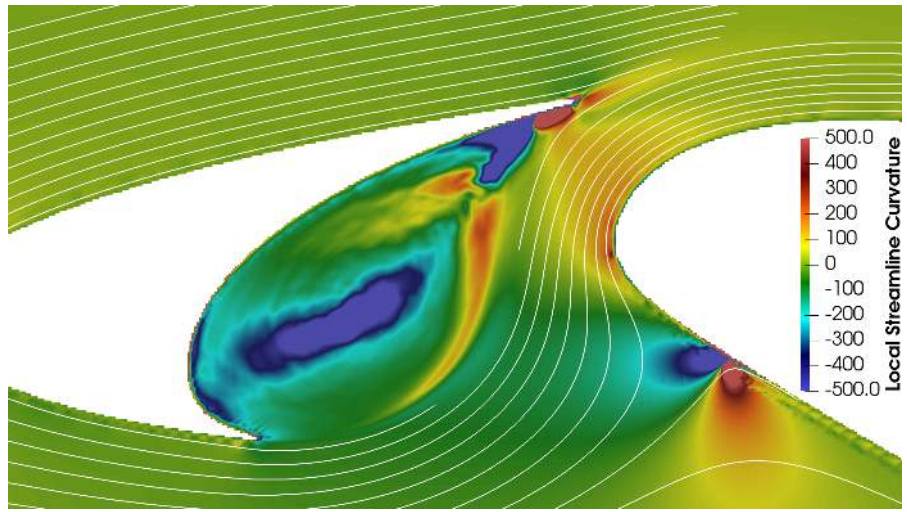


Figure 6.3: Streamline curvature contour obtained under the inviscid assumption for Case 22 demonstrating the identification of impingement location

The second way to calculate local curvature is by using geometrical formula on a select mean streamline. For the same, we first extract the point coordinates of the mean streamlines. The geometrical curvature is then calculated as

$$R = \left[\left(\frac{\partial^2 x}{\partial s^2} \right)^2 + \left(\frac{\partial^2 y}{\partial s^2} \right)^2 \right]^{-\frac{1}{2}} \quad (6.3)$$

where s is the path length along the streamline. A more elaborate account of the path line calculation and curvature are provided in Section 4.7 in Chapter 4. The geometrical curvature is free from the hydrodynamic calculations and hence it is free from the approximations for inviscid flow. The computed curvature is plotted for each case and is available in Appendix B. A few select cases are given in Fig.6.4.

Here, the numerical value of curvature provides a more agreeable picture of the streamline curvature. Case 22, which is the most noisy case can be noted to be one with an average curvature of $30 m^{-1}$. The curvature corresponding to inverse slat chord is $25.6 m^{-1}$ and hence the shear layer in all noisy cases have the mean curvature as same order of magnitude as the inverse slat chord. Good examples of such cases are Case [7, 10, 13, 15, 20, 21, 22, 23, 24, 29, and 31]. To enable a useful comparison, we choose to use the streamline path length until the position of the slat trailing edge as the standard length. All cases

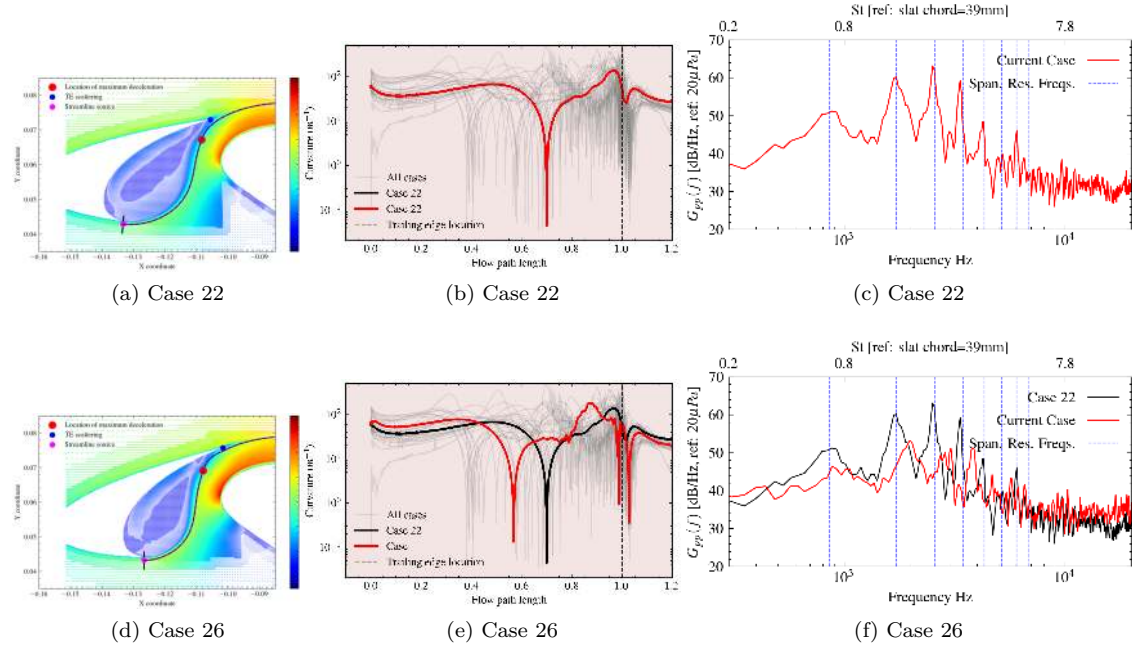


Figure 6.4: Curvature distribution along the shear layer for Cases 22 and 26 computed using Eq.6.3, along with the corresponding shear layer shapes and farfield noise spectra.

are then standardized using this length obtaining the trailing edge location at 1.0 such that the noise characteristics can be compared based on the behavior near the trailing edge.

The main characteristics of the curvature distribution on the streamline are the following:

1. The magnitude of curvature has atleast one null point along the shear layer where the direction of curvature inverts. This occurs when the initial shear layer which is redirected towards the slat gap has to correct the curvature in order to redirect the flow through the slat gap.
2. Depending on the proximity of the slat with respect to the main element, and if the initial curvature is insufficient, the curvature can spike before the inflection point, as in Case 4. This is particularly the case when the slat overlap is increased.
3. Upon impingement the streamline enters a region of strong turbulence which also have low frequency and intermittent behaviors. The region is also close to the slat wall where the mean flow solution is not well converged using the 5 chord pass times used to average the flow. This leads to noise in the streamline calculated using the mean flow and therefore the curvature calculation has a strong error. Case [4,5,6,25,27, and 28] can be noted to have this problem after the impingement location. These cases have a high slat overlap leading to the impingement point being far inside the cavity also attenuating both tonal and broadband characteristic noise.
4. The vortex impingement location on the slat upper wall will generate a strong curvature. This spike in curvature is the second sharp peak after the first inflection.

The curvature profiles thus analyzed is very much in agreement with the qualitative deductions in the previous sections. More precisely, a shear layer which maintains a curvature lower or same order of magnitude as inverse slat chord with the most delayed point of inflection, which consequently leads to a delayed impingement location closest to slat trailing edge, tend to be a more efficient noise generator. The proximity of the impingement location, identifiable as a feature from the curvature profile also has a

strong influence on the noise levels. A good example is the comparison of Case 22 and Case 26 as shown in Fig.6.4. For Case 22, the trajectory have a regularized curvature with the impingement location close to the trailing edge, while for Case 26, the impingement location is moved to the interior. For the latter, although the exit velocity is higher at the slat gap, the noise levels are lower than Case 22, suggesting that the location of impingement plays a crucial role in determining the source efficiency. Moreover, in addition to the effect of impingement at the wall, the region around the impingement by nature of the centrifugal instability leads to a reduction of spanwise coherence of structures. Hence we theorized that the curvature history prior to the trailing edge is the noise-determining feature and not the impingement location by itself.

That being the observations based on raw curvature along the streamline, the centrifugal effects also depends on the streamline velocity. A shear layer that maintains a higher streamline velocity must therefore accrue a larger effect of centrifugal instability, which here is the generation of streamwise vortices at the expense of spanwise vorticity. Therefore, we proceed to investigate shear layer shapes based on the suggestions from Bradshaw and Young [140] and Liou [128].

6.5 The Curvature Richardson Number

As mentioned in the introduction, an early work looking into the fundamental problem of the effect of curvature on the turbulence characteristics can be seen in attempt by Bradshaw [139]. It was then deduced that the curvature effects are significant if the shear layer thickness exceeds $1/300^{th}$ of the radius of curvature. From the characterization of curvatures, we can deduce that the streamline curvature of the slat shear layer is of the same order as that of the slat chord and consequently a shear layer thickness of $1 \times 10^{-4} m$ will be large enough to be unstable. From the observation of the slat flow cases, the standard initial shear layer thickness is of the order of $10^{-3} m$ as shown in Fig.4.31a in Chapter 4, suggesting that the curvature must have a non-trivial effect. The effect also becomes increasingly significant as the shear layer spreads towards the impingement where the curvature is maximized and the shear layer thickness is large enough to be fully unstable. A later work of Bradshaw and Young [140] suggested that a curved streamline will also have the same dynamic balance between curvature driven centrifugal force and fluid dynamic forces as in the case of forces with density stratified flows. For the latter, the buoyancy force appears as a source term in the momentum equations whereas for curved streamlines the centrifugal force appears as a source term when the Navier-Stokes momentum equations are written in the streamline coordinates. The equivalence of terms were then exploited to obtain an equivalent curvature-Richardson number such that it can capture the effect of curvature on the streamline turbulence.

In the work of Liou [128] using linear stability analysis, the effect of curvature on a slightly curved shear layer was shown to have two important effects: first being a partial stabilization of the K-H instability due to the curvature and the other being the existence of curvature driven steady spanwise modes. For the latter, the curvature is particularly identified as unstable if the Rayleigh criterion is satisfied, i.e. if the angular momentum decreases radially outward across the curvature. From the distribution of mean flow in the slat cove, we can deduce that this condition is satisfied only in the later part of the shear layer towards the impingement region. This is due to the high velocity stream being on the concave side of the curvature in the slat gap and hence qualitatively explains the generation of the streamwise vorticity in this region. Now, to obtain a quantitative measure of how curvature affects the shear layer, the linearized streamline equations in curvilinear coordinates were used by Liou [128] to obtain the kinetic energy production terms in streamwise and spanwise direction. The ratio of the same then capture the vorticity transfer into streamwise structures. This ratio also came out as the curvature Richardson number as originally suggested by Bradshaw [139] and have the definition

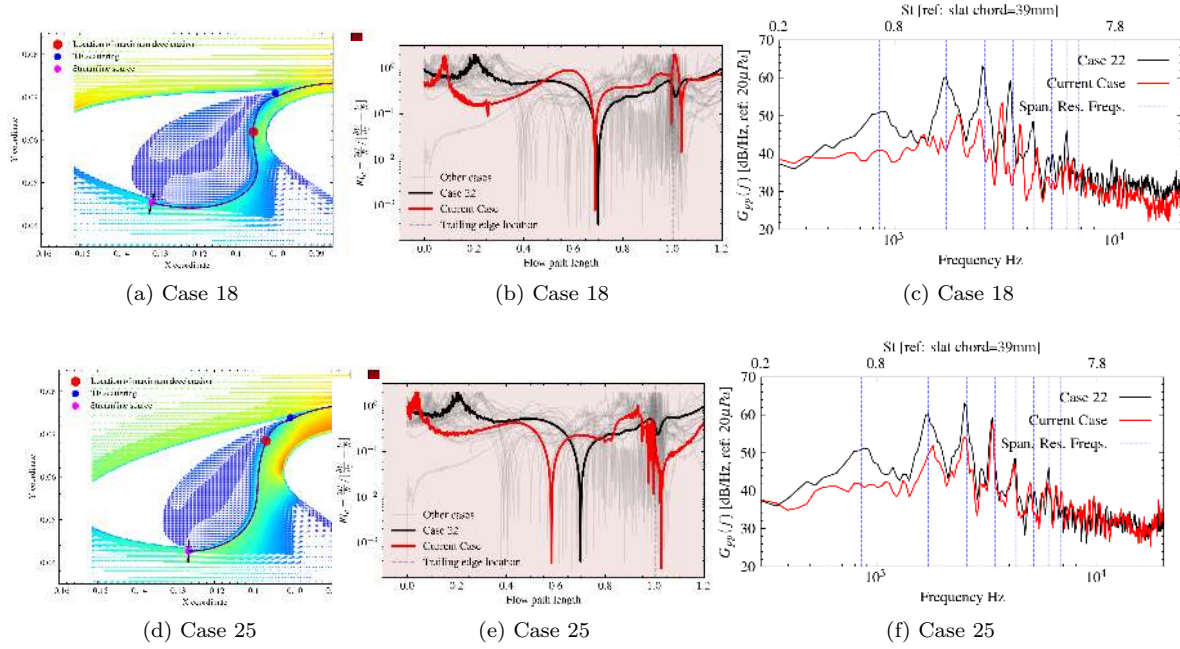


Figure 6.5: Comparison of shear layer shape, Curvature Richardson number profile and far-field noise of select cases

$$R_f = \frac{\frac{2U}{R}}{\frac{dU}{dy} + \frac{U}{R}}$$

where U is the streamline velocity and R is the local radius of curvature. Here the term $\frac{U}{R} = \frac{1}{ds} \left[\frac{U^2}{R} \frac{ds}{U} \right]$ represents the momentum transfer that is effected when a fluid mass traverses a unit distance under the influence of centrifugal force $\frac{U^2}{R}$. A more elaborate thought on the works of Bradshaw and Liou and why their ideas are valid for the slat cove dynamics is given in Chapter 4. Here we proceed to use the same for a comparative analysis.

The curvature Richardson number profiles along the shear layer for a few select cases are shown in Fig.6.6 and a full dataset is given in Appendix B. A first case of interest with a clearly interpretable result is with Case 18 and 25, and is shown separately in Fig.6.5. This case clearly have a positive slat overlap with a reduced slat gap leading to choking of the flow. However, the tonal noise components are still evident, particularly the third and fourth tones which show a strong SPL above the mean noise levels. This hints at the nature of non-linear interaction between the harmonic tones such that the first two tones transfer energy to the higher order modes. Such non-linear interactions were discussed recently in the work of Wei and Liu [101]. The same effect can be noticed in Case 25, which has an improved exit velocity but still less than Case 23 for example. Hence Case 25 also have a diminished broadband level and the third and the fourth tone maintains the same SPL as the most noisy Case 22. Interestingly these cases exhibit an increase in the curvature Richardson number owing to the effect of sharp curvature near the impingement. As can be inferred from the Richardson number plot, the impingement points for both these cases are slightly more upstream along the wall from the trailing edge than the standard Case 22, and shows the non-linear tonal relations at multiple flow exit velocities. However, despite our best efforts, a more direct relationship between the curvature effect and the non-linear frequency couplings are still elusive.

It can also be noted that the Richardson numbers are higher than 0.1 on average along the shear

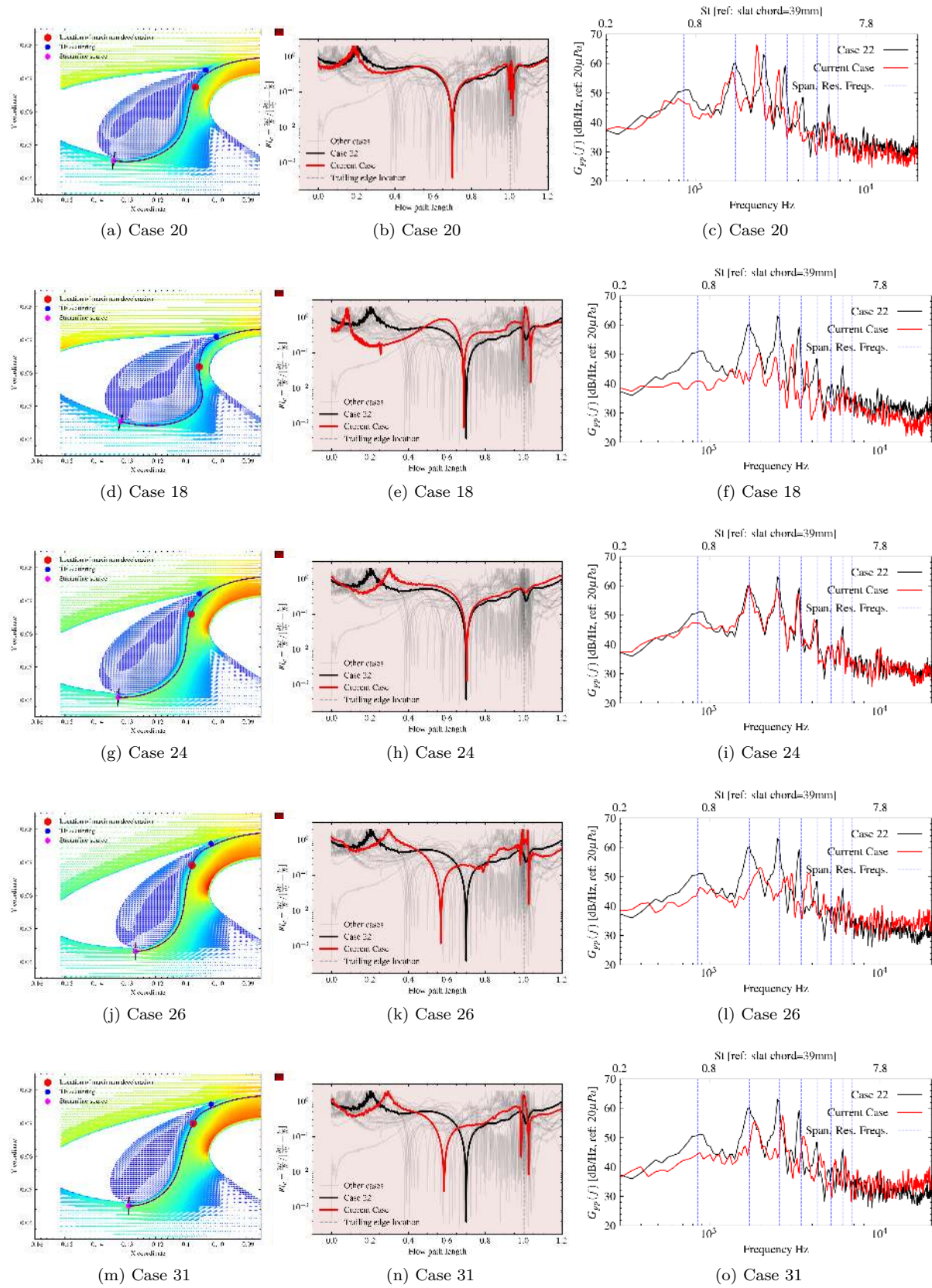


Figure 6.6: Comparison of shear layer shape, Curvature Richardson number profile and far-field noise of select cases

layers for all cases. In comparison, Liou [128] identified curvature instabilities for the case of slightly curved shear layers whose Richardson numbers were in the order of 10^{-2} . For the noisy case Case 22, the Richardson number has an initial value of 0.1 and rises to 0.9 before the curvature inflection. The region after the inflection, which then satisfies the Rayleigh criteria, maintains the Richardson number above 0.2 until impingement close to the trailing edge. This region between the curvature inflection and the impingement is hence where the shear layer vorticity is unstable due to the centrifugal effects and therefore lead to rapid generation of streamwise structures.

On observing the same region for the Richardson numbers in the noisy cases in the dataset, it can be observed that Case 22 maintains a lower bound for the Richardson number for this region i.e. all other cases which have the characteristic broadband and tonal components but with a lower SPL over the broadband range tend to maintain a higher Richardson number in the region before the impingement. Hence it can be inferred that the lowest Richardson number is one factor than contributes to the noise efficiency of Case 22 by allowing higher spanwise coherence. However again, to infer the contribution of curvature quantitatively requires a more meticulous approach since the broadband noise is primarily dependent on the exit velocity past the slat trailing edge. In Fig.6.6, a few select cases are shown which have a similar exit velocity but with a variation of the sound levels.

On comparing Case 24 with Case 26 with reference Case 22, the exit velocity magnitude in the slat gap for Case 24 is lower than that of Case 26. But the noise level of Case 24 is higher and agrees well with Case 22. On comparing their Richardson number profiles, the Case 24 and 22 agrees closely whereas for Case 26, the curvature inflection point occurs earlier in the shear layer. Hence the Case 26 has more length along the shear layer which is unstable to the centrifugal instability thereby leading to a sharp reduction of the spanwise coherence. Now comparing Case 26 to Case 31, there is a smoother evolution of the shear layer shape for Case 31 than the former since for this case the impingement location is closer to the trailing edge. Hence the effect of impingement is further reduced than Case 26 thereby recovering the spectra closer to the standard case. However, despite the exit velocity being still higher than Case 24, the Case 31 does not recover the same levels. This suggest that the effect of curvature driven decoherence holds relevance for the noise efficiency in addition to the exit velocity and the proximity of impingement.

However, an acoustic model or a quantitative correction based on the curvature profile is rather more subtle since the actual noise efficiency is much more strongly affected by the location of the impingement which occurs rather simultaneously with increased curvature effects. The normal pressure gradient calculation also have a high sensitivity near the impingement location since stagnation pressure near impingement causes a distortion of the pressure profile such that the normal pressure gradient is not representative of the pressure gradient in the shear layer. Therefore, although we demonstrate the role of the curvature in the vorticity conversion and noise efficiency, a practical acoustic model must rely comprehensively on all of the other factors too and thus the noise computation method using LBM-FWH approach or surrogate modelling is still suggested.

That being the effect of vorticity transfer due to curvature, another effect of the streamline curvature is the generation of larger scale spanwise vorticity cells. This is explored in the next section.

6.6 Spanwise Modes

The second characteristic cove flow phenomena that we are particularly interested is the existence of spanwise modes. As shown for the standard positioning of the slat in Chapter 4, the spanwise velocity inside the cove close to the shear layer tends to develop a spanwise modulation with amplitudes upto $0.15U_\infty$. This leads to formation of converging and diverging planes which necessitate that a mass continuity is established between them. However, this continuity cannot be met since the outer stream

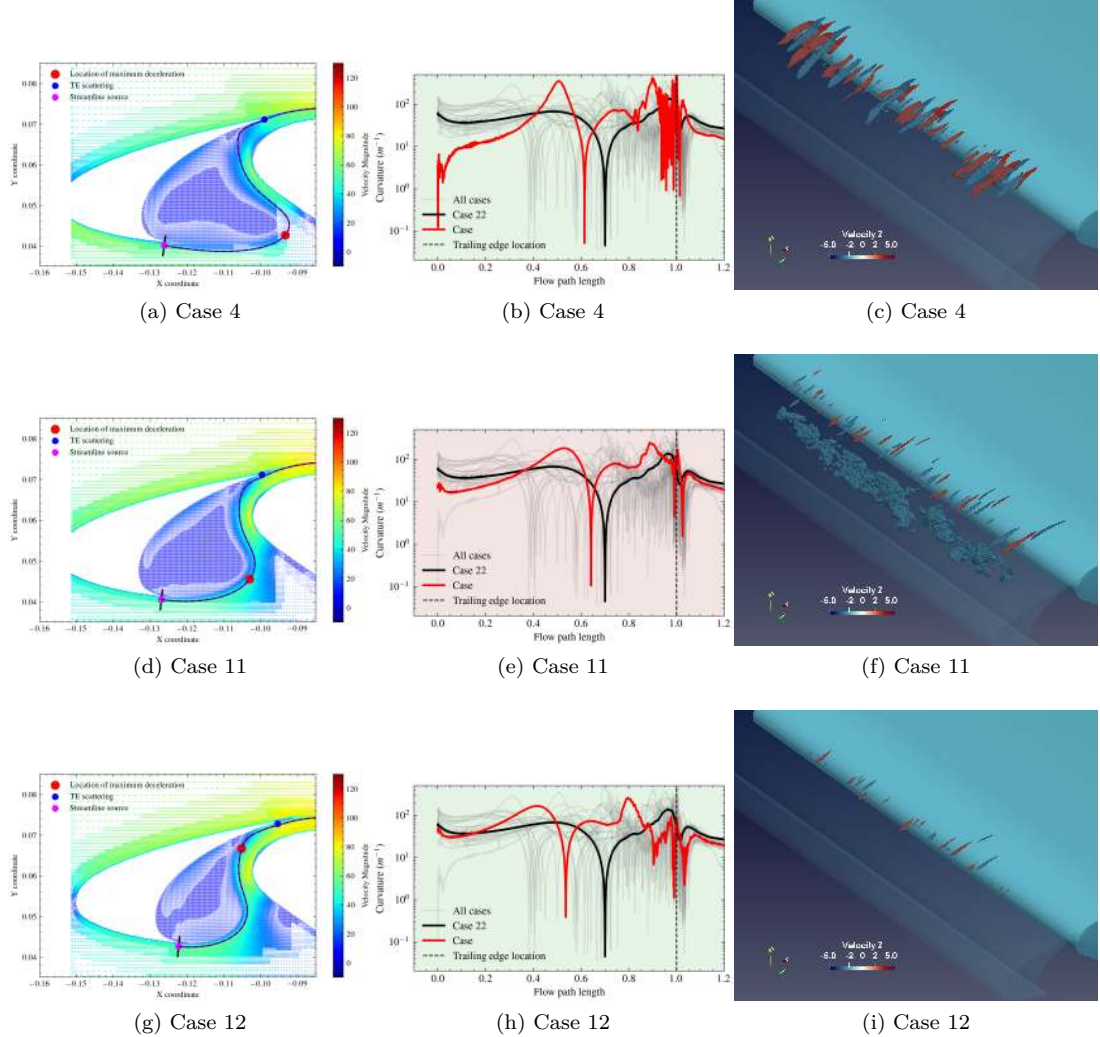


Figure 6.7: Comparison of the shear layer shape, curvature profile, and the spanwise modulations in three cases with initial curvature lower than Case 22.

entrains the flow from the converging planes faster than the inner low speed recirculation which replenishes the diverging planes leading to periodic bursting of the cove. This periodic bursting were shown to have a slat chord based Strouhal number of $St = 0.156$ (200Hz) for the standard slat position and will be investigated for all the cases in the dataset.

One critical parameter related to the spanwise modes is its wave number. In the case of backward facing step studied by Barkley et al. [2], spanwise wavelength was approximately ≈ 7 times the step height. For cavity flows, the spanwise wave number was approximately one cavity depth as suggested by Brès et al. [106]. Complementing their suggestions, Liou [128] also demonstrated the spanwise steady modes in curved free shear layers. Although such a step height or cavity depth is difficult to define in the slat cove case, the slat chord $C_s = 0.039\text{m}$ can be taken for an equivalent diameter for a circumcircle that passes through both the slat cusp and the trailing edge. In other words, C_s can be taken for an equivalent cavity depth. For the standard case we showed that the non-dimensional wave number using the same for spanwise modulation, $\Lambda_z = \frac{\lambda_z}{C_s}$, would then range between 1.0 for 5 cells to 1.7 for 3 cells, or zero when no cells are formed.

Consequently, and following Barkley, Bres and Liou, the spanwise modulation in slat cove is also reasoned to be primarily influenced by initial shear layer curvature with the exact value determined by

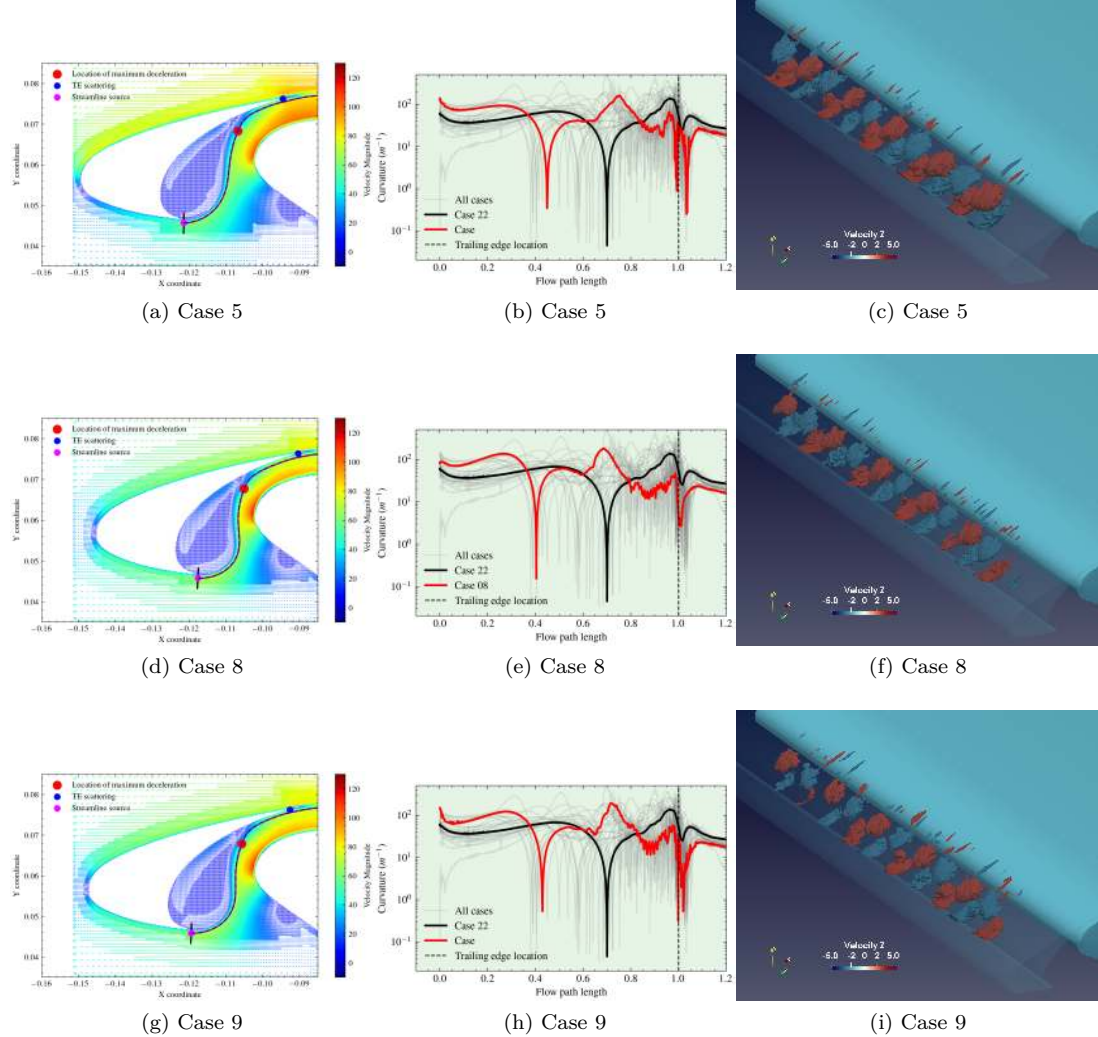


Figure 6.8: Comparison of shear layer shape, curvature profile, and spanwise velocity modulations of three cases with initial curvature higher than Case 22

the snapping necessitated by spanwise extend of the simulation. The snapping occurs since although the periodic condition represents an infinite spatial domain for the flow, it ensures that all variables have identical values on both spanwise edges at all time steps. This means that any standing wave pattern along spanwise direction will have to select a wave number such that the flow is congruent between the domain ends. The wave number is thus selected as the nearest whole number that fits the span length. For our simulations, the spanwise wavelength is 0.2m and as the slat position is varied, the degree of centrifugal modes are first driven by the curvature of the shear layer and then the periodic condition leads to selection of the nearest possible whole number. Note that the same effect occurs in the presence of walls where the Dirichlet condition in pressure and velocity causes the spanwise wave number to snap to whole numbers.

These spanwise velocity cells for all cases are given in the Appendix B. Among them the Cases [4, 11, 12, 18, and 19] have no cells corresponding to a null wave number. On comparing their shear layer curvatures from Fig.6.7, it can be noted that these cases have shear layers which have a low curvature on the early region near the cusp. Case 4 is a clear anomaly where the slat overlap causes a delayed curvature with the initial shear layer parallel to the outer wall of slat cusp. For Case 11, the case develops a weak spanwise homogeneous flow however not forming cells due to the fact that the initial curvature

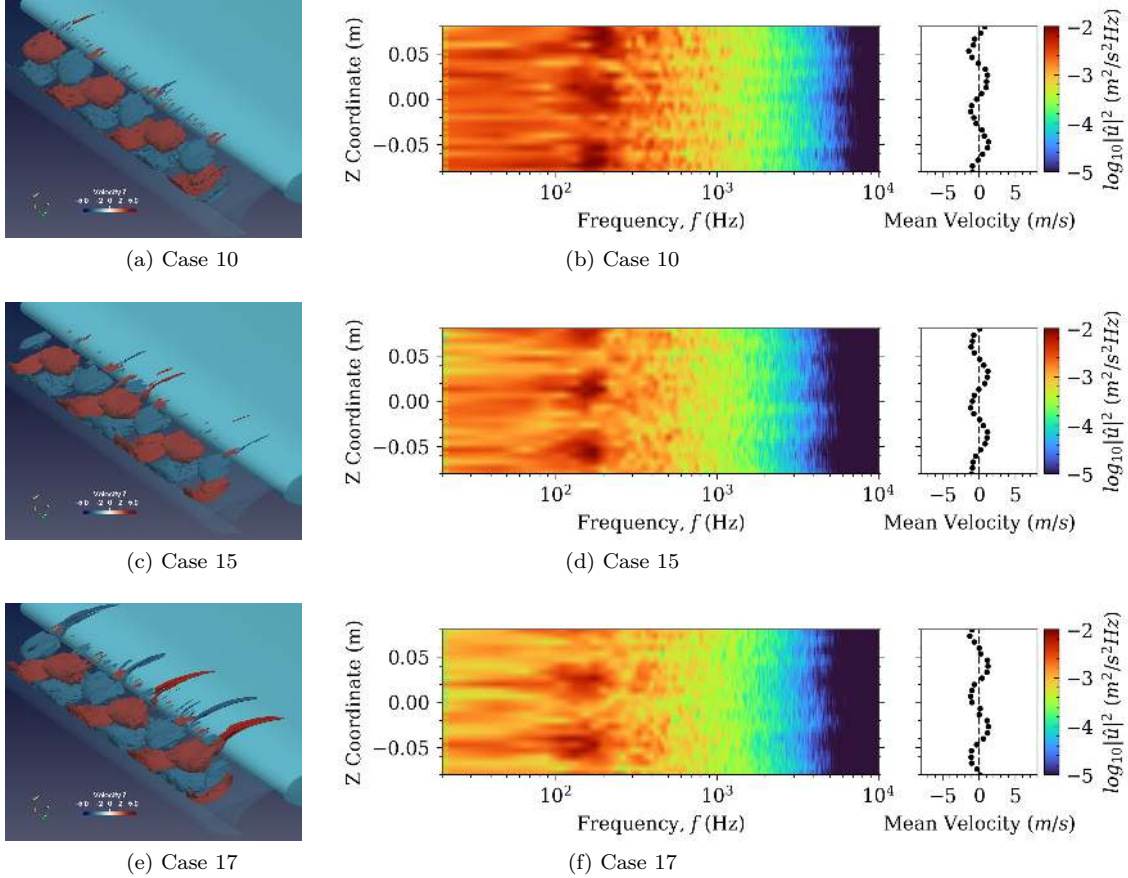


Figure 6.9: Power spectral density of spanwise velocity component as a function of spanwise location for cases which has spanwise mode formations. The low frequency oscillations are localized in the diverging planes of the modes where the spanwise velocity $U_z = 0$ and $\frac{\partial U_z}{\partial z} > 0$

is low, and with a significantly low exit velocity. The reduced exit velocity reduces both the streamline velocity along the shear layer and the recirculation velocity, and hence reduces the growth of centrifugal related instabilities. The same follows for Case 18 and 19 where the shear layers are initially parallel to the incoming flow and the curvature increases in the mid-trajectory to compensate the delay and redirect the flow. Thus, in comparison with Case 22, whose wave length is $\Lambda_z = 1.7$, the above-mentioned cases have a lower initial curvature. This suggest two things: one is that it is additional proof that the spanwise modes are driven by the curvature of the shear layer since the wave number varies proportional to the initial curvature. The second is that unlike for the vorticity conversion, only the early part of the shear layer is significant as a driver of the mode formation. This could be possibly due to the fact that the initial shear layer curvature determines the radial of the recirculation bubble which ultimately determines the strength of centrifugal effects.

Investigating this proposition further, Cases [5, 8, 9, 14, 27, and 30] have the smallest wavelength of $\Lambda_z = 1.025$. Comparing the shear layer profiles from Fig.6.8, these cases clearly have its initial curvatures as highest in the dataset and also an impingement point farthest from the trailing edge due to a high slat overlap. Thus the reduced diameter of the recirculation cavity explains the decrease in the spanwise cell size. These cases can also be noted to have a low broadband and tonal characteristic noise (See Appendix B for spectra) and owes to the early impingement leading to a complete decoherence of the ejected vorticity at trailing edge.

In contrast, as can be noted from Cases [10, 15, 17, 20, 21, 22, 24] (see Appendix B), whose wavelength

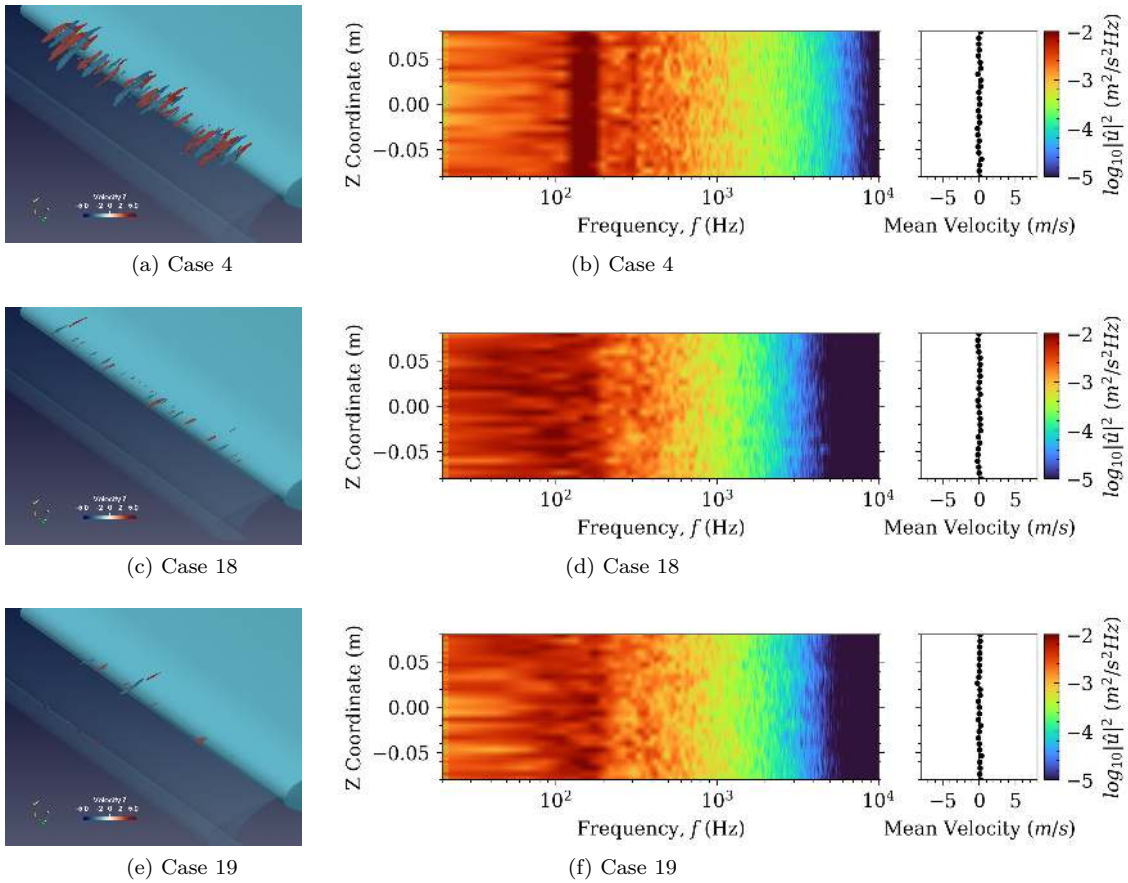


Figure 6.10: Power spectral density of spanwise velocity component as a function of spanwise location. The low frequency oscillations spanwise homogeneous.

$\Lambda_z = 1.7$, these arrangements produce the most noisy cases. Hence the presence of modes does not directly imply that the characteristic noise sources including the aeroacoustic resonance are significantly disrupted solely by presence of these modes. Rather, they induce additional dynamics arising from their periodicity. In Chapter 4, we showed that for the standard positioning of the slat, there exists a low frequency “bursting” of the divergent planes at frequency corresponding to $St = 0.156$. This oscillation modulates the spanwise coherence of the shear layer such that the aeroacoustic loop is not driven by a steady shedding and impingement of spanwise coherent vortices but with an intermittent modulation of the coherence length of the impinging turbulence. We proposed that the resulting tones hence will also be amplitude modulated thereby developing side bands.

To investigate the spanwise mode oscillations further, we now extract the spanwise distribution of the velocity spectra for the modulated spanwise component. As shown in Fig.6.9 and 6.10, the power spectra of spanwise velocity component has a localized spike around 200 Hz corresponding to $St = 0.156$ for all the cases studied. A particular statement can be that for the Case 15 in Fig.6.9. Here it can be observed that the case have three wavelengths within the spanwise domain. Hence, for the region near the slat trailing edge, there are 3 diverging planes and 3 converging planes. For the figure, the power spectral densities of velocity is obtained for a reduced spanwise length of 0.1 m and hence the 2 diverging planes close to the mid-plane are captured. Also note that for positioning of the diverging cells, the lower and upper array of cells in the slat cove have a shifted phase by a quarter of wavelength. These spikes can be noticed to occur at the locations of the diverging planes where the spanwise velocity is zero and increasing. These spanwise localization is also present in all cases that have the cell formation and can be deduced from the

exhaustive dataset presented in Appendix B.

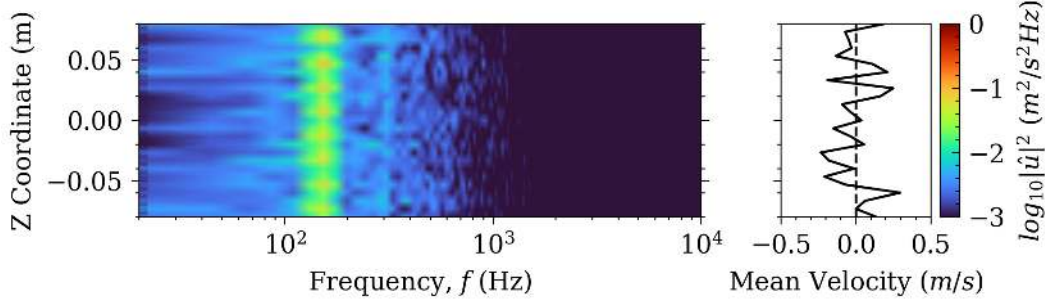


Figure 6.11: Spanwise variation of low frequency components of the spanwise velocity for Case 4.

In contrast, for cases which does not have a spanwise modulation of the velocity due to its low insufficient initial curvature, the oscillation is still present but not localized along the span, i.e. the oscillation is homogeneous. This is demonstrated in Fig. 6.10. The low frequency range of the spectra also shows saturation of the standard color map below 200Hz suggesting high amplitude of oscillation compared to the cases where they are absent. On examining one of these cases further using a better color map, the particular Case 04 as shown in Fig.6.11, it can be observed that these oscillations have a low amplitude spanwise structure at a very high wave number than the rest of the cases and a low amplitude variation of the spanwise velocity across the span or of the order of $0.1U_\infty$. This can be attributed to the recirculation of the streamwise structures which are periodically generated at the impingement and convected back to the early shear layer region by the recirculation. These cases are thus not forming the larger scale spanwise cells that are present in other cases but is only a spanwise homogeneous oscillation corresponding to the same low frequency of around 200Hz.

The low frequency fluctuations present in both cases with and without the spanwise modes suggest that this frequency itself is not directly connected to the centrifugal instability but rather a feature of a different flow dynamics. To investigate this, we choose an arbitrary position inside the cove, in close proximity to the slat cusp, where if a streamline is sourced would generate one that enters the recirculation after the impingement location. The three dimensional length of this streamline is then used to obtain the velocity profile, the time of travel along which can be used to obtain the recirculation frequency. The recirculation frequency as a function of the streamline path length for Cases [5, 11, 22, and 29] are shown in Fig.6.12 to 6.15. The recirculation frequencies for these cases show that the time taken for a streamline particle from the vicinity of the slat cusp to return to the same vicinity via the recirculation explains the oscillation at 200Hz. This is true in the case of the three dimensional recirculation where the streamline is not necessarily two dimensional and the spanwise velocity leads to spanwise drifting. The frequency finds a better matching when the spanwise modes are formed as in the case of Case 22 and 29.

For Case 11 where the shear layer has a low initial curvature, the oscillation is spanwise homogeneous with a frequency slightly lower than the recirculation. Precisely, in this case, the frequency of spanwise oscillation is 100Hz and the recirculation frequency is at 170Hz, i.e. the ratio of spanwise homogeneous oscillation frequency to that of recirculation is at approximately 0.6. We do not put forward an explanation for this but only suggest that it can be possibly due to the presence of a spanwise homogeneous drift velocity present in this case causing the recirculation loop to be a spiral with axis along the span, as seen in the streamline visualization in Fig.6.13. In contrast, for the other cases with presence of spanwise modes, the modes constrain the spanwise velocity to have opposing polarity with the cells and the oscillations to occur at the diverging planes. Then at this frequency, the diverging spanwise velocity leads to a saturation of the low pressure thereby bursting the shear layer at the recirculation frequency.

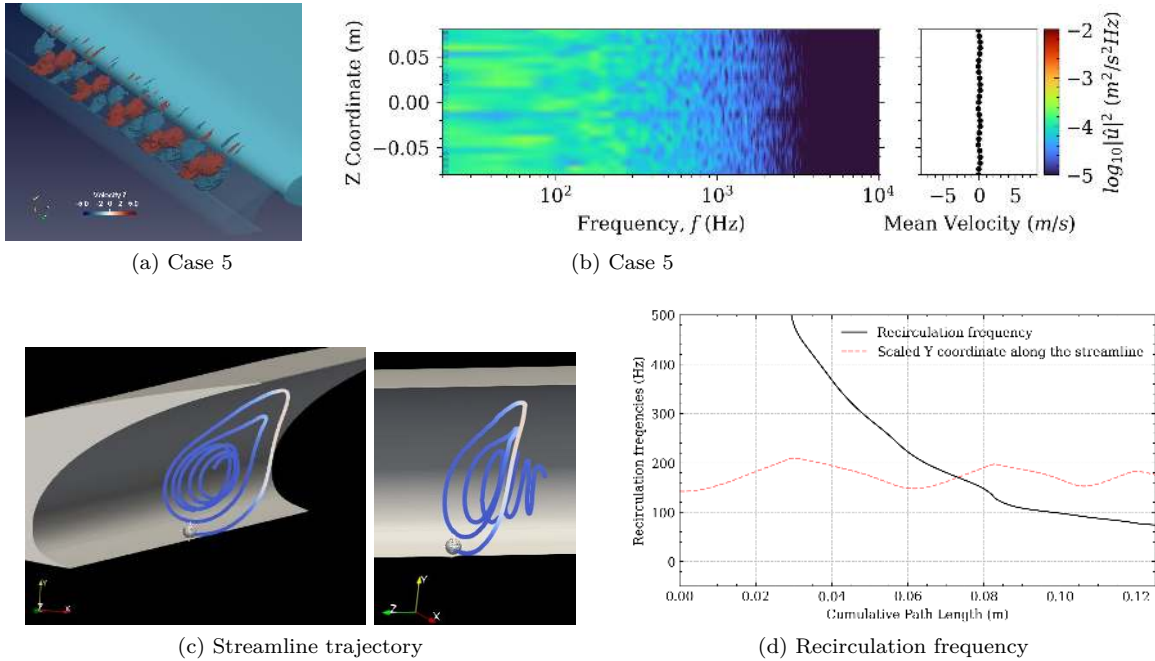


Figure 6.12: Streamline extracted from the mean flow profile for Case 5 suggest that the recirculation in the cove maintains a frequency of 210Hz.

6.7 Conclusions

In this last chapter, we utilized the LBM based ProLB solver and high-fidelity data generated using same to investigate the slat cove dynamics. We parameterized the slat positioning with respect to the main element using a four variable coordinate and used a surrogate model based automated exploration using Bayesian Active Learning to collect the dataset such that maximum information pertaining to the variation of the spectra is captured. The flow recordings were then investigated to uncover the slat cove dynamics.

On inspecting the dataset, it was first showed that the spectra showed strong sensitivity to the shape of the shear layer as expected. Following the theory of Terracol et al. [14] that the tone frequencies are selected by the Rossiter mechanism, we investigated the effect of shear layer shape in determining the strength of the resonance. For this we followed the suggestion of Liou [128] that a curved free shear layer has instabilities related to the centrifugal forces and can develop steady spanwise modes as well as Görtler like vortices. Based on [139] and Liou [128], we characterized the slat shear layer for each case using its distribution of curvature and Richardson number. It was shown that the Richardson number for all cases are well in the unstable regime near the slat trailing edge. Nevertheless, the variation of Richardson number and corresponding variation in the spanwise coherence near the trailing edge is less significant than what would be caused by the effect of the position of the impingement location. The movement of the impingement location to the closest to the trailing edge is hence a better predictor for the strength of the tones. It happens geometrically that it is only possible to produce an additional curvature near the trailing edge by inadvertently making the impingement point to move upstream. The decoherence effect by the impingement then trumps the effect of additional curvatures.

A second and novel finding related to the cove dynamics was presented in Chapter 04, i.e. the presence of spanwise modulated spanwise velocity. We showed using the dataset that the slat chord normalized wavelength of these modes $\Lambda_z = \frac{\lambda_z}{C_s}$ ranges between 1.0 to 1.7, the exact value dictated by the spanwise

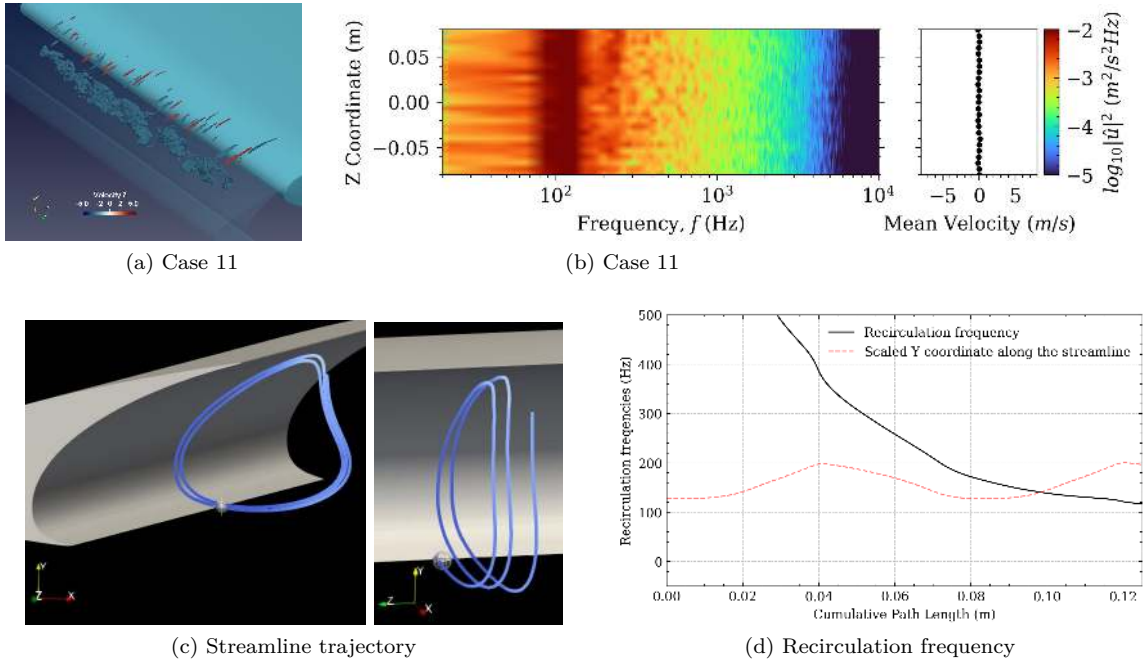


Figure 6.13: Streamline extracted from the mean flow profile for Case 11 suggest that the recirculation in the cove maintains a frequency of 170Hz

length of the cove. We also demonstrated using the curvature distribution of shear layers that a high initial curvature is the characteristic that leads to a stronger modulation leading to smaller wavelength of the spanwise velocity. Further investigation of the spanwise distribution of velocity spectra then revealed that there exist spanwise localized oscillations at 200Hz.

The investigation of this spanwise distribution for all cases in the dataset showed that oscillation is present in all cases which develops the spanwise modes, and the localization is always in the diverging planes. The oscillations were also found to be always within the range of 100 to 200Hz for all cases in the dataset. In search of the source of this frequency, the three dimensional recirculating streamlines were generated and the recirculation times were then shown to fall in the same range around 200Hz. Hence it is theorized that the low frequency oscillation is the effect of the periodic recirculation, often referred to as the “pulsation of the cove” in recent literature.

Moreover, the low frequency oscillations were also visualized in the previous chapter using the Q-criterion demonstrating that this phenomena is a periodic bursting of the shed spanwise vorticity at the slat cusp. The spanwise coherence of the spanwise vorticity is hence periodically disrupted at its initial shedding phase leading to generation of small scale streamwise vortices. Being generated in diverging planes, these small scale structure is then convected by either positive or negative spanwise velocity. Being a turbulent process, the effect of this bursting and breaking of spanwise coherence is thus intractable periodically at the region farther from the cusp region. This very well explain the mode switching behavior that is attributed to the variation of coherence length and dominant tonal fluctuations across the spanwise extend reported in very recent literature[101]. This also explains the apparent stochasticity of the slat tones reported in the experimental investigations of Kamliya Jawahar et al. [29]. Here it must be emphasized that the experimental investigations which selects the spanwise mid-plane to place the wall pressure and hot-wire probes may or may not be at the center of a diverging plane depending of the development of the cells. Hence, the studied characteristics will inevitably tend to diverge between the experimental observations from different wind tunnel cases in view of periodicity. The turbulence ejection

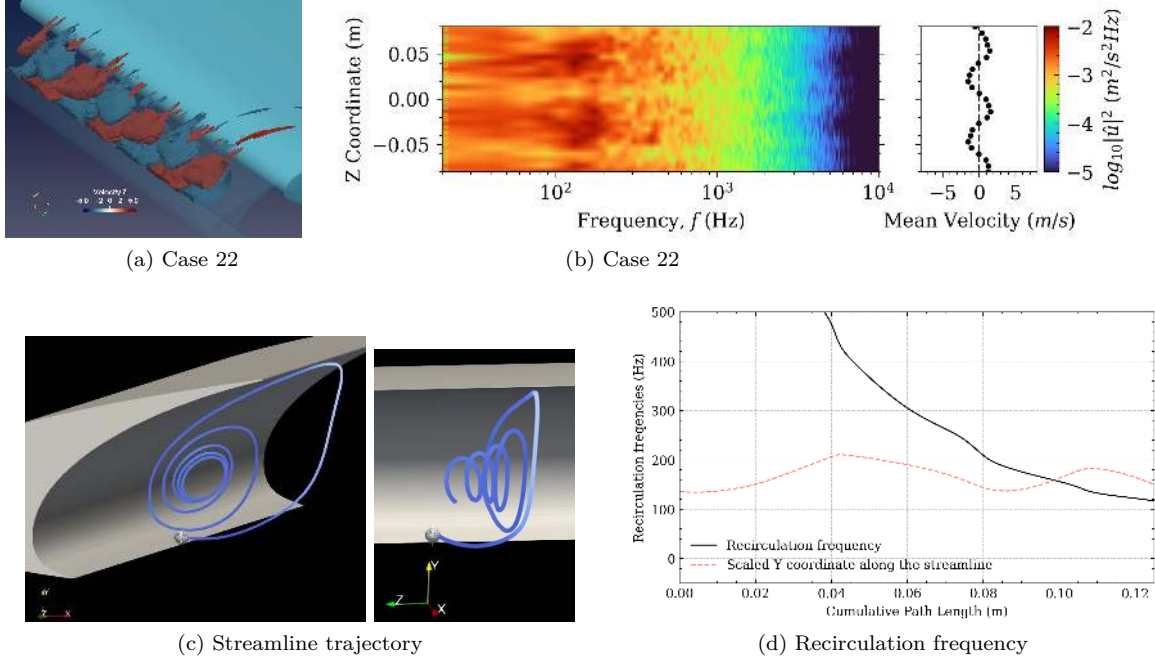


Figure 6.14: Streamline extracted from the mean flow profile for Case 22 suggest that the recirculation in the cove maintains a frequency of 190Hz

that accompanies the bursting phenomena will also appear to induce intermittency in the turbulence characteristics in the slat gap since the periodicity of bursting is robust only in the very early shear layer near the slat cusp and the generated vorticity from each event is then convected along with the rest of turbulence.

Here, the fact that the bursting occurs at the diverging planes due to saturation of a suction pressure at diverging planes is not entirely consistent with the fact that its frequency is close to the recirculation frequency. The saturation of low pressure could have been synchronized with other modes which are more probable, for example with the first Rossiter mode, and the flow recirculation frequency is an unintuitive candidate to synchronize with the spanwise mode oscillation, thereby suggesting a non-trivial coupling between the bursting phenomena and the recirculation. This aspect hence is an intriguing line of experimentation for future investigations. Nevertheless, with the current understanding from our dataset and the presented results herein, it is overwhelmingly evident that the low frequency oscillation associated with the recirculation phenomena is pertinent to the establishment of characteristic noise sources in the cove dynamics.

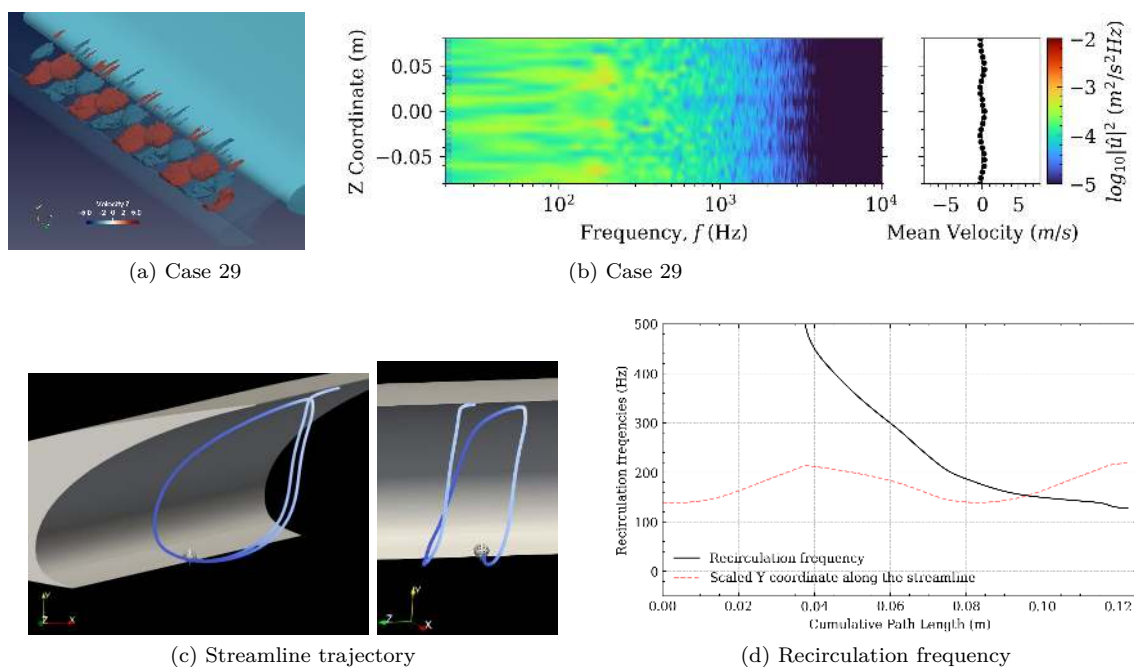


Figure 6.15: Streamline extracted from the mean flow profile for Case 29 suggest that the recirculation in the cove maintains a frequency of 190Hz

Chapter 7

Conclusions and Future Perspectives

The research presented in this thesis is an attempt to advance the understanding of leading-edge slat noise through high-fidelity simulations and detailed flow analysis. An innovative surrogate modeling approach, not previously used for aeroacoustic simulations, is also deployed with particular focus on approximating the far-field noise spectrum. The main findings from each chapter can be summarized as follows:

Literature Review – Aeroacoustic Noise Mechanisms and Slat Noise: In Chapter 1, a generic introduction to slat noise and the background of the thesis is presented. In Chapter 2, a survey of past studies was presented and highlighted the canonical aeroacoustic mechanisms with the objective to explain the leading-edge slat noise. One striking feature of slat noise research is that there exists a discrepancy between the experiment and flight test for the tonal nature of its noise. The tones are not acknowledged to exist in the flight test data but are a prominent feature in subscale noise testing from early on. Also despite extensive experimental efforts and analytical models, the complex cove flow dynamics of slats remained only partially understood, with phenomena like intermittent behavior of the aeroacoustic tones reported but not fully explained. This motivated the use of advanced computational approaches. The Lattice Boltzmann Method (LBM) emerged as a promising tool for aeroacoustic simulation of such flows, offering inherently low dissipation and excellent parallel scalability for capturing acoustic sources in the slat cove. The literature review thus suggested both the need for high-fidelity analysis of slat noise mechanisms to investigate it in light of known aeroacoustic mechanisms and the potential of LBM to meet this need.

Simulation Framework – LBM validation for Aeroacoustics: In Chapter 3, a comprehensive study of the theoretical underpinning of LBM and a validation of the LBM solver *ProLB* was carried out for a standard slat position configuration of the HLD in free-stream conditions. The solver was able to reproduce the mean flow field and surface pressure distribution on the HLD with good accuracy when compared to experimental data. In particular, the simulated wall-pressure coefficients on the slat and main element showed the correct trends and magnitude, with minor discrepancies attributable to differences of experimental setup from that of simulation. The far-field sound predictions using a Ffowcs Williams–Hawkins (FWH) acoustic analogy also demonstrated a close agreement across the frequency range of interest, confirming that the LBM-FWH approach can capture both broadband and tonal noise components of the slat. This validation helped establish confidence in the numerical framework’s capability for high-fidelity aeroacoustic simulation of slat noise.

Flow Physics of the Slat Cove: Using the validated solver, an in-depth analysis of the baseline (standard) slat geometry was performed, in Chapter 4, to investigate the noise-generation mechanisms.

The study revealed the details of a highly complex unsteady flow in the slat cove region characterized by spanwise-periodic cellular structures in the recirculation bubble. These spanwise cells – alternating converging and diverging flow regions along the span – are driven by a centrifugal instability of the curved shear layer in the cove. As the shear layer rolls over the slat cusp, it forms spanwise coherent vortices that initially organize according to the cellular pressure pattern. During this thesis, we uncovered a previously unknown localised and periodic “bursting” phenomenon at a characteristic non-dimensional frequency around $St \approx 0.16$ (based on slat chord and freestream velocity) which corresponds to the recirculation frequency of the slat cove. The spanwise coherent vortical structures shed from the cusp also abruptly breaks down into smaller-scale streamwise vortices. This bursting occurs preferentially at the diverging planes of the spanwise cells (where a pressure deficit accumulates) and convects downstream with the shear layer. The result is a recurrent injection of turbulence into the shear layer. These findings expand on the current understanding of slat cove dynamics by pinpointing a specific mechanism for the transition from large coherent structures to fine-scale turbulence via an intrinsic unsteady mode of the recirculation flow. Notably, the estimated frequency of the cove “pulsation” matches the low-frequency tone observed in slat noise spectra, suggesting a direct link between the unsteady recirculation and acoustic emissions.

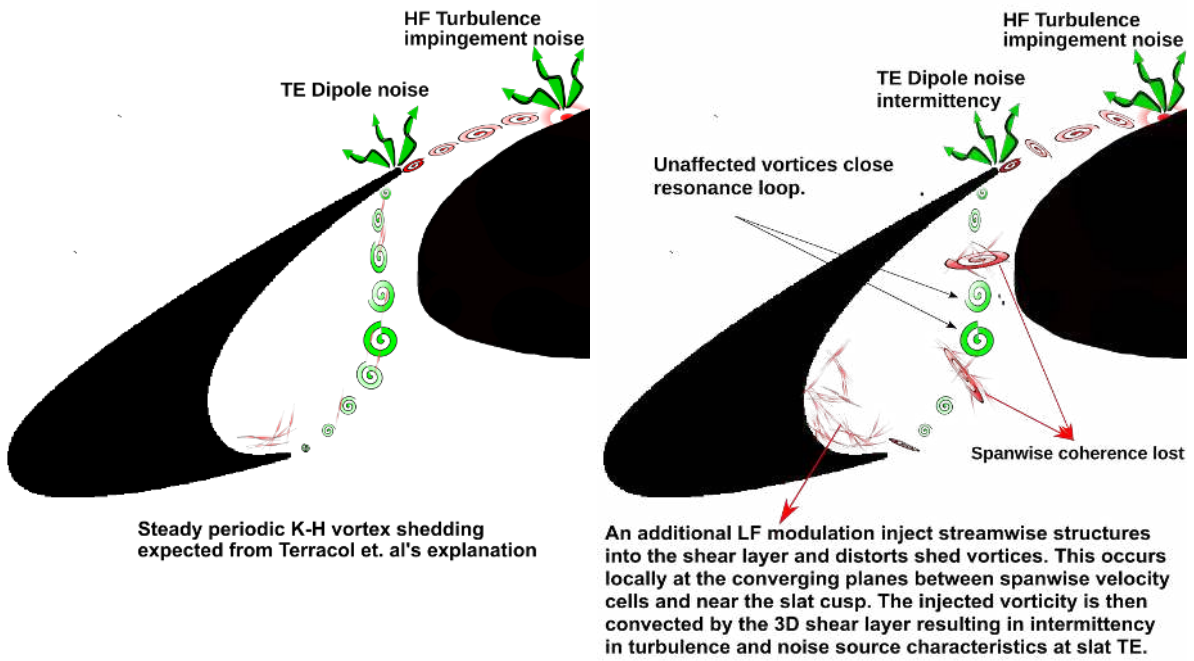


Figure 7.1: Schematic of the suggested mechanism that explains the intermittency of slat tones observed by Jawahar et al. [4]. The non-dimensional frequency of the bursting has also been established as the recirculation frequency of the cove flow using VALIANT geometry.

Slat Noise Generation Mechanisms: As part of Chapter 4, the flow features thus understood translated into clear noise-generation pathways as well. The shear layer emanating from the slat cusp impinges on the slat trailing edge, and its unsteadiness induces pressure fluctuations. These fluctuations can emanate as far-field noise but also interact with the vortex shedding at the slat cusp to cause an aeroacoustic resonance. The resonant modes act as sources of tonal noise. The intermittent breakdown of spanwise

coherence in the shear layer explains the tone intermittency and mode switching reported in experiments for slat noise – essentially, the effective coherence length of the noise sources in the gap can shorten when a burst occurs, leading to a temporary reduction or shift of tonal noise, before coherence rebuilds and tones re-emerge. Thus, the study provides a physical explanation for the stochastic behavior of slat tones (as observed by Jawahar et al. [4] and others) by relating it to the intrinsic variability of the cove flow. A schematic of the suggested mechanism is given in Fig.7.1.

In summary, the dominant slat noise sources were found to be: (1) the unsteady shear layer impingement causing aeroacoustic resonance, producing a primary tonal noise at the burst frequency and its harmonics, and (2) additional broadband contributions from the smaller-scale turbulent structures convected through the gap. Importantly, no evidence was found of purely artificial acoustic modes due to the computational setup – the spanwise cellular pattern was confirmed to be a physical feature rather than a numerical artifact, as it persisted when varying the spanwise domain length, boundary conditions, and slat positioning. The variability from no cell formation to wave numbers of $L_z/5$, where L_z is the spanwise length, provides a validation of the same fact.

Surrogate Modeling and Parametric Study: To extend the analysis beyond a single geometry, a surrogate modeling framework was developed in Chapter 5 to investigate slat noise across a range of slat positions. Using a Gaussian Process (GP) regression as the surrogate, coupled with an active learning strategy (Upper Confidence Bound, UCB), the study explored a three-dimensional parameter space of slat gap, overlap, and deflection angle, i.e. positions relative to the main element. The use of a statistical surrogate model has the objective of maximizing the sampling efficiency for the parametric simulation, and also to introduce such methods to aeroacoustic engineering research. The surrogate model was trained on a limited set of high-fidelity LBM simulations and was able to predict the noise spectra for any intermediate slat setting, along with an estimate of its own uncertainty. This approach was also presented as an optimization tool: the UCB-driven sampling iteratively selected new simulation cases that were pinned to case that maximize the far-field noise. As a result, the most acoustically critical slat setting in the considered design space was identified with far fewer runs than a naive parameter sweep. The surrogate's predictions of sound pressure levels were in close agreement with subsequent LBM simulations for those noisiest configurations, demonstrating the model's utility and the benefit of uncertainty-based sampling. Beyond optimization, this parametric campaign yielded a rich dataset that allowed us to examine the generality of the cove flow phenomena: indeed, the spanwise cell formation and bursting mechanism were observed across all tested slat positions, though the exact frequency and strength of the bursts showed some dependence on slat geometry. For instance, moving the slat outboard (increasing gap and overlap) tended to slightly alter the recirculation size and shift the burst frequency, but the qualitative behavior remained the same. These observations confirm that the centrifugal-instability-driven unsteadiness is an inherent feature of slat cove flows. In summary, the surrogate modeling effort not only facilitated rapid evaluation of slat noise performance for different geometries, but also supported the physical analysis by expanding the range of conditions under which the newly identified noise mechanism has been validated.

Overall, this thesis combined high-fidelity LBM simulations and data-driven surrogate modeling to gain new insights into slat noise. We have demonstrated that LBM can reliably capture the intricate flow physics and acoustics of a leading-edge slat, provided sufficient care in its numerical setup. The discovery of the spanwise cellular instability and its role in modulating the noise generation is a key scientific contribution, offering a deeper mechanistic understanding of slat noise that bridges previously disparate observations (tone interactions, intermittency, etc.). Meanwhile, the surrogate modeling approach represents a step towards practical aeroacoustic design optimization, showing how costly simulations can be leveraged in an intelligent manner to explore design changes. The tools and knowledge developed in

this work lay a foundation for more efficient framework and eventually an aeroacoustic surrogate model applicable to real world design problems.

Future Perspectives

From the conclusions of this thesis, several avenues are proposed for future work. These include immediate next steps that naturally extend the current study, as well as long-term research directions that apply emerging techniques to the problem of slat noise prediction and reduction.

Expanded Parametric Studies: A logical and first next step is to broaden the parameter space investigated for slat noise characteristics. In this thesis we varied the slat positioning parameters for a fixed airfoil geometry – the VALIANT 2 element configuration – at a single angle of attack, Mach number, and Reynolds number. Future studies should consider a more comprehensive parametric sweep, including different slat deflection angles, gap sizes, profile shapes, and incoming velocity. Varying the flow conditions – such as the freestream velocity (Reynolds number) or angle of attack of the main wing – would provide insight into the scaling of the noise sources. Expanding the dataset in these ways would not only enhance the surrogate model (making it more general), but also test the limits of the current conclusions. For instance, it can answer questions like whether the bursting Strouhal number remain around 0.16 for other free stream velocities, or does it shift with different flow parameters. Variation of the Reynolds number can also shed light on whether the strength of spanwise modes and its wave number increases as the Reynolds number increases, and thus whether such an increased instability explain the complete attenuation of tonal noise at flight Reynolds numbers. Answering such questions would help generalize the slat noise theory and potentially lead to low-order design tools.

Further Validation and Diagnostics: Although a validation was performed for the baseline case, it would strengthen the conclusions to seek additional experimental or high-fidelity data for comparison. Near-term efforts could involve collaborating with experimental researchers to obtain detailed measurements for a few key cases for instance, the loudest slat position identified by our surrogate model. Comparing measured and simulated far-field spectra, as well as any measured flow features, would provide a rigorous test of the new physical insights. This could include checking if the predicted burst frequency and spanwise mode pattern occur in reality. The recent experiments by Kamliya Jawahar et al. [29] on slat noise intermittency, for example, might be re-examined in light of our findings to probe whether their wall-pressure traces or acoustic spectra show signatures consistent with a recirculation bubble pulsation; or whether the characteristics vary along the spanwise directions. A targeted experimental campaign on a slat-only configuration could directly look for the spanwise cellular flows or the unsteady recirculation bubble hypothesized here. Validating these flow features is challenging, but indirect evidence could support our conclusions.

Machine Learning Surrogates with Enhanced Capability: A major long-term goal is to leverage advanced machine learning (ML) techniques to create surrogate models of slat noise that go beyond the limited-parameter Gaussian Process model developed here. This thesis sets the basic structure and theoretical ideas for it, but has implemented the surrogate primarily for Active Learning purposes. The same model, if continually trained for further acquisition steps can provide a noise surrogate, including for variations of the Reynolds number. Moreover, the method can be extended for more complex cases other than slat noise by utilizing the same method of feature reductions and representation of spectral data and their uncertainties. Finally the stochastic Upper Confidence Bound acquisition function that

we deployed is only one among many possible techniques, which are also evolving in their own literature. An upgrade using a more optimal acquisition function for sampling will be highly beneficial for industrial use.

Integration into Design and Noise Mitigation: In the long run, the insights and tools developed here can be directed towards practical noise reduction strategies for high-lift devices. One vision is to incorporate the surrogate model (enhanced by ML as discussed above) into a multi-objective optimization framework for aircraft design. For example, an optimizer could adjust the slat geometry or deployment angle to minimize noise, perhaps aiming to disrupt the coherence or reduce the strength of the cove instabilities, while still meeting lift and aerodynamic requirements. The fast evaluation provided by a surrogate model would make it feasible to explore a vast design space and identify novel configurations or add-on devices such as slat cove fillers or serrated slat cusps that achieve a better noise-performance trade-off. Any promising designs coming out of such computational optimization could then be validated by targeted high-fidelity simulations and experiments.

Extending High-Fidelity Simulations: As computing power continues to grow, it will become increasingly feasible to apply high-fidelity methods like LBM to more complex and realistic scenarios, which is another long-term avenue. Future researchers could build on this work by simulating a full wing with both slat and flap in deployed position, or a complete aircraft landing configuration, capturing the interplay between multiple noise sources (slat, flap, landing gear, etc.). While today this would be enormously demanding, trends in GPU-based computing and algorithmic improvements (e.g. adaptive mesh refinement in LBM, better boundary conditions, coupling with Large-Eddy Simulation turbulence models for finer near-wall resolution) may bring such computations within reach. These simulations would validate whether the noise mechanisms identified in an isolated slat hold in the presence of other components and whether new noise source interactions emerge. They could also provide high-fidelity data to guide standards and regulations by virtually testing noise abatement scenarios. In summary, the long-term trajectory of this research field will likely see a convergence of data-driven models and intensive simulations: the former (ML surrogates) will rapidly explore design changes and hypotheses, while the simulation tools like LBM as a next-generation high-fidelity simulation method will verify and deepen our understanding, each feeding into the other.

In closing, the work accomplished in this thesis, in our expectations, has laid a groundwork for statistical surrogate methodology in aeroacoustic design and augmented the physical insights for addressing slat noise. By amalgamating an advanced CFD approach (LBM) with modern surrogate modeling, we have shown a pathway to analyze, predict, and possibly mitigate the complex noise generated by high-lift devices. The method is also generalisable to other aeroacoustic cases where complex industrial geometries need to be studied parametrically but where each experimentation is computationally expensive. Finally, the findings on the flow dynamics and aeroacoustic mechanisms that we presented not only assist in solving pieces of the long-standing puzzle of slat noise dynamics, but also open the door to innovative research directions. Continued efforts along the lines described will bring us closer to the goals of deeper scientific understanding and practical noise reduction, contributing to the broader aim of more environmentally sustainable aviation.

Bibliography

- [1] Daniel Coutu. *Conception et Exploitation d'une Structure Active Pour Une Aile Laminaire Adaptative Expérimentale*. PhD thesis, École de technologie supérieure, 2010.
- [2] Dwight Barkley, M. Gabriela M. Gomes, and Ronald D. Henderson. Three-dimensional instability in flow over a backward-facing step. *Journal of Fluid Mechanics*, 473:167–190, December 2002. ISSN 0022-1120, 1469-7645. doi: 10.1017/S002211200200232X.
- [3] Guillaume A. Brès and Tim Colonius. Three-dimensional instabilities in compressible flow over open cavities. *Journal of Fluid Mechanics*, 599:309–339, March 2008. ISSN 0022-1120, 1469-7645. doi: 10.1017/S0022112007009925.
- [4] Hasan Kamliya Jawahar, Stefano Meloni, Roberto Camussi, and Mahdi Azarpeyvand. Intermittent and stochastic characteristics of slat tones. *Physics of Fluids*, 33(2):25120, February 2021. ISSN 10897666. doi: 10.1063/5.0033827.
- [5] A.R. Weyl. High-Lift Devices and Tailless Aeroplanes. *Aircraft Engineering and Aerospace Technology*, 17(11):325–330, January 1945. ISSN 0002-2667. doi: 10.1108/eb031306.
- [6] Martin R. Fink. Noise component method for airframe noise. *Journal of Aircraft*, 16(10):659–665, 1979. ISSN 00218669. doi: 10.2514/3.58586.
- [7] Homer G. Morgan and Jay C. Hardin. Airframe noise—the next aircraft noise barrier. *Journal of Aircraft*, 12(7):622–624, 1975. ISSN 00218669. doi: 10.2514/3.59844.
- [8] Dominique Collin. Overview of Aviation Noise research effort supported by the European Union. *International Civil Aviation Organization*, Environmental Report, 2016.
- [9] European Commission. Directorate General for Mobility and Transport. and European Commission. Directorate-General for Research and Innovation. *Flightpath 2050 : Europe's Vision for Aviation: Maintaining Global Leadership and Serving Society's Needs*. 2011. ISBN 978-92-79-19724-6. doi: 10.2777/50266.
- [10] Laurent Leylekian. *Aviation Noise Impact Management*. 2022. ISBN 978-3-030-91193-5. doi: 10.1007/978-3-030-91194-2.
- [11] Werner Dobrzynski. Almost 40 years of airframe noise research: What did we achieve? *Journal of Aircraft*, 47(2):353–367, 2010. ISSN 15333868. doi: 10.2514/1.44457.
- [12] Werner Dobrzynski, Kiyoshi Nagakura, Burkhard Gehlhar, and Andreas Buschbaum. Airframe noise studies on wings with deployed high-lift devices. *4th AIAA/CEAS Aeroacoustics Conference*, 1998. doi: 10.2514/6.1998-2337.

- [13] Meelan Choudhari and Kazuomi Yamamoto. Integrating CFD, CAA, and Experiments towards Benchmark Datasets for Airframe Noise Problems. *5th Symposium on Integrating CFD and Experiments in Aerodynamics*, October 2012. doi: <https://ntrs.nasa.gov/citations/20120016320>.
- [14] M. Terracol, E. Manoha, and B. Lemoine. Investigation of the unsteady flow and noise generation in a slat cove. *AIAA Journal*, 54(2):469–489, 2016. ISSN 00011452. doi: 10.2514/1.J053479.
- [15] Eric Manoha, Marc Terracol, Benoît Lemoine, Ingrid Le Griffon, and Thomas Le Garrec. Slat noise measurement and numerical prediction in the VALIANT programme. *18th AIAA/CEAS Aeroacoustics Conference (33rd AIAA Aeroacoustics Conference)*, (June):4–6, 2012. doi: 10.2514/6.2012-2100.
- [16] Sophie Perennes and Michel Roger. Aerodynamic noise of a two-dimensional wing with high-lift devices. *4th AIAA/CEAS Aeroacoustics Conference*, pages 772–782, 1998. doi: 10.2514/6.1998-2338.
- [17] Nicolas Molin and Michel Roger. The use of Amiet’s methods in predicting the noise from 2D high-lift devices, 2000.
- [18] Nicolas Molin, Michel Roger, and Sébastien Barré. Prediction of aircraft high-lift device noise using dedicated analytical models. *9th AIAA/CEAS Aeroacoustics Conference and Exhibit*, pages 1–11, 2003. doi: 10.2514/6.2003-3225.
- [19] David P. Lockard and Meelan M. Choudhari. Noise radiation from a leading-edge slat. *15th AIAA/CEAS Aeroacoustics Conference (30th AIAA Aeroacoustics Conference)*, (May), 2009. doi: 10.2514/6.2009-3101.
- [20] Meelan Choudhari, David Lockard, Mehdi Khorrami, and Raymond Mineck. Slat Noise Simulations: Status and Challenges. In *INTER-NOISE 2011*, volume 1, pages 361–368, September 2011. doi: <https://ntrs.nasa.gov/citations/20110015496>.
- [21] Kyle A. Pascioni and Louis N. Cattafesta. Aeroacoustic measurements of leading-edge slat noise. *22nd AIAA/CEAS Aeroacoustics Conference, 2016*, (September), 2016. doi: 10.2514/6.2016-2960.
- [22] Carlos C. Pagani, Daniel S. Souza, and Marcello A.F. Medeiros. Experimental investigation on the effect of slat geometrical configurations on aerodynamic noise. *Journal of Sound and Vibration*, 394: 256–279, 2017. ISSN 10958568. doi: 10.1016/j.jsv.2017.01.013.
- [23] Laura Botero Bolívar, Lourenço T.L. Pereira, Daniel Acevedo-Giraldo, Fernando M. Catalano, Danillo C. Reis, and Eduardo L.C. Coelho. Parametric analysis of the influence of slat geometry on acoustic noise. *2018 AIAA/CEAS Aeroacoustics Conference*, 2018. doi: 10.2514/6.2018-3593.
- [24] Alexander Kolb, Peter Faulhaber, Roger Drobietz, and Michael Grünewald. Aeroacoustic wind tunnel measurements on a 2D high-lift configuration. In *13th AIAA/CEAS Aeroacoustics Conference (28th AIAA Aeroacoustics Conference)*, page 3447, 2007. doi: 10.2514/6.2007-3447.
- [25] Michael Pott-Pollenske, Julian Alvarez-Gonzalez, and Werner Dobrzynski. Effect of Slat Gap/Overlap on Farfield Radiated Noise. (May), 2003. doi: 10.2514/6.2003-3228.
- [26] Laura Botero Bolivar, Martinus Sanders, and C H Venner. Analysis of a Semi-Empirical Leading-Edge Slat Noise Prediction Analysis of a Semi-Empirical Leading-Edge Slat Noise Prediction Model . 2(December):1507–1514, December 2020. doi: 10.48465/FA.2020.0686.

- [27] Yueping Guo. Slat noise modeling and prediction. *Journal of Sound and Vibration*, 331(15): 3567–3586, 2012. ISSN 0022460X. doi: 10.1016/j.jsv.2012.03.016.
- [28] Daniel S. Souza, Daniel Rodríguez, Fernando H.T. Himeno, and Marcello A.F. Medeiros. Dynamics of the large-scale structures and associated noise emission in airfoil slats. *Journal of Fluid Mechanics*, 875:1004–1034, 2019. ISSN 14697645. doi: 10.1017/jfm.2019.496.
- [29] Hasan Kamliya Jawahar, Stefano Meloni, Roberto Camussi, and Mahdi Azarpeyvand. Intermittent and stochastic characteristics of slat tones. *Physics of Fluids*, 33(2):025120, February 2021. ISSN 1070-6631, 1089-7666. doi: 10.1063/5.0033827.
- [30] Kazuomi Yamamoto, Kentaro Tanaka, Tohru Hirai, and Mitsuhiro Murayama. A Numerical Study on Noise Generation Caused by Slat Tracks. In *AIAA AVIATION 2023 Forum*, San Diego, CA and Online, June 2023. American Institute of Aeronautics and Astronautics. ISBN 978-1-62410-704-7. doi: 10.2514/6.2023-4478.
- [31] Meelan M Choudhari and Mehdi R Khorrami. Effect of three-dimensional shear-layer structures on slat cove unsteadiness. *AIAA journal*, 45(9):2174–2186, 2007. doi: 10.2514/1.24812.
- [32] Damiano Casalino, Ignacio Gonzalez-Martino, and Simone Mancini. On the Rossiter-Heller frequency of resonant cavities. *Aerospace Science and Technology*, 131:108013, December 2022. ISSN 12709638. doi: 10.1016/j.ast.2022.108013.
- [33] J. E. Rossiter. Wind tunnel experiments on the flow over rectangular cavities at subsonic and transonic speeds. Technical report, Cranfield University, 1964.
- [34] Taro Imamura, Shunji Enomoto, Yuzuru Yokokawa, and Kazuomi Yamamoto. Simulation of the broadband noise from a slat using zonal LES/RANS hybrid method. *Collection of Technical Papers - 45th AIAA Aerospace Sciences Meeting*, 4(January):2675–2688, 2007. doi: 10.2514/6.2007-226.
- [35] Laura Botero Bolivar. *Parametric Analysis of the Influence of Slat Geometry on Airframe Noise by a Commercial Code*. Mestrado Em Aeronaves, Universidade de São Paulo, São Carlos, January 2020.
- [36] Julie Hayes, W. Horne, Paul Soderman, Paul Bent, Julie Hayes, W. Horne, Paul Soderman, and Paul Bent. Airframe noise characteristics of a 4.7 percent scale DC-10 model. In *3rd AIAA/CEAS Aeroacoustics Conference*, Atlanta, GA, U.S.A., May 1997. American Institute of Aeronautics and Astronautics. doi: 10.2514/6.1997-1594.
- [37] Stéphane Moreau. The third golden age of aeroacoustics. *Physics of Fluids*, 34(3):031301, March 2022. ISSN 1070-6631, 1089-7666. doi: 10.1063/5.0084060.
- [38] Simon Marié, Denis Ricot, and Pierre Sagaut. Comparison between lattice Boltzmann method and Navier–Stokes high order schemes for computational aeroacoustics. *Journal of Computational Physics*, 228(4):1056–1070, March 2009. ISSN 00219991. doi: 10.1016/j.jcp.2008.10.021.
- [39] Rajani Satti, Yanbing Li, Richard Shock, and Swen Noelting. Unsteady flow analysis of a multi-element airfoil using lattice boltzmann method. *AIAA Journal*, 50(9):1805–1816, 2012. ISSN 00011452. doi: 10.2514/1.J050906.
- [40] Jian Fang, Aleksandr A. Zheltovodov, Yufeng Yao, Charles Moulinec, and David R. Emerson. On the turbulence amplification in shock-wave/turbulent boundary layer interaction. *Journal of Fluid Mechanics*, 2020. ISSN 14697645. doi: 10.1017/jfm.2020.350.

- [41] Malav Soni, Roland Ewert, Jan Delfs, and Kannan Masilamani. Towards Wall-Modeled LES with Lattice Boltzmann Method for Aeroacoustics: Application and Understanding. In *28th AIAA/CEAS Aeroacoustics 2022 Conference*, Southampton, UK, June 2022. American Institute of Aeronautics and Astronautics. ISBN 978-1-62410-664-4. doi: 10.2514/6.2022-2918.
- [42] Daniel Sampaio Souza, Filipe Amaral, Fernando Himeno, Carlos Pagani, Leandro Simões, Daniel Rodriguez, and Marcello Medeiros. New insights on slat noise based on a revisit of previous experimental-numerical studies. In *28th AIAA/CEAS Aeroacoustics 2022 Conference*, Southampton, UK, June 2022. American Institute of Aeronautics and Astronautics. ISBN 978-1-62410-664-4. doi: 10.2514/6.2022-2809.
- [43] Guillaume Brès and Tim Colonius. Direct Numerical Simulations of Three-Dimensional Cavity Flows. In *13th AIAA/CEAS Aeroacoustics Conference (28th AIAA Aeroacoustics Conference)*, Rome, Italy, May 2007. American Institute of Aeronautics and Astronautics. ISBN 978-1-62410-003-1. doi: 10.2514/6.2007-3405.
- [44] Thomas Astoul. *Towards Improved Lattice Boltzmann Aeroacoustic Simulations with Non-Uniform Grids : Application to Landing Gears Noise Prediction*. Doctoral Thesis, Aix-Marseille, 2021.
- [45] J. E. Ffowcs Williams and D. L. Hawkings. Sound Generation by Turbulence and Surfaces in Arbitrary Motion. *Philosophical Transactions of the Royal Society of London. Series A, Mathematical and Physical Sciences*, 264(1151):321–342, 1969. doi: 10.1098/rsta.1969.0031.
- [46] Damiano Casalino. An advanced time approach for acoustic analogy predictions. *Journal of Sound and Vibration*, 261(4):583–612, April 2003. ISSN 0022460X. doi: 10.1016/S0022-460X(02)00986-0.
- [47] M A Mendez, A Iapiro, Bernd R. Noack, and S.L Brunton. *Data-Driven Fluid Mechanics: Combining First Principles and Machine Learning*. Cambridge University Press, Cambridge, 2023. ISBN 978-1-108-89621-4.
- [48] J. E. Ffowcs Williams and L. H. Hall. Aerodynamic sound generation by turbulent flow in the vicinity of a scattering half plane. *Journal of Fluid Mechanics*, 40(04):657, March 1970. ISSN 0022-1120, 1469-7645. doi: 10.1017/S0022112070000368.
- [49] M J Lighthill. On sound generated aerodynamically I. General theory. *Proceedings of the Royal Society of London. Series A. Mathematical and Physical Sciences*, 211(1107):564–587, 1952. ISSN 0080-4630. doi: 10.1098/rspa.1952.0060.
- [50] R.K. Amiet. Noise due to turbulent flow past a trailing edge. *Journal of Sound and Vibration*, 47 (3):387–393, August 1976. ISSN 0022460X. doi: 10.1016/0022-460X(76)90948-2.
- [51] M.S. Howe. A review of the theory of trailing edge noise. *Journal of Sound and Vibration*, 61(3): 437–465, December 1978. ISSN 0022460X. doi: 10.1016/0022-460X(78)90391-7.
- [52] D G Crighton. The Kutta Condition in Unsteady Flow. *Annual Review of Fluid Mechanics*, 17: 411–445, 1985. ISSN 1545-4479. doi: 10.1146/annurev.fl.17.010185.002211.
- [53] Richard D Sandberg and Neil D Sandham. Noise due to unsteady flow past trailing edges. In *ECCOMAS CFD 2006: Proceedings of the European Conference on Computational Fluid Dynamics, Egmond Aan Zee, the Netherlands, September 5-8, 2006*. Delft University of Technology; European Community on Computational Methods ..., 2006.

- [54] André V. G. Cavalieri and Anurag Agarwal. Coherence decay and its impact on sound radiation by wavepackets. *Journal of Fluid Mechanics*, 748:399–415, June 2014. ISSN 0022-1120, 1469-7645. doi: 10.1017/jfm.2014.186.
- [55] Michel Roger and Stéphane Moreau. Back-scattering correction and further extensions of Amiet’s trailing-edge noise model. Part 1: Theory. *Journal of Sound and Vibration*, 286(3):477–506, 2005. ISSN 0022460X. doi: 10.1016/j.jsv.2004.10.054.
- [56] Björn Greschner, J. Grilliat, M.C. Jacob, and F. Thiele. Measurements and wall Modeled LES Simulation of Trailing Edge Noise Caused by a Turbulent Boundary Layer. *International Journal of Aeroacoustics*, 9(3):329–355, May 2010. ISSN 1475-472X, 2048-4003. doi: 10.1260/1475-472X.9.3.329.
- [57] Arthur Finez, Marc Jacob, Emmanuel Jondeau, and Michel Roger. Experimental Investigation of Trailing-Edge Noise from a Linear Cascade of Cambered Airfoils. In *17th AIAA/CEAS Aeroacoustics Conference (32nd AIAA Aeroacoustics Conference)*, Aeroacoustics Conferences. American Institute of Aeronautics and Astronautics, June 2011. doi: 10.2514/6.2011-2876.
- [58] Alex Sano, Leandra I. Abreu, André V. G. Cavalieri, and William R. Wolf. Trailing-edge noise from the scattering of spanwise-coherent structures. *Physical Review Fluids*, 4(9):094602, September 2019. ISSN 2469-990X. doi: 10.1103/PhysRevFluids.4.094602.
- [59] Antonio Alguacil, Michaël Bauerheim, Marc C. Jacob, and Stéphane Moreau. Correcting the Prediction of Noise Scattering at Sharp Edges for a Spatio-Temporal Deep Learned Acoustic Surrogate. In *AIAA AVIATION 2023 Forum*, AIAA AVIATION Forum. American Institute of Aeronautics and Astronautics, June 2023. doi: 10.2514/6.2023-3341.
- [60] Stéphane Redonnet, Turzo Bose, Arjit Seth, and Larry K.B. Li. Airfoil self-noise prediction using deep neural networks. *Engineering Analysis with Boundary Elements*, 159:180–191, February 2024. ISSN 09557997. doi: 10.1016/j.enganabound.2023.11.024.
- [61] F Brooks, D Stuart, and A Marcolini. Airfoil Self-Noise and Prediction. *NASA Reference Publication*, July 1989.
- [62] Stephane Moreau, Michel Roger, and Julien Christophe. Flow Features and Self-Noise of Airfoils Near Stall or in Stall. In *15th AIAA/CEAS Aeroacoustics Conference (30th AIAA Aeroacoustics Conference)*, Miami, Florida, May 2009. American Institute of Aeronautics and Astronautics. ISBN 978-1-60086-967-9. doi: 10.2514/6.2009-3198.
- [63] Andrea Arroyo Ramo, Stéphane Moreau, Richard D. Sandberg, Michaël Bauerheim, and Marc C. Jacob. Controlled Diffusion airfoil self-noise, an acoustic far-field prediction. In *AIAA AVIATION 2023 Forum*, AIAA AVIATION Forum. American Institute of Aeronautics and Astronautics, June 2023. doi: 10.2514/6.2023-3505.
- [64] Giovanni Lacagnina, Paruchuri Chaitanya, Tim Berk, Jung-Hoon Kim, Phillip Joseph, Bharathram Ganapathisubramani, Seyed Mohammad Hasheminejad, Tze Pei Chong, Oksana Stalnov, Kwing-So Choi, Muhammad Farrukh Shahab, Mohammad Omidyeganeh, and Alfredo Pinelli. Mechanisms of airfoil noise near stall conditions. *Physical Review Fluids*, 4(12):123902, December 2019. ISSN 2469-990X. doi: 10.1103/PhysRevFluids.4.123902.

- [65] Alex Laratro, Maziar Arjomandi, Benjamin Cazzolato, and Richard Kelso. Self-noise and directivity of simple airfoils during stall: An experimental comparison. *Applied Acoustics*, 127:133–146, December 2017. ISSN 0003682X. doi: 10.1016/j.apacoust.2017.05.027.
- [66] H. Arbey and J. Bataille. Noise generated by airfoil profiles placed in a uniform laminar flow. *Journal of Fluid Mechanics*, 134:33–47, 1983. ISSN 14697645. doi: 10.1017/S0022112083003201.
- [67] Martin Lowson, Steven Fiddes, and Emma Nash. Laminar boundary layer aero-acoustic instabilities. In *32nd Aerospace Sciences Meeting and Exhibit*, page 358, 1994. doi: 10.2514/6.1994-358.
- [68] R.E. Longhouse. Vortex shedding noise of low tip speed, axial flow fans. *Journal of Sound and Vibration*, 53(1):25–46, July 1977. ISSN 0022460X. doi: 10.1016/0022-460X(77)90092-X.
- [69] Dhanush Vittal-Shenoy, Romain Gojon, Thierry Jardin, and Marc C. Jacob. Angle-of-attack and Mach number effects on the aeroacoustics of an SD7003 airfoil at Reynolds number 60,000. *International Journal of Aeroacoustics*, 22(1-2):131–152, March 2023. ISSN 1475-472X, 2048-4003. doi: 10.1177/1475472X221150173.
- [70] Thomas F Brooks and Michael A Marcolini. Scaling of airfoil self-noise using measured flow parameters. *AIAA journal*, 23(2):207–213, 1985. doi: 10.2514/3.8896.
- [71] William K. Blake and S. Temkin. Mechanics of Flow-Induced Sound and Vibration. Vol. I: General Concepts and Elementary Sources. (1), January 1988. ISSN 0001-4966, 1520-8524. doi: 10.1121/1.396227.
- [72] M. J. Bilka, S. C. Morris, C. Berntsen, J. C. Silver, and D. W. Shannon. Flowfield and Sound from a Blunt Trailing Edge with Varied Thickness. *AIAA Journal*, 52(1):52–61, January 2014. ISSN 0001-1452, 1533-385X. doi: 10.2514/1.J052550.
- [73] R. Parker and M.C. Welsh. Effects of sound on flow separation from blunt flat plates. *International Journal of Heat and Fluid Flow*, 4(2):113–127, June 1983. ISSN 0142727X. doi: 10.1016/0142-727X(83)90014-0.
- [74] B. Thompson and R. Lotz. Flow around a blunt and divergent trailing edge. *Experiments in Fluids*, 33(3):374–383, September 2002. ISSN 0723-4864, 1432-1114. doi: 10.1007/s00348-002-0421-z.
- [75] Michel Roger, Stéphane Moreau, and Alain Guédel. Vortex-Shedding Noise and Potential-Interaction Noise Modeling by a Reversed Sears' Problem. In *12th AIAA/CEAS Aeroacoustics Conference (27th AIAA Aeroacoustics Conference)*, Cambridge, Massachusetts, May 2006. American Institute of Aeronautics and Astronautics. ISBN 978-1-62410-021-5. doi: 10.2514/6.2006-2607.
- [76] Caroline O.L. Hamilton Smith, Nicholas Lawson, and Gareth A. Vio. History, review and summary of the cavity flow phenomena. *European Journal of Mechanics - B/Fluids*, 108:32–72, November 2024. ISSN 09977546. doi: 10.1016/j.euromechflu.2024.07.005.
- [77] V. Strouhal. Ueber eine besondere Art der Tonerregung. *Annalen der Physik*, 241(10):216–251, January 1878. ISSN 0003-3804, 1521-3889. doi: 10.1002/andp.18782411005.
- [78] A. F. Charwat, J. N. ROOS, F. C. Dewey, and J. A. Hitz. An investigation of separated flows - part I: The pressure field. *Journal of the Aerospace Sciences*, 28(6):457–470, 1961. doi: 10.2514/8.9037.
- [79] Francesco Scarano, Marc C. Jacob, and Erwin R. Gowree. Drag reduction by means of an array of staggered circular cavities at moderate Reynolds numbers. *International Journal of Heat and Fluid Flow*, 102:109142, August 2023. ISSN 0142727X. doi: 10.1016/j.ijheatfluidflow.2023.109142.

- [80] Robert L Stallings and Floyd J Wilcox. Experimental Cavity Pressure Distributions at Supersonic Speeds. *National Aeronautics and Space Administration, Scientific and Technical Information Office*, 1987.
- [81] Marc Jacob, Vincent Gradoz, Alain Louisot, Daniel Juve, and Sylvie Guerrand. Comparison of sound radiated by shallow cavities and backward facing steps. In *5th AIAA/CEAS Aeroacoustics Conference and Exhibit*, 1999. doi: 10.2514/6.1999-1892.
- [82] Marc C. Jacob, Alain Louisot, Daniel Juvé, and Sylvie Guerrand. Experimental Study of Sound Generated by Backward-Facing Steps Under Wall Jet. *AIAA Journal*, 39(7):1254–1260, July 2001. ISSN 0001-1452, 1533-385X. doi: 10.2514/2.1467.
- [83] Y. Addad, D. Laurence, C. Talotte, and M.C. Jacob. Large eddy simulation of a forward–backward facing step for acoustic source identification. *International Journal of Heat and Fluid Flow*, 24(4): 562–571, August 2003. ISSN 0142727X. doi: 10.1016/S0142-727X(03)00050-X.
- [84] Damien Leclercq, Marc Jacob, Alain Louisot, and Corinne Talotte. Forward-backward facing step pair - Aerodynamic flow, wall pressure and acoustic characterisation. In *7th AIAA/CEAS Aeroacoustics Conference and Exhibit*, 2012. doi: 10.2514/6.2001-2249.
- [85] O. Marsden, C. Bailly, C. Bogey, and E. Jondeau. Investigation of flow features and acoustic radiation of a round cavity. *Journal of Sound and Vibration*, 331(15):3521–3543, July 2012. ISSN 0022460X. doi: 10.1016/j.jsv.2012.03.017.
- [86] Francesco Scarano, Marc C. Jacob, Romain Gojon, Xavier Carbonneau, and Erwin R. Gowree. Modification of a turbulent boundary layer by circular cavities. *Physics of Fluids*, 34(6):065134, June 2022. ISSN 1070-6631, 1089-7666. doi: 10.1063/5.0091110.
- [87] Francesco Scarano, Marc C. Jacob, Xavier Carbonneau, and Erwin R. Gowree. On the turbulent boundary layer over a flat plate at moderate Reynolds numbers. *Physics of Fluids*, 34(11):115150, November 2022. ISSN 1070-6631. doi: 10.1063/5.0124498.
- [88] Y. P. Guo. A model for slat noise generation. *3rd AIAA/CEAS Aeroacoustics Conference*, pages 1–11, 1997. doi: 10.2514/6.1997-1647.
- [89] Mehdi R. Khorrami, Mert E. Berkman, and Meelan Choudhari. Unsteady flow computations of a slat with a blunt trailing edge. *AIAA Journal*, 38(11):2050–2058, 2000. doi: 10.2514/2.892.
- [90] Christopher K. W. Tam and Nikolai Pastouchenko. Gap tones. *AIAA Journal*, 39(8):1442–1448, 2001. ISSN 0001-1452. doi: 10.2514/3.14887.
- [91] Y. P. Guo and M. C. Joshi. Noise characteristics of aircraft high lift systems. *AIAA Journal*, 41 (7):1247–1256, 2003. ISSN 00011452. doi: 10.2514/2.2093.
- [92] Anurag Agarwal and Philip J. Morris. Broadband noise from the unsteady flow in a slat cove. *AIAA Paper*, (January):9574–9585, 2004. doi: 10.2514/6.2004-854.
- [93] K. Takeda, X. Zhang, and P. A. Nelson. Computational aeroacoustic simulations of leading-edge slat flow. *Journal of Sound and Vibration*, 270(3):559–572, 2004. ISSN 0022460X. doi: 10.1016/j.jsv.2003.09.046.
- [94] R. Ewert and R. Emunds. CAA slat noise studies applying stochastic sound sources based on solenoidal digital filters. *Collection of Technical Papers - 11th AIAA/CEAS Aeroacoustics Conference*, 2(May):785–806, 2005. doi: 10.2514/6.2005-2862.

- [95] Kristian Kaepernick, Lars Koop, and Klaus Ehrenfried. Investigation of the Unsteady Flow Field Inside a Leading Edge Slat Cove. In *11th AIAA/CEAS Aeroacoustics Conference*, Monterey, California, May 2005. American Institute of Aeronautics and Astronautics. ISBN 978-1-62410-052-9. doi: 10.2514/6.2005-2813.
- [96] Mehdi R Khorrami and David P Lockard. Effects of geometric details on slat noise generation and propagation. *International Journal of aeroacoustics*, 9(4):655–678, 2010. doi: 10.1260/1475-472X.9.4-5.6.
- [97] D. König, S. R. Koh, M. Meinke, and W. Schröder. Two-step simulation of slat noise. *Computers and Fluids*, 39(3):512–524, 2010. ISSN 00457930. doi: 10.1016/j.compfluid.2009.10.004.
- [98] Meelan Choudhari and David Lockard. Simulations & Measurements of Airframe Noise : A BANC Workshops Perspective. *Nato Otan*, pages 1–19, 2017.
- [99] Mitsuhiro Murayama, Kazuyuki Nakakita, Kazuomi Yamamoto, Hiroki Ura, Yasushi Ito, and Meelan M. Choudhari. Experimental study of slat noise from 30P30N three-element high-lift airfoil in JAXA hard-wall low-speed wind tunnel. *20th AIAA/CEAS Aeroacoustics Conference*, (June):6–13, 2014. doi: 10.2514/6.2014-2080.
- [100] Renke Wei, Yu Liu, Xiaodong Li, and Haoyu Zhang. Experimental study on the oscillation of the shear layer of the slat cavity for 30P30N Multi-Element High-Lift Airfoil. In *AIAA Aviation 2023 Forum*, San Diego, CA and Online, June 2023. American Institute of Aeronautics and Astronautics. ISBN 978-1-62410-704-7. doi: 10.2514/6.2023-4482.
- [101] Renke Wei and Yu Liu. Experimental study on the mode switching of strong-amplitude tones in slat noise. *Experiments in Fluids*, 66(2):25, February 2025. ISSN 0723-4864, 1432-1114. doi: 10.1007/s00348-025-03956-8.
- [102] Laura Botero, Lourenço T. Lima Pereira, Daniel Acevedo, Fernando Catalano, Danillo C. Reis, and Eduardo L. Coelho. Parametric Analysis of the Influence of Slat Geometry on Acoustic Noise. In *2018 AIAA/CEAS Aeroacoustics Conference*, Atlanta, Georgia, June 2018. American Institute of Aeronautics and Astronautics. ISBN 978-1-62410-560-9. doi: 10.2514/6.2018-3593.
- [103] Hasan Kamliya Jawahar. *Aerodynamic and Aeroacoustic Performance of Morphing Structures*. PhD thesis, University of Bristol, May 2019.
- [104] Hasan Kamliya Jawahar, Syamir Alihan Showkat Ali, Mahdi Azarpeyvand, and Carlos R. Ilário da Silva. Aerodynamic and aeroacoustic performance of high-lift airfoil fitted with slat cove fillers. *Journal of Sound and Vibration*, 479:115347, 2020. ISSN 10958568. doi: 10.1016/j.jsv.2020.115347.
- [105] Fernando H.T. Himeno, Daniel S. Souza, Filipe R. Amaral, Daniel Rodríguez, and Marcello A.F. Medeiros. SPOD analysis of noise-generating Rossiter modes in a slat with and without a bulb seal. *Journal of Fluid Mechanics*, 915:1–24, 2021. ISSN 14697645. doi: 10.1017/jfm.2021.93.
- [106] Guillaume A. Brès, Franck Pérot, and David Freed. Properties of the Lattice-Boltzmann method for acoustics. *15th AIAA/CEAS Aeroacoustics Conference (30th AIAA Aeroacoustics Conference)*, (May):11–13, 2009. doi: 10.2514/6.2009-3395.
- [107] Thomas Astoul, Gauthier Wissocq, Jean François Boussuge, Alois Sengissen, and Pierre Sagaut. Analysis and reduction of spurious noise generated at grid refinement interfaces with the lattice Boltzmann method. *Journal of Computational Physics*, 418:109645, 2020. ISSN 10902716. doi: 10.1016/j.jcp.2020.109645.

- [108] Mehdi R. Khorrami and David P. Lockard. Effects of geometric details on slat noise generation and propagation. *Collection of Technical Papers - 12th AIAA/CEAS Aeroacoustics Conference*, 6(4):3413–3438, 2006. ISSN 1475-472X. doi: 10.1260/1475-472x.9.4-5.655.
- [109] Yongliang Feng, Pierre Boivin, Jérôme Jacob, and Pierre Sagaut. Hybrid recursive regularized thermal lattice Boltzmann model for high subsonic compressible flows. *Journal of Computational Physics*, 394:82–99, 2019. doi: 10.1016/j.jcp.2019.05.031.
- [110] U. Frisch, B. Hasslacher, and Y. Pomeau. Lattice-Gas Automata for the Navier-Stokes Equation. *Physical Review Letters*, 56(14):1505–1508, April 1986. ISSN 0031-9007. doi: 10.1103/PhysRevLett.56.1505.
- [111] Weibing Feng, Bing He, Anping Song, Yang Wang, Miao Zhang, and Wu Zhang. Compressible Lattice Boltzmann Method and Applications. In David Hutchison, Takeo Kanade, Josef Kittler, Jon M. Kleinberg, Friedemann Mattern, John C. Mitchell, Moni Naor, Oscar Nierstrasz, C. Pandu Rangan, Bernhard Steffen, Madhu Sudan, Demetri Terzopoulos, Doug Tygar, Moshe Y. Vardi, Gerhard Weikum, Wu Zhang, Zhangxin Chen, Craig C. Douglas, and Weiqin Tong, editors, *High Performance Computing and Applications*, volume 5938, pages 17–26. Springer Berlin Heidelberg, Berlin, Heidelberg, 2010. ISBN 978-3-642-11841-8 978-3-642-11842-5. doi: 10.1007/978-3-642-11842-5_3.
- [112] Timm Krüger, Halim Kusumaatmaja, Alexandr Kuzmin, Orest Shardt, Goncalo Silva, and Erlend Magnus Viggen. *The Lattice Boltzmann Method: Principles and Practice*. Graduate Texts in Physics. Springer International Publishing : Imprint: Springer, Cham, 1st ed. 2017 edition, 2017. ISBN 978-3-319-44649-3. doi: 10.1007/978-3-319-44649-3.
- [113] P. L. Bhatnagar, E. P. Gross, and M. Krook. A Model for Collision Processes in Gases. I. Small Amplitude Processes in Charged and Neutral One-Component Systems. *Physical Review*, 94(3):511–525, May 1954. ISSN 0031-899X. doi: 10.1103/PhysRev.94.511.
- [114] R Benzi, S Succi, and M Vergassola. Turbulence Modelling by Nonhydrodynamic Variables. *Europhysics Letters (EPL)*, 13(8):727–732, December 1990. ISSN 0295-5075, 1286-4854. doi: 10.1209/0295-5075/13/8/010.
- [115] R. Benzi, S. Succi, and M. Vergassola. The lattice Boltzmann equation: Theory and applications. *Physics Reports*, 222(3):145–197, 1992. ISSN 03701573. doi: 10.1016/0370-1573(92)90090-M.
- [116] Björn Greschner, Frank Thiele, Marc C. Jacob, and Damiano Casalino. Prediction of sound generated by a rod-airfoil configuration using EASM DES and the generalised Lighthill/FW-H analogy. *Computers & Fluids*, 37(4):402–413, May 2008. ISSN 00457930. doi: 10.1016/j.compfluid.2007.02.013.
- [117] Damiano Casalino, Marc Jacob, and Michel Roger. Prediction of Rod-Airfoil Interaction Noise Using the Ffowcs-Williams-Hawkins Analogy. *AIAA Journal*, 41(2):182–191, February 2003. ISSN 0001-1452, 1533-385X. doi: 10.2514/2.1959.
- [118] Jérôme Boudet, Joëlle Caro, Bo Li, Emmanuel Jondeau, and Marc C Jacob. Zonal large-eddy simulation of a tip leakage flow. *International Journal of Aeroacoustics*, 15(6-7):646–661, October 2016. ISSN 1475-472X, 2048-4003. doi: 10.1177/1475472X16659215.
- [119] F Farassat. Derivation of Formulations 1 and 1A of Farassat. pages 1–20, August 2013.

- [120] S. Mendez, M. Shoeybi, S. K. Lele, and P. Moin. On the Use of the Ffowcs Williams-Hawkins Equation to Predict Far-Field Jet Noise from Large-Eddy Simulations. *International Journal of Aeroacoustics*, 12(1-2):1–20, January 2013. ISSN 1475-472X, 2048-4003. doi: 10.1260/1475-472X.12.1-2.1.
- [121] Gauthier Wissocq, Nicolas Gourdain, Orestis Malaspinas, and Alexandre Eyssartier. Regularized characteristic boundary conditions for the Lattice-Boltzmann methods at high Reynolds number flows. *Journal of Computational Physics*, 331:1–18, February 2017. ISSN 00219991. doi: 10.1016/j.jcp.2016.11.037.
- [122] O. Malaspinas and P. Sagaut. Wall model for large-eddy simulation based on the lattice Boltzmann method. *Journal of Computational Physics*, 275:25–40, October 2014. ISSN 00219991. doi: 10.1016/j.jcp.2014.06.020.
- [123] J. Boudet, E. Lévêque, and H. Touil. Unsteady Lattice Boltzmann Simulations of Corner Separation in a Compressor Cascade. *Journal of Turbomachinery*, 144(1):011010, January 2022. ISSN 0889-504X, 1528-8900. doi: 10.1115/1.4052017.
- [124] Martha A. Gallivan, David R. Noble, John G. Georgiadis, and Richard O. Buckius. An evaluation of the bounce-back boundary condition for lattice Boltzmann simulations. *International Journal for Numerical Methods in Fluids*, 25(3):249–263, August 1997. ISSN 0271-2091, 1097-0363. doi: 10.1002/(SICI)1097-0363(19970815)25:3<249::AID-FLD546>3.0.CO;2-7.
- [125] David P Lockard, Meelan M Choudhari, and Veer N Vatsa. Aeroacoustic Simulations of the High-Lift Common Research Model and Validation with Experiment. pages 1–28, 2022. doi: 10.2514/6.2022-2806.
- [126] Yang Zhang, Louis Cattafesta, Kyle Pascioni, and Meelan Choudhari. Slat noise in high-lift systems. *Progress in Aerospace Sciences*, 146:100996, April 2024. ISSN 03760421. doi: 10.1016/j.paerosci.2024.100996.
- [127] M. D. Neary and K. D. Stephanoff. Shear-layer-driven transition in a rectangular cavity. *The Physics of Fluids*, 30(10):2936–2946, October 1987. ISSN 0031-9171. doi: 10.1063/1.866071.
- [128] William W Liou. Linear instability of curved free shear layers. *Phys. Fluids*, 6, 2014. doi: 10.1063/1.868350.
- [129] Lord Rayleigh. On the dynamics of revolving fluids. *Proceedings of the Royal Society of London. Series A, Containing Papers of a Mathematical and Physical Character*, 93(648):148–154, 1917. doi: 10.1098/rspa.1917.0010.
- [130] Jiangsheng Wang, Jinjun Wang, and Kyung Chun Kim. Wake/shear layer interaction for low-Reynolds-number flow over multi-element airfoil. *Experiments in Fluids*, 60(1):16, January 2019. ISSN 0723-4864, 1432-1114. doi: 10.1007/s00348-018-2662-5.
- [131] Jiang Sheng Wang and Jin Jun Wang. Vortex dynamics for flow around the slat cove at low Reynolds numbers. *Journal of Fluid Mechanics*, 919:1–33, 2021. ISSN 14697645. doi: 10.1017/jfm.2021.385.
- [132] Vincent Clair and Gwénaël Gabard. Spectral broadening of acoustic waves by convected vortices. *Journal of Fluid Mechanics*, 841:50–80, April 2018. ISSN 0022-1120, 1469-7645. doi: 10.1017/jfm.2018.94.

- [133] Jean-Christophe Giret, Alois Sengissen, Stéphane Moreau, Marlène Sanjosé, and Jean-christophe Jouhaud. Prediction of the sound generated by a rod-airfoil configuration using a compressible unstructured LES solver and a FW-H analogy. In *18th AIAA/CEAS Aeroacoustics Conference (33rd AIAA Aeroacoustics Conference)*, Colorado Springs, CO, June 2012. American Institute of Aeronautics and Astronautics. ISBN 978-1-60086-932-7. doi: 10.2514/6.2012-2058.
- [134] Marc C. Jacob, Jérôme Boudet, Damiano Casalino, and Marc Michard. A rod-airfoil experiment as a benchmark for broadband noise modeling. *Theoretical and Computational Fluid Dynamics*, 19(3):171–196, July 2005. ISSN 0935-4964, 1432-2250. doi: 10.1007/s00162-004-0108-6.
- [135] Hao Wu, Julian Winkler, Richard D. Sandberg, and Stephane Moreau. Direct Numerical Simulation of Transitional Airfoil Noise. In *23rd AIAA/CEAS Aeroacoustics Conference*, Denver, Colorado, June 2017. American Institute of Aeronautics and Astronautics. ISBN 978-1-62410-504-3. doi: 10.2514/6.2017-3368.
- [136] Julian CR Hunt, Alan A Wray, and Parviz Moin. Eddies, streams, and convergence zones in turbulent flows. *Studying turbulence using numerical simulation databases, 2. Proceedings of the 1988 summer program*, December 1988.
- [137] W S Saric. Görtler Vortices. *Annual Review of Fluid Mechanics*, 26(1):379–409, January 1994. ISSN 0066-4189, 1545-4479. doi: 10.1146/annurev.fl.26.010194.002115.
- [138] J M Floryan. On the Gortler instability of boundary layers. *Progress in Aerospace Sciences*, 28(3):235–271, 1991. ISSN 0376-0421. doi: 10.1016/0376-0421(91)90006-P.
- [139] P. Bradshaw. The analogy between streamline curvature and buoyancy in turbulent shear flow. *Journal of Fluid Mechanics*, 36(1):177–191, March 1969. ISSN 0022-1120, 1469-7645. doi: 10.1017/S0022112069001583.
- [140] Peter Bradshaw and A. D. Young. Effects of Streamline Curvature on Turbulent Flow. Technical report, University of Minnesota, Paris, July 2016.
- [141] John Corry Wyngaard. *An Experimental Investigation of the Small-Scale Structure of Turbulence in a Curved Mixing Layer*. PhD thesis, The Pennsylvania State University, 1967.
- [142] H.S. Ribner. The generation of sound by turbulent jets. volume 8 of *Advances in Applied Mechanics*, pages 103–182. Elsevier, 1964. doi: 10.1016/S0065-2156(08)70354-5.
- [143] Roland Ewert and Johannes Kreuzinger. Hydrodynamic/acoustic splitting approach with flow-acoustic feedback for universal subsonic noise computation. *Journal of Computational Physics*, 444:110548, November 2021. ISSN 00219991. doi: 10.1016/j.jcp.2021.110548.
- [144] Renke Wei and Yu Liu. On the shear-layer oscillation and low-frequency tonal noise in a slat cove. *Physics of Fluids*, 37(3):034113, March 2025. ISSN 1070-6631, 1089-7666. doi: 10.1063/5.0260403.
- [145] Guillaume A. Brès and Tim Colonius. Three-dimensional instabilities in compressible flow over open cavities. *Journal of Fluid Mechanics*, 599:309–339, March 2008. ISSN 0022-1120, 1469-7645. doi: 10.1017/S0022112007009925.
- [146] S. Albensoeder, H. C. Kuhlmann, and H. J. Rath. Three-dimensional centrifugal-flow instabilities in the lid-driven-cavity problem. *Physics of Fluids*, 13(1):121–135, January 2001. ISSN 1070-6631, 1089-7666. doi: 10.1063/1.1329908.

- [147] Mark J Anderson. *DOE Simplified: Practical Tools for Effective Experimentation*. Productivity Press, third edition edition, 2015.
- [148] Slawomir Koziel, Leifur Leifsson, and Xin-She Yang. *Solving Computationally Expensive Engineering Problems: Methods and Applications*, volume 97. Springer, 2014.
- [149] Weidong Shao and Jun Li. Review of Lattice Boltzmann Method Applied to Computational Aeroacoustics. *Archives of Acoustics*, 44(2):215–238, 2019. ISSN 0137-5075, 2300-262X. doi: 10.24425/aoa.2019.128486.
- [150] Reza Alizadeh, Janet K. Allen, and Farrokh Mistree. Managing computational complexity using surrogate models: A critical review. *Research in Engineering Design*, 31(3):275–298, July 2020. ISSN 0934-9839, 1435-6066. doi: 10.1007/s00163-020-00336-7.
- [151] André I Khuri and Siuli Mukhopadhyay. Response surface methodology. *Wiley interdisciplinary reviews: Computational statistics*, 2(2):128–149, 2010. doi: 10.1002/wics.73.
- [152] Shawn E. Gano, John E. Renaud, Jay D. Martin, and Timothy W. Simpson. Update strategies for kriging models used in variable fidelity optimization. *Structural and Multidisciplinary Optimization*, 32(4):287–298, October 2006. ISSN 1615-147X, 1615-1488. doi: 10.1007/s00158-006-0025-y.
- [153] Daniel Kottke, Marek Herde, Christoph Sandrock, Denis Huseljic, Georg Kreml, and Bernhard Sick. Toward optimal probabilistic active learning using a Bayesian approach. *Machine Learning*, 110(6):1199–1231, June 2021. ISSN 0885-6125, 1573-0565. doi: 10.1007/s10994-021-05986-9.
- [154] Joseph Berkson. Bayes’ theorem. *The Annals of Mathematical Statistics*, 1(1):42–56, 1930. doi: <https://www.jstor.org/stable/2957673>.
- [155] José M Bernardo and Adrian FM Smith. *Bayesian Theory*, volume 405 of *Wiley Series in Probability and Statistics*. John Wiley & Sons, 2009. ISBN 978-0-471-49464-5.
- [156] Carl Edward Rasmussen and Christopher K. I. Williams. *Gaussian Processes for Machine Learning*. Adaptive Computation and Machine Learning. MIT Press, Cambridge, Mass., 3. print edition, 2008. ISBN 978-0-262-18253-9.
- [157] Ingo Steinwart and Clint Scovel. Mercer’s Theorem on General Domains: On the Interaction between Measures, Kernels, and RKHSs. *Constructive Approximation*, 35(3):363–417, June 2012. ISSN 0176-4276, 1432-0940. doi: 10.1007/s00365-012-9153-3.
- [158] Jared L. Deutsch and Clayton V. Deutsch. Latin hypercube sampling with multidimensional uniformity. *Journal of Statistical Planning and Inference*, 142(3):763–772, March 2012. ISSN 03783758. doi: 10.1016/j.jspi.2011.09.016.
- [159] John A Nelder and Roger Mead. A Simplex Method for Function Minimization. *The computer journal*, 7(4):308–313, 1965. doi: 10.1093/comjnl/7.4.308.
- [160] Paul Saves. SMT 2.0 : A Surrogate Modeling Toolbox with a focus on hierarchical and mixed variables Gaussian processes. *Advances in Engineering Software*, 188: <https://doi.org/10.1016/j.advengsoft.2023.103571>, 2024. ISSN 0965-9978. doi: 10.1016/j.advengsoft.2023.103571.

- [161] Paul Saves, Remi Lafage, Nathalie Bartoli, Youssef Diouane, Jasper Bussemaker, Thierry Lefebvre, John T. Hwang, Joseph Morlier, and Joaquim R. R. A. Martins. SMT 2.0: A Surrogate Modeling Toolbox with a focus on Hierarchical and Mixed Variables Gaussian Processes. arXiv, October 2023. doi: 10.48550/arXiv.2305.13998.
- [162] J. Mockus, Vytautas Tiesis, and Antanas Zilinskas. The application of Bayesian methods for seeking the extremum. In *Towards Global Optimization*, volume 2, pages 117–129. 1978. ISBN 0-444-85171-2.
- [163] Benjamin Letham, Brian Karrer, Guilherme Ottoni, and Eytan Bakshy. Constrained Bayesian Optimization with Noisy Experiments, June 2018.
- [164] Dawei Zhan and Huanlai Xing. Expected improvement for expensive optimization: A review. *Journal of Global Optimization*, 78(3):507–544, November 2020. ISSN 0925-5001, 1573-2916. doi: 10.1007/s10898-020-00923-x.
- [165] Philipp Hennig and Christian J Schuler. Entropy Search for Information-Efficient Global Optimization. *J. Mach. Learn. Res.*, 14:1809–1837, 2012. doi: <https://dl.acm.org/doi/10.5555/2188385.2343701>.
- [166] Emilie Kaufmann, Olivier Cappe, and Aurelien Garivier. On Bayesian Upper Confidence Bounds for Bandit Problems. In *Proceedings of the Fifteenth International Conference on Artificial Intelligence and Statistics*, volume 22, pages 592–600, 2012. doi: <https://proceedings.mlr.press/v22/kaufmann12.html>.
- [167] JiangSheng Wang, Yang Xu, and JinJun Wang. Slat cove dynamics of multi-element airfoil at low Reynolds number. *Science China Technological Sciences*, 66(4):1166–1179, April 2023. ISSN 1674-7321, 1869-1900. doi: 10.1007/s11431-022-2308-7.
- [168] Paul J. Dellar. Bulk and shear viscosities in lattice Boltzmann equations. *Physical Review E - Statistical Physics, Plasmas, Fluids, and Related Interdisciplinary Topics*, 64(3):11, 2001. ISSN 1063651X. doi: 10.1103/PhysRevE.64.031203.

Appendix A

Flow and Acoustic computation details

A.1 Acoustic Pulse Propagation

A.1.1 Wave Propagation according to Linearized Navier-Stokes

A reduced form of linearized Navier-Stokes equation that captures the adiabatic sound propagation in an isothermal fluid can be written of the form

$$\left(c_0^2 + \left[\frac{4}{3}\nu + \nu_B\right] \frac{\partial}{\partial t}\right) \nabla^2 P' = \frac{\partial^2 P'}{\partial t^2} \quad (\text{A.1})$$

which represent a lossy wave equation. Here c_0 is the thermodynamic speed of sound, $\nu = \mu/\rho_0$ is the kinematic shear viscosity and $\nu_B = \mu_B/\rho_0$ is the kinematic bulk viscosity of the fluid. It has been shown by Dellar [168] that the kinematic bulk viscosity in LBM-BGK isothermal model is $\nu_B = 2\nu/3$ and hence the effective viscosity is $\left[\frac{4}{3}\nu + \nu_B\right] = 2\nu$.

The equation is thus

$$\left(c_0^2 + 2\nu \frac{\partial}{\partial t}\right) \nabla^2 P' = \frac{\partial^2 P'}{\partial t^2} \quad (\text{A.2})$$

Here a definition of the viscous relaxation time, τ_s can be useful and is defined as

$$\tau_s = \left(\frac{4}{3}\eta + \eta_B\right)/\rho_0 c^2 \quad (\text{A.3})$$

and typical values of this quantity are approximately $10^{-10}s$ for gases and $10^{-12}s$ in liquids. Now, a plane wave solution can be assumed of the form

$$P' = \hat{A} \exp[i(\hat{k}x - \hat{\omega}t)] \quad (\text{A.4})$$

On substituting this equation to Eq.(A.2) one obtains the dispersion relation

$$(c_0^2 - i\hat{\omega}2\nu)\hat{k}^2 = \hat{\omega}^2 \quad (\text{A.5})$$

A.1.2 Temporal Analysis

Here if \hat{k} is prescribed as an arbitrary real wave number vector k , a discretised version of Eq.(A.2) reduces to a generalized eigen value problem. The analytical solution for this problem was described by Marié et al. [38] and is of the form

$$\hat{\omega} = -ik^2\nu \pm kc_o\sqrt{1 - (k\nu/c_0)^2} \quad (\text{A.6})$$

The solutions thus represent the acoustic modes propagating with phase speeds $c_T = \text{Re}(\hat{\omega})/k$ and temporal dissipation $\alpha_T = -\text{Im}(\hat{\omega})$, hence of the form

$$P' = \hat{A} \exp(-\alpha_T t) \exp[ik(x - c_T t)] \quad (\text{A.7})$$

where

$$c_T = c_o \sqrt{1 - \left(\frac{k\nu}{c_0}\right)^2} \quad \text{and} \quad \alpha_T = k^2\nu \quad (\text{A.8})$$

A.1.3 Spatial Analysis

If instead of prescribing a real spatial wave number, we can specify a real frequency $\hat{\omega}$, and Eq.(A.5) can be solved for the complex wave number \hat{k} to get $\hat{k} = \pm \frac{\omega}{\sqrt{c_0^2 - i\omega^2\nu}}$. In practice, this captures the distortion in the wavelength and decay of amplitude as the plane wave of fixed frequency propagates in space. Now, the phase speed is given by $c_S = \omega/\text{Re}(\hat{k})$ and spatial dissipation rate as $\alpha_S = \text{Im}(\hat{k})$, thereby giving the form of propagating wave solution as

$$P' = \hat{A} \exp(-\alpha_S x) \exp[i\omega(x/c_S - t)] \quad (\text{A.9})$$

where,

$$c_S = \sqrt{2}c_0 \sqrt{\frac{1 + (\omega\tau_S)^2}{\sqrt{1 + (\omega\tau_S)^2} + 1}} \quad \text{and} \quad \alpha_S = \frac{\omega}{\sqrt{2}c_0} \sqrt{\frac{\sqrt{1 + (\omega\tau_S)^2} - 1}{1 + (\omega\tau_S)^2}} \quad (\text{A.10})$$

A.1.4 Gaster Transformation

Gaster transformation deals with relating the spatial and temporal formulations. If we assume that the spatial wavenumber \hat{k} and temporal frequency $\hat{\omega}$ are both analytic functions of each other in the complex domain, then Cauchy-Riemann equations can be used to show that $\text{Re}(\hat{k}_{\text{spatial}}) \approx \text{Re}(\hat{k}_{\text{temporal}})$ if we assume that $\text{Re}(\hat{\omega}_{\text{spatial}}) \approx \text{Re}(\hat{\omega}_{\text{temporal}})$ and neglect higher order terms. Then the temporal and spatial dissipation rates satisfy

$$\frac{\alpha_T}{\alpha_S} = C_g \quad (\text{A.11})$$

where C_g is the group velocity defined as $C_g = \frac{\partial \text{Re}(\hat{\omega})}{\partial \text{Re}(\hat{k})}$.

A.1.5 Useful approximation for Isothermal Adiabatic Pulse Propagation

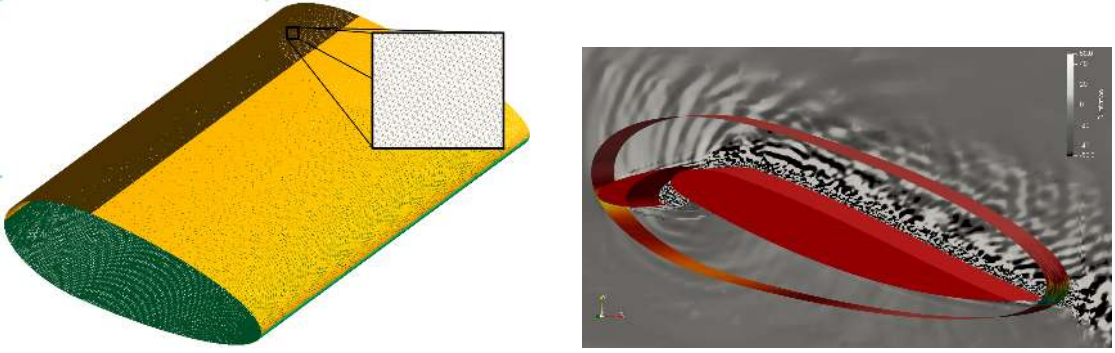
With the above three piece wise analyses, we can make approximations for the case of a typical fluid whose kinematic viscosity $\nu = 1.5 \times 10^{-5} \text{ m}^2/\text{s}$ and thermodynamic sound speed is $c_0 = 343 \text{ m/s}$. Here the terms $\omega\tau$ and $k\nu/c_0$ are of the order of 10^{-5} . Hence the phase velocities and dissipation rates from

temporal analysis reduces to $c_T \approx c_0$ and $\alpha_T \approx k^2\nu$ whereas the spatial sound speed and dissipation rates from spatial analysis reduces to $c_S \approx c_0$ and $\alpha_S \approx \frac{\omega^2}{2c_0}\tau_s = \frac{\omega^2}{c_0} \frac{\nu}{c_0^2}$.

A.2 FWH Surface Tests

A.2.0.1 Oval Surfaces

An oval shaped surface is first tested which is placed close to the airfoil to obtain a close fit to the surface, but large enough to contain the ejected vortices from the slat cove. The surface mesh used for recording the data are shown in Fig.A.1a. The surface together with the airfoil and a slice of the dilatation field are shown in Fig.A.1b. The upper and lower surface data are visualized in Fig.A.2.



(a) Surface geometry with structured meshing to enable calculation using TurbAcAn
(b) Schematic of the surface placement along with airfoil and the dilatation field

Figure A.1: Oval FWH surface geometry and placement

As can be noted, while using the oval surface, the farfield prediction at the suction side tends to generate spurious noise in frequencies greater than 5kHz. This is attributed to the effect of vorticity structures crossing the FWH surface which makes the quadrupole source terms significant[120] and needs to be included in the calculation. However, the volume integrals are computationally inefficient and instead surface truncation or data averaging is done such that neglecting them generates non-significant errors. As can be noted in Fig.A.3b, the spurious hump disappears in the calculated spectra if the surface is truncated at the downstream edge region.

This truncation, however, also cause a drop in the levels for broadband range. On comparing the sound levels in Fig.A.3a and A.3b, the drop in levels are approximately 4.5dB, on average, suggesting that the contribution for farfield sound from the truncated region is significant across the range. A further truncation of the surface to use only the bottom surface shows that a further filtering of the high frequency range is obtained but with little to no further loss in the broadband levels.

For very low frequency, the levels drop with surface truncation and is attributed to the fact that in the FWH routine, the fluctuating pressure is obtained by subtracting a uniform mean pressure from the FWH surface recording. This mean pressure is not the locally averaged pressure for each node and hence leads to an erroneous DC component in the predicted PSD. Nevertheless, very low frequencies typically $< 600\text{Hz}$ are not considered amenable to interpretation in the experimental data as well due to the presence of jet shear layer noise and other background noises in the experimental setup. Also since these additional sources are absent in the simplified simulation, levels at low frequencies are expected to be lower than the experiment.

On further visualization of the vorticity in the suction side using the Q-criterion, it can be seen that the upper side of the surface inevitably cross the path of large scale vortex structures with small magnitude

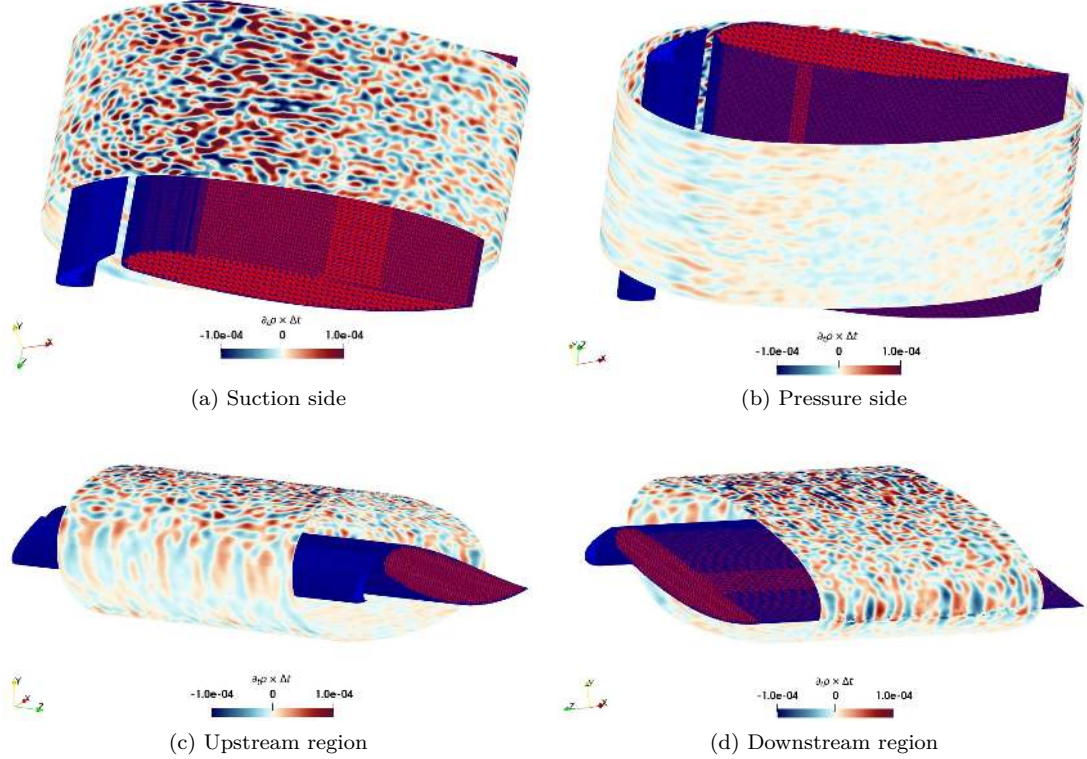


Figure A.2: Density gradient (temporal) on the oval FWH surface

of vorticity. This is visualized in Fig.A.4 using isocontours of a low value of Q_c with $\frac{Q_c}{M^2} = 200$. To avoid this problem we update the FWH surface using a larger C shaped surface that will allow for the upper surface to be placed farther from the HLD.

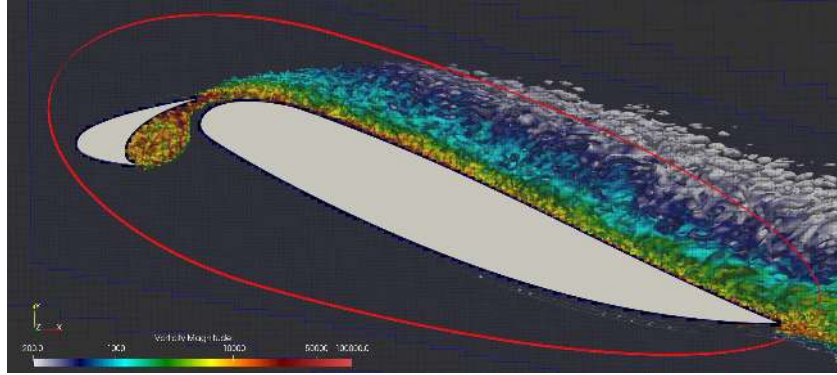
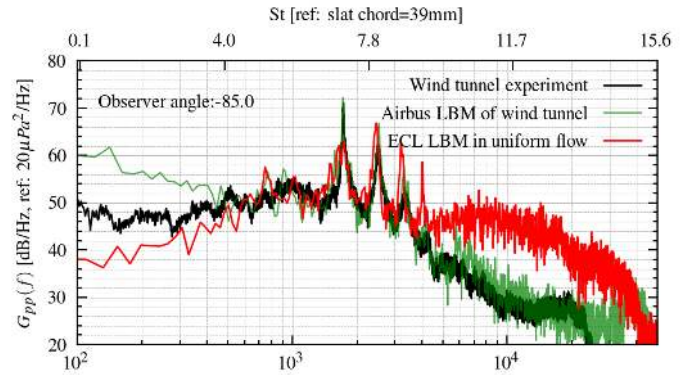
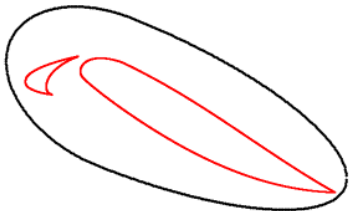


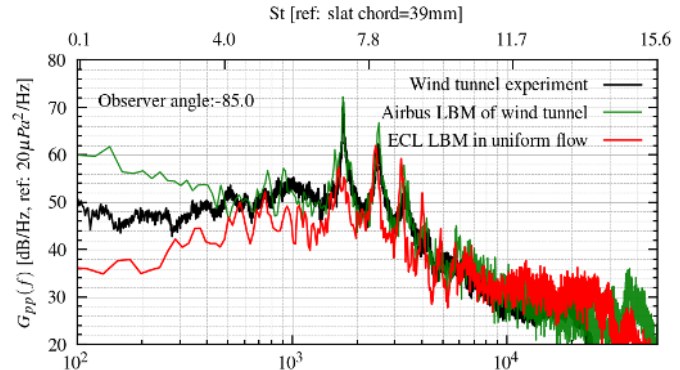
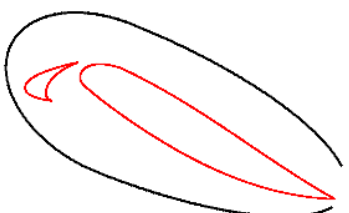
Figure A.4: Flow visualization to demonstrate the low vorticity structures crossing the upper side of FWH surface. Isocontours of Q criterion $\frac{Q_c}{M^2} = 200$ is used to identify the structures and are colored by logarithm of vorticity

A.3 Details of simulation that includes the Wind Tunnel Geometry:

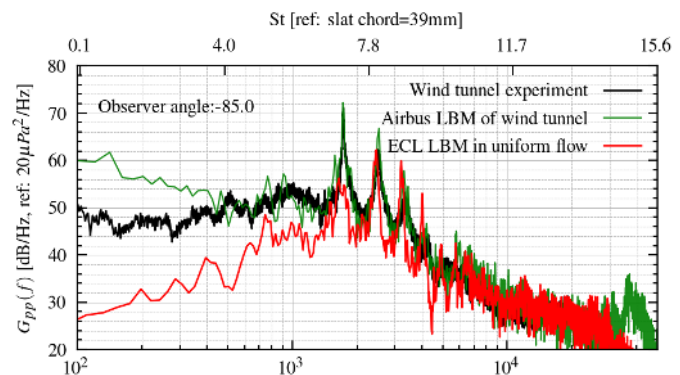
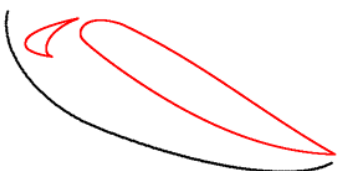
The complete configuration of the wind tunnel setup of the original VALIANT experiment, which includes the converging duct and the lateral support plates, were simulated using the same simulation parameters of the free stream simulation. This simulation was setup by Airbus engineers (Dr. Maxime Itasse and



(a) The full FWH surface without truncation and resulting prediction.



(b) The truncated FWH surface with open trailing edge and resulting prediction showing a reduced low and high frequency contents.



(c) The truncated FWH surface with only bottom surface and resulting prediction showing similar result to truncated full surface but with reduced low frequency contents.

Figure A.3: Farfield spectra obtained using the oval FWH surface compared to 1) a simulation of the same HLD while simulated by including the wind tunnel geometry and 2) the experimental data from VALIANT program[14]

Dr. Florian Guiho) and was reproduced at the ECL facility for the purpose of testing the version of the code for producing reference data. The full simulation requires significantly larger compute resources than free stream simulation since the three dimensional shear layers from the wind tunnel need to be resolved adequately to avoid spurious effects. Hence it needs a few adaptations which make the free stream simulation computationally cheaper while maintaining the same fidelity as when including the wind tunnel. As such, the wind tunnel simulation has the following differences from the free stream case:

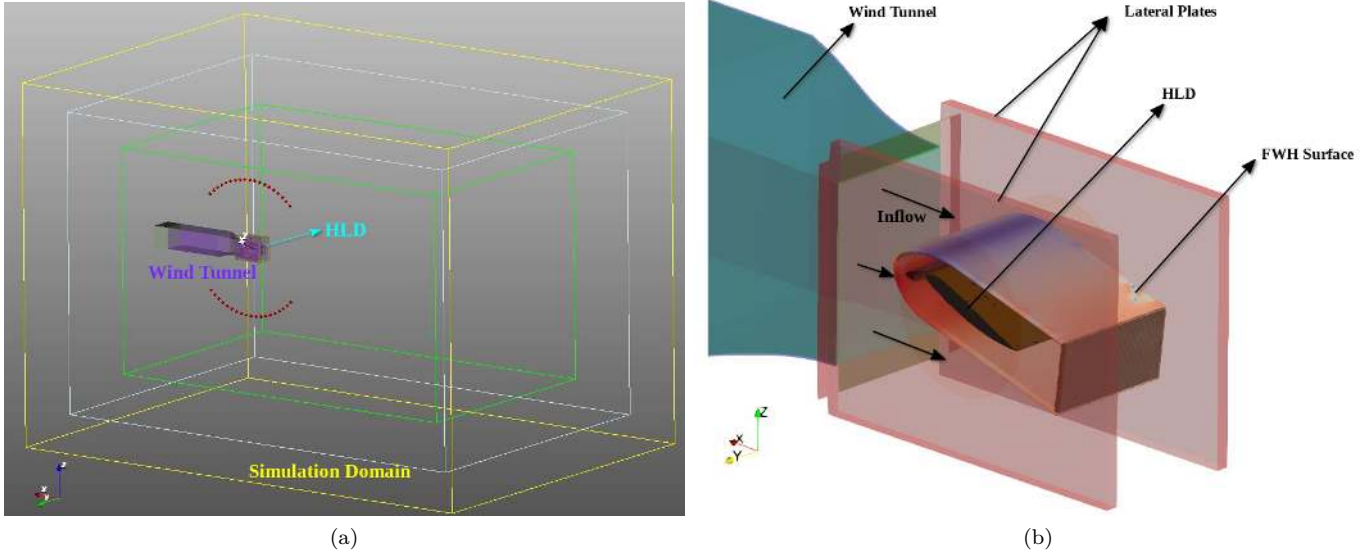


Figure A.5: Wind tunnel simulation setup in ProLB. A) The simulation domain of the wind tunnel geometry with the tunnel and HLD installed. b) Wind tunnel geometry with the FWH surface placed inside the flow

1. The total physical time of wind tunnel simulation is 0.078s, in comparison to 0.2s in the standard free stream case.
2. The spanwise length of the domain is 1 chord length, i.e. 0.3m for wind tunnel simulation whereas it is 0.2m for free flow simulations.
3. Spanwise boundary conditions are set to wall boundaries with no slip at the supporting wall surface and uses a wall model. In free flow simulation, periodic conditions are applied on spanwise boundaries to mimic an infinite spanwise domain.
4. The experimental setup has a nozzle geometry which creates an unsteady shear layer around the airfoil whereas the free flow simulations have only the airfoil surface as a solid generating turbulence and vorticity.
5. For the case of simulation with the inclusion of tunnel geometry, the coordinate axis are chosen differently. The flow is now aligned such that the downstream axis is along the X-coordinate axis and the spanwise direction is along the Y-coordinate axis.

Consequently, for spanwise periodic condition in the free stream case, the acoustic domain is theoretically infinite allowing the waves to propagate without being reflected by solid spanwise boundaries. However, the periodic condition numerically copies the data between the spanwise boundaries thereby enforcing

congruence of the flow variables at both boundaries. Hence, although the domain is infinite for acoustic propagation, it may trigger spurious periodic behaviors in the flow with wavelengths that confer to the domain length.

As mentioned in the Section 3.7 of main text, another known limitation of spanwise periodic conditions is their tendency to enforce artificial uniformity across the span when the computational width is insufficient to capture natural three-dimensional development. This has been investigated in previous works for the same geometry as that used in the present simulations[14] and also for other HLD configurations[31, 20, 98, 125, 126]. Lockard and Choudhari [19] showed that for the development of three-dimensionality of the coherent structures in the cove region, a spanwise extend of $0.8c_s$ is necessary. For the current case simulated, this corresponds to a length of 0.0312m while the actual simulated span length is 0.2m corresponding to more than 6 times the suggested value. Hence this factor is not expected to affect the features of the flow simulated in our case and the three dimensionality is expected to develop unhindered.

A schematic of the simulation setup using ProLB for the full simulation is shown in Fig.A.5a and the placement of FWH surface within the tunnel region is shown in Fig.A.5b. The FWH surface shape remains the same as the chosen C-shape surface from Chapter 04, but is now placed inside the tunnel such that the shear layer from the nozzle edges develops outside the FWH surface completely. Additionally, with a reduced signal length, the computation leads to spectra with a lower resolution.

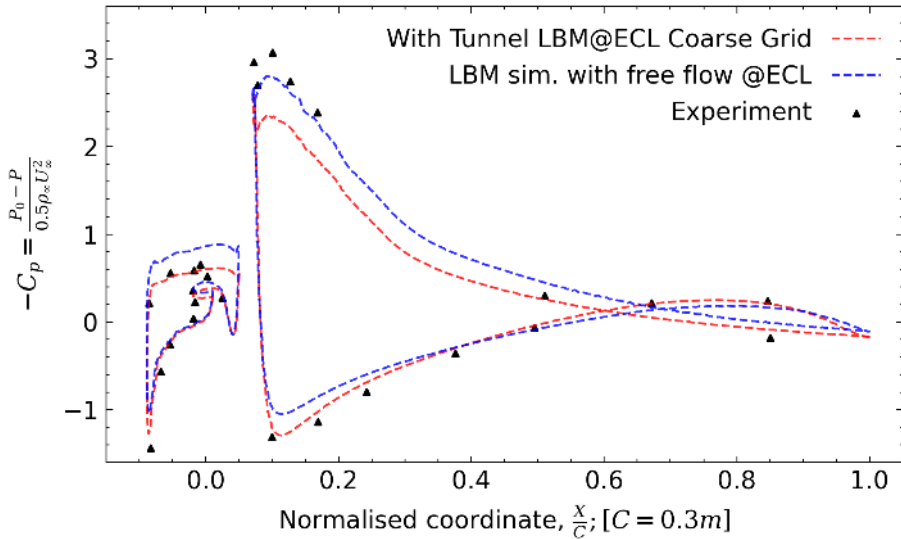


Figure A.6: Coefficient of pressure $-C_p$ over the surface of HLD obtained using the LBM simulations with and without wind-tunnel setup included are compared against the experimental data

The mean wall pressure distribution obtained for the wind tunnel simulation and the free stream simulation are shown in Fig.A.6 in comparison with the same from experiment. The wall pressure distribution on the slat and the pressure side of the airfoils shows a good agreement with the experimental values for both cases. However, there is a strong deviation of the suction peak at the leading edge of airfoil for both airfoil and the slat, and delivers a value lower than the experimental case. The free flow simulation also shows an overall shift in the data due to uncertainty arising from the mean pressure value P_0 used in the experiment which is however not available (we therefore use the standard pressure of 101325 Pa).

For comparison of the spectra obtained using the simulation that includes the wind-tunnel geometry against the experiment, the results are shown in Fig.A.7. A good agreement of the farfield noise with experiment can be noted particularly for the broadband noise levels in the range 1–10kHz. The agreement

is improved at the pressure side observers Probe 2 and 4, which are below and upstream of the HLD (See Fig.4.15 in Chapter 04 for the probe locations). This can be attributed to the effect of the plates affecting the directivity.

Finally, there is good agreement between the hi-fidelity simulation from Airbus and the ECL simulation reproducing the same level of accuracy against experimental data for capturing the noise source mechanisms thereby validating the ECL framework to be deployed to study slat noise.

A.4 Auxiliary data from free flow simulation

The free flow simulation of standard case discussed in Chapter 04 has few auxiliary data which are relevant for the cove dynamics. A more exhaustive set of wall pressure plots are given in Fig.A.8, A.9, A.10, and to show the variation of the spectra along the wall geometry. As can be noted the wall pressure spectra along the wall shows a progressive variation of the tonal peaks corresponding to the same in far-field spectra.

For slat geometry, in region near the cusp the turbulent fluctuations are weaker compared to the trailing edge and hence captures the tonal frequencies with a higher level than the turbulent fluctuations. Near the trailing edge, these tonal features are submerged by the stronger levels of turbulence.

For the main element, the strongest peak is seen for Probe 21 for 1771Hz, corresponding to the first main tone. This location is also close to the cusp. For other probes which are farther from the cove but on the pressure side, the tones are visible with progressively weakened levels towards the trailing edge. On the suction side, much like the slat trailing edge, the turbulent flow submerges the tonal perturbations to render a largely broadband spectra. Towards the main element trailing edge on the suction side, the periodic perturbations from the cove are weak and represent the hydrodynamic perturbations due to the reattached turbulence.

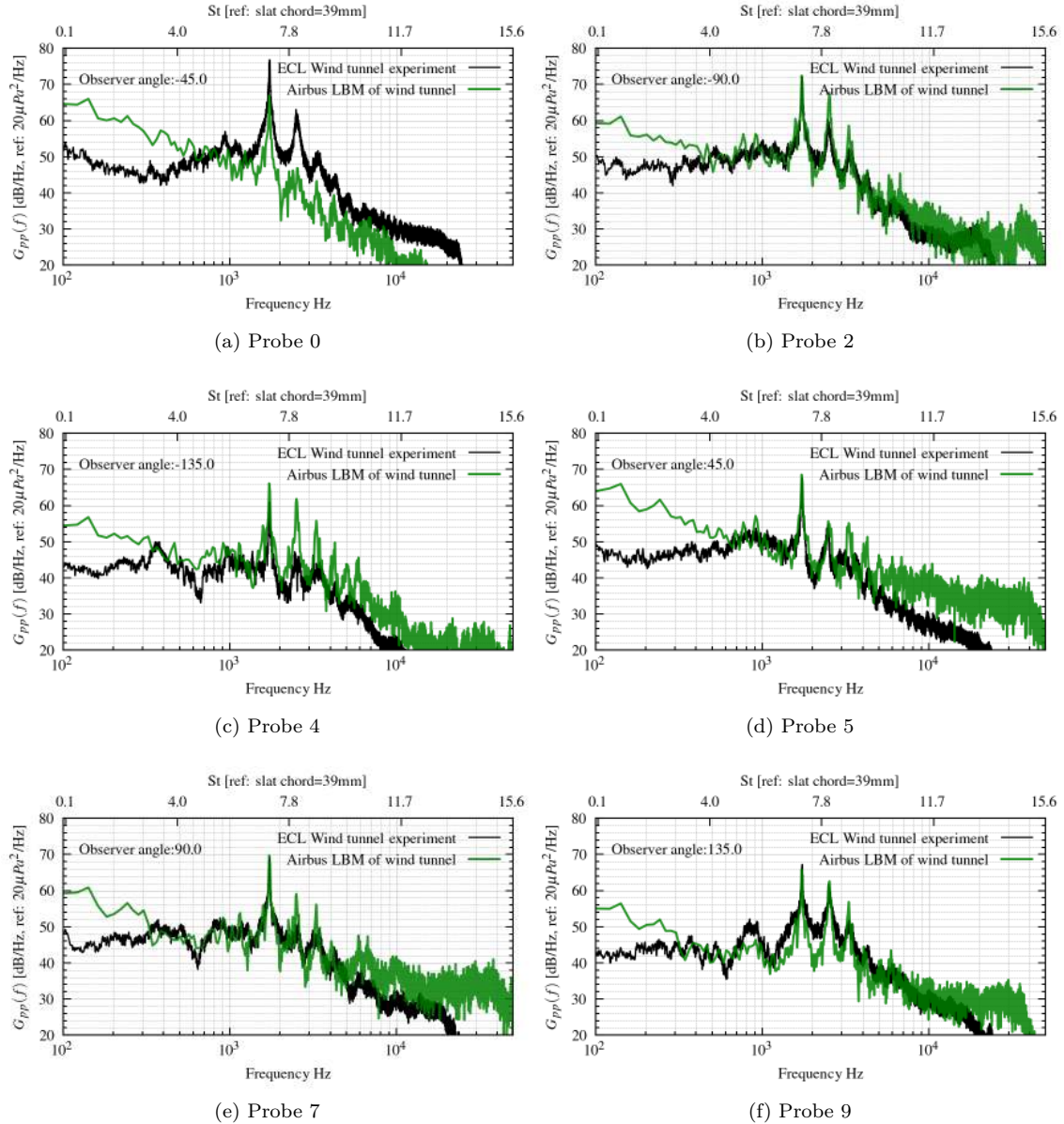


Figure A.7: The sound pressure spectra computed using simulation run by Airbus using *ProLB* and FWH approach for the full wind-tunnel installation and for physical time of 0.2s, obtaining a closer match between simulation and experiment. Signal spectra parameters: Total time= 0.2s, NFFT= 8100, Sampling Freq.= 180405 Hz, N.Avg.= 6 and $\Delta f = 22$ Hz

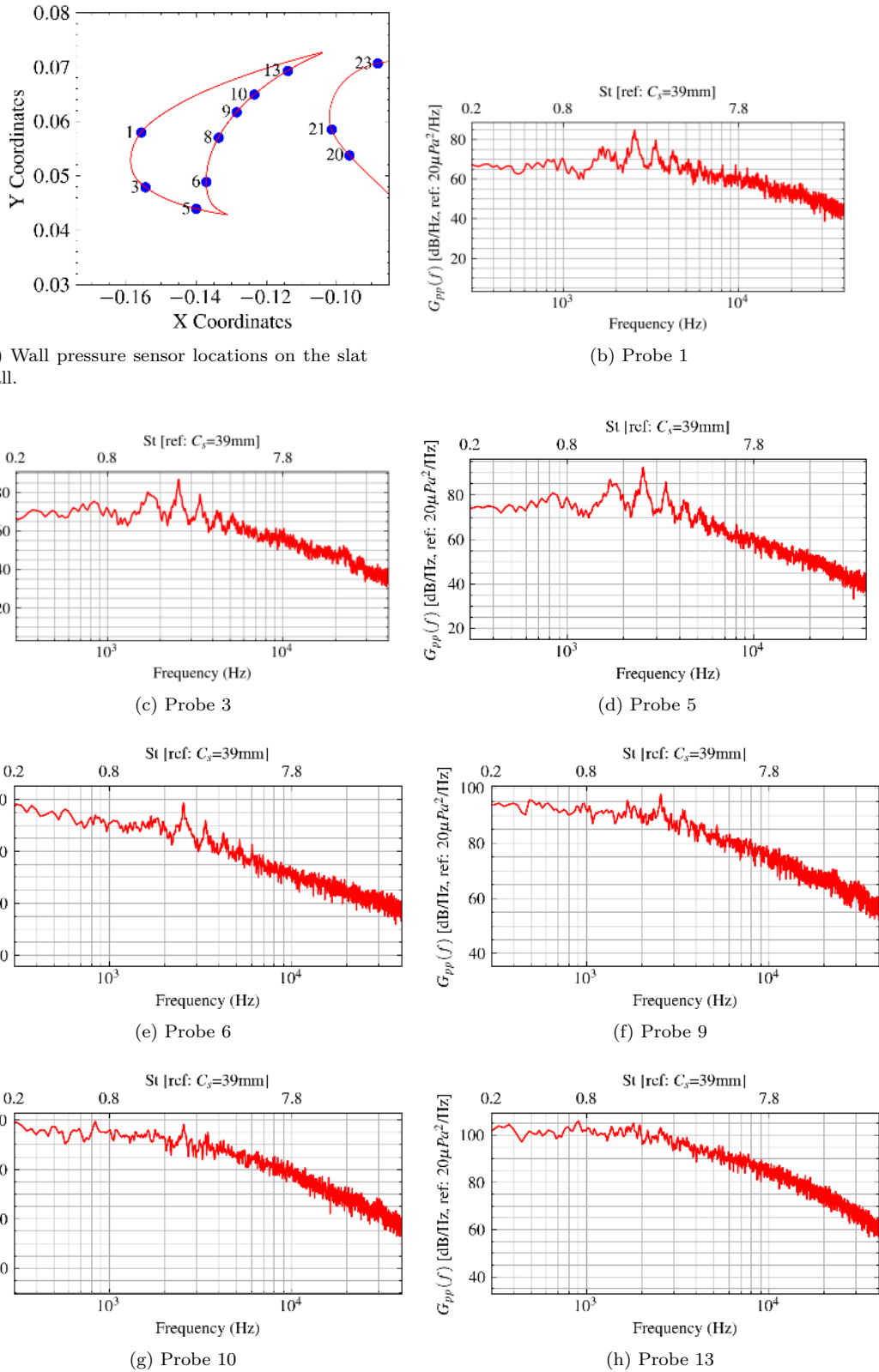
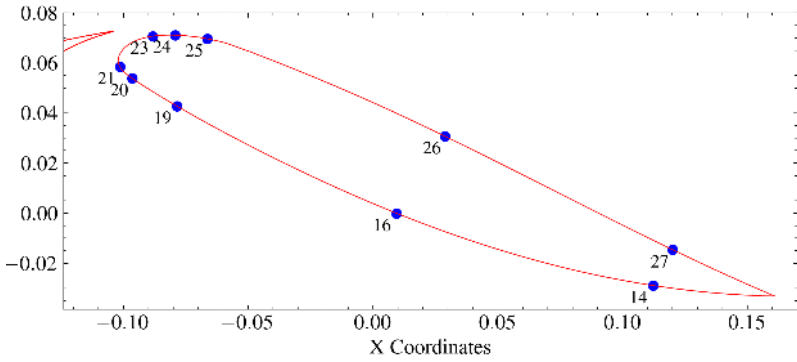


Figure A.8: Wall pressure spectra for select probes on the slat wall placed along the spanwise center plane



(a) Select wall pressure sensor locations on the main element.

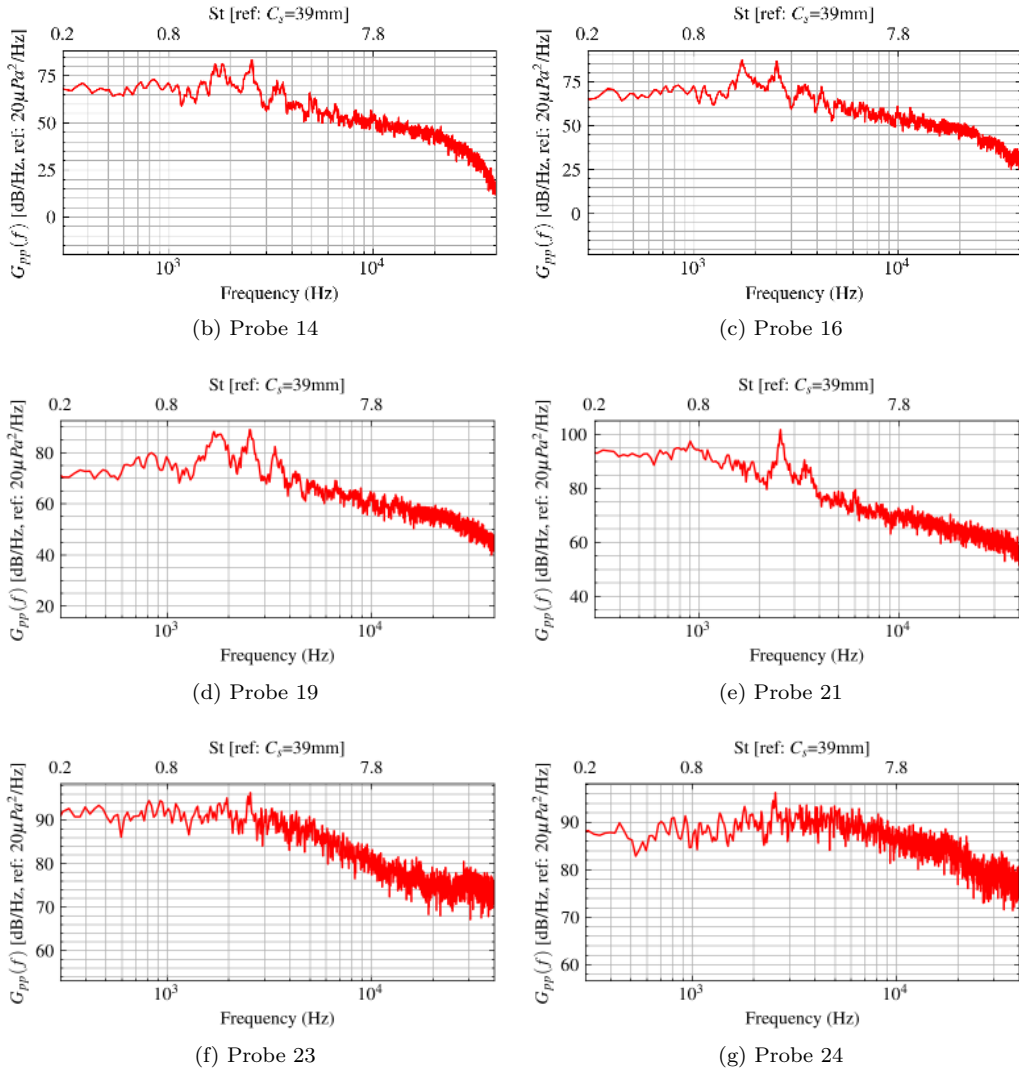


Figure A.9: Wall pressure spectra for select probes on the main element wall and on spanwise center plane.

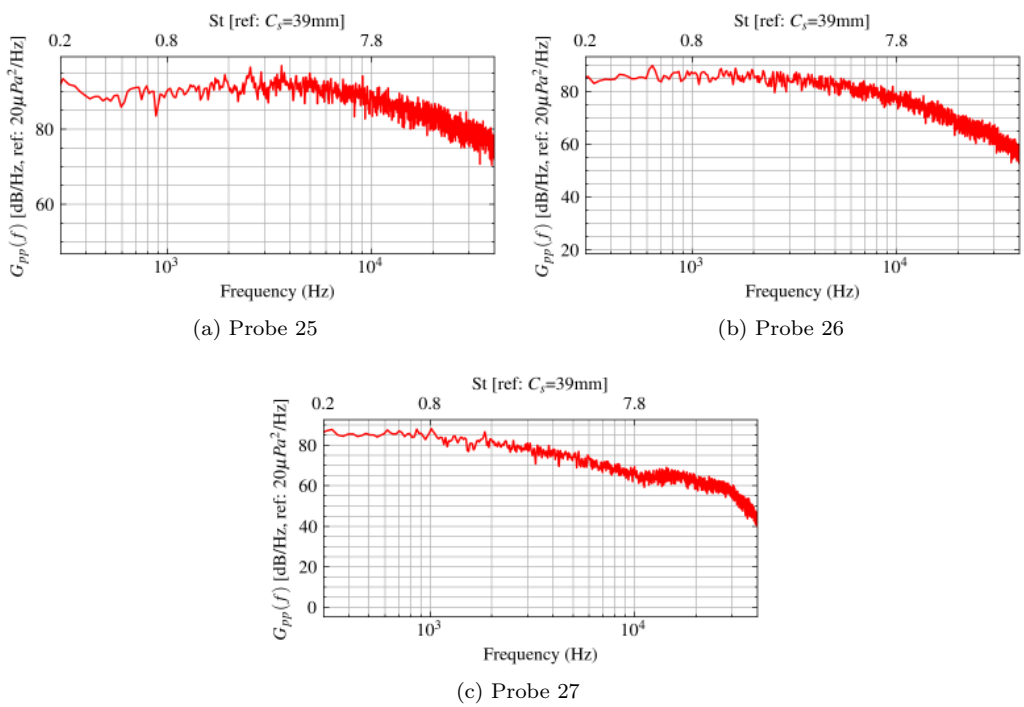


Figure A.10: Wall pressure spectra for select probes on the main element wall and on spanwise center plane.

Appendix B

Dataset from Bayesian Active Learning

B.1 Data Description

To enable reuse and further extension, the dataset we obtained from the current thesis work is documented here. It is first organized into cases representing different slat positions. For each case, the data used to generate the LBM simulation case files are available in the pre-processing folder “preproc” with the connected scripts in the “templates” folder for editing the files according to case specific needs. For the template based setup that we used, the configuration files are largely the same for different cases except for the slat geometry file which is updated with the coordinate translation necessary according to the slat coordinates. For each case we then use the following conventions.

Case names and regular expression:

Each test case for slat position coordinate is represented by a regular expression (regex). The four slat coordinates, namely Angle of Attack (AOA), Slat Deflection Angle (SDA), Slat Gap (SGP), and Slat Overlap (SOL), together with the coordinate values are used to form the case specific regex. Characters ‘p’ and ‘n’ are prepended to the value to denote positive and negative signs respectively. The python3 snippet used to generate the regex, given the four coordinate values are given below.

```
regex = f'AOA{AOA:+05.1f}'  
      + f'SDA{SDA:+05.1f}'  
      + f'SGP{SGP:+05.1f}'  
      + f'SOL{SOL:+05.1f}'  
  
regex = regex.replace('..', '')  
regex = regex.replace('+', 'p')  
regex = regex.replace('-', 'n')
```

Folder structure

Each of the simulation case data is stored in a folder named using the above-mentioned regex. Within each case folder, the data is archived as follows

- Pre-processing - The ‘preproc’ folder contains files that are inputs to the LBPre module. It includes case geometries in which the slat.stl file from master folder is transformed to obtain the file with case specific positioning, the probe coordinates transformed according to case requirement, and the FWH surface files. The data in this folder is then inputted to LBPre case file using its scripting features.
- Results - The folder ‘results’ contains, for each of the simulated case, the data files generated by ProLB solver. The result files are formatted consistently across cases and contains the following:
 1. Mean flow recording - MeanQuantities.xmf and corresponding .h5 data file:
The flow recordings are generated for the full domain of simulation and are recorded at full resolution of the mesh. Temporal averaging corresponds to 5 chord pass times and recording starts from the latest possible time step in the simulation.
 2. FWH surface recordings - FWH_PermeableSurface_Recording_outsurf.xmf and corresponding .h5 data file:
The FWH surface recordings are for velocity, pressure, and density data. Sampling rate is chosen according to requirements discussed in the main text. The recording frequency is 180405Hz, and has a total of 49200 timesteps enabling 6 averaging bins, with 8200 steps per bin for the Welch method for PSD calculation. The resulting spectra can be obtained at a resolution of 44Hz.
 3. Q-criterion and Vorticity - UnsteadyCoveRecordingRes1Set#_grad.xmf and corresponding .h5 data file:
Unsteady data for Q-Criterion and Vorticity vectors in the slat cove region are recorded for visualizing the cove vortex behavior. The sampling rate is kept lower than FWH surface recording to save storage space and its sampling at 22550Hz is found sufficient for unsteady visualizations of the cove vortex evolution. A total spanwise length of 0.016m are recorded around the span-center plane from a total of 0.2m of spanwise length of the simulation. The recordings are saved in 3 sets along with the spanwise length to enable faster post-processing also.
- Post-processing - The folder ‘postproc’ contains, for each of the simulated case, data files related to post-processing of the data. The post-processed data primarily has visualizations for the mean flow recordings, vorticity, and wall pressure coefficients. A slice of the mean recording in the cove region at center-span plane is also available as MeanData.csv. This recording is used for obtaining streamlines and the shear layer shape.

B.2 All simulations and results

All Flow Cases

All simulations that is a part of results in thesis are given in the Table.B.1. The variables are Angle of Attack (AOA), Slat Deflection Angle (SDA), Slat Gap (SGP) and Slat Overlap (SOL). All angles are in degrees and lengths in mm. A total of 33 cases are documented of which the first case is the reference case studied in Chapter 04. This corresponds to the default slat positioning with respect to the airfoil and the coordinates are obtained from geometry available from the original VALIANT project[15]. The first three cases are the result of simulations that varied only the slat gap progressively. Among simulation 4 to 32, 10 are selected using the Latin Hypercube with Multi-dimensional uniformity to enable initial exploration of parameter space and 18 are run using the Bayesian Active Learning sampling technique.

Case No.	AOA (deg)	SDA (deg)	SGP (mm)	SOL (mm)
Std.	18.0	35.2	7.94	-6.36
1	18.0	35.2	4.94	-6.36
2	18.0	35.2	8.94	-6.36
3	18.0	35.2	9.94	-6.36
4	13.0	36.0	4.00	-1.80
5	14.0	35.2	7.10	3.00
6	14.7	35.2	9.30	7.60
7	15.0	24.0	7.00	-3.60
8	15.2	35.2	6.30	7.20
9	15.9	35.2	6.70	5.10
10	16.0	32.0	8.20	-5.40
11	16.4	35.2	4.30	-2.30
12	16.4	35.2	4.30	2.30
13	17.4	35.2	8.50	-4.90
14	17.4	35.2	8.50	4.90
15	18.0	23.9	6.70	-5.10
16	18.0	24.0	6.40	-5.40
17	18.0	24.0	7.00	-5.40
18	18.0	25.5	4.30	-2.30
19	18.0	27.6	5.30	-6.30
20	18.0	28.6	7.80	-5.90
21	18.0	34.0	8.80	-8.10
22	18.0	34.0	9.40	-8.10
23	18.0	34.7	9.30	-7.60
24	18.0	36.0	8.80	-8.10
25	18.0	36.5	7.10	-3.00
26	18.0	39.3	9.40	-4.20
27	18.1	35.2	7.80	5.90
28	18.6	35.2	4.80	3.20
29	19.0	32.0	6.40	-0.90
30	19.2	35.2	5.30	6.30
31	19.5	35.2	9.40	-4.20
32	19.5	35.2	9.40	4.20

Table B.1: List of parametric cases simulated and data archived.

B.2.1 Auxiliary results

B.2.1.1 Shear layer and recirculation bubble shapes

The results for shear layer shape extraction for cases from Bayesian Active Learning simulations are given in Fig.B.1. The shear layer shape varies with respect to the position of the slat. The most sensitive variable to the shape is the Slat Overlap. As the slat overlap is negative by definition if the slat trailing edge is upstream of the leading edge of the main element, the value needs to decrease to increase slats proximity to the main element. As it is increased, the shear layer readjusts such that the flow has to reverse its direction progressively in order to circumvent the main element's leading edge. This introduces a strong reversal of curvature to the shear layer. The initial curvature is also affected such that when slat overlap is decreased, i.e. slat move closer to the main element, the initial shear layer from the slat cusp takes a more tangential path to the free stream flow, only to reverse its direction strongly. As the flow is more tangential to the incoming flow below the slat cusp, the initial curvature of the shear layer decreases leading to less instability effects due to curvature.

Conversely, when the slat overlap is decreased, i.e. the slat move further away from the main element, the cove recirculation shape converges such that the shear layer has a regularized curvature distribution. This can be noticed for Case 22, which is the most noisy case among the dataset and the coordinates are close to the standard configuration.

It is also possible to have configurations whose initial curvatures are excessively high by maintaining a high slat gap and a positive slat overlap. In such cases like Case 5, for example, the flow is strongly deviated towards the trailing edge from the initial shear layer instead of having a tangential flow. Such cases however also tend to have an early impingement with a significantly small recirculation region if the

slat overlap is too high.

B.2.2 Far-field Noise spectra

The farfield noise spectra for all cases simulated are given in Fig.B.2. All computations follow the same parameters as explained in Chapter 03 and 04. Case 22 has the strongest broadband and tonal components and since it is closest to the experimental case, this case is chosen as the basis of comparison.

For cases which are close to Case 22, the broadband and tonal noise are largely significant. Cases where the slat gap and overlap are suited, the tonal frequency also shows changes in the selection of frequency selection. The first four tones are shown to have a high degree of correlation in their variation with respect to the slat position. The fifth tone however maintain a stable frequency and can be present even in the absence of other tones.

B.2.3 Shear Layer Curvature Profiles

The shear layer curvature profiles are given in Fig.B.3. The curvatures are computed along the mean shear layer and for a streamline whose origin near the cusp is chosen as detailed in Chapter 04. The curvature is calculated as the geometric curvature of the streamline and for the mid-span plane.

The curvature inflection point can be noted as the location of local drop in the curvature magnitude for each case. The location of impingement is marked by the second sharp peak after this inflection. For most cases, the curvature calculation after impingement location accrues a strong numerical noise. This is due to the low convergence of the flow features due to low frequency oscillating components in the flow leading to non-smoothness of the streamline calculation from the averaged velocity field. Case 22 which serves as the most noisy case is included for all plots to enable comparison.

B.2.4 Curvature Richardson Numbers

The Curvature Richardson numbers for all cases in the dataset are given in Fig.B.4. The calculation is detailed in Chapter 04. The Curvature Richardson numbers are shown to have consistent distribution across cases where the mean value is maintained above 0.1 and with one inflection point along the shear layer where the curvature reverses sign.

The cases which shows a strong broadband and tonal noise given a red highlight whereas for cases whose characteristic noise is attenuated due to excessive overlap is given a green highlight. The Richardson number profile for the most noisy Case 22 is also included to enable comparison.

B.2.5 Spanwise Cells

The spanwise modulation of spanwise velocity is visualized using 3D isocontours for spanwise velocity. These cells vary according to the shear layer shape and recirculation cavity shape. The same for all cases in the dataset are shown in Fig.B.5. As can be noted, the formation of cells and their cell size is dependent on the cove recirculation shape driven by the slat positioning. The presence of the shapes is also seen to be dependent on the cases where there exists cases with no spanwise cell formation, cases with 3, 4, and 5 cells in total across the span. This also serves to bolster the notion that formation of the spanwise cells is not an artifact of the spanwise periodic condition but a physical manifestation of the centrifugal instability of the flow inside the cove recirculation.

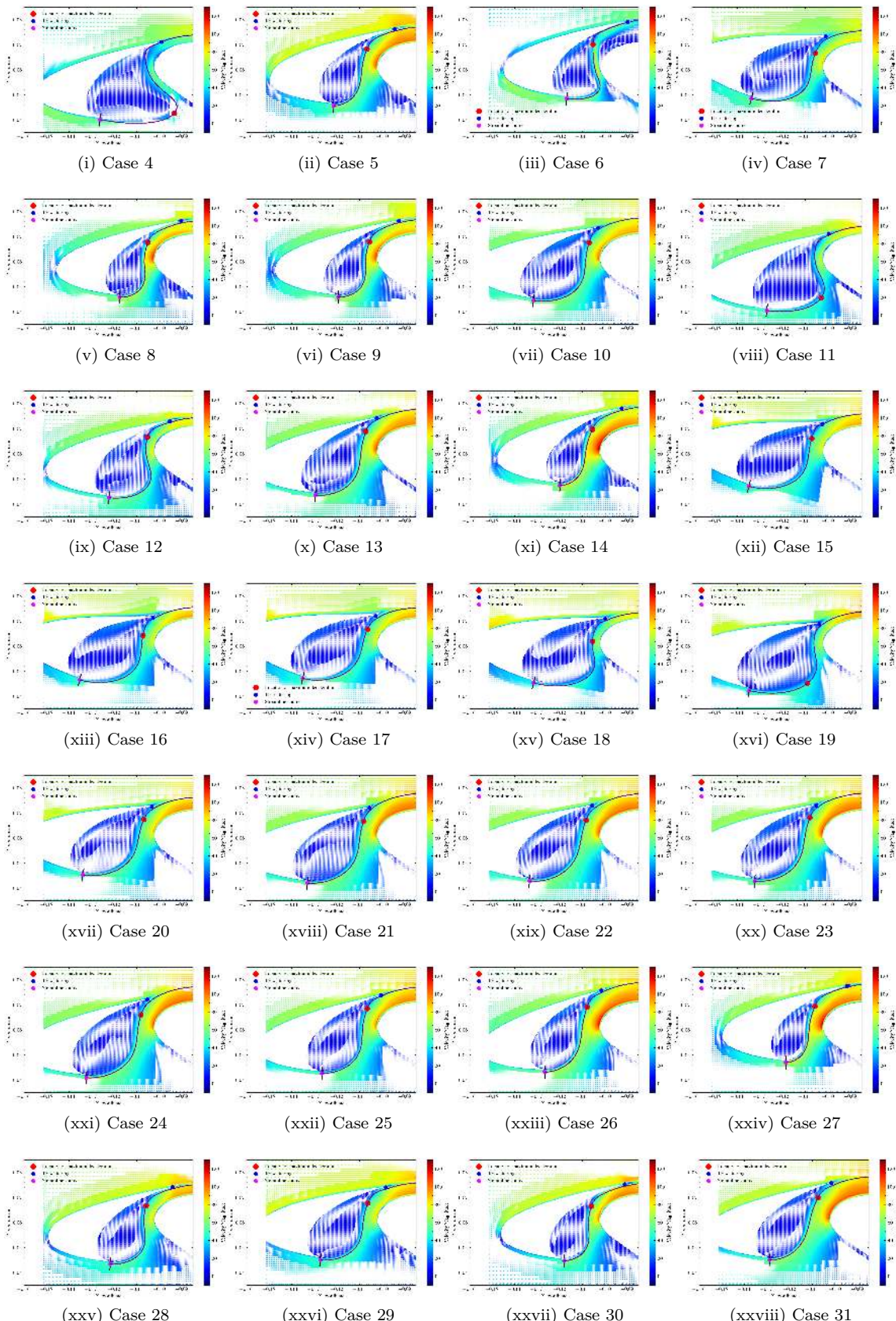


Figure B.1: The shear layer trajectory at mid-span plane obtained using time integration of the mean velocity field for parametric cases in the dataset.

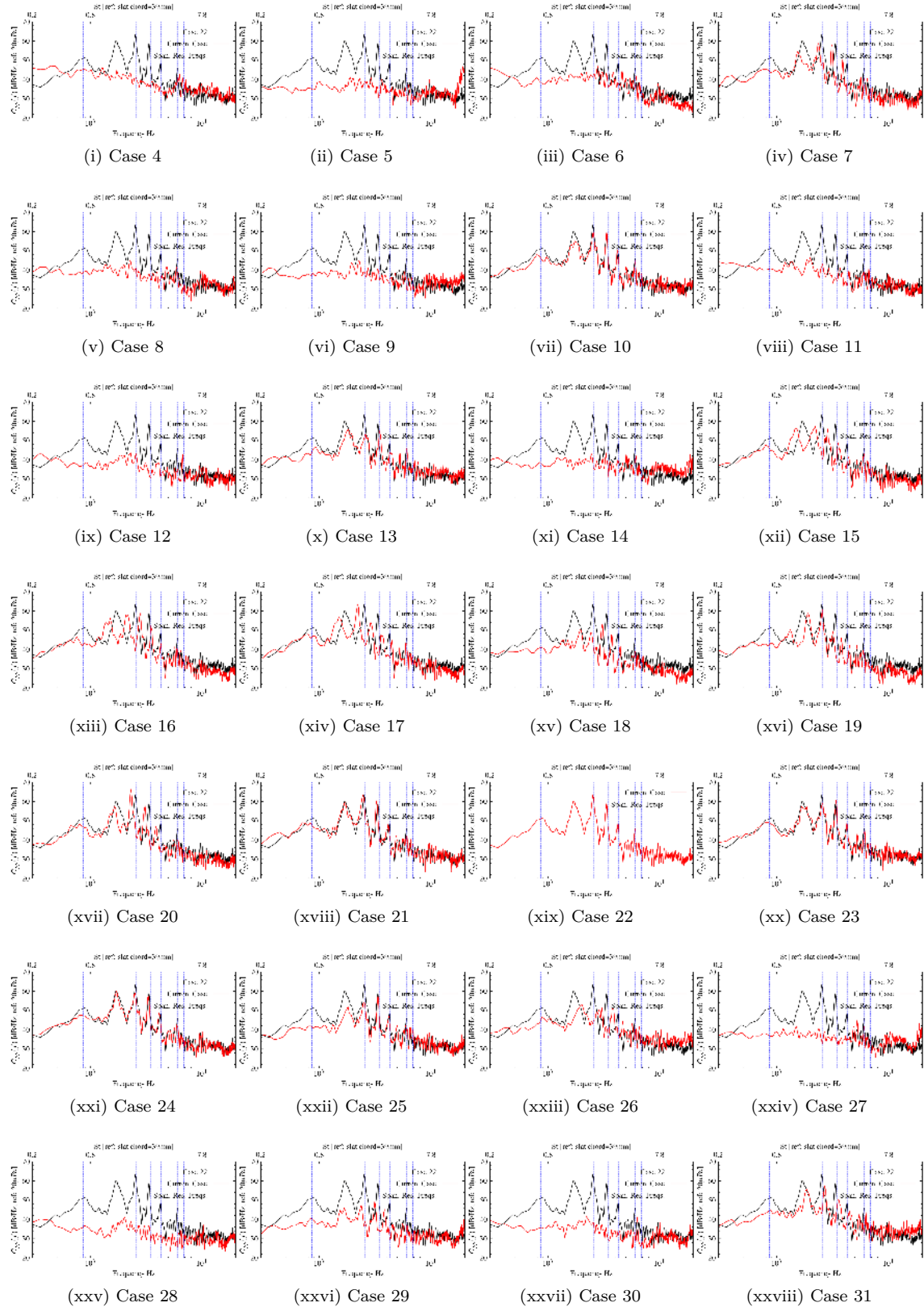


Figure B.2: Farfield noise spectra for parametric cases obtained using the LBM-FWH computation. Observer location is at 90° to the airfoil at the pressure side.

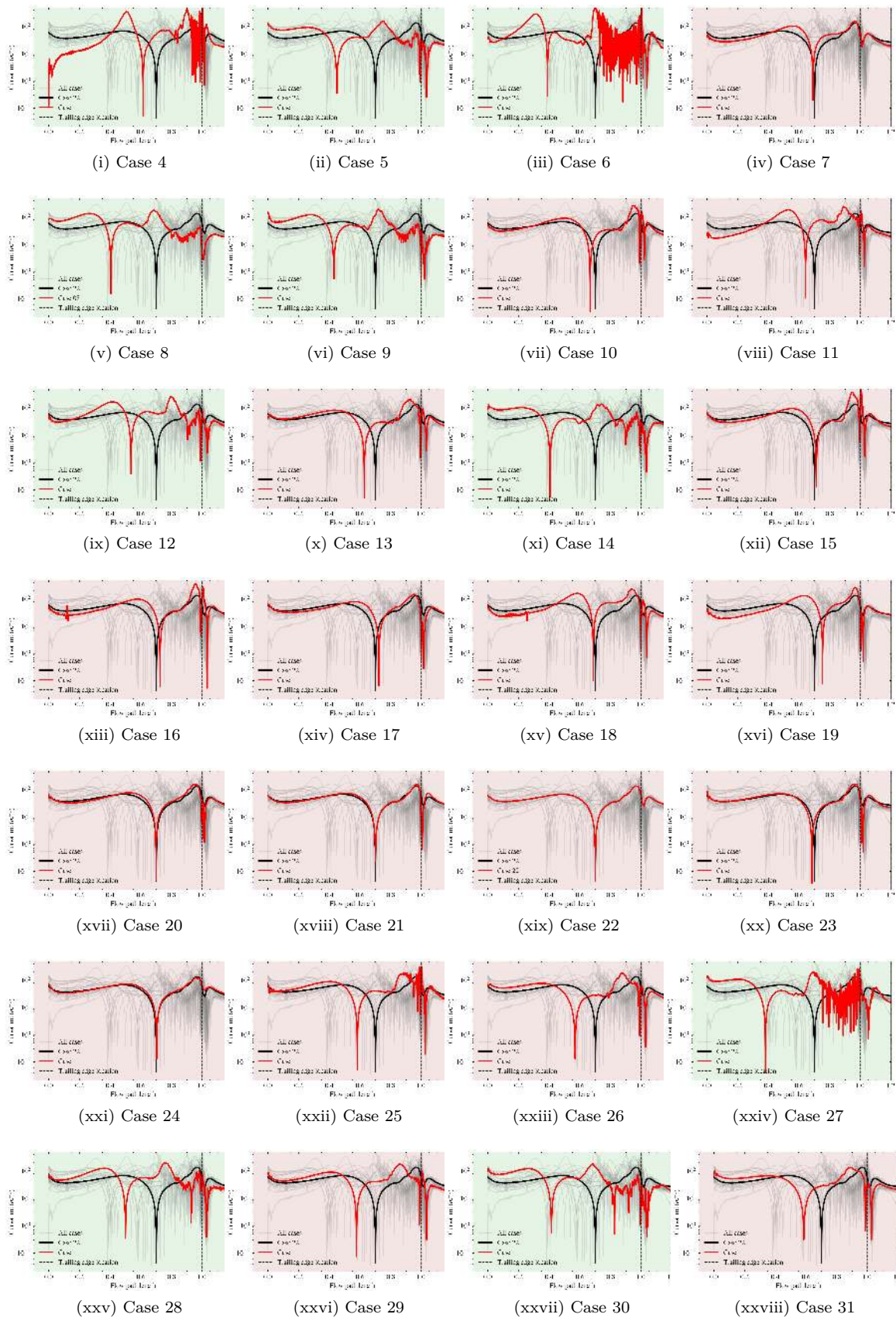


Figure B.3: Curvature profiles along the mean shear layer for parametric cases in the dataset

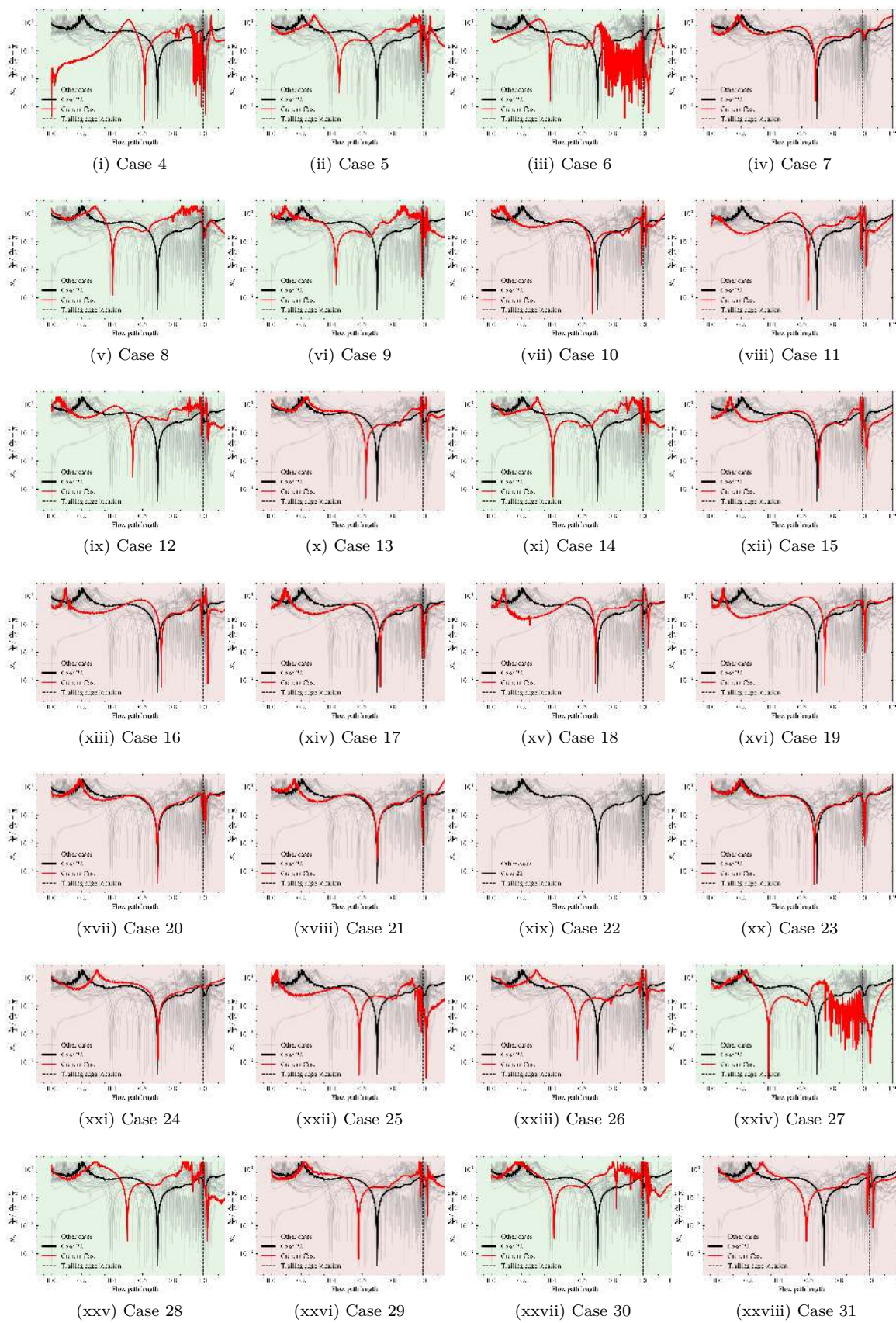


Figure B.4: Curvature Richardson Number profiles along the mean shear layer for all cases in the dataset

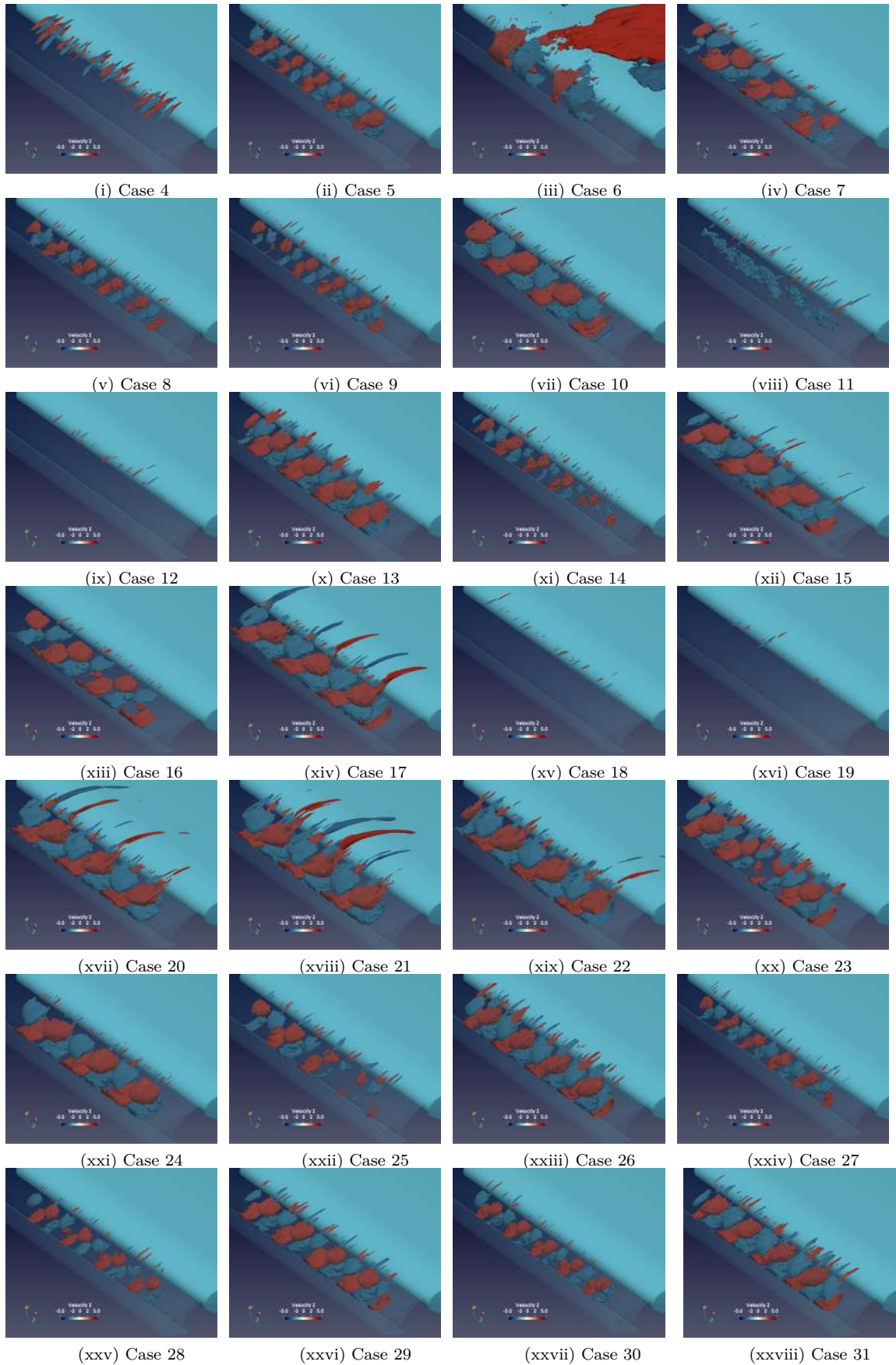


Figure B.5: Spanwise cells of spanwise velocity demonstrated using 3D isocontours of the same for all cases in the dataset.

B.2.6 Spanwise Variation of Spanwise-Velocity Spectra

The spanwise spectra of spanwise component of velocity near the slat cusp revealed a low frequency localized oscillation at the diverging planes. These oscillations were shown to be restricted to the vicinity of diverging planes in Chapter 04. The same was also shown to correspond to the recirculation frequency based on the low speed recirculation velocity inside the cove in Chapter 06. To demonstrate that this oscillation is a consistent feature across cases with consistency of the low frequency at around 200Hz, the spanwise variation of the spectra with appropriate color scale is shown in Fig.B.6, B.7 and B.8.

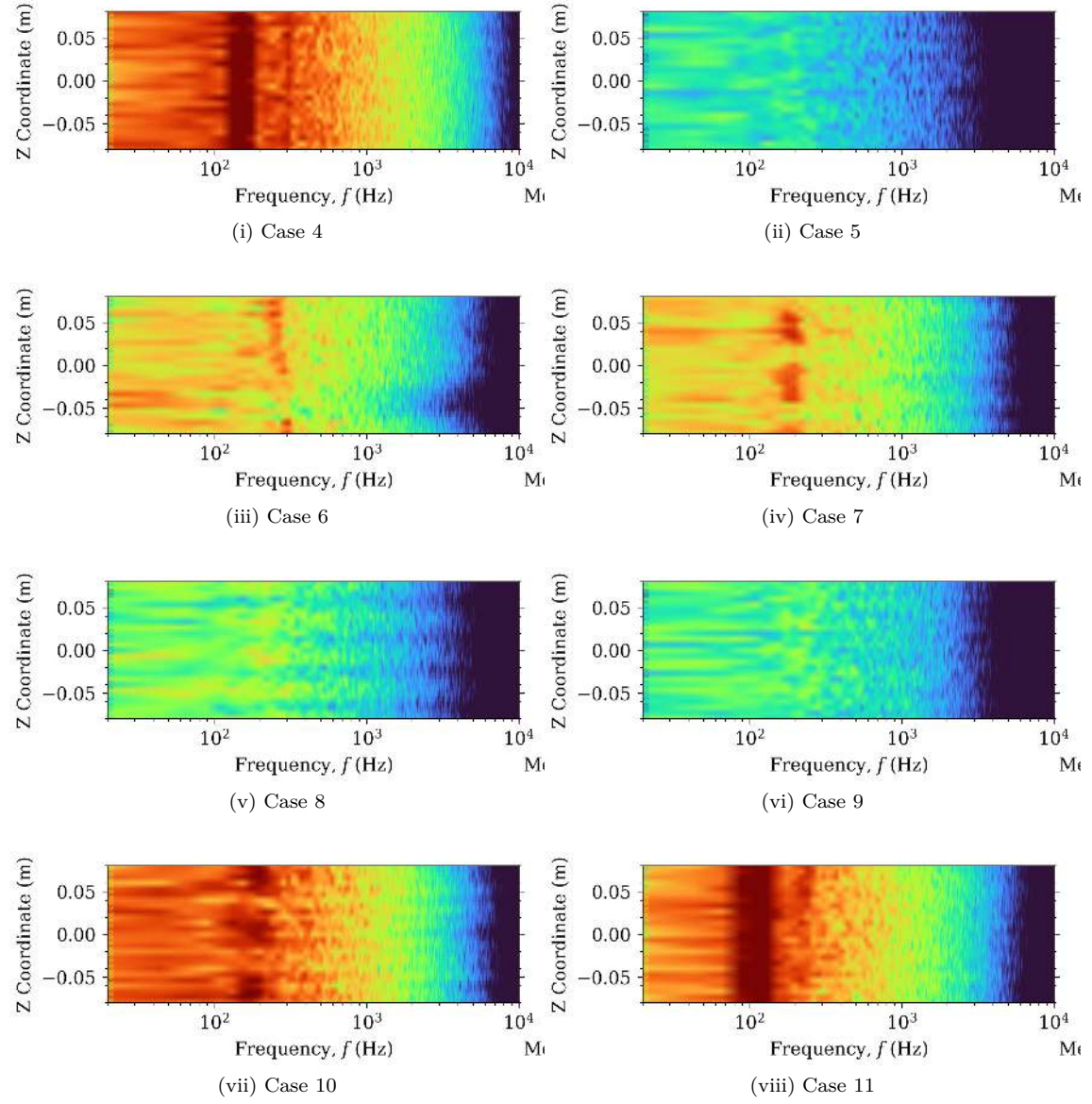


Figure B.6: Power spectral density of spanwise velocity component as a function of spanwise location

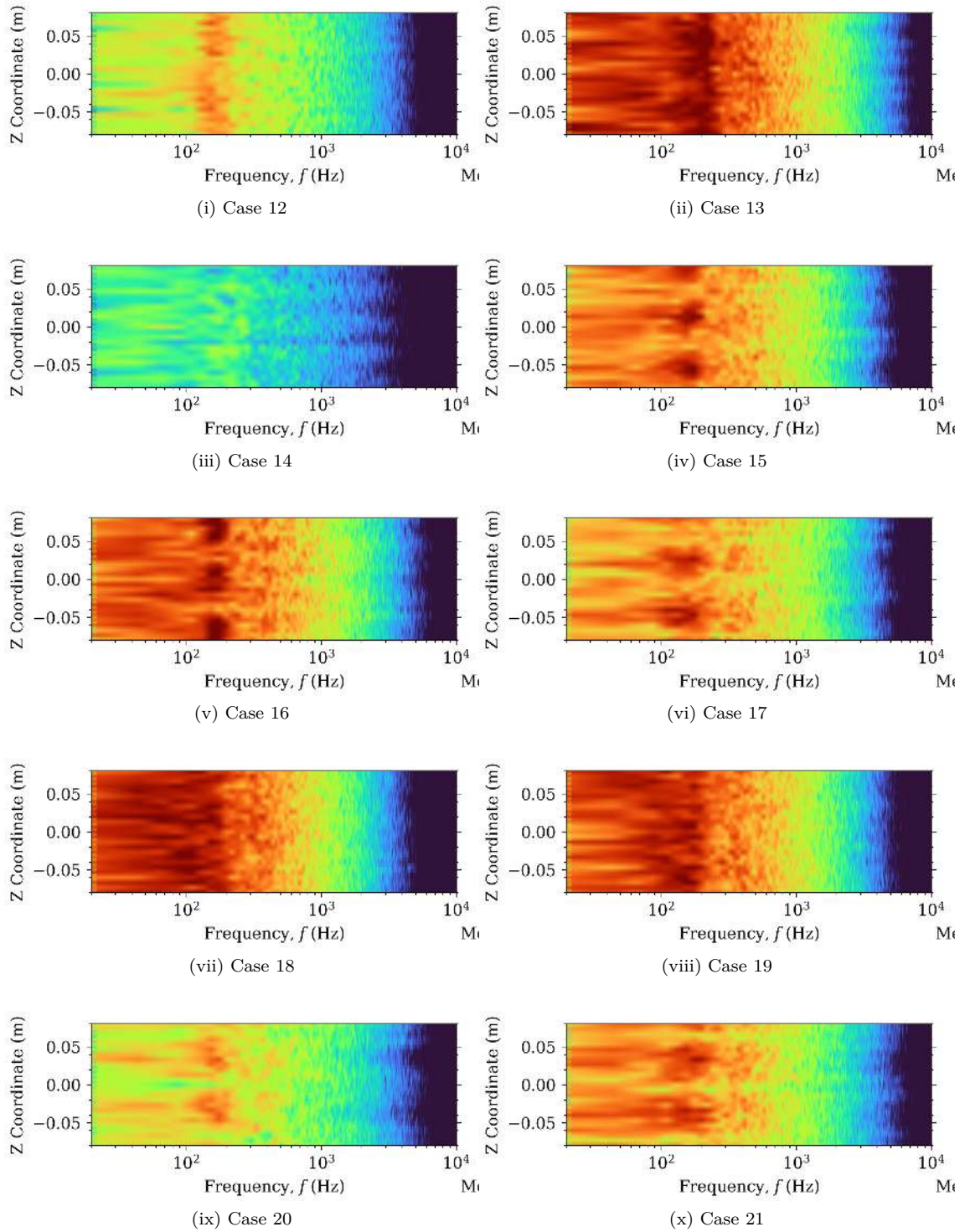


Figure B.7: Power spectral density of spanwise velocity component as a function of spanwise location

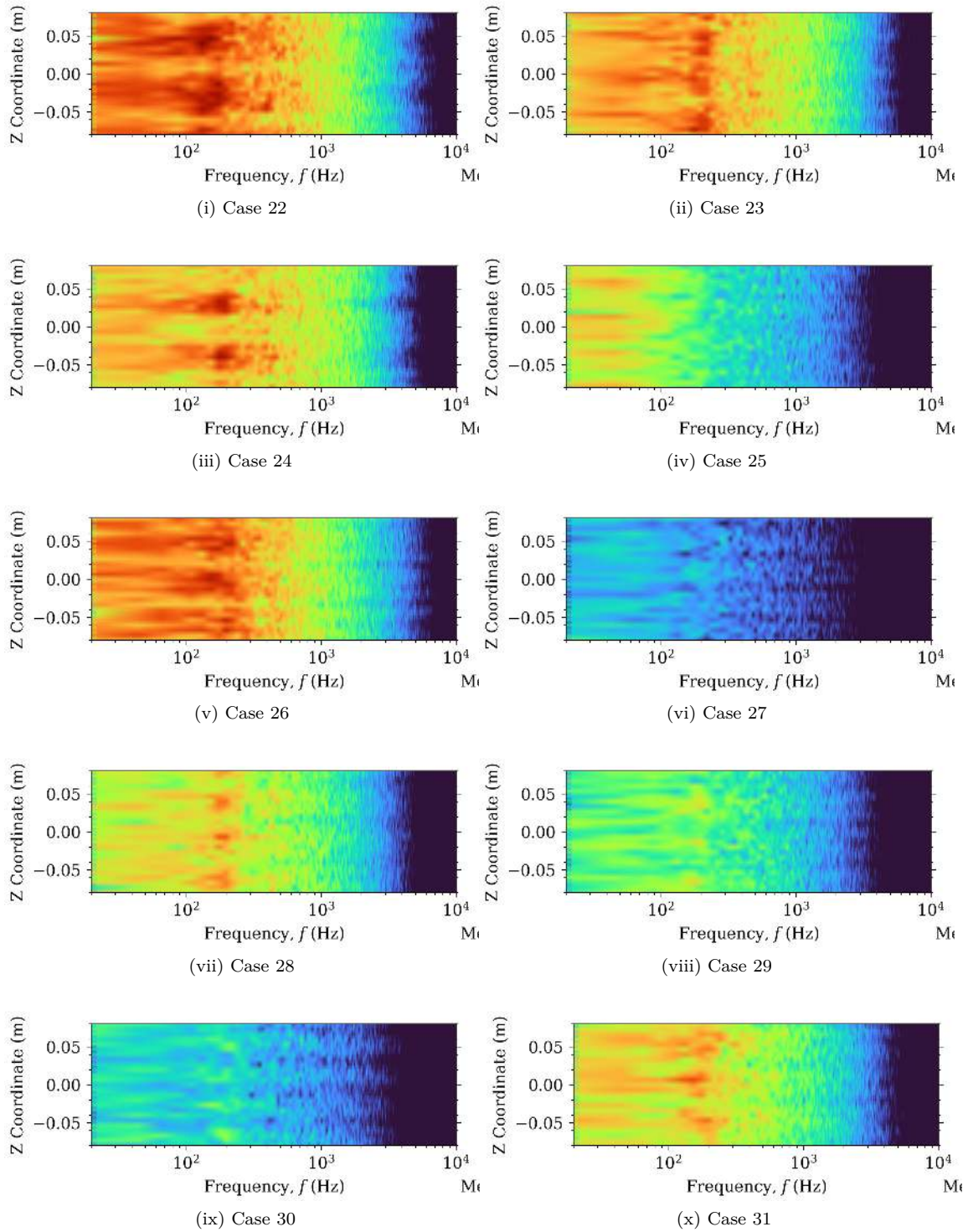


Figure B.8: Power spectral density of spanwise velocity component as a function of spanwise location